Springer Series in Solid and Structural Mechanics 8

Michel Frémond
Franco Maceri
Giuseppe Vairo *Editors*

Models, Simulation, and Experimental Issues in Structural Mechanics

Springer

Springer Series in Solid and Structural Mechanics

Volume 8

More information about this series at http://www.springer.com/series/10616

Michel Frémond · Franco Maceri
Giuseppe Vairo
Editors

Models, Simulation, and Experimental Issues in Structural Mechanics

Springer

Editors
Michel Frémond
Department of Civil Engineering
and Computer Science
University of Rome "Tor Vergata"
Rome
Italy

Franco Maceri
Department of Civil Engineering
and Computer Science
University of Rome "Tor Vergata"
Rome
Italy

Giuseppe Vairo
Department of Civil Engineering
and Computer Science
University of Rome "Tor Vergata"
Rome
Italy

ISSN 2195-3511 ISSN 2195-352X (electronic)
Springer Series in Solid and Structural Mechanics
ISBN 978-3-319-48883-7 ISBN 978-3-319-48884-4 (eBook)
DOI 10.1007/978-3-319-48884-4

Library of Congress Control Number: 2016956177

Printed on acid-free paper

This Springer imprint is published by Springer Nature
The registered company is Springer International Publishing AG
The registered company address is: Gewerbestrasse 11, 6330 Cham, Switzerland

...La filosofia è scritta in questo grandissimo libro che continuamente ci sta aperto innanzi a gli occhi, io dico l'Universo, ma non si può intendere se prima non s'impara a intender la lingua e conoscer i caratteri, ne' quali è scritto. Egli è scritto in lingua matematica, e i caratteri son triangoli, cerchi, ed altre figure geometriche, senza i quali mezzi è impossibile a intenderne umanamente parola; senza questi è un aggirarsi vanamente per un oscuro laberinto...

Galileo Galilei • *Il Saggiatore, VI, 1623*

Preface

The reader aware of structural mechanics will find in this book a source of fruitful knowledge and effective tools useful, joined with imagination, for creating and promoting novel and challenging developments.

A wide range of topics is faced, such as mechanics and geotechnics, vibration and damping, damage and friction, experimental methods and advanced structural materials. Analytical, experimental and numerical findings are presented, focusing on theoretical and practical issues and opening towards novel progresses in structural engineering.

Proposed contributions collect some recent results obtained in the framework of the Lagrange Laboratory, an European scientific research group, mainly consisting of Italian and French engineers, mechanicians and mathematicians.

This book is the most recent example of the long-term scientific cooperation between the well-established French and Italian schools in mechanics, mathematics and engineering.

The contribution of Stella Brach to prepare this volume is gratefully acknowledged.

Rome, Italy
July 2016

Michel Frémond
Franco Maceri
Giuseppe Vairo

Contents

Contributors

Giulio Alfano School of Engineering and Design, Brunel University, Uxbridge, UK

Anissa Allani École des Ponts, Laboratoire Navier, UMR 8205, IFSTTAR, CNRS, UPE, Champs-sur-Marne, France

Pierre Argoul Université Paris Est, IFSTTAR, MAST, SDOA, Marne-la-Vallée, France

Elena Bonetti Dipartimento "F. Enriques", Università di Milano, Milan, Italy

Stella Brach DICII, Università degli Studi di Roma "Tor Vergata", Rome, Italy; Institut D'Alembert, Université Pierre et Marie Curie, Paris, France

Domenico Bruno Department of Civil Engineering, University of Calabria, Rende (CS), Italy

Carlo Callari Università del Molise, Campobasso, Italy

Jean Canou UMR 8205 CNRS-ENPC-IFSTTAR, École des Ponts ParisTech, Laboratoire Navier Université Paris-Est, Marne-la-vallée, France

Gwendal Cumunel UMR 8205 CNRS-ENPC-IFSTTAR, École des Ponts ParisTech, Laboratoire Navier Université Paris-Est, Marne-la-vallée, France

Géry de Saxcé Université de Lille 1, Cité scientifique, Villeneuve d'Ascq, France

Luc Dormieux Ecole des Ponts ParisTech, UR Navier, Marne-la-vallée, France

Jean-Claude Dupla UMR 8205 CNRS-ENPC-IFSTTAR, École des Ponts ParisTech, Laboratoire Navier Université Paris-Est, Marne-la-vallée, France

Silvano Erlicher EGIS Industries, 4 rue Dolores Ibarruri, Montreuil, France

Michel Frémond Dipartimento di Ingegneria Civile e Ingegneria Informatica (DICII), Università degli Studi di Roma "Tor Vergata", Rome, Italy

Francesco Froiio École Centrale de Lyon, LTDS, Université de Lyon, Lyon, France

Fabrizio Greco Department of Civil Engineering, University of Calabria, Rende (CS), Italy

Bachar Kabalan École des Ponts ParisTech, Université Paris Est, Laboratoire Ville Mobilité Transport, Marne-la-Vallée, France

Laura Kerner UMR 8205 CNRS-ENPC-IFSTTAR, École des Ponts ParisTech, Laboratoire Navier Université Paris-Est, Marne-la-vallée, France

Djimédo Kondo Institut D'Alembert, Université Pierre et Marie Curie, Paris, France

Lorenzo Leonetti Department of Civil Engineering, University of Calabria, Rende (CS), Italy

Christian Licht Laboratoire de Mécanique et Génie Civil, Université Montpellier II, Montpellier, France; Department of Mathematics, Faculty of Science, Mahidol University, Bangkok, Thailand

Stefania Lo Feudo Université Paris–Saclay, ENSTA ParisTech, IMSIA, CNRS, EDF, CEA, Palaiseau, France

Paolo Lonetti Department of Civil Engineering, University of Calabria, Rende (CS), Italy

Franco Maceri Dipartimento di Ingegneria Civile e Ingegneria Informatica (DICII), Università degli Studi di Roma "Tor Vergata", Rome, Italy

Paolo Nevone Blasi Department of Civil Engineering, University of Calabria, Rende (CS), Italy

Quoc-Son Nguyen Laboratoire de Mécanique des Solides, École Polytechnique-ParisTech, Palaiseau Cedex, France

Michaël Peigney Laboratoire Navier (UMR 8205), CNRS, Ecole des Ponts ParisTech, IFSTTAR, Université Paris-Est, Marne la Vallée, France

Jean-Michel Pereira UMR 8205 CNRS-ENPC-IFSTTAR, École des Ponts ParisTech, Laboratoire Navier Université Paris-Est, Marne-la-vallée, France

Andrea Francesco Rotunno Dipartimento di Ingegneria Civile e Ingegneria Informatica (DICII), Università degli Studi di Roma "Tor Vergata", Rome, Italy; École Centrale de Lyon, LTDS, Université de Lyon, Lyon, France

Elio Sacco Dipartimento di Ingegneria Civile e Meccanica, Università di Cassino e del Lazio Meridionale, Cassino, Italy

Roberto Serpieri Dipartimento di Ingegneria, Università degli Studi del Sannio, Benevento, Italy

Claude Stolz École Centrale Nantes, GeM UMR CNRS 6183, Nantes, France; Université Paris Saclay, IMSIA UMR EDF/CNRS/CEA/ENSTA 9219, Palaiseau, France

Giuseppe Vairo DICII, Università degli Studi di Roma "Tor Vergata", Rome, Italy; Institut D'Alembert, Université Pierre et Marie Curie, Paris, France

Thibaut Weller Université Montpellier II, Laboratoire de Mécanique et Génie Civil, Montpellier, France

5-Dimensional Thermodynamics of Dissipative Continua

Géry de Saxcé

Abstract Present work aims to develop a geometrization of thermodynamics of continua within the classical approximation where the velocity of the light is considered infinite, but nevertheless in the spirit of relativity. The connection on the manifold represents the gravitation. The temperature has the status of a vector and its gradient, called friction, merges the temperature gradient and strain velocity. We claim that the energy-momentum-mass tensor is covariant divergence free. It is a geometrized version of the first principle. The modeling of the dissipative continua is based on an additive decomposition of the momentum tensor into reversible and irreversible parts. The second principle is based on a tensorial expression of the local production of entropy which provides its Galilean invariance. On this ground, we propose a relativistic version of the second principle compatible with Poincare's group.

1 Introduction

The concepts of thermodynamics were initially introduced independently of the mechanics of continua, but this two topics can be married. The key idea is to develop the concepts of thermodynamics for any volume element of the continuum. Local versions of the two principles are obtained, in the spirit of Truesdell's ideas [20] and its school. Another breakthrough idea is to construct a consistent theoretical framework for relativity and thermodynamics. As general relativity is widely based on differential geometry, we regard this construction as a geometrization of thermodynamics. Souriau proposed in [14, 15] such a formalism in general relativity. In his footstep, one can quote the works by Iglesias [8] and Vallée [22]. In his Ph.D. thesis [21], Vallée studied the invariance of constitutive laws in the context of special relativity where the gravitation effects are neglected. For other geometrizations of thermodynamics, the reader is referred to [10] for example.

G. de Saxcé (✉)
Université de Lille 1, Cité scientifique, bâtiment M6, F59655 Villeneuve d'Ascq, France
e-mail: gery.desaxce@univ-lille1.fr

M. Frémond et al. (eds.), *Models, Simulation, and Experimental Issues in Structural Mechanics*, Springer Series in Solid and Structural Mechanics 8,
DOI 10.1007/978-3-319-48884-4_1

In the present work, our goal is to develop a geometrization of thermodynamics within the classical approximation where the velocity of the light is considered infinite, but nevertheless in the spirit of relativity. In other words, we want to propose a thermodynamics of classical continua, consistent with the Galileo's principle of relativity. We draw our inspiration from the previously quoted geometrization in the frame of general and special relativity but with some important infringements that will be pointed out in the sequel. Now, let us roughly present the key ideas of our geometrization procedure without discussing all the details that will be given further. To be short, we exclude some important aspects such as chock waves, mixtures, chemical reactions, electromagnetism, complex dissipative phenomena (such as plasticity, viscoplasticity, damage) requiring additional internal variables. We only consider continuous fields, homogeneous continua and no additional internal variables.

This work is an expanded version of [6] taking into account the Galilean gravitation and is structured as follows. In Sect. 2, we add to the space-time an extra dimension roughly speaking linked to the energy. In Sect. 3, the temperature has the status of a vector and its gradient, called friction, merges the temperature and strain velocity. In Sect. 4, we define the energy-momentum-mass tensor (in short the momentum tensor) and claim that it is covariant divergence free. It is a geometrized version of the first principle. In Sect. 5, introducing Planck's potential reveals the structure of the momentum tensor for reversible processes and allows to deduce classical potentials, internal energy, free energy and the specific entropy. In Sect. 6, the modeling of the dissipative continua is based on an additive decomposition of the momentum tensor into reversible and irreversible parts. The second principle is based on a tensorial expression of the local production of entropy which provides its Galilean invariance. In Sect. 7, the constitutive laws are briefly discussed in the context of thermodynamics. Section 8 is devoted to the extension of the previous framework in presence of gravitation. In Sect. 9, we propose a relativistic version of the second principle compatible with Poincaré's group.

1.1 Differential Manifold

A manifold is an object which, locally, just looks as an open subset of Euclidean space, but whose global topology can be quite different. Although many manifolds are realized as subset of Euclidean spaces, the general definition worth reviewing. More precisely, a **manifold** $\mathscr{M}$ of dimension n and class C^p is a topological space equipped with a collection of regular maps ϕ called **coordinate charts** of which the definition sets are connected open subsets of $\mathbb{R}^n$, the value sets are open subsets of $\mathscr{M}$ covering it and the composite overlap maps $h = \phi^{-1} \circ \phi'$, called **coordinate changes**, are of class C^p. They allows to define on $\mathscr{M}$ local coordinate systems:

$$X = \phi^{-1}(\boldsymbol{X}) = \begin{pmatrix} X^1 \\ X^2 \\ \vdots \\ X^n \end{pmatrix} \in \mathbb{R}^n.$$

In practice, it is convenient to omit explicit reference to the coordinate map and to identify the points $\boldsymbol{X}$ with their local coordinate expressions X. Nevertheless, objects living on manifolds must be defined intrinsically, independent of any choice of local coordinates. Consequently, manifolds are suitable tools to develop a coordinate-free approach to the study of their intrinsic geometry. To distinguish them from their local expressions, intrinsic objects such as tensors are denoted with bold face. Main tools of differential geometry can be found in many classical textbooks. For a less standard presentation, the reader is referred to [12].

1.2 Space-Time

In the sequel, we adopt the following convention:

Convention 1 *Coordinate labels:*

- *Latin indices i, j, k and so on run over the spacial coordinate labels, usually,* $1, 2, 3$ *or* x, y, z.
- *Greek indices α, β, γ and so on run over the four space-time coordinate labels* $0, 1, 2, 3$ *or* t, x, y, z.

The space-time will be consider as a differential manifold $\mathscr{U}$ of dimension 4. A point $\boldsymbol{X} \in \mathscr{U}$ represents an event. The 4-column vector of its coordinates $(X^\alpha)_{0\leq\alpha\leq 3}$ in a chosen frame will be denoted X. The frames and the associated coordinate systems in which the distances and times are measured will be called Galilean. In such frames, $X^0 = t$ is the time and $X^i = x^i$ for $1 \leq i \leq 3$ are the spatial coordinates, so we can write

$$X = \begin{pmatrix} t \\ x \end{pmatrix}$$

1.3 Galileo's Group

The affine transformations $dX' = PdX + C$, where $P \in \mathbb{GL}(4)$ and $C \in \mathbb{R}^4$, preserving the distances, the time durations, the uniform straight motions and the oriented volumes are called **Galilean transformations**. Their linear part is of the form:

$$P = \begin{pmatrix} 1 & 0 \\ u & R \end{pmatrix} \tag{1}$$

where $u \in \mathbb{R}^3$ is the velocity of transport, or Galilean boost, and $R \in \mathbb{SO}(3)$ is a spatial rotation. The set of all these transformations is a subgroup G of $\mathbb{GL}(4)$ called Galileo's group. It equips the space-time with a structure equivalent to the one proposed by Toupin [18], taken up later on by Noll [11] and Künzle [9]. The Toupinian structure of the space-time is based on two canonical tensors, a semi-metric and a linear form called time arrow in the sequel. This neoclassic modelling offers a theoretical frame for the universal or absolute time.

Of course, the Euclidean transformations are particular Galilean transformations only compounded of a space translation and a rotation. As there are Euclidean tensors, we can consider **Galilean tensors** by restricting the general action of the linear group $\mathbb{GL}(4)$ to the subgroup of linear Galilean transformations.

1.4 Galilean Coordinate Systems

Any coordinate change representing a rigid body motion and a clock change:

$$x' = (R(t))^T (x - x_0(t)), \quad t' = t + \tau_0$$

where $t \mapsto R(t) \in \mathbb{SO}(3)$ and $t \mapsto x_0(t) \in \mathbb{R}^3$ are smooth mappings, and $\tau_0 \in \mathbb{R}$ is a constant, is called a **Galilean coordinate change**. Indeed, a coordinate change is Galilean if and only if the corresponding Jacobean matrix is a linear Galilean transformation [9]:

$$P^{-1} = \frac{\partial X'}{\partial X} = \begin{pmatrix} 1 & 0 \\ -R^T u & R^T \end{pmatrix}$$

where:

$$u = \varpi(t) \times (x - x_0(t)) + \dot{x}_0(t) \tag{2}$$

is the well-known **velocity of transport**, with Poisson's vector ϖ such that: $\dot{R} = j(\varpi) R$, $j(\varpi)$ being the 3×3 skew-symmetric matrix such that $j(\varpi) v = \varpi \times v$. There exists a family of coordinate systems which are deduced one from each other by such coordinate changes. We call them **Galilean coordinate systems**. Now we can state **Galileo's principle of relativity**:

Principle 1 *The statement of the physical laws of the classical mechanics is the same in all the Galilean coordinate systems.*

To respect this principle in practice, the laws are expressed in a **covariant form**, using the connection, a tool of differential geometry.

1.5 Linear Connections

Let $\pi_E : E \to \mathscr{M}$ be a vector bundle. A linear connection on E is a bilinear map $\boldsymbol{\Gamma}$ from the bundle product $T\mathscr{M} \times_{\mathscr{M}} E$ into TE such that, for any tangent vector $\overrightarrow{\boldsymbol{dX}}$ at $\boldsymbol{X} \in \mathscr{M}$, $\pi_E\, \boldsymbol{\Gamma}\, (\overrightarrow{\boldsymbol{dX}}, \overrightarrow{\boldsymbol{W}}) = \boldsymbol{X}$ and $T\pi_E\, \boldsymbol{\Gamma}\, (\overrightarrow{\boldsymbol{dX}}, \overrightarrow{\boldsymbol{W}}) = \overrightarrow{\boldsymbol{dX}}$. The **covariant derivative** of a smooth vector field $\boldsymbol{X} \mapsto \overrightarrow{\boldsymbol{W}}(\boldsymbol{X}) \in E_{\boldsymbol{X}}$ is:

$$\nabla_{\overrightarrow{\boldsymbol{dX}}} \overrightarrow{\boldsymbol{W}} = T\overrightarrow{\boldsymbol{W}}\, \overrightarrow{\boldsymbol{dX}} + \boldsymbol{\Gamma}\, (\overrightarrow{\boldsymbol{dX}}, \overrightarrow{\boldsymbol{W}}) = \nabla \overrightarrow{\boldsymbol{W}}\, \overrightarrow{\boldsymbol{dX}}$$

(W^A) being the components of $\overrightarrow{\boldsymbol{W}}$ in a local chart of E and (dX^A) the ones of $\overrightarrow{\boldsymbol{dX}}$, its local expression is:

$$\nabla_{dX} W^A = dW^A + \Gamma^A_B(dX)\; W^B = \nabla_\beta W^A dX^\beta$$

where, using Christoffel symbols:

$$\nabla_\beta W^A = \frac{\partial W^A}{\partial X^\beta} + \Gamma^A_{\beta B}\; W^B. \tag{3}$$

For sake of easy calculations, we shall prefer as soon as possible the matrix form:

$$\nabla_{dX} W = dW + \Gamma(dX)\; W \tag{4}$$

keeping the tensorial notation when it is strictly necessary. If the covariant derivative of $\overrightarrow{\boldsymbol{W}}$ is null, we say it is **parallel-transported**. If E is the tangent bundle $T\mathscr{M}$ and the connection $\boldsymbol{\Gamma}$ is **symmetric**, one has:

$$\Gamma^\alpha_{\beta\gamma} = \Gamma^\alpha_{\gamma\beta}.$$

Hence $\nabla \overrightarrow{\boldsymbol{W}}$ is represented by the matrix:

$$\nabla W = \frac{\partial W}{\partial X} + \Gamma(W) \tag{5}$$

such that $\nabla_{dX} W = \nabla W\, dX$.

1.6 Galilean Connections

At each group of transformation is associated a family of connections and the corresponding geometry. We call **Galilean connections** the symmetric connections on the tangent bundle $T\mathscr{U}$ associated to Galileo's group [9, 18, 20], i.e. such that the two

canonical tensors of the Toupinian structure are parallel-transported. In a Galilean coordinate system, they are given by the 4×4 connection matrix:

$$\Gamma = \begin{pmatrix} 0 & 0 \\ j(\Omega)\, dx - g\, dt & j(\Omega)\, dt \end{pmatrix} \tag{6}$$

where g is a column-vector collecting the $g^j = -\Gamma^j_{00}$ and identified to the gravity [2, 17], while Ω is a 3-column vector associated by the mapping j^{-1} to the skew-symmetric matrix the elements of which are $\Omega^i_j = \Gamma^i_{j0}$. The vector Ω can be interpreted as representing Coriolis' effects [17].

1.7 Equations of Motion

In a given Galilean coordinate system X', let us consider a particle of velocity $v' \in \mathbb{R}^3$. The tangent vector $\overrightarrow{U}$ to its trajectory $t \mapsto X'(t)$ in the space-time is called 4-**velocity** and is represented in this coordinate system by:

$$U' = \frac{dX'}{dt} = \begin{pmatrix} 1 \\ v' \end{pmatrix}$$

Considering another Galilean coordinate system X, the 4-velocity components change as the ones of a vector:

$$U = P\, U' = \begin{pmatrix} 1 \\ \dot{x} \end{pmatrix} = \begin{pmatrix} 1 \\ v \end{pmatrix} = \begin{pmatrix} 1 & 0 \\ u & R \end{pmatrix} \begin{pmatrix} 1 \\ v' \end{pmatrix}. \tag{7}$$

Thus the velocity in the new coordinate system is:

$$v = u + R\, v'. \tag{8}$$

This is the velocity addition formula. The linear momentum of a particle of mass m being $p = mv$, the linear 4-momentum is defined as:

$$T = m\, U = \begin{pmatrix} m \\ p \end{pmatrix}. \tag{9}$$

Following Cartan [2], we claim that the motion of a particle of mass m embedded in a gravitation field is governed by the covariant equation:

$$\nabla_{dX} T = dT + \Gamma(dX)\, T = 0$$

or, dividing by dt:

$$\nabla_U T = \dot{T} + \Gamma(U)\, T = 0. \tag{10}$$

Taking into account (6), (7) and (9), Eq. (10) becomes:

$$\begin{pmatrix} \dot{m} \\ \dot{p} \end{pmatrix} + \begin{pmatrix} 0 & 0 \\ \Omega \times v - g & j(\Omega) \end{pmatrix} \begin{pmatrix} m \\ p \end{pmatrix} = \begin{pmatrix} 0 \\ 0 \end{pmatrix},$$

which can be itemized as:

$$\dot{m} = 0, \qquad \dot{p} = m\,(g - 2\,\Omega \times v). \tag{11}$$

The first equation reveals the mass conservation. The second one expresses the time rate of the linear momentum in terms of the gravitation. Introducing the expression of p into this equation and because the mass does not depends on time, we obtain **Souriau's covariant equation of motion** [13]:

$$m\dot{v} = m\,(g - 2\,\Omega \times v), \tag{12}$$

allowing to determine the trajectory of the particle. It can be recovered in a variational way by introducing the **Lagrangian**:

$$\mathscr{L}(t, x, v) = \frac{1}{2} m \parallel v \parallel^2 - m\,\phi + mA \cdot v, \tag{13}$$

provided:

$$g = -grad\,\phi - \frac{\partial A}{\partial t}, \qquad \Omega = \frac{1}{2}\, curl\, A \tag{14}$$

where $(t, x) \longmapsto \phi(t, x) \in \mathbb{R}$ and $(t, x) \longmapsto A(t, x) \in \mathbb{R}^3$ are the scalar and vector **potentials of the Galilean gravitation**. ϕ and g are well-known but A and Ω are the good tools to revisit Foucault's pendulum topic without neglecting the centripetal force [7].

1.8 Modeling the Matter and Its Evolution

Following Souriau [12], a continuum can be easily described identifying a material particle by a reference position $\boldsymbol{X}_0 = \pi_0(\boldsymbol{X})$. In local charts, it is represented by $s' \in \mathbb{R}^3$ (its position at a given date) and its motion is determined thanks to a mapping $(t, x) \mapsto s' = \kappa(t, x)$ which identifies the material point located at position x at time t. The space-time coordinates (t, x) are Eulerian while (t, s') are Lagrangian. Obviously s' being an invariant of the motion, the material derivative vanishes

$$\frac{ds'}{dt} = \frac{\partial s'}{\partial t} + \frac{\partial s'}{\partial x}\frac{dx}{dt} = 0 \tag{15}$$

or, owing to Eq. (7):

$$\frac{\partial s'}{\partial X}\, U = 0 \tag{16}$$

1.9 Key Hypothesis of the Theory

Now, we present in axiomatic form the corner stones of the theory involving an underlying geometric structure of the Nature. This theoretical frame can now appear rather arbitrary but that will be justified further by the agreement of the with the physical phenomena. Therefore, we propose the following statements for a Galilean thermodynamics including gravitational effects:

(H1) There exists a line bundle $\pi_0 : \mathscr{U} \mapsto \mathscr{U}_0$ which characterizes the *matter* and its evolution where $\mathscr{U}$ is a manifold of dimension 4 called *space-time*.

(H2) The universe is a line bundle $\pi : \hat{\mathscr{U}} \mapsto \mathscr{U}$ where the manifold $\hat{\mathscr{U}}$ is of dimension 5. $\mathscr{U}$ is seen as a submanifold of $\hat{\mathscr{U}}$.

(H3) $\mathscr{U}$ is equipped with a Galilean connexion and $\hat{\mathscr{U}}$ with the corresponding Bargmannian connection representing the *gravitation*.

(H4) There exists on $\mathscr{U}$ a smooth field $\boldsymbol{X} \mapsto \hat{\overrightarrow{\boldsymbol{W}}}(\boldsymbol{X}) \in T_{\boldsymbol{X}}\hat{\mathscr{U}}$ called the *temperature 5-vector*. The covariant derivative of its projection $\overrightarrow{\boldsymbol{W}} = T\pi\ \hat{\overrightarrow{\boldsymbol{W}}}$ onto $T_{\boldsymbol{X}}\mathscr{U}$

$$\mathbf{f} = \nabla\, \overrightarrow{\boldsymbol{W}}$$

is called the *friction tensor*.

(H5) There exists a smooth section $\boldsymbol{X} \mapsto \hat{\mathbf{T}}(\boldsymbol{X}) \in Hom\ (T_{\boldsymbol{X}}\hat{\mathscr{U}}, T_{\boldsymbol{X}}\mathscr{U})$ called the *momentum tensor*. It is covariant divergence free:

$$Div\ \hat{\mathbf{T}} = \mathbf{0} \tag{17}$$

The first hypothesis have been already discussed. Let us develop now the other ones.

2 An Extra Dimension

The cornerstone idea is to add to the space-time an extra dimension roughly speaking linked to the energy:

$$e = \frac{1}{2}\, m \parallel v \parallel^2 \tag{18}$$

by a three step method that we shall be going to present in an heuristic way:

- As we are concerned with the uniform straight motion, we do not consider provisionally the gravitation. We start with a fictitious 5-dimensional affine space $\hat{\mathscr{U}}$ containing the space-time $\mathscr{U}$. We claim that any point $\hat{\boldsymbol{X}}$ of $\hat{\mathscr{U}}$ can be represented in some suitable coordinate systems by a column:

$$\hat{X} = \begin{pmatrix} X \\ z \end{pmatrix} \in \mathbb{R}^5,$$

  in such way that the space-time is identified to the subspace $\hat{X}^4 = z = 0$ of $\hat{\mathscr{U}}$ and X gathers Galilean coordinates.
- We wish to build a group of affine transformations $d\hat{X}' \mapsto d\hat{X} = \hat{P}\, d\hat{X}' + \hat{C}$ of $\mathbb{R}^5$ which are Galilean when acting on the space-time only. Clearly, the 5×5 matrix $\hat{P}$ is structured as:

$$\hat{P} = \begin{pmatrix} P & 0 \\ \Phi & \alpha \end{pmatrix},$$

  where the 4-row Φ and the scalar α have to take an appropriate physical meaning.
- It is worth to notice that under a Galilean coordinate change $X' \longmapsto X$ characterized by a boost u and a rotation R, using the velocity addition formula (8), its transformation law is:

$$e = \frac{1}{2} m \parallel u + R\, v' \parallel^2 = \frac{1}{2} m \parallel u \parallel^2 + m\, u \cdot (R\, v') + \frac{1}{2} m \parallel v' \parallel^2,$$

  that is:

$$e = \frac{1}{2} m \parallel u \parallel^2 + m\, u \cdot (R\, v') + e'. \tag{19}$$

  Next we claim that the extra coordinate is linked to the energy as follows:

$$dz = \frac{e}{m}\, dt, \qquad dz' = \frac{e'}{m}\, dt' \tag{20}$$

  $e\, dt$ is the element of action for the free particle. The division by m is guided by the fact that we wish the extra coordinate being universal, independent of the mass of particle moving in the space-time. According to $dt = dt'$ and $dx' = v' dt'$, we obtain:

$$dz = \frac{1}{2} \parallel u \parallel^2 dt' + u^T R\, dx' + dz'.$$

On this ground, we state:

Definition 1 The **Bargmannian transformations** are affine transformations $d\hat{X}' \mapsto d\hat{X} = \hat{P}\, d\hat{X}' + \hat{C}$ of $\mathbb{R}^5$ such that.

$$\hat{P} = \begin{pmatrix} 1 & 0 & 0 \\ u & R & 0 \\ \frac{1}{2} \parallel u \parallel^2 & u^T R & 1 \end{pmatrix}. \tag{21}$$

It is straightforward to verify that the set of the Bargmannian transformations is a subgroup of $\mathbb{A}ff(5)$ called **Bargmann's group** and denoted $\mathbb{B}$ in the sequel. Bargmann's group was introduced to solve problems of group quantization [1]. In fact, Galileo's group is not quantizable [13, 16] and the reason of this failure is cohomologic. For more explanation about the construction of Bargmann's group, the reader is referred to [4]. Although Bargmann's group was introduced for applications to quantum mechanics, it turns out to be also very useful in thermodynamics.

The subgroup of Bargmannian linear transformations is denoted $\mathbb{B}_0$. In particular, the inverse of (21) is:

$$\hat{P}^{-1} = \begin{pmatrix} 1 & 0 & 0 \\ -R^T u & R^T & 0 \\ \frac{1}{2} \parallel u \parallel^2 & -u^T & 1 \end{pmatrix}. \tag{22}$$

It is worth to remark that the calculus may be organized by working in $\mathbb{R}^6$. The Bargmannian transformation looks like a linear transformation $d\tilde{X} = \tilde{P}\, d\tilde{X}'$ if the column $d\hat{X}$ and $\hat{a} = (\hat{C}, \hat{P})$ are represented respectively by:

$$d\tilde{X} = \begin{pmatrix} 1 \\ d\hat{X} \end{pmatrix} \in \mathbb{R}^6 \qquad \tilde{P} = \begin{pmatrix} 1 & 0 \\ \hat{C} & \hat{P} \end{pmatrix},$$

with:

$$\begin{aligned} \tilde{P} &= \begin{pmatrix} 1 & 0 & 0 & 0 \\ \tau & 1 & 0 & 0 \\ k & u & R & 0 \\ \eta & \frac{1}{2} \parallel u \parallel^2 & u^T R & 0 \end{pmatrix}, \\ \tilde{P}^{-1} &= \begin{pmatrix} 1 & 0 & 0 & 0 \\ \tau' & 1 & 0 & 0 \\ k' & -R^T u & R^T & 0 \\ \eta' & \frac{1}{2} \parallel u \parallel^2 & -u^T & 0 \end{pmatrix}. \end{aligned} \tag{23}$$

Definition 2 In absence of gravitation, the coordinate systems of $\hat{\mathscr{U}}$, which are deduced one from the other by Bargmanian transformations are called **Bargmannian coordinate systems**.

This Definition is meaningful only in absence of gravitation and will be modified in Sect. 4.

Galilean transformations preserve some objects—uniform straight motions, durations, distances and angles, oriented volumes—but what Bargmannian transformations preserve? Combining Eqs. (18) and (20) leads to:

$$\| dx \|^2 - 2\, dz\, dt = 0,$$

in every Bargmannian coordinate system. The left hand member is a quadratic form in $d\hat{X}$ that suggest to introduce a symmetric 2-covariant tensor $\hat{\mathbf{G}}$ represented in Bargmannian coordinate systems by:

$$\hat{G} = \begin{pmatrix} 0 & 0 & -1 \\ 0 & 1_{\mathbb{R}^3} & 0 \\ -1 & 0 & 0 \end{pmatrix}. \tag{24}$$

As it is regular, $\hat{\mathbf{G}}$ is a covariant metric tensor. It is preserved by Bargmannian linear transformations:

$$\forall \hat{P} \in \mathbb{B}_0, \qquad \hat{P}^T \hat{G}\, \hat{P} = \hat{G}. \tag{25}$$

It is easy to verify that:

$$\hat{G}^2 = 1_{\mathbb{R}^5},$$

that proves the contravariant metric tensor $\hat{\mathbf{G}}^{-1}$ is represented by the same matrix as the covariant one:

$$\hat{G}^{-1} = \hat{G}.$$

3 Temperature Vector and Friction Tensor

As there are Euclidean and Galilean tensors, we can consider **Bargmannian tensors** by restricting the general action of the linear group $\mathbb{GL}(5)$ to the subgroup of linear Bargmannian transformations. To begin with, let us study the Bargmannian vectors $\overrightarrow{\hat{W}}$ represented by a 5-column:

$$\hat{W} = \begin{pmatrix} W \\ \zeta \end{pmatrix} = \begin{pmatrix} \beta \\ w \\ \zeta \end{pmatrix}, \tag{26}$$

where $W \in \mathbb{R}^4$, $w \in \mathbb{R}^3$ and $\beta, \zeta \in \mathbb{R}$. According to (22), their transformation law $\hat{W}' = \hat{P}^{-1}\hat{W}$ gives:

$$\beta' = \beta\,, \qquad w' = R^T(w - \beta u), \qquad \zeta' = \zeta - w \cdot u + \frac{\beta}{2} \| u \|^2\,. \tag{27}$$

Bargmannian transformations leave β invariant and there is no trouble to put β instead of β' in the sequel. To obtain the other invariants of $\overrightarrow{\hat{W}}$ in the case that β does not vanish, we start in any Bargmannian coordinate system $\hat{X}$ and we choose the Galilean boost:

$$u = \frac{w}{\beta},$$

which annihilates w' and reduces the last component to the generally non vanishing expression:

$$\zeta' = \zeta - \frac{1}{2\,\beta} \parallel w \parallel^2 .$$

This suggests to consider the quantity:

$$\zeta_{int} = \zeta - \frac{1}{2\,\beta} \parallel w \parallel^2 .$$

Taking into account Eq. (27), we verify that it is invariant by Bargmannian transformation. Conversely, let us consider a Bargmannian coordinate system $\hat{X}'$ in which the vector $\hat{\overrightarrow{W}}$ has a **reduced form**:

$$\hat{W}' = \begin{pmatrix} \beta \\ 0 \\ \zeta_{int} \end{pmatrix}.$$

Now, we claim the considered elementary volume is at rest. Let X be another Galilean coordinate system obtained from X' through a Galilean boost v. Applying the inverse transformation law of (22) with a Galilean boost v, we obtain:

$$\hat{W} = \begin{pmatrix} \beta \\ \beta\, v \\ \zeta_{int} + \frac{\beta}{2} \parallel v \parallel^2 \end{pmatrix}.$$

As $w = \beta\, v$, the last components becomes:

$$\zeta = \zeta_{int} + \frac{1}{2\beta} \parallel w \parallel^2 \tag{28}$$

Under Bargmannian transformations, β is invariant. It is independent from the coordinate system and, for reasons that will appear latter, we claim that:

Definition 3 When $\beta = 1 / \theta = 1 / k_B T$ is **reciprocal temperature**, k_B being Boltzmann constant and T the absolute temperature, $\hat{\overrightarrow{W}}$ is named **temperature vector**.

Let us observe also that:

$$\overrightarrow{W} = \beta\, \overrightarrow{U}$$

The temperature 4-vector $\overrightarrow{W}$ is a column, decomposed by block as:

$$W = \begin{pmatrix} \beta \\ w \end{pmatrix}. \tag{29}$$

Definition 4 **Friction tensor** is the 1-covariant and 1-contravariant mixed tensor:

$$\mathbf{f} = \nabla \overrightarrow{W}$$

As the gravitation is provisionally neglected, we assume for the moment the connection vanishes and, taking into account Eq. (5), it is represented in a Galilean coordinate system by the 4×4 matrix:

$$f = \nabla W = \frac{\partial W}{\partial X} = \begin{pmatrix} \dfrac{\partial \beta}{\partial t} & \dfrac{\partial \beta}{\partial x} \\ \dfrac{\partial\, w}{\partial t} & \dfrac{\partial\, w}{\partial x} \end{pmatrix}. \tag{30}$$

4 Momentum Tensors and the First Principle

Definition 5 A **momentum tensor** is a 1-covariant tensor $\hat{\boldsymbol{T}}$ on the 5-dimensional space $\hat{\mathscr{U}}$ with vector values in the space-time $\mathscr{U}$, represented in a Bargmannian coordinate system by a 4×5 matrix structured as follows:

$$\hat{T} = \begin{pmatrix} \mathscr{H} & -p^T & \rho \\ k & \sigma_* & p \end{pmatrix}, \tag{31}$$

where $\mathscr{H} \in \mathbb{R}$, $p, k \in \mathbb{R}^3$ and $\sigma_* \in \mathbb{M}_{33}^{symm}$.

In indicial notation, the components of $\hat{\boldsymbol{T}}$ are:

$$\hat{T}^0_0 = \mathscr{H}, \qquad \hat{T}^0_i = -\delta_{ik} p^k, \qquad \hat{T}^0_4 = \rho,$$

$$\hat{T}^j_0 = k^j, \qquad \hat{T}^j_i = \sigma^j_{*i}, \qquad \hat{T}^j_4 = p^j.$$

The transformation law of $\hat{\boldsymbol{T}}$:

$$\hat{T}' = P^{-1}\, \hat{T}\, \hat{P}, \tag{32}$$

itemizes in:

$$\rho' = \rho\,, \tag{33}$$

$$p' = R^T\,(p - \rho u)\,, \tag{34}$$

$$\sigma'_\star = R^T\,(\sigma_\star + u\,p^T + p\,u^T - \rho\,u\,u^T)\,R\,, \tag{35}$$

$$\mathscr{H}' = \mathscr{H} - u\cdot p + \frac{\rho}{2}\parallel u\parallel^2\,, \tag{36}$$

$$k' = R^T\,(k - \mathscr{H}'u + \sigma_* u + \frac{1}{2}\parallel u\parallel^2 p). \tag{37}$$

It is worth noting that the hypothesis of symmetry of $\sigma_\star$ is consistent with the rule (35). The components ρ, p and $\sigma_\star$ can be physically identified with the mass density, the linear momentum and the dynamical stresses. To interpret the other components, we intend to annihilate components of $\hat{\boldsymbol{T}}$. We discuss only the case of non zero mass density. Starting in any Bargmannian coordinate system $\hat{X}$, we choose the Galilean boost:

$$u = \frac{p}{\rho} \tag{38}$$

which annihilates p', reduces Eq. (35) to

$$\sigma'_\star = R^T\left(\sigma_\star + \frac{1}{\rho}\,p\,p^T\right)R. \tag{39}$$

This suggests to cast a glance to the matrix:

$$\sigma = \sigma_\star + \frac{1}{\rho}\,p\,p^T. \tag{40}$$

Taking into account Eqs. (33)–(35), we obtain its transformation law:

$$\sigma' = R^T\sigma\,R. \tag{41}$$

Besides, Eq. (38) allows to transform Eqs. (36) and (37) as follows:

$$\mathscr{H}' = \mathscr{H} - \frac{1}{2\rho}\parallel p\parallel^2,$$

$$k' = R^T\left(k - \mathscr{H}\frac{p}{\rho} + \sigma_\star\frac{p}{\rho}\right).$$

The components $\mathscr{H}'$ and k' obviously cannot be annihilated by a convenient choice of a rotation R. At the very most, we could diagonalize the symmetric matrix $\sigma_\star$ but it not useful now.

Conversely, let us consider a Bargmannian coordinate system in which the tensor field $\hat{\boldsymbol{T}}$ at a given point of coordinates $\hat{X}'$ has a **reduced form**:

$$\hat{T}' = \begin{pmatrix} \rho e_{int} & 0 & \rho \\ h' & \sigma' & 0 \end{pmatrix},$$

for an elementary volume around the point x' at rest at time t'. Let $\hat{X}$ be another Bargmannian coordinate system obtained from $\hat{X}'$ through a Galilean boost v combined with a rotation R. Applying the inverse transformation law of Eq. (32):

$$\hat{T} = P\,\hat{T}'\hat{P}^{-1}, \tag{42}$$

we obtain:

$$p = \rho v, \qquad \sigma_\star = \sigma - \rho v v^T,$$

$$\mathscr{H} = \rho \left(\frac{1}{2} \parallel v \parallel^2 + e_{int} \right), \tag{43}$$

$$k = h + \mathscr{H} v - \sigma v, \tag{44}$$

according to the transformation law in Eq. (41) of the spatial stresses σ and provided:

$$h = R\,h'. \tag{45}$$

The previous method turns out the physical meaning of the components:

- the mass density ρ and the dynamic stresses $\sigma_\star$,
- the Hamiltonian density $\mathscr{H}$, apart from the potential ϕ (the gravitation being considered only latter),
- and the **energy flux** k composed of h –further identified to the **heat flux**–, the **Hamiltonian flux** $\mathscr{H} v$ and the **stress flux** σv.

We could name $\hat{\boldsymbol{T}}$ the stress-mass-energy-momentum tensor but for briefness we call it momentum tensor. Finally, it has the form:

$$\hat{T} = \begin{pmatrix} \mathscr{H} & -p^T & \rho \\ h + \mathscr{H} v - \sigma v & \sigma - v p^T & \rho v \end{pmatrix}. \tag{46}$$

In the last column of relationship (46), we spot the 4-**flux of mass**:

$$N = \rho\, U. \tag{47}$$

Therefore, we can write:

$$\hat{T} = \begin{pmatrix} T & N \end{pmatrix}, \tag{48}$$

with:

$$T = \begin{pmatrix} \mathscr{H} & -p^T \\ h + \mathscr{H} v - \sigma v & \sigma - v p^T \end{pmatrix}.$$

In fact, it is more convenient to express the momentum tensor as in Eq. (46), accounting for the following proposition.

Theorem 1 *The expression (46) of the momentum tensor is standard provided σ and h are changing according respectively to the rules (41) and (45).*

Proof Matrix in Eq. (46) can be recast as:

$$\hat{T} = \begin{pmatrix} \mathscr{H} & -p^T & \rho \\ h + \mathscr{H}\,\dfrac{p}{\rho} - \sigma\,\dfrac{p}{\rho} & \sigma - \dfrac{1}{\rho}\,p\,p^T & p \end{pmatrix}. \tag{49}$$

Owing to (33), (41) and (34), one has:

$$\sigma'_* = \sigma' - \frac{1}{\rho'}\,p'\,p'^T = R^T\sigma\,R^T - \frac{1}{\rho}\,R^T(p-\rho u)(p^T-\rho u^T)\,R\,,$$

and developing:

$$\sigma'_\star = R^T\,(\sigma - \frac{1}{\rho}\,p\,p^T + u\,p^T + p\,u^T - \rho\,u\,u^T)\,R\,,$$

which, owing to (40), is nothing else the transformation law (35).

In a similar way, taking into account (33), (45), (41) and (34), it holds:

$$k' = h' + \mathscr{H}'\,\frac{p'}{\rho'} - \sigma'\,\frac{p'}{\rho'} = R^T h + \frac{\mathscr{H}'}{\rho}\,R^T(p-\rho u) - \frac{1}{\rho}\,R^T\sigma\,(p-\rho u).$$

Taking into account (36) gives:

$$k' = R^T h + \left(\mathscr{H} - u\cdot p + \frac{\rho}{2}\parallel u\parallel^2\right)\,R^T\frac{p}{\rho} + \mathscr{H}'R^T u - R^T\sigma\,\frac{p}{\rho} + R^T\sigma\,u\,,$$

and with some arrangements:

$$k' = R^T\left[h + \mathscr{H}\,\frac{p}{\rho} - \sigma\,\frac{p}{\rho} - \mathscr{H}'u + \left(\sigma - \frac{1}{\rho}\,p\,p^T\right)\,u + \frac{1}{2}\parallel u\parallel^2 p\right],$$

which, owing to (44) and (40), is nothing else the transformation law (37). □

The advantage of the standard form (46) is that transformation laws (41) and (45) for σ and h are easier to manipulate that the corresponding transformation laws (35) and (37) for $\sigma_\star$ and k.

Also, introducing:

$$\Pi = \left(\mathscr{H}\;\; -p^T\right), \tag{50}$$

it is worth noting that the momentum (46) can be recast as:

$$T = U\ \Pi + \begin{pmatrix} 0 & 0 \\ h - \sigma v & \sigma \end{pmatrix}. \tag{51}$$

Owing to (30), (51) and the symmetry of σ leads to:

$$Tr\ (T\ f) = \Pi\ \frac{\partial W}{\partial X}\ U + Tr\ \left(\sigma\ \left(grad_s\ w - \frac{1}{2}\left(v\ \frac{\partial \beta}{\partial x} + grad\ \beta\ v^T\right)\right)\right) + h \cdot grad\ \beta. \tag{52}$$

The first principle of thermodynamics claims that the total energy of a system is conserved. We are now able to proposed an enhanced local version including the balance of mass and the equation of the motion (balance of linear momentum). It is based on the following result.

Theorem 2 *If $\hat{T}$ is divergence free:*

$$div_X\ \hat{T} = 0,$$

then, we have:

- ◇ ***balance of mass***: $\dfrac{\partial \rho}{\partial t} + div\ (\rho\ v) = 0,$
- ♡ ***balance of linear momentum***: $\rho\ \left[\dfrac{\partial v}{\partial t} + \dfrac{\partial v}{\partial x}\ v\right] = (div\ \sigma)^T\ ,$
- ♠ ***balance of energy***: $\dfrac{\partial \mathscr{H}}{\partial t} + div\ \ (h + \mathscr{H} v - \sigma v) = 0.$

Proof To calculate the divergence of the 4×5 matrix $\hat{T}$, we use

$$div\ (\hat{T}_0, \ldots, \hat{T}_4) = (div\ \hat{T}_0, \ldots, div\ \hat{T}_4)$$

that achieves the proof. □

On this ground and envolving the gravitation, we state the **first principle of the thermodynamics**:

Principle 2 *The momentum tensor of a continuum is covariant divergence free:*

$$\boldsymbol{Div\ \hat{T} = 0}. \tag{53}$$

The covariant form of equation makes it consistent with Galileo's principle of relativity. It is general in the sense that it is valid for both reversible and dissipative continua. We are going now to describe successively these two kinds of media.

5 Reversible Processes and Thermodynamical Potentials

To modelize the reversible processes, we have to add a new hypothesis to our axiomatic theory. The pioneering works [14, 15, 21] give rise to assume that

(H6) there exists a smooth numerical function $\boldsymbol{X} \mapsto \zeta(\pi_0(\boldsymbol{X}), T_{\boldsymbol{X}}\pi_0, \mathbf{W}(\boldsymbol{X})) \in \mathbb{R}$ giving the value of the fifth bargmannian coordinate $z = \hat{X}^4$ and called **Planck's thermodynamic potential** (or **Massieu's potential**). It satisfies the principle of material indifference which claims that the behaviour of a material must be independent of the observer.

Considering a coordinate system, it is represented by a smooth mapping $X \mapsto \zeta(s', \partial s'/\partial X, W) \in \mathbb{R}$. To satisfy the principle of material indifference, ζ is assumed to depend on $\partial s'/\partial X$ through its invariants by any Galilean transformations $dX' = P\, dX$. A straightforward calculation shows that Planck's potential ζ depends on $\partial s'/\partial X$ through right Cauchy strains $C = F^T F$ where $F = \partial x/\partial s'$ [7].

On this ground, we prove the following proposition.

Theorem 3 *If ζ is a smooth function of s', C and W, then:*

$$T_R = U\, \Pi_R + \begin{pmatrix} 0 & 0 \\ -\sigma_R v & \sigma_R \end{pmatrix}, \tag{54}$$

with:

$$\Pi_R = -\rho\, \frac{\partial \zeta}{\partial W}, \tag{55}$$

$$\sigma_R = -\frac{2\rho}{\beta}\, F\, \frac{\partial \zeta}{\partial C}\, F^T, \tag{56}$$

is such that:

- ♢ $Tr\left(\hat{T}_R \nabla \hat{W}\right) = 0$,
- ♡ $T_R\, U = -\rho \left(\dfrac{\partial \zeta}{\partial W}\, U\right) U$,
- ♠ $\hat{T}_R = \left(T_R\, N\right)$ *represents a momentum tensor* $\hat{\boldsymbol{T}}_R$,
- ♣ $\hat{T}_R\, \hat{W} = \left(\zeta - \dfrac{\partial \zeta}{\partial W}\, W\right) N$.

Proof Taking into account (26), (30) and (48), condition ♢ reads:

$$(\nabla \zeta)\, N = -Tr\, (T_R f)\,, \tag{57}$$

or, in absence of gravitation:

$$\frac{\partial \zeta}{\partial X}\, N = -Tr\, (T_R f) \tag{58}$$

On the other hand, owing to (47), one has:

$$\frac{\partial \zeta}{\partial X}\, N = \rho\, (\frac{\partial \zeta}{\partial t} + \frac{\partial \zeta}{\partial x}\, v) = \rho \frac{d\zeta}{dt}.$$

As ζ depends on X through s', C and W, one has:

$$\frac{\partial \zeta}{\partial X}\, N = \rho \left(\frac{\partial \zeta}{\partial s'}\, \frac{ds'}{dt} + \frac{\partial \zeta}{\partial W}\, \frac{dW}{dt} + Tr \left(\frac{\partial \zeta}{\partial C}\, \frac{dC}{dt} \right) \right). \tag{59}$$

Owing to (16), the first term of the right hand side vanishes. Taking into account (55), the second term is:

$$\rho\, \frac{\partial \zeta}{\partial W}\, \frac{dW}{dt} = -\Pi_R\, \frac{\partial W}{\partial X}\, U. \tag{60}$$

Next, we have to transform the last term of (59). Because:

$$\frac{dC}{dt} = 2\, F^T D\, F \tag{61}$$

where:

$$D = \left(\frac{\partial v}{\partial x} + \left(\frac{\partial v}{\partial x} \right)^T \right) = grad_s v \tag{62}$$

is the **strain velocity** and owing to (56), one has:

$$\rho\, Tr \left(\frac{\partial \zeta}{\partial C}\, \frac{dC}{dt} \right) = Tr \left(2\rho F\, \frac{\partial \zeta}{\partial C}\, F^T D \right) = -Tr\, (\sigma_R \beta\, D) = -Tr\, (\sigma_R \beta\, grad_s\, v)\,,$$

that leads to:

$$\rho\, Tr \left(\frac{\partial \zeta}{\partial C}\, \frac{dC}{dt} \right) = -Tr \left(\sigma_R \left(grad_s\, w - \frac{1}{2} \left(v\, \frac{\partial \beta}{\partial x} + grad\, \beta\, v^T \right) \right) \right). \tag{63}$$

Introducing the expressions (60) and (63) into (59) gives (58) and proves $\diamondsuit$, owing to (52). Moreover, owing to (54) and (55), it holds:

$$T_R\, U = U\, \Pi_R\, U + \begin{pmatrix} 0 & 0 \\ -\sigma_R v & \sigma_R \end{pmatrix} \begin{pmatrix} 1 \\ v \end{pmatrix} = (\Pi_R\, U)\; U = -\rho \left(\frac{\partial \zeta}{\partial W}\, U \right) U,$$

that proves $\heartsuit$. Statement $\spadesuit$ results of the fact that (54) has the standard form (51). Consequently, taking into account (26) and (48), one has:

$$S = T_R\, W + \zeta\, N = \rho\, \left(\zeta - \beta \frac{\partial \zeta}{\partial W}\, U\right)\, U = \left(\zeta - \frac{\partial \zeta}{\partial W}\, W\right)\, N,$$

and ♣ is satisfied. □

Planck's potential ζ is a prototype of scalar functions called **thermodynamical potentials** and derived as follows:

- Comparing (51), (54) and (55) allows writing $\Pi_R = \left(\mathscr{H}_R \; -p^T\right)$ with:

$$\mathscr{H}_R = -\rho\, \frac{\partial \zeta}{\partial \beta}, \qquad p = \rho\, grad_w\, \zeta. \tag{64}$$

  Taking into account (28), it holds:

$$\mathscr{H}_R = -\rho\, \frac{\partial \zeta_{int}}{\partial \beta} + \frac{\rho}{2\beta^2}\, \| w \|^2,$$

  which allows recovering (43) because $w = \beta v$ and provided:

$$e_{int} = -\frac{\partial \zeta_{int}}{\partial \beta}. \tag{65}$$

  This potential, called **internal energy** (by unit volume), is function of s', C and W as derivative of ζ_{int}.
- The 4-vector $\overrightarrow{S} = \hat{\mathbf{T}}_R\, \overrightarrow{\hat{W}}$ is a 4-flux that reads for convenience:

$$\overrightarrow{S} = \rho\, s\, \overrightarrow{U} = s\, \overrightarrow{N}$$

  represented by a 4-column:

$$S = \hat{T}_R\, \hat{W}. \tag{66}$$

  Then, setting $S = s\, N$ and taking into account ♣ of Theorem 3, one has:

$$s = \zeta - \frac{\partial \zeta}{\partial \beta}\, \beta - \frac{\partial \zeta}{\partial w}\, w = \zeta_{int} + \frac{1}{2\beta}\, \| w \|^2 - \left(\frac{\partial \zeta_{int}}{\partial \beta} - \frac{1}{2\beta^2}\, \| w \|^2\right)\, \beta - \frac{1}{\beta} w^T w,$$

  that leads to:

$$s = \zeta_{int} - \beta\, \frac{\partial \zeta_{int}}{\partial \beta}$$

  This quantity is called **specific entropy** and $\overrightarrow{S}$ is its 4-flux. Hence, $-s$ appears as Legendre's transform of ζ_{int} with respect to β. The latter equation and (65) are called **state equations** of the continuum.
- Moreover, we introduce a new potential called **Helmholtz free energy** (by unit volume):

$$\psi = -\frac{1}{\beta}\,\zeta_{int} = -\theta\,\zeta_{int}. \tag{67}$$

By simple calculations, we obtain:

$$-e_{int} = \theta\,\frac{\partial \psi}{\partial \theta} - \psi, \tag{68}$$

$$-s = \frac{\partial \psi}{\partial \theta}.$$

Hence, $-e_{int}$ appears as Legendre's transform of the free energy $\psi\ (s', C, \theta)$ with respect to θ. It is a function of s', C and $-s$ such that:

$$\theta = \frac{\partial e_{int}}{\partial s}.$$

Finally, we can find a nice integral of the motion:

Theorem 4 *For reversible processes, the* 4*-flux S is divergence free and the specific entropy s is an integral of the motion.*

Proof Taking into account (66), it holds:

$$div\, S = (div\, \hat{T}_R)\,\hat{W} + Tr\left(\hat{T}_R \frac{\partial\, \hat{W}}{\partial X}\right).$$

The momentum tensor $\hat{T}_R$ satisfies condition $\diamond$ of Theorem 3 and, according to the first principle (relationship (53)), it is divergence free. Then the divergence of the 4-flux of specific entropy S vanishes and one has:

$$div\, S = div\,(s\,N) = \frac{\partial s}{\partial X}\,N + s\,div\,N = 0.$$

But, as seen in Theorem 2, the freeness of the divergence implies the balance of mass. This condition means the flux of mass N is divergence free and the last term of the previous equation vanishes. Hence one has:

$$div\, S = \frac{\partial s}{\partial X}\,N = \rho\,\frac{\partial s}{\partial X}\,U = \rho\left(\frac{\partial s}{\partial t} + \frac{\partial s}{\partial x}v\right) = \rho\,\frac{ds}{dt} = 0,$$

that achieves the proof. □

6 Dissipative Continuum and Heat Transfer Equation

In Sect. 4, we showed that the thermodynamical behaviour of a continuum is modeled by the momentum tensor $\hat{\mathbf{T}}$. By Theorem 1 we prove that $\hat{\mathbf{T}}_R$ is a momentum tensor. We define $\hat{\mathbf{T}}_I = \hat{\mathbf{T}} - \hat{\mathbf{T}}_R$, that amounts to introduce an additive decomposition of the momentum tensor:

$$\hat{\mathbf{T}} = \hat{\mathbf{T}}_R + \hat{\mathbf{T}}_I, \tag{69}$$

into a reversible part $\hat{\mathbf{T}}_R$ defined by Theorem 3 and an irreversible part $\hat{\mathbf{T}}_I$ of which we will examine now the detailed representations. Owing to (64), the momentum tensor $\hat{\mathbf{T}}_R$ given by (54) is represented by:

$$\hat{T}_R = \begin{pmatrix} \mathscr{H}_R & -p^T & \rho \\ \mathscr{H}_R v - \sigma_R v & \sigma_R - v p^T & \rho v \end{pmatrix}.$$

Subtracting the previous matrix to (46) leads to:

$$\hat{T}_I = \begin{pmatrix} \mathscr{H}_I & 0 & 0 \\ h + \mathscr{H}_I v - \sigma_I v & \sigma_I & 0 \end{pmatrix}, \tag{70}$$

where:

- the Hamiltonian density $\mathscr{H}_I = \mathscr{H} - \mathscr{H}_R$ is the opposite of the **irreversible heat source** (by unit volume),
- The column h is the **heat flux**,
- The symmetric 3×3 matrix $\sigma_I = \sigma - \sigma_R$ represents dissipative stresses (for instance due to viscous effects).

The transformation laws (36) and (41) give:

$$\mathscr{H}_I' = \mathscr{H}_I, \tag{71}$$

$$\sigma_I' = R^T \sigma_I R. \tag{72}$$

Introducing also for convenience the **specific irreversible heat source** q_I such that:

$$\mathscr{H}_I = -\rho q_I, \tag{73}$$

we have $\mathscr{H} = \rho\, \eta$, where:

$$\eta = \frac{1}{2} \parallel v \parallel^2 + e_{int} - q_I.$$

Taking into account:

$$\rho \frac{d\eta}{dt} = \frac{\partial \mathscr{H}}{\partial t} + div\,(\mathscr{H} v)$$

the balance energy (♠ of Theorem 2) reads:

$$\rho \frac{d\eta}{dt} + div\, h - (div\, \sigma)\, v - Tr\left(\frac{\partial v}{\partial x}\right) = 0.$$

Taking into account 62, the symmetry of σ and the balance of linear momentum (♡ of Theorem 2), the balance of energy becomes:

$$\rho \frac{de_{int}}{dt} = Tr\ (\sigma\, D) - div\, h + \rho \frac{dq_I}{dt}. \tag{74}$$

A cornerstone consequence is the heat transfer equation. By differentiation of (68), we have:

$$\rho \frac{de_{int}}{dt} = \rho \left(\frac{d\psi}{dt} - \frac{d\theta}{dt}\frac{\partial \psi}{\partial \theta} - \theta \frac{d}{dt}\left(\frac{\partial \psi}{\partial \theta}\right)\right).$$

Taking into account $\psi = \psi\ (s', C, \theta)$ and $ds'/dt = 0$, one has:

$$\rho \frac{de_{int}}{dt} = -\rho\, \theta \frac{\partial^2 \psi}{\partial \theta^2}\frac{d\theta}{dt} + \rho\, Tr\left(B \frac{dC}{dt}\right), \tag{75}$$

with:

$$B = \frac{\partial \psi}{\partial C} - \theta \frac{\partial}{\partial \theta}\left(\frac{\partial \psi}{\partial C}\right). \tag{76}$$

On the other hand, owing to (28) and (67), one has:

$$\frac{\partial \zeta}{\partial C} = -\beta \frac{\partial \psi}{\partial C}.$$

Hence, (56) becomes:

$$\sigma_R = 2\rho\, F \frac{\partial \psi}{\partial C} F^T,$$

and consequently:

$$\sigma_R - \theta \frac{\partial \sigma_R}{\partial \theta} = 2\rho\, F\, B\, F^T.$$

Owing to (61), the last term in (75) becomes:

$$\rho\, Tr\left(B \frac{dC}{dt}\right) = 2\,\rho\, Tr\ \left(F\, B\, F^T D\right) = Tr\left(\left(\sigma_R - \theta \frac{\partial \sigma_R}{\partial \theta}\right) D\right).$$

Introducing it into (75) gives:

$$\rho \frac{de_{int}}{dt} = \rho c_v \frac{d\theta}{dt} + Tr \left(\left(\sigma_R - \theta \frac{\partial \sigma_R}{\partial \theta} \right) D \right),$$

where:

$$c_v = \theta \frac{\partial s}{\partial \theta} = -\theta \frac{\partial^2 \psi}{\partial \theta^2},$$

is the **heat capacity at constant volume**. Combining with the form (74) of the balance of energy leads to the **equation of heat transfer**:

$$\rho c_v \frac{d\theta}{dt} = \theta \, Tr \left(\frac{\partial \sigma_R}{\partial \theta} D \right) + Tr \, (\sigma_I D) - div \, h + \rho \frac{dq_I}{dt}. \tag{77}$$

The physical interpretation of this equation is that the variation of reversible thermal energy, at the left hand member, is equal, at the right hand member, to the contributions of each term to the dissipation due to:

- the reversible stress variation resulting from the temperature one,
- the dissipative stresses,
- the heat flux,
- the irreversible heat sources.

We are now able to state the **second principle of thermodynamics**:

Principle 3 *The **local production of entropy** of a continuous medium characterized by fields of velocity vector $\overrightarrow{U}$, temperature vector $\overrightarrow{\hat{W}}$ and momentum tensor $\hat{\mathbf{T}}$ is non negative:*

$$\Phi = \boldsymbol{Div} \left(\hat{T} \, \overrightarrow{\hat{W}} \right) - \left(e^0(f(\overrightarrow{U})) \right) \left(e^0(T_I(\overrightarrow{U})) \right) \geq 0, \tag{78}$$

and vanishes if and only if the process is reversible.

In this expression, $\overrightarrow{U}$ is the 4-velocity and e^0 is the linear form dt, called time arrow and represented in any Galilean coordinate system by the 4-row:

$$e^0 = \begin{pmatrix} 1 & 0 & 0 & 0 \end{pmatrix}. \tag{79}$$

It can be verified that this expression is a Galilean invariant, according to the transformation law of the linear forms $e^{0'} = e^0 P$ and Eq. (1). In terms of tensor fields, expression (78) is covariant, then consistent with Galileo's principle of relativity (namely, Principle 1). As scalar field, the value of Φ is invariant. Without gravitation and in any Galilean coordinate system, the expression of the local production of entropy is:

$$\Phi = div \left(\hat{T} \, \hat{W} \right) - \left(e^0 f \, U \right) \left(e^0 \, T_I U \right) \geq 0, \tag{80}$$

If the process is reversible, $T_I = 0$ and, because of Theorem 4:

$$\Phi = div\ \left(\hat{T}_R\ \hat{W}\right) = div\ S = \rho\ \frac{ds}{dt} = 0,$$

thus the entropy is constant, that explains the name of Φ. Conversely, if the local production of entropy is positive, it cannot be proved that the process is dissipative, reason for which it is a principle—i.e., an axiom—and not a theorem.

Next, let us calculate explicitly the expression of the local production of entropy. Owing to (79), (30) and (7), the former factor of the second term of (80):

$$e^0 f\ U = \begin{pmatrix} 1 & 0 \end{pmatrix} \begin{pmatrix} \dfrac{\partial \beta}{\partial t} & \dfrac{\partial \beta}{\partial x} \\ \dfrac{\partial\ w}{\partial t} & \dfrac{\partial\ w}{\partial x} \end{pmatrix} \begin{pmatrix} 1 \\ v \end{pmatrix} = \frac{\partial \beta}{\partial t} + \frac{\partial \beta}{\partial x}\ v = \frac{d\beta}{dt},$$

is invariant under any Galilean transformation. Besides, (70) gives:

$$e^0\ T_I U = \begin{pmatrix} 1 & 0 \end{pmatrix} \begin{pmatrix} \mathscr{H}_I & 0 \\ h + \mathscr{H}_I v - \sigma_I v & \sigma_I \end{pmatrix} \begin{pmatrix} 1 \\ v \end{pmatrix} = \mathscr{H}_I,$$

which is a Galilean invariant too. Thus the local production of entropy reads also:

$$\Phi = div\ \left(\hat{T}\ \hat{W}\right) - \mathscr{H}_I\ \frac{d\beta}{dt} \geq 0. \tag{81}$$

Now, we establish a new expression of the production of entropy.

Theorem 5 *If the momentum tensor* $\hat{\mathbf{T}}$ *is divergence free, the local production of entropy (80) is given by:*

$$\Phi = h \cdot grad\ \beta + \beta\ Tr\ \ (\sigma_I\ D) \geq 0. \tag{82}$$

Proof Expanding (81) gives:

$$\Phi = (Div\ \hat{T})\ \hat{W} + Tr\left(\hat{T}\ \frac{\partial \hat{W}}{\partial X}\right) - \mathscr{H}_I\ \frac{d\beta}{dt} \geq 0$$

owing to the first principle 53, it holds:

$$\Phi = Tr\ \left(\hat{T}\ \frac{\partial \hat{W}}{\partial X}\right) - \mathscr{H}_I \frac{d\beta}{dt} = Tr\ \ (T\ f) + \frac{\partial \zeta}{\partial X} N + q_I\ \frac{d\beta}{dt}.$$

Because of Theorem 3 $\diamond$ or equivalently (58), one has:

$$\Phi = Tr\ (T f) - Tr\ (T_R f) + q_I \frac{d\beta}{dt} = Tr\ (T_I f) + q_I \frac{d\beta}{dt}.$$

Using expression (30) of the friction and (70) of the irreversible momentum tensor:

$$Tr\ (T_I f) = -q_I \left(\frac{\partial \beta}{\partial t} + \frac{\partial \beta}{\partial x} v\right) + \frac{\partial \beta}{\partial x} h + Tr\left(\sigma_I \left(\frac{\partial w}{\partial x}\right) - v \frac{\partial \beta}{\partial x}\right).$$

Owing to $w = \beta v$, it holds:

$$Tr\ (T_I f) = -q_I \frac{d\beta}{dt} + h \cdot grad\ \beta + \beta\ Tr\left(\sigma_I \frac{\partial v}{\partial x}\right),$$

and because σ_I is symmetric:

$$Tr\ (T_I f) + q_I \frac{d\beta}{dt} = h \cdot grad\ \beta + \beta\ Tr\ (\sigma_I D),$$

that achieves the proof. □

Through the relation:

$$\Phi = h \cdot a + Tr\ (\sigma_I A),$$

the interest of Theorem 5 is turning out a correspondance between:

- **thermodynamic forces** (or **affinities**)

$$a = grad\ \beta$$

$$A = \beta\ grad_s v = \beta\ D, \tag{83}$$

- and the corresponding **thermodynamic fluxes** h, σ_I.

$\hat{\mathbf{T}}_I$ being represented by $\tau_I = (h,\ \sigma_I)$ and $\mathbf{f}$ by $\alpha = (a,\ A)$, this dual pairing reads:

$$\Phi = \langle \tau_I,\ \alpha \rangle .$$

7 Constitutive Laws in Thermodynamics

To define completely the dissipative processes of the material, we need an additional relation called the constitutive law. In the most simple situations, it is given by a map $g : \alpha \mapsto \tau_I$, or more explicitly in terms of fluxes and affinities:

$$(a, A) \mapsto (h, \sigma_I) = g\ (a, A).$$

Before discussing some aspects of the constitutive laws, we want to characterize the non dissipative processes thanks to the following proposition:

Theorem 6 *For a continuum occupying a connected domain, let $g : \alpha \mapsto \tau_I$ be a continuous map defining a constitutive law and verifying the second principle*

$$\forall\, \alpha, \qquad \Phi = \langle g\ (\alpha),\ \alpha \rangle \geq 0. \tag{84}$$

Then, if the friction tensor field is identically null,

- ◇ *the temperature field is uniform and the motion of the continuum is rigid,*
- ♡ *the heat conduction flux and the viscous stresses vanish.*

Proof As the friction is null, $a = grad\ \beta = 0$ then β and $\theta = 1/\beta$ are uniform on a connected domain. Besides, $A = \beta\, D = 0$ and $\beta > 0$, then $D = grad_s v = 0$. In a connected domain, there exist maps $t \mapsto v_0(t) \in \mathbb{R}^3$ and $t \mapsto \omega(t) \in \mathbb{R}^3$ such that:

$$v\ (t, r) = v_0(t) + \omega\ (t) \times r,$$

that defines a rigid motion of the continuum and proves ◇.

If λ is a real number, the condition (84) gives:

$$\langle g\ (\lambda\alpha),\ \lambda\alpha \rangle = \lambda\ \langle g\ (\lambda\alpha),\ \alpha \rangle \geq 0,$$

which means that λ and $\langle g\ (\lambda\alpha),\ \alpha \rangle$ have the same sign. As λ approaches 0, by continuity:

$$\langle g\ (0),\ \alpha \rangle = 0.$$

As this occurs for any α, it is possible only if $\tau_I = g\ (0) = 0$. Then h and σ_I vanish, that proves ♡. □

Our aim is now to find the explicit form of the constitutive law in relatively simple situations, for instance when the behaviour of the continuum is isotropic and the law is linear. First of all, we have to discuss how the components of $\mathbf{f}$ and $\mathbf{T_I}$ change under Galilean and Bargmannian transformations. Let us consider a Galilean transformation with boost u and rotation R:

$$P = \begin{pmatrix} 1 & 0 \\ u & R \end{pmatrix}.$$

The transformation law of 1-covariant and 1-contravariant tensors gives for f:

$$f' = P^{-1} f\, P,$$

then:

$$\frac{\partial \beta'}{\partial t'} = \frac{\partial \beta}{\partial t} + \frac{\partial \beta}{\partial x}\, u\,, \tag{85}$$

$$\frac{\partial \beta'}{\partial x'} = \frac{\partial \beta}{\partial x}\, R\,, \tag{86}$$

$$\frac{\partial w'}{\partial t'} = R^T \left(\frac{\partial w}{\partial t} + \frac{\partial w}{\partial x}\, u \right) - \left(\frac{\partial \beta}{\partial t} + \frac{\partial \beta}{\partial x}\, u \right) R^T u\,, \tag{87}$$

$$\frac{\partial w'}{\partial x'} = R^T \left(\frac{\partial w}{\partial x} - u\, \frac{\partial \beta}{\partial x} \right) R. \tag{88}$$

By transposing relation (86), one has:

$$a' = R^T a. \tag{89}$$

Also, taking into account (86), (88) and the velocity addition formula (8), one gets:

$$\frac{\partial w'}{\partial x'} - v'\, \frac{\partial \beta'}{\partial x'} = R^T \left(\frac{\partial w}{\partial x} - v\, \frac{\partial \beta}{\partial x} \right) R.$$

Hence, the transformation law of (83) is:

$$A' = R^T A\, R. \tag{90}$$

Now, we can determine the invariants of α. It is easy to verifiy that there are the 3 eigenvalues of A, $\| a \|$, $\| A\, a \|$ and $a^T A\, a$.

The transformation laws (45) and (72) of h and σ_I are formally the same as the ones (89) and (90) of a and A. By analogy with α, the 6 independent invariants of τ_I are the 3 eigenvalues of σ_I, $\| h \|$, $\| \sigma_I h \|$ and $h^T \sigma_I\, h$. Once again, we can verify that the production of entropy is invariant:

$$h' \cdot a' + Tr\, (\sigma'_I A') = h \cdot a + Tr\, (\sigma_I A).$$

On this ground, we can construct constitutive laws. For instance, an isotropic linear law has the form:

$$h = k_1 a, \tag{91}$$

$$\sigma_I = k_2\, Tr\, (A)\, I_{\mathbb{R}^3} + k_3\, A, \tag{92}$$

where $k_1, k_2, k_3 \in \mathbb{R}$. Introducing (91) and (92) into the production of entropy (82) gives:

$$\Phi = k_1\ \| a \|^2 + k_2\ (Tr\, A)^2 + k_3\, Tr\ \left(A^2\right),$$

which is satisfied if the following restrictions are imposed to the material parameters:

$$k_1 \geq 0, \qquad k_3 \geq 0, \qquad k_2 + \frac{k_3}{3} \geq 0.$$

Law 1 *In terms of temperature, the constitutive laws are:*

- ***Fourier's law** or **law of heat conduction**:*

$$h = -k\, grad\, \theta, \tag{93}$$

*where $k = k_1 \,/\, \theta^2 \geq 0$ is the **thermal conductivity**,*

- ***Newton's viscous flow law**:*

$$\sigma_I = \eta\, (div\, v)\, I_{\mathbb{R}^3} + 2\mu\, grad_s\, v, \tag{94}$$

*where $\eta = k_2 \,/\, \theta$ and $\mu = k_3 \,/\, 2\theta \geq 0$ is the **dynamic viscosity**.*

For simple fluids, the law can be simplified by assuming that the viscous stresses σ_I are traceless (Stokes hypothesis), that leads to Navier-Stokes equations.

8 Thermodynamics and Galilean Gravitation

Until now, we are concerned only with the uniform straight motion which can be described by the calculus of variation with a Lagrangian equal to the kinetic energy. This expression of the Lagrangian is not general and, for a particle subjected to a Galilean gravitation, it must be replaced by 13:

$$\mathscr{L}(t, x, v) = \frac{1}{2} m \parallel v \parallel^2 - m\phi + mA \cdot v,$$

containing the gravitation potential ϕ and A. Let us introduce a coordinate system $\hat{X}'$ for which one:

$$dz' = \frac{\mathscr{L}}{m}\, dt.$$

This extra coordinate z' has the physical dimension and the meaning of an **action by unit mass**. Taking into account (20), we obtain:

$$dz' = dz - \phi\, dt + A \cdot dx,$$

which can be completed by:

$$dt' = dt, \qquad dx' = dx,$$

to define a linear transformation:

$$d\hat{X}' = \hat{Q}^{-1}\, d\hat{X}$$

where:

$$\hat{Q}^{-1} = \begin{pmatrix} 1 & 0 & 0 \\ 0 & 1_{\mathbb{R}^3} & 0 \\ -\phi & A^T & 1 \end{pmatrix}, \qquad \hat{Q} = \begin{pmatrix} 1 & 0 & 0 \\ 0 & 1_{\mathbb{R}^3} & 0 \\ \phi & -A^T & 1 \end{pmatrix}. \tag{95}$$

What is the physical interpretation of these transformations? Before applying it, the particle is, in absence of gravitation, in Uniform Straight Motion (USM). The effect of applying such a transformation is to embed the particle into the gravitation field. It is straightforward to verify that the set of such transformation matrix is an Abelian subgroup of the affine group $\mathbb{A}ff(5)$. It is also worth to notice that, according to the transformation law of 2-covariant tensors, Gram's matrix of the covariant metric tensor $\hat{\mathbf{G}}$ in the new coordinate system $\hat{X}'$ is given by:

$$\hat{G}' = \hat{Q}^T \hat{G}\, \hat{Q},$$

that gives for the metric embedded in the gravitation field:

$$\hat{G}' = \begin{pmatrix} -2\phi & A^T & -1 \\ A & 1_{\mathbb{R}^3} & 0 \\ -1 & 0 & 0 \end{pmatrix}. \tag{96}$$

Our starting point is now to work in these coordinate systems $\hat{X}'$ that we call **Bargmannian coordinate systems**. To know more about them, the reader is referred to [7]. When equipped with the previous covariant metric, the 5-dimensional space $\hat{\mathscr{U}}$ is now a **Riemannian manifold** and $\mathscr{U}$ a 4-dimensional submanifold thereof.

On a Riemannian manifold, there exists one and only one symmetric connection such that the covariant differential of the metric vanishes. It is called **Levi-Civita connection** and given by:

$$\Gamma^{\mu}_{\rho\alpha} = \hat{G}^{\mu\beta} \frac{1}{2} \left(\frac{\partial \hat{G}_{\alpha\beta}}{\partial \hat{X}^{\rho}} + \frac{\partial \hat{G}_{\beta\rho}}{\partial \hat{X}^{\alpha}} - \frac{\partial \hat{G}_{\rho\alpha}}{\partial \hat{X}^{\beta}} \right)$$

For the Bargmannian metrics, the only non vanishing Christoffel's symbols are:

$$\Gamma^{j}_{00} = -g^{j}, \qquad \Gamma^{j}_{0k} = \Gamma^{j}_{k0} = \Omega^{j}_{k}, \tag{97}$$

$$\Gamma^{4}_{00} = \frac{\partial \phi}{\partial t} - A \cdot g, \qquad \Gamma^{4}_{ij} = \frac{1}{2} \left(\frac{\partial A_i}{\partial x^j} + \frac{\partial A_j}{\partial x^i} \right) = (grad_s A)^{i}_{j}, \tag{98}$$

$$\Gamma^{4}_{0i} = \Gamma^{4}_{i0} = \frac{\partial \phi}{\partial x^i} - \frac{1}{2} \left(\frac{\partial A_i}{\partial x^j} - \frac{\partial A_j}{\partial x^i} \right) A^j = (grad\, \phi - \Omega \times A)^{i}. \tag{99}$$

It is worth to observe that we recover Christoffel's symbols Γ^j_{00} and Γ^j_{0k} of the Galilean connection. In matrix form, the gravitation of the space $\hat{\mathscr{U}}$ reads:

$$\hat{\Gamma}(d\hat{X}) = \begin{pmatrix} 0 & 0 & 0 \\ \varsigma_1 & \varsigma_2 & 0 \\ \varsigma_3 & \varsigma_4 & 0 \end{pmatrix},$$

where

$$\begin{aligned} \varsigma_1 &= j(\Omega)\, dx - g\, dt \\ \varsigma_2 &= j(\Omega)\, dt \\ \varsigma_3 &= \left(\frac{\partial \phi}{\partial t} - A \cdot g\right) dt + (grad\, \phi - \Omega \times A) \cdot dx \\ \varsigma_4 &= [(grad\, \phi - \Omega \times A)\ dt - grad_s A\, dx]^T \end{aligned}$$

It is the expansion of the space-time gravitation (6) to the fifth dimension.

In a similar way, the thermodynamical tensors can be embedded into the gravitation field. Applying the matrix $\hat{Q}^{-1}$ given by (95) preserves β, w and embeds the ζ component in the gravitation, that reads omitting the bar:

$$\zeta = \zeta_{int} + \frac{1}{2\beta} \parallel w \parallel^2 - \beta\, \phi + A \cdot w.$$

Taking into account (5), the friction tensor is represented in a Galilean coordinate system by the 4×4 matrix:

$$f = \nabla W = \begin{pmatrix} & \dfrac{\partial \beta}{\partial t} & \dfrac{\partial \beta}{\partial x} \\ \dfrac{\partial\, w}{\partial t} - \beta g + \Omega \times w & & \dfrac{\partial\, w}{\partial x} + \beta j(\Omega) \end{pmatrix}. \tag{100}$$

Let us calculate the expression of the momentum tensor enbedded in the gravitation field. The transformation law (32) reads:

$$\hat{T}' = Q^{-1} \hat{T}\, \hat{Q},$$

where $\hat{T}$ is given by (46), $\hat{Q}$ is given by (95) and the corresponding Q is $1_{\mathbb{R}^4}$, that leads to:

$$\hat{T}' = \begin{pmatrix} \mathscr{H}' & -\pi^T & \rho \\ h + \mathscr{H}' v - \sigma v & \sigma - v\pi^T & \rho v \end{pmatrix}, \tag{101}$$

where occurs :

- the Hamiltonian density: $\mathscr{H}' = \rho\,\left(\frac{1}{2}\parallel v\parallel^2 + \phi + e_{int} - q_I\right)$,
- the generalized linear momentum: $\pi = \rho\,(v + A)$.

In the sequel, we are implicitly supposed to work in Bargmannian coordinate systems but the prime shall be omitted for sake of easiness. Let us examine now the expression of the first principle of the thermodynamics (53) in presence of gravitation.

Theorem 7 *If $\hat{T}$ is covariant divergence free:*

$$Div_X\,\hat{T} = 0,$$

then, we have:

♢ ***balance of mass***: $\dfrac{\partial \rho}{\partial t} + div\,(\rho\, v) = 0,$

♡ ***balance of linear momentum***:

$$\rho\left[\frac{\partial v}{\partial t} + \frac{\partial v}{\partial x}\,v\right] = (div\,\sigma)^T + \rho\,\left(g - 2\,\Omega\times v\right),$$

♠ ***balance of energy***: $\dfrac{\partial \mathscr{H}}{\partial t} + div\;\left(h + \mathscr{H} v - \sigma v\right) = \rho\left(\dfrac{\partial \phi}{\partial t} - \dfrac{\partial A}{\partial t}\cdot v\right).$

Proof As the space-time $\mathscr{U}$ is a submanifold of the 5-dimensional space $\hat{\mathscr{U}}$, an event $\boldsymbol{X}\in\mathscr{U}$ belongs also to $\hat{\mathscr{U}}$. We consider a momentum field $\boldsymbol{X}\mapsto\hat{\boldsymbol{T}}(\boldsymbol{X})$ where $\hat{\boldsymbol{T}}(\boldsymbol{X})$ is a 1-covariant tensor on the tangent space $T_{\boldsymbol{X}}\hat{\mathscr{U}}$ with vector values in $T_{\boldsymbol{X}}\mathscr{U}$ (which can be identified to a linear map from $T_{\boldsymbol{X}}\hat{\mathscr{U}}$ to $T_{\boldsymbol{X}}\mathscr{U}$):

$$\hat{\boldsymbol{T}} : T_{\boldsymbol{X}}\hat{\mathscr{U}} \to T_{\boldsymbol{X}}\mathscr{U} : \hat{\overrightarrow{\boldsymbol{V}}} \mapsto \hat{\boldsymbol{T}}(\hat{\overrightarrow{\boldsymbol{V}}}). \tag{102}$$

We wish to calculate its covariant divergence. In addition to Convention 1, we adopt the extra one: Greek indices $\hat{\alpha}, \hat{\beta}, \hat{\gamma}$ and so on run over the five coordinate labels 0, 1, 2, 3, 4. The basis $(\overrightarrow{\boldsymbol{e}}_\alpha)$ of $T_{\boldsymbol{X}}\mathscr{U}$ is completed by $\overrightarrow{\boldsymbol{e}}_4$ to build a basis $(\overrightarrow{\boldsymbol{e}}_{\hat{\alpha}})$ of $T_{\boldsymbol{X}}\hat{\mathscr{U}}$ in which the momentum tensor is decomposed as:

$$\hat{\boldsymbol{T}} = \hat{T}^\gamma \boldsymbol{e}_\gamma, \qquad \hat{T}^\gamma = \hat{T}^\gamma_{\hat{\alpha}}\boldsymbol{e}^{\hat{\alpha}}.$$

Its covariant differential is:

$$\nabla_{\overrightarrow{d\boldsymbol{X}}}\,\hat{\boldsymbol{T}} = \nabla_{\overrightarrow{d\boldsymbol{X}}}\,(\hat{T}^\gamma\,\overrightarrow{\boldsymbol{e}}_\gamma) = (\nabla_{\overrightarrow{d\boldsymbol{X}}}\,\hat{T}^\gamma)\,\overrightarrow{\boldsymbol{e}}_\gamma + \hat{T}^\gamma\,(\nabla_{\overrightarrow{d\boldsymbol{X}}}\,\overrightarrow{\boldsymbol{e}}_\gamma) = (\nabla_{\overrightarrow{d\boldsymbol{X}}}\,\hat{T}^\gamma + \Gamma^\gamma_\rho\,\hat{T}^\rho)\,\overrightarrow{\boldsymbol{e}}_\gamma,$$

where:

$$\nabla_{\overrightarrow{d\boldsymbol{X}}}\,\hat{T}^\gamma = \nabla_{d\boldsymbol{X}}\,(\hat{T}^\gamma_{\hat{\alpha}}\boldsymbol{e}^{\hat{\alpha}}) = d\hat{T}^\gamma_{\hat{\alpha}}\,\boldsymbol{e}^{\hat{\alpha}} + \hat{T}^\gamma_{\hat{\alpha}}\,\nabla_{d\boldsymbol{X}}\,\boldsymbol{e}^{\hat{\alpha}} = (d\hat{T}^\gamma_{\hat{\alpha}} - \hat{T}^\gamma_{\hat{\beta}}\,\Gamma^{\hat{\beta}}_{\hat{\alpha}})\,\boldsymbol{e}^{\hat{\alpha}}.$$

Hence, we obtain:

$$\nabla_{\overrightarrow{dX}}\,\hat{\boldsymbol{T}} = \left[\nabla_{dX}\hat{T}^{\gamma}_{\hat{\alpha}}\,\boldsymbol{e}^{\hat{\alpha}}\right]\,\overrightarrow{\boldsymbol{e}}_{\gamma},$$

with:

$$\nabla_{dX}\hat{T}^{\gamma}_{\hat{\alpha}} = d\hat{T}^{\gamma}_{\hat{\alpha}} + \Gamma^{\gamma}_{\rho}\hat{T}^{\rho}_{\hat{\alpha}} - \hat{T}^{\gamma}_{\hat{\beta}}\Gamma^{\hat{\beta}}_{\hat{\alpha}}$$

Hence, there exists a field $\nabla\,\hat{\boldsymbol{T}}$ of 2-covariant and 1-contravariant tensors such that:

$$\nabla_{\overrightarrow{dX}}\,\hat{\boldsymbol{T}} = (\nabla\,\hat{\boldsymbol{T}})\cdot\overrightarrow{d\boldsymbol{X}}.$$

Using Christoffel's symbols, one has:

$$\nabla\,\hat{\boldsymbol{T}} = \left[\nabla_{\sigma}\hat{T}^{\gamma}_{\hat{\alpha}}\,\boldsymbol{e}^{\hat{\alpha}}\right]\,\overrightarrow{\boldsymbol{e}}_{\gamma}\otimes\boldsymbol{e}^{\sigma},$$

with:

$$\nabla_{\sigma}\hat{T}^{\gamma}_{\hat{\alpha}} = \frac{\partial\hat{T}^{\gamma}_{\hat{\alpha}}}{\partial X^{\sigma}} + \Gamma^{\gamma}_{\rho\sigma}T^{\rho}_{\hat{\alpha}} - \hat{T}^{\gamma}_{\hat{\beta}}\Gamma^{\hat{\beta}}_{\hat{\alpha}\sigma}.$$

By contraction, we define the **covariant divergence** of the momentum tensor:

$$\boldsymbol{Div}\,\hat{\boldsymbol{T}} = \nabla_{\gamma}\hat{T}^{\gamma}_{\hat{\alpha}}\,\boldsymbol{e}^{\hat{\alpha}},$$

with:

$$\nabla_{\gamma}\hat{T}^{\gamma}_{\hat{\alpha}} = \frac{\partial\hat{T}^{\gamma}_{\hat{\alpha}}}{\partial X^{\gamma}} + \Gamma^{\gamma}_{\rho\gamma}T^{\rho}_{\hat{\alpha}} - \hat{T}^{\gamma}_{\hat{\beta}}\Gamma^{\hat{\beta}}_{\hat{\alpha}\gamma}. \tag{103}$$

In indicial notation, the components of $\hat{\boldsymbol{T}}$ are:

$$\hat{T}^{0}_{0} = \mathscr{H}, \qquad \hat{T}^{0}_{i} = -\delta_{ik}\pi^{k}, \qquad \hat{T}^{0}_{4} = \rho, \tag{104}$$

$$\hat{T}^{j}_{0} = h^{j} + \mathscr{H}v^{j} - \sigma^{j}_{k}v^{k}, \qquad \hat{T}^{j}_{i} = \sigma^{j}_{i} - v^{j}\delta_{ik}\pi^{k}, \qquad \hat{T}^{j}_{4} = p^{j}. \tag{105}$$

The first principle of the thermodynamics (53) reads:

$$\nabla_{\gamma}\hat{T}^{\gamma}_{\hat{\alpha}} = 0,$$

where Christoffel's symbols are given by (97), (98) and (99). Putting $\hat{\alpha} = 4$ in the previous equation and taking into account the vanishing terms, one has:

$$\nabla_{\gamma}\hat{T}^{\gamma}_{4} = \frac{\partial\hat{T}^{\gamma}_{4}}{\partial X^{\gamma}} = 0,$$

that allows to recover the balance of mass $\diamondsuit$. Similarly, putting $\hat{\alpha} = i$ and taking into account the non vanishing terms, it holds:

$$\nabla_\gamma \hat{T}_i^\gamma = \frac{\partial \hat{T}_i^\gamma}{\partial X^\gamma} - \hat{T}_j^0 \Gamma_{i0}^j - \hat{T}_4^0 \Gamma_{i0}^4 - \hat{T}_4^j \Gamma_{ij}^4 = 0,$$

or, owing to the momentum components (104) and (105):

$$-\frac{\partial}{\partial t}(\delta_{ik}\pi^k) + \frac{\partial}{\partial x^j}(\sigma_i^j - v^j \delta_{ik}\pi^k) + \delta_{jk}\pi^k \Omega_i^j - \rho\, \Gamma_{i0}^4 - p^j \Gamma_{ij}^4 = 0.$$

It reads in matrix form:

$$-\frac{\partial}{\partial t}(\rho\,(v+A)^T) + div\,\sigma - div\,(\rho v)\,(v+A)^T - \rho v^T grad\,(v+A)$$

$$+\rho\,(v+A)^T j(\Omega) - \rho\,\,(grad\,\phi - \Omega \times A)^T + \rho\, v^T grad_s\, A = 0.$$

But, owing to (14), it holds:

$$grad_s\, A = \frac{\partial A}{\partial x} - j(\Omega)$$

After simple calculations, we obtain the balance of linear momentum $\heartsuit$.
Finally, putting $\hat{\alpha} = 0$ and taking into account the non vanishing terms, it holds:

$$\nabla_\gamma \hat{T}_0^\gamma = \frac{\partial \hat{T}_0^\gamma}{\partial X^\gamma} - \hat{T}_j^0 \Gamma_{00}^j - \hat{T}_j^i \Gamma_{i0}^4 - \hat{T}_4^0 \Gamma_{00}^4 - \hat{T}_4^j \Gamma_{j0}^4 = 0,$$

which reads in matrix form, after some simplifications:

$$\frac{\partial \mathscr{H}}{\partial t} + div\,\,(h + \mathscr{H} v - \sigma v) - \rho\left(v \cdot (g + grad\,\phi) + \frac{\partial \phi}{\partial t}\right) = 0.$$

But, owing to (14), it holds:

$$v \cdot g + \frac{d\phi}{dt} = v \cdot (g + grad\,\phi) + \frac{\partial \phi}{\partial t} = \frac{\partial \phi}{\partial t} - v \cdot \frac{\partial A}{\partial t} \tag{106}$$

which leads to the balance of energy $\spadesuit$ and achieves the proof. □

Theorem 3 concerning the reversible processes remains true. Only the demonstration of $\diamondsuit$ is different. Before calculating, it is worth noting that the covariant derivative of ζ is meaningfull because ζ is not a scalar but a component of the temperature vector. We can verify that:

$$(\nabla\zeta)\,N = \rho\left(\frac{d\zeta}{dt} - \beta g\cdot v\right)$$

the remaing part of the calculation is straightforward taking into account the expression (100) of the friction embedded into the gravitation field.

For the dissipative continua, the equation of heat transfer (77) is slightly modified. Wet let the reader to show that (74) is replaced by:

$$\rho\,\frac{d}{dt}\,(e_{int}+\phi) = Tr\ (\sigma\,D) - div\,h + \rho\,\frac{dq_I}{dt} + \rho\left(\frac{\partial\phi}{\partial t} - \frac{\partial A}{\partial t}\cdot v\right),$$

or, taking into account (106):

$$\rho\,\frac{de_{int}}{dt} = Tr\ (\sigma\,D) + g\cdot v - div\,h + \rho\,\frac{dq_I}{dt}.$$

Next, the **equation of heat transfer with gravitation** is:

$$\rho\,c_v\,\frac{d\theta}{dt} = \theta\ Tr\left(\frac{\partial\sigma_R}{\partial\theta}\,D\right) + Tr\ (\sigma_I\,D) + g\cdot v - div\,h + \rho\,\frac{dq_I}{dt}. \tag{107}$$

Taking into account the expression (100) of the friction, the reader can also easily verify that the expression (81) of the production of entropy is replaced by:

$$\Phi = Div\,\left(\hat{T}\,\hat{W}\right) - \mathscr{H}_I\,\frac{d\beta}{dt} \geq 0, \tag{108}$$

where occurs now the covariant divergence in the first term. To be consistent with Galileo's principle of relativity 1, Theorem 5 is replaced by:

Theorem 8 *If the momentum tensor* $\hat{\mathbf{T}}$ *is* ***covariant*** *divergence free, the local production of entropy (80) is given by (82):*

$$\Phi = h\cdot\ grad\ \beta + \beta\ Tr\ (\sigma_I\,D) \geq 0.$$

Proof We start with the rule:

$$\boldsymbol{Div}\,(\hat{\boldsymbol{T}}\cdot\hat{\boldsymbol{W}}) = (\boldsymbol{Div}\,\hat{\boldsymbol{T}})\cdot\hat{\boldsymbol{W}} + \hat{\boldsymbol{T}} : \nabla\hat{\boldsymbol{W}},$$

or in local coordinates:

$$Div(\hat{T}\,\hat{W}) = (Div\,\hat{T})\,\hat{W} + Tr\,(\hat{T}\,\nabla\hat{W}),$$

hence, starting from (108) and owing to the first principle expressed by Eq. (53) (namely, Principle 2), it holds:

$$\Phi = Tr\ \left(\hat{T}\,\nabla\hat{W}\right) - \mathscr{H}_I\frac{d\beta}{dt} = Tr\ (T\,f) + (\nabla\zeta)\,N + q_I\,\frac{d\beta}{dt}.$$

Because of Theorem 3 $\Diamond$ or equivalently (57), one has:

$$\Phi = Tr\ (T_I\,f) + q_I\,\frac{d\beta}{dt},$$

and the proof follows the one of Theorem 5, that achieves the proof. □

The reader can verify that, starting from (81) and using the balance of mass, the local production of entropy reads:

$$\Phi = \rho\,\frac{ds}{dt} - \frac{\rho}{\theta}\,\frac{dq_I}{dt} + div\,\left(\frac{h}{\theta}\right) \geq 0. \tag{109}$$

This relation is known in the literature as **Clausius-Duhem inequality** but it seems first appearing in Truesdell's works [19, 20].

9 Relativistic Version of the Second Principle

By opposition to Galilean relativity, Lorentz-Poincaré-Einstein one is based on the experimental fact that the speed of the light—even if it is huge—has a finite value c for every observer. Which are the underlying transformation group and geometry? In absence of gravitation, the light rays are straight lines and the particles of light—the photons—move at the constant velocity c in any coordinate system X where the observer takes measures to identify the events. Hence we are interested in determining the coordinate changes $X' \mapsto X$ preserving the straight lines in the space-time of equation $dx = v\,dt$ with $\parallel v \parallel = c$. Equivalently, they preserve the relation:

$$\parallel dx \parallel^2 - c^2 dt^2 = 0.$$

thus **Minkowski's metrics** G defined by Gram's matrix:

$$G = \begin{pmatrix} c^2 & 0 \\ 0 & -1_{\mathbb{R}^3} \end{pmatrix}. \tag{110}$$

The affine transformations $dX = P\,dX' + C$ preserving this metrics:

$$P^T G P = G$$

are called **Poincarean transformations**. Their linear part P are called **Lorentzian transformations**. They can be unically decomposed as the product:

$$P = P_u P_R$$

of two Lorentzian transformations, P_u associated to a boost u and P_R associated to an orthogonal transformation $R \in \mathbb{O}(3)$:

$$P_u = \begin{pmatrix} \gamma & \frac{1}{c^2}\gamma\, u^T \\ \gamma\, u & 1_{\mathbb{R}^3} + \frac{1}{c^2}\frac{\gamma^2}{\gamma+1} u\, u^T \end{pmatrix}, \qquad P_R = \begin{pmatrix} \varepsilon & 0 \\ 0 & \varepsilon' R \end{pmatrix}, \tag{111}$$

where $\gamma = \mid 1 - \parallel u \parallel^2 / c^2 \mid^{-1/2}$, $\varepsilon, \varepsilon' \in \{-1, 1\}$.

Let us achieve this quick review of relativity by a smidgen of thermodynamics of continua. The motivation in Galilean relativity to introduce the momentum tensor $\hat{\boldsymbol{T}}$ of Definition 5 was to obtain, according to Theorem 2, the balance of both the mass and energy as expression of the first principle of the thermodynamics 2. In Lorentz-Poincaré-Einstein relativity, we just saw that mass and energy are identical, the factor c^2 aside. It is not necessary to use the artefact of the fifth dimension and we work in the space-time only with the **temperature** 4-**vector** $\overrightarrow{\boldsymbol{W}}$ represented by a column:

$$W' = \begin{pmatrix} \beta \\ 0 \end{pmatrix},$$

in a coordinate system X' where the elementary volume is at rest. In another coordinate system X obtained from X' by a boost v, the temperature vector reads:

$$W = P\, W' = \begin{pmatrix} \gamma & \frac{1}{c^2}\gamma\, v^T \\ \gamma\, v & 1_{\mathbb{R}^3} + \frac{1}{c^2}\frac{\gamma^2}{\gamma+1} v\, v^T \end{pmatrix} \begin{pmatrix} \beta \\ 0 \end{pmatrix} = \begin{pmatrix} \gamma\, \beta \\ \gamma\, \beta\, v \end{pmatrix}.$$

Then the absolute temperature is transformed as:

$$\theta' = \frac{\theta}{\gamma} = \theta \mid 1 - \parallel v \parallel^2 / c^2 \mid^{1/2}.$$

According to Planck's theory, when the velocity of the elementary volume increases with respect to the observer, the temperature measured by her or him decreases. This is the **temperature contraction**.

To every vector $\overrightarrow{\boldsymbol{U}}$ is associated one and only one linear form $\overrightarrow{\boldsymbol{V}} \mapsto \boldsymbol{G}(\overrightarrow{\boldsymbol{U}}, \overrightarrow{\boldsymbol{V}}) = \overrightarrow{\boldsymbol{U}} \cdot \overrightarrow{\boldsymbol{V}}$ denoted $\boldsymbol{U}^*$. The covariant components of $\boldsymbol{U}^*$ depends on the contravariant components of $\overrightarrow{\boldsymbol{U}}$ through the operation of **lowering the index**:

$$U_i = G_{ij} U^j$$

which reads in matrix form:

$$U^* = U^T G \tag{112}$$

Let $\boldsymbol{A}$ be a linear map from an Euclidean space $\mathscr{T}$ into itself. Its **adjoint** is the linear map $\boldsymbol{A}^*$ from $\mathscr{T}$ into itself such that:

$$\forall \overrightarrow{\boldsymbol{U}}, \overrightarrow{\boldsymbol{V}} \in \mathscr{T}, \qquad \overrightarrow{\boldsymbol{U}} \cdot (\boldsymbol{A}\, \overrightarrow{\boldsymbol{V}}) = (\boldsymbol{A}^* \overrightarrow{\boldsymbol{U}}) \cdot \overrightarrow{\boldsymbol{V}}$$

The linear map is **self-adjoint** if $\boldsymbol{A} = \boldsymbol{A}^*$.

In general relativity, we use Levi-Civita connection associated to the Riemannian structure. The **Poincarean friction tensor** is the self-adjoint 1-covariant and 1-contravariant tensor:

$$\mathbf{f} = \frac{1}{2}\left(\nabla \overrightarrow{\boldsymbol{W}} + \left(\nabla \overrightarrow{\boldsymbol{W}}\right)^*\right).$$

The **Poincarean momentum tensor** is a self-adjoint 1-covariant and 1-contravariant tensor $\boldsymbol{T}$ on the space-time. The relativistic version of the **first principle of the thermodynamics** claims that it is covariant divergence free:

$$\boldsymbol{Div}\, \boldsymbol{T} = \mathbf{0}.$$

Inspiring from the **second principle of the thermodynamics** 3, the relativistic version claims that the **local production of entropy**:

$$\Phi = \boldsymbol{Div}\left(\boldsymbol{T}\, \overrightarrow{\boldsymbol{W}} + \zeta\, \overrightarrow{\boldsymbol{N}}\right) - \frac{1}{c^2}\left(\boldsymbol{U}^*(\boldsymbol{f}(\overrightarrow{\boldsymbol{U}}))\right) \frac{1}{c^2}\left(\boldsymbol{U}^*(\boldsymbol{T}_I(\overrightarrow{\boldsymbol{U}}))\right) \geq 0,$$

of a continuous medium characterized by fields of Planck's potential ζ, velocity vector $\overrightarrow{\boldsymbol{U}}$, mass flux vector $\overrightarrow{\boldsymbol{N}}$, temperature vector $\overrightarrow{\boldsymbol{W}}$ and momentum tensor $\boldsymbol{T}$ is non negative and vanishes if and only if the process is reversible.

The reason is that when the speed of the light approaches the infinite, the linear form $\boldsymbol{U}^*$, is represented by the 4-row (112):

$$U^T G = (\gamma, \gamma\, v^T) \begin{pmatrix} c^2 & 0 \\ 0 & -1_{\mathbb{R}^3} \end{pmatrix} = c^2 \left(\gamma, -\frac{1}{c^2}\gamma\, v^T\right),$$

which approaches $c^2 \boldsymbol{e}^0$ where $\boldsymbol{e}^0$ is the time arrow and we recover the expression (78) of the Galilean local production of the entropy. The reader interested by the relativistic thermodynamics of continua is referred to [21, 22].

10 Conclusions

The key tool of this work are the energy-momentum tensor $\hat{\mathbf{T}}$ and a 5-vector of temperature $\hat{\mathbf{W}}$. This allows to develop a premetric geometrization of the first principle of thermodynamics, able to treat at one go the classic and relativistic cases, in the form

$$Div\ \hat{\mathbf{T}} = \mathbf{0}$$

The geometrization of the second principle reads

$$\Phi = \boldsymbol{Div}\left(\hat{T}\ \hat{\overrightarrow{W}}\right) - \left(e^0(f(\overrightarrow{U}))\right)\ \left(e^0(T_I(\overrightarrow{U}))\right) \geq 0$$

but it is only valid for the classical approximation. We proved its invariance in Galilean relativity and its equivalence with the usual formulation of Clausius-Duhem inequality. We did not follow in this work all the ideas developed in [21, 22]. They would suggest rather to conjecture that

$$Div\left(\hat{\mathbf{T}}\ \hat{\overrightarrow{W}}\right) \geq 0$$

Finally, we generalized the formalism to include the gravitation in a consistent way and we propose a relativistic version of the second principle.

The way opened in this work seems to be promising and we hope to consider in the future some important aspects that were not treated:

(i) Our formalism can represent the heat transfer by conduction, convection but not radiation, that would need to examine the coupling with the electromagnetism.

(ii) In a previous work [3, 5, 7], we proposed revisiting the theory of continuous media with the tool of the affine tensors, by opposition to the classical linear tensors. We introduce a contravariant 2-rank affine tensor called torsor. Claiming that it is affine divergence free allows recovering the balance equations of the mass and momentum. In the same spirit, we hope generalizing in the future the momentum tensor $\hat{\mathbf{T}}$ as a mixed 2-rank affine tensor.

(iii) Bargmann group was introduced to solve problems of group quantization. In fact, Galileo's group is not quantizable and the reason of this failure is cohomologic. Same kind of pitfall occurs in symplectic mechanics where, considering the action of Galileo's group on the momentum mappings, the class of symplectic cohomology is not null [4, 13, 16]. Why Bargmann group appears in thermodynamics modelization? We think that the reason is quite similar and this suggests to do more pervasive investigations on this topics in the frame of the multisymplectic mechanics.

References

1. Bargmann V (1954) On unitary representation of continuous groups. Ann Math 59:1–46
2. Cartan É (1923) Sur les variétés à connexion affine et la théorie de la relativité généralisée (première partie). Ann de l'École Normale Supérieure 40:325–412
3. de Saxcé G, Vallée C (2003) Affine tensors in shell theory. J Theor Appl Mech 41:593–621
4. de Saxcé G, Vallée C (2010) Construction of a central extension of a Lie group from its class of symplectic cohomology. J Geometry Phys 60:165–174
5. de Saxcé G, Vallée C (2011) Affine tensors in mechanics of freely falling particles and rigid bodies. Math Mech Solid J 17:413–430
6. de Saxcé G, Vallée C (2012) Bargmann group, momentum tensor and Galilean invariance of Clausius-Duhem inequality. Int J Eng Sci 50:216–232
7. de Saxcé G, Vallée C (2016) Galilean mechanics and thermodynamics of continua. Wiley-ISTE
8. Iglesias P (1981) Essai de thermodynamique rationnelle des milieux continus. Ann de l'Institut Henri Poincaré 34:1–24
9. Künzle HP (1972) Galilei and Lorentz structures on space-time: comparison of the corresponding geometry and physics. Ann de l'Institut Henri Poincaré 17:337–362
10. Misner C, Thorne K, Wheeler J (1973) Gravitation. Freeman
11. Noll W (1973) Lectures on the foundations of continuum mechanics and thermodynamics. Arch Ration Mech Anal 52:62–92
12. Souriau JM (1964) Géométrie et relativité. Collection Enseignement des sciences. Hermann, Paris
13. Souriau JM (1970) Structure des systèmes dynamique. Dunod, Paris
14. Souriau JM (1976/1977). Thermodynamique et géométrie. Lecture Notes in Mathematics 676:369–397
15. Souriau JM (1978) Thermodynamique relativiste des fluides. Rendiconti del Seminario Matematico Università Politecnico di Torino 35:21–34
16. Souriau JM (1997) Structure of dynamical systems. A symplectic view of physics. Birkhäuser, New York
17. Souriau J (1997) Milieux continus de dimension 1, 2 ou 3: statique et dynamique. In: Proceeding of the 13eme Congrès Français de Mécanique, pp 41–53, Poitiers-Futuroscope
18. Toupin R (1957/1958) World invariant kinematics. Arch Ration Mech Anal 1:181–211
19. Truesdell C (1952) The mechanical foundation of elasticity and fluid dynamics. J Ration Mech Anal 1:125–171
20. Truesdell C, Toupin R (1960) The classical field theories. In: Encyclopedia of Physics, S. Flügge, Vol II/1, Principles of classical mechanics and field theory. Springer, Berlin
21. Vallée C (1978) Lois de comportement des milieux continus dissipatifs compatibles avec la physique relativiste. Ph.D. thesis, University of Poitiers
22. Vallée C (1981) Relativistic thermodynamics of continua. Int J Eng Sci 19:589–601

Quinze Ans Après...

Christian Licht and Thibaut Weller

Abstract We aim to present mathematical models of smart devices and smart structures. Smart devices are made of materials which present significant multiphysical couplings. They are integrated in smart structures which take technological advantages of some multiphysical effects. We first propose simplified but accurate models of thin plates or slender rods made of piezoelectric or electromagneto-elastic materials in both static and dynamic cases. Then we focus on smart structures such as piezoelectric patches bonded on a linearly elastic body and piezoelectric junctions between two linearly piezoelectric or elastic bodies.

1 Introduction

On November 2000, Franco Maceri came to the LMGC to present the next Colloquium Lagrangianum in Taormina and a recent study [2] on piezoelectric plates. Here we present all the studies about mathematical modeling in piezoelectricity (a topic totally new for us) we did after this stimulating talk.

In the first part we intend to propose simplified but accurate models of devices made of piezoelectric or elecromagneto-elastic materials, these devices (thin plates, slender rods) presenting one or two small dimensions. We also studied the not so well-known case of piezoelectricity with electric field gradient. The models are obtained by a rigorous study of the asymptotic behavior of a three dimensional body when some of its dimensions, considered as parameters, tend to zero. We used various

C. Licht (✉) · T. Weller
Université Montpellier II, Laboratoire de Mécanique et Génie Civil, UMR 5508
CNRS-UM 2, c.c. 48, Place Eugène Bataillon, 34095 Montpellier, France
e-mail: christian.licht@umontpellier.fr

C. Licht
Mahidol University, Department of Mathematics, Faculty of Science,
Bangkok 10400, Thailand

T. Weller
e-mail: thibaut.weller@umontpellier.fr

M. Frémond et al. (eds.), *Models, Simulation, and Experimental Issues in Structural Mechanics*, Springer Series in Solid and Structural Mechanics 8,
DOI 10.1007/978-3-319-48884-4_2

tools of variational and functional analysis, the point being to consider boundary value problems depending on small parameters. This study has been carried out in the steady-state and transient cases. We outline that different kinds of models appear at the limit, depending on the electrical loading. These models correspond to the physical situation when the device behaves as a sensor or as an actuator. Moreover, we are able to show that depending on the crystalline symmetry class of the material, a striking structural switch-off may appear at the limit, the device being no more piezoelectric.

The essential technological interest of piezoelectric devices being the monitoring of a deformable body they are bonded to or integrated in, the second part is devoted to smart structures. The obtained results are discussed in detail in Sect. 3.

Of course, this field of research has led in the past 20 years to a considerable amount of literature. In this paper, we limit ourselves to our own work. The reader will find in the references of our studies a great number of articles published in this area.

2 Mathematical Modelings of Smart Devices

As usual we make no difference between the physical space and $\mathbb{R}^3$ whose basis is denoted (e_1, e_2, e_3). For all $\xi = (\xi_1, \xi_2, \xi_3)$ in $\mathbb{R}^3$, we denote (ξ_1, ξ_2) by $\widehat{\xi}$. Greek indices for coordinates take their values in $\{1, 2\}$ whereas Latin indices run from 1 to 3.

Let $\mathbb{H} = \mathbb{S}^3 \times \mathbb{R}^3$, where $\mathbb{S}^3$ denotes the set of all 3×3 real and symmetric matrices. The set of all linear mappings from a space V into a space W is denoted $\mathscr{L}(V, W)$ and by $\mathscr{L}(V)$ if $V = W$.

In the sequel, for every domain G in $\mathbb{R}^N$, the subspace of the Sobolev space $H^1(G)$ whose elements vanish on Γ, included in the boundary ∂G of G, will be denoted by $H^1_\Gamma(G)$.

2.1 Piezoelectric Thin Plates

Finding the equilibrium of a thin linearly piezoelectric plate can be formulated as follows. The reference configuration of a linearly piezoelectric thin plate is the closure in $\mathbb{R}^3$ of the set $\Omega^\varepsilon := \omega \times (-\varepsilon, \varepsilon)$, where ω is a bounded domain of $\mathbb{R}^2$ with Lipschitz boundary $\partial\omega$ and ε a small positive number. Let $\Gamma^\varepsilon_{\text{lat}} := \partial\omega \times (-\varepsilon, \varepsilon)$, $\Gamma^\varepsilon_\pm := \omega \times \{\pm\varepsilon\}$ and two suitable partitions of $\partial\Omega^\varepsilon$: $(\Gamma^\varepsilon_{mD}, \Gamma^\varepsilon_{mN})$ and $(\Gamma^\varepsilon_{eD}, \Gamma^\varepsilon_{eN})$ with Γ^ε_{mD} and Γ^ε_{eD} of strictly positive surface measures. The plate is clamped along Γ^ε_{mD} and at an electrical potential φ^ε_0 on Γ^ε_{eD}. It is subjected to body forces f^ε in Ω^ε and to surface forces g^ε in Γ^ε_{mN}. Furthermore, we will consider an electrical loading d^ε on Γ^ε_{eN}. We note n^ε the outward unit normal to $\partial\Omega^\varepsilon$ and assume that $\Gamma^\varepsilon_{mD} = \gamma_0 \times (-\varepsilon, \varepsilon)$, with $\gamma_0 \subset \partial\omega$. The equations determining the piezoelectric state $s^\varepsilon := (u^\varepsilon, \varphi^\varepsilon)$ at equilibrium are:

$$\mathscr{P}(\Omega^\varepsilon)\quad\begin{cases}\operatorname{div}\sigma^\varepsilon+f^\varepsilon=0\ \text{ in }\Omega^\varepsilon,\ \sigma^\varepsilon n^\varepsilon=g^\varepsilon\ \text{ on }\Gamma^\varepsilon_{mN},\ u^\varepsilon=0\ \text{ on }\ \Gamma^\varepsilon_{mD},\\ \operatorname{div}D^\varepsilon=0\ \text{in }\Omega^\varepsilon,\ D^\varepsilon\cdot n^\varepsilon=d^\varepsilon\ \text{ on }\Gamma^\varepsilon_{eN},\ \varphi^\varepsilon=\varphi^\varepsilon_0\ \text{ on }\Gamma^\varepsilon_{eD},\\ (\sigma^\varepsilon,D^\varepsilon)=M^\varepsilon(x)(e(u^\varepsilon),\nabla\varphi^\varepsilon)\ \text{in }\Omega^\varepsilon,\end{cases}$$

where u^ε, φ^ε, σ^ε, $e(u^\varepsilon)$ and D^ε respectively stand for the displacement, the electrical potential, the stress tensor, the tensor of small strains (*i.e.* the symmetrized gradient) and the electric induction. The operator M^ε is an element of $\mathscr{L}(\mathscr{H})$ such that:

$$\begin{aligned}\sigma^\varepsilon &= a^\varepsilon\, e(u^\varepsilon)\ - b^\varepsilon\,\nabla\varphi^\varepsilon\\ D^\varepsilon &= {b^\varepsilon}^T\, e(u^\varepsilon)+c^\varepsilon\,\nabla\varphi^\varepsilon\end{aligned}\tag{1}$$

with ${b^\varepsilon}^T$ the transpose of the piezoelectric tensor b^ε, the elastic tensor a^ε and the dielectric one c^ε being symmetric and positive. Note that because of the piezoelectric coupling, M^ε is not symmetric.

It is easy to give a weak (or variational) formulation of the previous linear boundary problem and to conclude to the existence and the uniqueness of a solution in suitable Sobolev spaces through the Stampacchia theorem.

Nevertheless, due to the very low thickness of the plate, this classical model may be difficult to tackle numerically. The essence of our proposal of simplified but accurate modeling is to consider ε as a small *parameter* and to study the asymptotic behavior of s^ε when ε goes to 0. In fact, two different limit behaviors indexed by $p\in\{1,2\}$ will occur, according to the type of boundary condition in $\mathscr{P}(\Omega^\varepsilon)$.

From the mathematical point of view it is convenient to proceed to a change of coordinates Π^ε and of unknowns $s_p(\varepsilon)=S_p(\varepsilon)s^\varepsilon$ in order to consider functional spaces defined on a fixed domain $\Omega=\omega\times(-1,1)$:

$$\begin{aligned}x=(x_1,x_2,x_3)\in\overline{\Omega}\mapsto\Pi^\varepsilon x=(x_1,x_2,\varepsilon x_3)\in\overline{\Omega}^\varepsilon\\ s_p(\varepsilon):=(u(\varepsilon)(x),\varphi_p(\varepsilon)(x))\ =\ ((\varepsilon^{-1}\hat{u}^\varepsilon(\Pi^\varepsilon x),u_3^\varepsilon(\Pi^\varepsilon x)),\varepsilon^{-p}\varphi^\varepsilon(\Pi^\varepsilon x)).\end{aligned}\tag{2}$$

The formulae defining $S_p(\varepsilon)$ stem from the assumptions on the magnitude of the electromechanical loading and are justified by the convergence results they lead to. If we consider forces and displacements, these hypotheses are the ones of [3] and supply a mathematical justification of the Kirchhoff-Love theory of thin linearly elastic plates. In addition, we assume that φ_0^ε has an extension into Ω^ε still denoted by φ_0^ε and that $\varphi_0\in H^1(\Omega)$ is such that $\varphi_0^\varepsilon(\Pi^\varepsilon x)=\varepsilon^p\varphi_0(x)$ with:

$$\begin{cases}\text{if } p=1:\ \varphi_0 \text{ does not depend on } x_3.\\ \text{if } p=2:\ \text{the closure of the projection of } \Gamma^\varepsilon_{eD} \text{on } \omega \text{ coincides with } \overline{\omega},\\ \qquad\qquad \text{moreover, either } d^\varepsilon=0 \text{ on } \Gamma^\varepsilon_{eN}\cap\Gamma^\varepsilon_{\text{lat}} \text{ or } \Gamma^\varepsilon_{eN}\cap\Gamma^\varepsilon_{\text{lat}}=\emptyset.\end{cases}\tag{3}$$

Thus $s(\varepsilon)$ is the solution of the variational problem:

$$\begin{cases} \text{Find } s_p(\varepsilon) \in (0,\varphi_0) + V = \{r = (v,\psi) \in H^1_{\Gamma_{mD}}(\Omega)^3 \times H^1_{\Gamma_{eD}}(\Omega)\} \text{ such that} \\ \int_\Omega M(x)\, k_p(\varepsilon,s)\cdot k_p(\varepsilon,r)\,dx = L(r),\ \forall r \in V \end{cases}$$

where the linear form L does not depend on ε and

$$\begin{cases} k_p(\varepsilon,r) = k_p(\varepsilon,(v,\psi)) = (e(\varepsilon,v), \nabla_p(\varepsilon,\psi)), \\ e(\varepsilon,v)_{\alpha\beta} = e(v)_{\alpha\beta},\ e(\varepsilon,v)_{\alpha 3} = \varepsilon^{-1}e(v)_{\alpha 3},\ e(\varepsilon,v)_{33} = \varepsilon^{-2}e(v)_{33}, \\ \widehat{\nabla}_p(\varepsilon,\psi) = \varepsilon^{p-1}\widehat{\nabla}\psi,\ \nabla_p(\varepsilon,\psi)_3 = \varepsilon^{p-2}\partial_3\psi. \end{cases} \tag{4}$$

The signs of the various powers of ε in the components of $k_p(\varepsilon,r)$ induce an orthogonal decomposition of $\mathbb{H}$ in subspaces $\mathbb{H}^\star_p$, with $\star \in \{-,0,+\}$, which is crucial to fully describe plates models in all admissible crystal classes. We denote by $h^\star_p$ the projection on $\mathbb{H}^\star_p$ of any element h of $\mathbb{H}$ so that M can then be decomposed in nine elements $M^{\star\diamond}_p \in \mathscr{L}(\mathbb{H}^\diamond_p, \mathbb{H}^\star_p)$, with $\star,\diamond \in \{-,0,+\}$. Because M^{00}_p and M^{--}_p are positive operators on $\mathbb{H}^0_p$ and $\mathbb{H}^-_p$, the Schur complement

$$\widetilde{M}_p := M^{00}_p - M^{0-}_p (M^{--}_p)^{-1} M^{-0}_p \tag{5}$$

is an element of $\mathscr{L}(\mathbb{H}^0_p)$. The key point of the asymptotic study is to show that if $\overline{k}_p$ is the limit (in a suitable topology) of $k_p(\varepsilon, s_p(\varepsilon))$, then $(M\,\overline{k}_p)^-_p = (\overline{k}_p)^+_p = 0$. This will enable us to exhibit $\widetilde{M}_p$ *as the operator governing the limit constitutive equations* due to the fundamental relation:

$$(M\,h)^-_p = h^+_p = 0 \Rightarrow \widetilde{M}_p\, h^0_p = (M\,h)^0_p \text{ and } \widetilde{M}_p\, h^0_p \cdot h^0_p = M\,h\cdot h. \tag{6}$$

The limit space of displacements will be the space of Kirchhoff-Love displacements defined by $\mathbf{V}_{KL} := \{v \in H^1_{\Gamma_{mD}}(\Omega)^3;\, e_{i3}(v) = 0\}$ while the limit electrical spaces will be $\Phi_{e,1} := \{\psi \in H^1_{\Gamma_{eD}}(\Omega);\, \partial_3\psi = 0\}$ and $\Phi_{e,2} := \{\psi \in H^1_{\partial_3}(\Omega);\, \psi_{|\Gamma_{eD}\cap\Gamma^\pm} = 0\}$, where $H^1_{\partial_3}(\Omega) := \{\psi \in L^2(\Omega);\, \partial_3\psi \in L^2(\Omega)\}$ and where Γ_{eD} stands for the image of Γ^ε_{eD} by $\Pi^{\varepsilon^{-1}}$. Finally, we have the following convergence result:

Let $\mathbf{K}_1 := H^1(\Omega)$ *and* $\mathbf{K}_2 := H^1_{\partial_3}(\Omega)$. *When* $\varepsilon \to 0$, *the family* $(s_p(\varepsilon))_{\varepsilon>0}$ *of the unique solutions of* $\mathscr{P}(\varepsilon,\Omega)_p$ *strongly converges in* $\mathbf{X}_p := H^1_{\Gamma_{mD}}(\Omega)^3 \times \mathbf{K}_p$ *to the unique solution* $\overline{s}_p$ *of*

$$\overline{\mathscr{P}}(\Omega)_p \qquad \begin{cases} \text{Find } s \in (0,\varphi_0) + \mathbf{S}_p \text{ such that} \\ \int_\Omega \widetilde{M}_p\, k(s)^0_p \cdot k(r)^0_p\,dx = L(r),\ \forall r \in \mathbf{S}_p := \mathbf{V}_{KL} \times \Phi_{e,p}. \end{cases}$$

To get physically meaningful results, we define an electromechanical state $\overline{s}_p^{\varepsilon}$ over the real plate Ω^{ε} by the descaling $\overline{s}_p^{\varepsilon} = S_p(\varepsilon)^{-1}\overline{s}_p$: it is the unique solution of a problem $\overline{\mathscr{P}}(\Omega^{\varepsilon})_p$ posed over Ω^{ε} which is the transportation by Π^{ε} of the (limit scaled) problem $\overline{\mathscr{P}}(\Omega)_p$. This transported problem is our proposal to model the thin linearly piezoelectric plate of thickness 2ε. Our model in fact involves two dimensional problems set on ω, which is very attractive and favourable from the numerical point of view. It is also accurate in the sense that the convergence result on the scaled states implies that s^{ε} is asymptotically equivalent to $\overline{s}_p^{\varepsilon}$.

The first model ($p = 1$) with $\varphi_0 = 0$ deals with the physical situation when the plate is used as a sensor, the second model corresponds to an actuator. The model involves "reduced" state variables, the sole component k_p^0 of the couple strain/gradient of the electrical potential, and the constitutive equation are supplied by the Schur complement (or the "condensation" of the initial operator M^{ε}) with respect to the maintained components. This identification is the keypoint for obtaining some decoupling and symmetry properties very important in practice (see [4, 19, 20]) by due account of the influence of the crystalline symmetries on the coefficients of $\widetilde{M}_p$. More precisely, it is possible to list some properties of the operator $\widetilde{M}_p$ ($p = 1, 2$), which supplies the constitutive equations of the piezoelectric plate.

The fundamental coupling property of M remains true for $\widetilde{M}_p$:

$$\widetilde{M}_{p_{me}} = -(\widetilde{M}_{p_{em}})^T, \tag{7}$$

where m and e respectively denote the mechanical and electrical components of the generalized kinematics and stresses.

Considering the influence of crystalline symmetries on the three-dimensional constitutive law (see [13] for example), we can deduce, in the case of a polarization normal to the plate, that:

- $\widetilde{M}_{2_{mm}}$ involves mechanical terms only,
- $\widetilde{M}_{1_{mm}} = \widetilde{M}_{2_{mm}}$ for the crystalline classes m, 32, 422, $\bar{6}$, 622 and $\bar{6}m2$,
- $\widetilde{M}_{1_{mm}}$ involves electrical terms except for these previous classes,
- when $p = 1$, there is an electromechanical decoupling ($\widetilde{M}_{p_{me}} = 0$) for the classes 2, 222, $2\,mm$, 4, $\bar{4}$, 422, $4\,mm$, $\bar{4}2m$, 6, 622, $6\,mm$ and $\bar{2}3$, when $p = 2$, this decoupling occurs with the classes m, 32, 422, $\bar{6}$, 622 and $\bar{6}m2$, nevertheless the operators $\widetilde{M}_{p_{mm}}$ and $\widetilde{M}_{p_{ee}}$ involve a mixture of elastic, piezoelectric and dielectric coefficients. In these cases, the plate can be considered as no more piezoelectric. We are then in a situation of a *structural switch-off* of the piezoelectric effect.

Let us consider for example a thin piezoelectric plate constituted by a material whose crystalline symmetry class is 222. Then Eq. (1) takes the following form:

$$\begin{pmatrix} \sigma_{11} \\ \sigma_{22} \\ \sigma_{33} \\ \sqrt{2}\,\sigma_{23} \\ \sqrt{2}\,\sigma_{31} \\ \sqrt{2}\,\sigma_{12} \\ D_1 \\ D_2 \\ D_3 \end{pmatrix} = \left(\begin{array}{cccccc|ccc} a_{11} & a_{12} & a_{13} & 0 & 0 & 0 & 0 & 0 & 0 \\ a_{12} & a_{22} & a_{23} & 0 & 0 & 0 & 0 & 0 & 0 \\ a_{13} & a_{23} & a_{33} & 0 & 0 & 0 & 0 & 0 & 0 \\ 0 & 0 & 0 & a_{44} & 0 & 0 & -b_{41} & 0 & 0 \\ 0 & 0 & 0 & 0 & a_{55} & 0 & 0 & -b_{52} & 0 \\ 0 & 0 & 0 & 0 & 0 & a_{66} & 0 & 0 & -b_{63} \\ \hline 0 & 0 & 0 & b_{41} & 0 & 0 & c_{11} & 0 & 0 \\ 0 & 0 & 0 & 0 & b_{52} & 0 & 0 & c_{22} & 0 \\ 0 & 0 & 0 & 0 & 0 & b_{63} & 0 & 0 & c_{33} \end{array}\right) \cdot \begin{pmatrix} e_{11}(u) \\ e_{22}(u) \\ e_{33}(u) \\ \sqrt{2}\,e_{23}(u) \\ \sqrt{2}\,e_{31}(u) \\ \sqrt{2}\,e_{12}(u) \\ \varphi_{,1} \\ \varphi_{,2} \\ \varphi_{,3} \end{pmatrix}. \tag{8}$$

Therefore, Eq. (5) leads to

$$\widetilde{M}_1 = \left(\begin{array}{ccc|cc} \frac{a_{11}a_{33}-a_{13}^2}{a_{33}} & \frac{a_{12}a_{33}-a_{13}a_{23}}{a_{33}} & 0 & 0 & 0 \\ \frac{a_{12}a_{33}-a_{13}a_{23}}{a_{33}} & \frac{a_{22}a_{33}-a_{23}^2}{a_{33}} & 0 & 0 & 0 \\ 0 & 0 & \frac{a_{66}c_{33}+b_{63}^2}{c_{33}} & 0 & 0 \\ \hline 0 & 0 & 0 & \frac{c_{11}a_{44}+b_{41}^2}{a_{44}} & 0 \\ 0 & 0 & 0 & 0 & \frac{c_{22}a_{55}+b_{52}^2}{a_5} \end{array}\right) \tag{9}$$

in the sensor case and to

$$\widetilde{M}_2 = \left(\begin{array}{ccc|c} \frac{a_{11}a_{33}-a_{13}^2}{a_{33}} & \frac{a_{12}a_{33}-a_{13}a_{23}}{a_{33}} & 0 & 0 \\ \frac{a_{12}a_{33}-a_{13}a_{23}}{a_{33}} & \frac{a_{22}a_{33}-a_{23}^2}{a_{33}} & 0 & 0 \\ 0 & 0 & a_{66} & -b_{63} \\ \hline 0 & 0 & b_{63} & c_{33} \end{array}\right) \tag{10}$$

in the actuator case.

As outlined previsouly, the relation (9) shows that σ and D respectively depend only on $e(u)$ and $\nabla\varphi$ when the plate acts as a sensor, so that it can be considered as no more piezoelectric. But, when the same plate acts as an actuator, the piezoelectric coupling does not vanishes as it can be seen in Eq. (10).

2.2 *Electromagneto-Elastic Thin Plates*

Besides the piezoelectric coupling, some materials are sensitive to magnetic effects, thus in [22] we extended the previous modeling to linearly electromagneto-elastic thin plates. Now the state is described by $s^\varepsilon = (u^\varepsilon, \varphi^\varepsilon, \phi^\varepsilon)$ where the additional variable ϕ^ε denotes the magnetic potential and the constitutive equations read as:

$$\begin{aligned} \sigma^\varepsilon &= a^\varepsilon\, e(u^\varepsilon) \;- b^\varepsilon\, \nabla\varphi^\varepsilon \;- d^\varepsilon\, \nabla\phi^\varepsilon, \\ D^\varepsilon &= {b^\varepsilon}^T\, e(u^\varepsilon) + c^\varepsilon\, \nabla\varphi^\varepsilon \;+ e^\varepsilon\, \nabla\phi^\varepsilon, \\ B^\varepsilon &= {d^\varepsilon}^T\, e(u^\varepsilon) + {e^\varepsilon}^T\, \nabla\varphi^\varepsilon \;+ f^\varepsilon\, \nabla\phi^\varepsilon. \end{aligned} \tag{11}$$

In these constitutive equations, d^ε, e^ε and f^ε respectively stand for the piezomagnetic, electromagnetic coupling and magnetic permeability tensors, while B^ε denotes the magnetic induction.

A similar mathematical analysis of the asymptotic behavior of s^ε can be done to derive a simplified but accurate model of thin electromagneto-elastic plate. It involves reduced state variable and constitutive equations supplied by the condensation $\widetilde{M}^\varepsilon$ of M^ε with respect to the maintained components of $(e(u^\varepsilon), \nabla\varphi^\varepsilon, \nabla\phi^\varepsilon)$.

But the novelty here is that *four* limit behaviors may appear according to the type of boundary conditions and the magnitude of the data on the electric *and* magnetic fields. These cases can be described as previously but by a couple of indices $(p, q) \in \{1, 2\}^2$ in place of the sole index p. The physical situation when the thin plate is used as an electrical (resp. magnetic) sensor corresponds to $p = 1$ (resp. $q = 1$) while the actuator case corresponds to $p, q = 2$. It therefore appears two original mixed behaviors when $p \neq q$. In these situations, the plate is *at the same time* a sensor *and* an actuator excepted for the classes for which the plate is no more electromagneto-elastic (*i.e.* the electromechanical and magnetomechanical coefficients in $\widetilde{M}^\varepsilon$ vanishes). The two cases $p \neq q$ allow the modeling of electrically commanded magnetic devices and of magnetically commanded electric ones, which is of considerable interest in the development of non-volatile magnetic random access memories. We emphasize on the point that this behavior is here fully described for any admissible crystal class.

2.3 Piezoelectric Plates with Electric Field Gradient

In the 1960s the study of unexplained aspects of piezoelectricity led Mindlin [10] to extend the classical Voigt theory [17] in Toupin's formulation [15] by assuming that the stored energy function not only depends on the strain tensor and polarization vector but also on the polarization gradient tensor. What motivated Mindlin to study the effects of the polarization gradient was the capacitance of a very thin dielectric film. Experiments showed that the capacitance of a very thin film is systematically smaller than the classical prediction. Moreover, performing experimental tests, Mead [9] showed that piezoelectric effects can also appear in centrosymmetric crystals, which is in contradiction with classical Voigt theory. And, indeed, the Mindlin's theory of elastic dielectrics with polarization gradient accommodates the observed and experimentally measured phenomena, such as electromechanical interactions in centrosymmetric materials, capacitance of thin dielectric films, surface energy of polarization, deformation and optical activity in quartz.

As in the classical piezoelectric case the physical state is described by $s^\varepsilon = (u^\varepsilon, \varphi^\varepsilon)$. However, the constitutive equations read as:

$$\begin{aligned} \sigma^\varepsilon &= a^\varepsilon\, e(u^\varepsilon) - b^\varepsilon\, \nabla\varphi^\varepsilon - \alpha^\varepsilon\, \nabla^2\phi^\varepsilon, \\ D^{1,\varepsilon} &= b^{\varepsilon^T}\, e(u^\varepsilon) + c^\varepsilon\, \nabla\varphi^\varepsilon + \beta^\varepsilon\, \nabla^2\phi^\varepsilon, \\ D^{2,\varepsilon} &= \alpha^{\varepsilon^T}\, e(u^\varepsilon) + \beta^{\varepsilon^T}\, \nabla\varphi^\varepsilon + \gamma^\varepsilon\, \nabla^2\phi^\varepsilon. \end{aligned} \tag{12}$$

Depending on the type of electric loading, three different models indexed by p appear at the limit. This result extends our previous study in [23] and shows that gradient theory broadens the understanding of sensors and actuators. When $p = 2$ and $p = 3$ we are able to express the constitutive laws as a Schur complement of the second order piezoelectric tensor in a framework valid for any symmetry class, which means that we do not make any simplifying assumptions dealing with the crystal symmetry of the material constituting the plate. When $p = 1$, we are not able to explicitly derive the constitutive law of the limit model. Therefore, as in the case of first order piezoelectric rods treated treated in the next section, it seems very likely to us that non-local terms appear in this delicate situation. The study of the influence of the crystal symmetries on our models for $p = 2, 3$ shows that even for second order piezoelectricity, an electromechanical switch-off may appear in the structure if the plate is designed with specific materials.

2.4 Piezoelectric Slender Rods

From a technological point of view, piezoelectric materials can also be used in wires or slender rods. Now, the reference configuration of the piezoelectric structure is $\Omega^\varepsilon = \varepsilon \times (0, L)$ with L a fixed positive real number. The equations describing the equilibrium of the structure are the same as in the Sect. 2.1 but of course the geometry of the various boundaries is different: we assume that $\Gamma^\varepsilon_{mD} = \varepsilon\omega \times \{0, L\}$.

To get our simplified models, we proceed as in the case of plates. Due to classical assumptions on the mechanical loading (which permits the justification of Bernoulli-Navier theory of elastic slender rods (see [11, 16]) and on electrical loading:

$$\begin{cases} p = 1 : \text{ extension of } \varphi^\varepsilon_0 \text{ into } \Omega^\varepsilon \text{ does not depend on } \hat{x} \text{ and } \Gamma^\varepsilon_{eD} \subset \varepsilon\omega \times \{0, L\}, \\ p = 2 : \text{ there exists } \gamma_e \subset \partial\omega \text{ such that } \Gamma^\varepsilon_{eD} \subset \varepsilon \times (0, L). \end{cases} \tag{13}$$

the scaling is defined by:

$$\begin{cases} x = (\hat{x}, x_3) \in \overline{\Omega} = \omega \times (0, L) \mapsto \Pi^\varepsilon x = (\varepsilon\hat{x}, x_3) \in \overline{\Omega}^\varepsilon \\ s_p(\varepsilon) = S_p(\varepsilon) s^\varepsilon \\ (\hat{u}(\varepsilon)(x), u_3(\varepsilon)(x), \varphi(\varepsilon)(x)) = (\hat{u}^\varepsilon(\Pi^\varepsilon x), \varepsilon^{-1} u^\varepsilon_3(\Pi^\varepsilon x), \varepsilon^{-p}\varphi^\varepsilon(\Pi^\varepsilon x)) \end{cases} \tag{14}$$

so that $s_p(\varepsilon)$ is the unique solution of the variational problem:

$$\text{Find } s_p(\varepsilon) \in (0, \varphi_0) + V \text{ such that } \int_\Omega M(x) k_p(\varepsilon, s(\varepsilon)) \cdot k_p(\varepsilon, r) = L(r), \ \forall r \in V,$$

with now:

$$k_p(\varepsilon, (v, \psi)) = ((\varepsilon^2 e_{\alpha\beta}(v), \varepsilon e_{\alpha 3}(v), e_{33}(v)), (\varepsilon^{p-2}\hat{\nabla}\psi, \varepsilon^{p-1}\partial_3\psi)).$$

As in the case of purely elastic slender rods (see [11]), finding the limit is a little bit more difficult and the limit problems are as follows:

$$\overline{\mathscr{R}}(\Omega)_1 \qquad \begin{cases} \text{Find } (\overline{u}, \overline{v}, \overline{w}, \overline{\phi}, \overline{\psi}) \in V_1 \text{ such that} \\ \int_\Omega M(x)\, k_1(\overline{u}, \overline{v}, \overline{w}, \overline{\phi}, \overline{\psi}) \cdot k_1(u', v', w', \phi', \psi')\, dx = L(u'), \\ \forall\, (u', v', w', \phi', \psi') \in V_1, \end{cases}$$

with

$$\begin{cases} V_1 = V_{BN}(\Omega) \times R_b(\Omega) \times RD_2^\perp \times \Phi \times \Psi, \\ V_{BN}(\Omega) = \{v \in H^1_{\Gamma_{mD}}(\Omega)^3;\, e_{\alpha\beta}(v) = e_{\alpha 3}(v) = 0\}, \\ R_b(\Omega) = \{v;\, \exists c \in H_0^1(0, L);\, \widehat{v}(x) = c(x_3)(-x_2, x_1),\, v_3 \in L^2(0, L; H_m^1(\omega))\}, \\ H_m^1(\omega) = \{v \in H^1(\omega);\, \int_\omega \psi(\widehat{x})\, d\widehat{x} = 0\}, \\ RD_2^\perp(\Omega) = \{\omega;\, \widehat{w} \in L^2(0, L; H_m^1(\omega)^2),\, w_3 = 0 \text{ and} \\ \qquad\qquad \int_\omega (-x_2 w_1(\widehat{x}, x_3) + x_1 w_2(\widehat{x}, x_3))\, d\widehat{x} = 0, \;\; a.e.\; x_3 \in (0, L)\}, \\ \Phi = \{\phi \in H_0^1(0, L);\, \phi(x) = \phi(x_3)\}, \\ \Psi = L^2(0, L; H_m^1(\omega)), \\ k_1(u, v, w, \phi, \psi) = (\widehat{e}(w), e_{\alpha 3}(v), e_{33}(u), \widehat{\nabla}\psi, \frac{d\phi}{dx_3}) \end{cases} \tag{15}$$

and

$$\overline{\mathscr{R}}(\Omega)_2 \qquad \begin{cases} \text{Find } (\overline{u}, \overline{v}, \overline{w}, \phi) \in V_2 \text{ such that} \\ \int_\Omega M(x)\, k_2(\overline{u}, \overline{v}, \overline{w}, \phi) \cdot k_2(u', v', w', \phi')\, dx = L(u'), \\ \forall\, (u', v', w', \phi') \in V_2, \end{cases}$$

with

$$\begin{cases} V_2 = V_{BN}(\Omega) \times R_b(\Omega) \times RD_2^\perp \times L^2(0, L; H^1_{\gamma_e}(\omega)), \\ k_2(u, v, w, \phi) = (\widehat{e}(w), e_{\alpha 3}(v), e_{33}(u), \widehat{\nabla}\phi). \end{cases} \tag{16}$$

The space $V_{BN}(\Omega)$ is the Bernoulli-Navier displacements space.

Of course, our proposal of model is obtained by taking the inverse scaling, that is to say a transported problem $\overline{\mathscr{R}}(\Omega^\varepsilon)_p$ posed over Ω^ε. On the contrary to the case of plates, the state variables of the model do not reduce to the couple displacement/electrical potential but involve additional variables: two fields of displacements (easy to interpret mechanically) and a scalar field of electrical nature. Nevertheless,the kinematics of the state variables is simpler than the one of the genuine three-dimensional model which is very favourable from a numerical point of view. As in the purely elastic case it is worthwhile to note that for particular classes of monoclinic materials the additional variables v, w and ψ disappear [18]. Anyway, in the case $p = 1$, the additional variables can be eliminated but it leads to non standard equations involving non local terms.

2.5 *Dynamical Response of Piezoelectric Plates*

The interest of an efficient modeling of the dynamic response of piezoelectric plates lies in the fact that a major technological application of piezoelectric effects is the control of vibrations of structures through very thin plates or patches. We present two models depending on the various extents to which the magnetic effects are taken into account. Actually, because of the large discrepancy between the celerities of the mechanical and electromechanical waves, magnetic effects can be disregarded. That is why first we propose a modeling in the appropriate framework of the quasi-electrostatic approximation which claims that the electrical field still derives from an electrical potential.

2.5.1 Quasi-electrostatic Case

Now a new parameter appears: the density ρ of the plate. In the framework of the realistic quasi-electrostatic approximation, the electrical equilibrium equation remains true but the mechanical equilibrium equation is replaced by

$$\operatorname{div} \sigma^{\varepsilon} + f^{\varepsilon} = \rho \ddot{u}^{\varepsilon} \quad \text{in } \Omega^{\varepsilon}$$

where the upper dot denotes the differentiation with respect to time. Under mild assumptions on the initial state and the essential assumption

$$\int_{-1}^{+1} x_3 \widetilde{M}_1(x_1, x_2, x_3)\, dx_3, \quad \widetilde{M}_2 \text{ independent from } x_3 \tag{17}$$

it is possible to proceed to the study of the convergence of s_p^{ε} when ε goes to zero [19, 21], the result depends strongly on the relative behaviour of ε and ρ. A unified accurate and simplified modeling is then obtained by simply adding $\int_{\Omega^{\varepsilon}} \rho \ddot{\overline{u}}_p^{\varepsilon}\, dx$ to the left hand side of the equation defining the descaled limit problem $\overline{\mathscr{P}}(\Omega^{\varepsilon})_p$. Thus the relationship between the *reduced* stress, electric displacement, strain and gradient of electrical potential remains the same as in the static case: $\widetilde{M}_p^{\varepsilon}$ really describes the constitutive equations of the plate. The displacement fields involved in our simplified modeling being of Kirchoff-Love type, clearly four cases, indexed by q, of relative behaviours of the parameters determine the *essential* nature of the limit response of the plate to the electromechanical loading:

$$\begin{array}{l} q = 1 : \rho \to \overline{\rho} \in (0, +\infty) \quad , \; q = 2 : \rho \to 0 \text{ and } \rho/\varepsilon^2 \to \infty \\ q = 3 : \rho/\varepsilon^2 \to \overline{\overline{\rho}} \in (0, +\infty) \; , \; q = 4 : \rho = o(\varepsilon^2). \end{array} \tag{18}$$

In the cases $q = 2$ and $q = 4$, the limit response of the plate to the electromechanical loading is essentially quasi-static, while the cases $q = 1$ and $q = 3$ involve the acceleration of the displacement. Moreover, because of the assumption (17), appears

a decoupling between the membrane motion and the flexural one. If $q = 1, 2$, the flexure is negligible and the membrane response is dynamic if $q = 1$, quasi-static if $q = 2$. When $q = 3, 4$, the membrane response is quasi-static whereas the flexural response is dynamic if $q = 3$ and quasi-static if $q = 4$. In these last two cases, the equation giving the flexion does not involve the limit electric potential if $p = 1$. The uncoupled elliptic and hyperbolic involved problems are two-dimensional and set on ω.

The steps of the derivation of our model are the following. First we proceed to the same scaling as in Sect. 2.1 and to a decomposition $s(\varepsilon) = s(\varepsilon)_e + s(\varepsilon)_r$, where $s(\varepsilon)_e$ solves a problem like $\mathscr{P}(\varepsilon, \Omega)_p$ and consequently whose asymptotic behavior is provided by Sect. 2.1. Hence $s(\varepsilon)_r = (u(\varepsilon)_r, \varphi(\varepsilon)_r)$ satisfies an homogeneous variational evolution equation. Because the time derivatives do not act on $\varphi(\varepsilon)_r$, it is possible to exhibit a linear evolution equation for $u(\varepsilon)_r$ governed by a maximal monotone operator in a suitable Hilbert space whose norm depends on (ε, ρ). Since the Trotter results of convergence of semi-groups of linear operators acting on variables spaces claim that the study of convergence of the transient problems reduces to the static case, the asymptotic behavior of $u(\varepsilon)_r$, and consequently of $s(\varepsilon)_r$ is easily determined by straightforward variants of the convergence results of the Sect. 2.1.

2.5.2 The Fully Dynamic Case

In the previous case, the electrical field E^ε was assumed to be curl-free and, consequently, equal to the gradient of the so-called electrical potential φ^ε. If we want to take into account the magnetic effects, the state of the plate is now described by a triplet $z^\varepsilon = (u^\varepsilon, E^\varepsilon, H^\varepsilon)$ where H^ε is the magnetic field and the equations of the problem read as:

$$\begin{cases} \operatorname{div} \sigma^\varepsilon + f^\varepsilon = \rho \ddot{u}^\varepsilon \text{ in } \Omega^\varepsilon \\ \dot{D}^\varepsilon = c \operatorname{curl} H^\varepsilon \text{ in } \Omega^\varepsilon \\ \mu \dot{H}^\varepsilon = -c \operatorname{curl} E^\varepsilon \text{ in } \Omega^\varepsilon \\ (\sigma^\varepsilon, D^\varepsilon) = M^\varepsilon(e(u^\varepsilon), E^\varepsilon) \text{ in } \Omega^\varepsilon \end{cases}$$

with two kind of boundary conditions intimately linked to those of the previous cases (and, then, still indexed by p):

$$p = 1 : \ H^\varepsilon \wedge n^\varepsilon = j^\varepsilon \text{ on } \partial\Omega^\varepsilon, \quad p = 2 : \ E^\varepsilon \wedge n^\varepsilon = E_0^\varepsilon \wedge n^\varepsilon \text{ on } \partial\Omega^\varepsilon$$

Here $c, \mu, j^\varepsilon, E_0^\varepsilon$ stand for the light celerity, the magnetic permeability, the surface current density and the exterior electrical field respectively. We will assume that there exist sufficiently smooth fields E_0, j such that:

$$\begin{cases} E_0^\varepsilon(\Pi^\varepsilon) = \varepsilon^2 E_0(x), \ \forall x \in \partial\Omega, \quad j^\varepsilon(\Pi^\varepsilon) = \varepsilon^2 j(x), \ \forall x \in \Gamma_\pm \\ j_\alpha^\varepsilon(\Pi^\varepsilon x) = \varepsilon j_\alpha(x), \quad j_3^\varepsilon(\Pi^\varepsilon) = \varepsilon^2 j_3(x), \ \forall x \in \Gamma_{lat}. \end{cases} \tag{19}$$

Let

$$\begin{cases} \overline{E}_1^\varepsilon = \{E \in L^2(\Omega^\varepsilon)^3;\ E_3 = 0,\ \partial_3 E_\alpha = 0\}, \\ \overline{E}_2^\varepsilon = \{E;\ E_3 \in L^2(\Omega^\varepsilon);\ \partial_3(\partial_\alpha E_3 - \partial_3 E_\alpha) = 0,\ E_\alpha = 0 \text{ on } \Gamma_\pm^\varepsilon\}, \\ \overline{H}_1^\varepsilon = \{H \in L^2(\Omega^\varepsilon)^3;\ H_\alpha = 0,\ \partial_3 H_3 = 0\}, \\ \overline{H}_2^\varepsilon = \{H \in L^2(\Omega^\varepsilon)^3;\ H_3 = 0,\ \partial_3 H_\alpha = 0\}, \\ \overline{Z}_p^\varepsilon = \overline{V}^\varepsilon \times \overline{E}_p^\varepsilon \times \overline{H}_p^\varepsilon, \\ k_1(v, E) = (e_{\alpha\beta}(v), E_\alpha),\ k_2(v, E) = (e_{\alpha\beta}(v), E_3),\ 1 \leqslant \alpha, \beta \leqslant 3. \end{cases} \tag{20}$$

Under (17) and (19) and mild assumptions on the smoothness of the initial state, it can be shown that the state z_p^ε is asymptotically equivalent to $\overline{z}_p^\varepsilon = (\overline{u}_p^\varepsilon, \overline{E}_p^\varepsilon, \overline{H}_p^\varepsilon)$ which satisfies:

$$\begin{cases} \int_{\Omega^\varepsilon} \rho \ddot{\overline{u}}_p^\varepsilon \cdot v\, dx + \int_{\Omega^\varepsilon} \widetilde{M}_p^\varepsilon k_p(\overline{u}_p^\varepsilon, \overline{E}_p^\varepsilon) \cdot k_p(v, 0)\, dx = L_p^\varepsilon(v, 0),\ \forall v \in V_{KL}(\Omega^\varepsilon) \\ (\dot{\overline{D}}_1^\varepsilon)_1(\widehat{x}) = -c\, \partial_2(\overline{H}_1^\varepsilon)_3(\widehat{x}) + j_1^\varepsilon(\widehat{x}, \varepsilon) + j_1^\varepsilon(\widehat{x}, -\varepsilon),\ \forall \widehat{x} \in \omega \\ (\dot{\overline{D}}_1^\varepsilon)_2(\widehat{x}) = c\, \partial_1(\overline{H}_1^\varepsilon)_3(\widehat{x}) + j_2^\varepsilon(\widehat{x}, \varepsilon) + j_2^\varepsilon(\widehat{x}, -\varepsilon),\ \forall \widehat{x} \in \omega \\ (\dot{\overline{D}}_2^\varepsilon)_2(\widehat{x}) = c\, (\partial_1(\overline{H}_2^\varepsilon)_2 - \partial_2(\overline{H}_2^\varepsilon)_1)(\widehat{x}),\ \forall \widehat{x} \in \omega \\ \mu(\dot{\overline{H}}_1^\varepsilon)_3(\widehat{x}) = -c\, (\partial_1(\overline{E}_1^\varepsilon)_2 - \partial_2(\overline{E}_1^\varepsilon)_1)(\widehat{x}),\ \forall \widehat{x} \in \omega \\ \mu(\dot{\overline{H}}_2^\varepsilon)_1(\widehat{x}) = -c\, (\partial_2(\overline{E}_2^\varepsilon)_3 - \partial_3(\overline{E}_2^\varepsilon)_2)(\widehat{x}),\ \forall \widehat{x} \in \omega \\ \mu(\dot{\overline{H}}_2^\varepsilon)_2(\widehat{x}) = -c\, (\partial_3(\overline{E}_2^\varepsilon)_1 - \partial_1(\overline{E}_2^\varepsilon)_3)(\widehat{x}),\ \forall \widehat{x} \in \omega \\ (\overline{\sigma}_p^\varepsilon, \overline{D}_p^\varepsilon) = \widetilde{M}_p^\varepsilon k_p(\overline{u}_p^\varepsilon, \overline{E}_p^\varepsilon) \end{cases} \tag{21}$$

with the boundary conditions:

$$\overline{H}_1^\varepsilon \wedge n^\varepsilon = \frac{1}{2\varepsilon} \int_{-\varepsilon}^{+\varepsilon} j^\varepsilon(\cdot, x_3)\, dx_3 \text{ on } \Gamma_{lat}^\varepsilon,\ \overline{E}_2^\varepsilon \wedge n^\varepsilon = \overline{E}_0^\varepsilon \wedge n^\varepsilon \text{ on } \Gamma_\pm^\varepsilon. \tag{22}$$

The structure of the equations of our model is the same that those of the genuine model, but the problems are two-dimensional and with a lesser number of degrees of freedom for the state fields.

Again, the key-point is to formulate a suitable scaling of the problems in terms of an evolution equation governed by a maximal monotone operator in an Hilbert space of possible states with finite scaled energy. By using Trotter theory we only have to consider the limit behavior of a perturbation of the variational equation which defines $\mathscr{P}(\varepsilon, \Omega)_p$. This perturbation taking into account a scaling of the curl operator, the limit behavior is obtained by using weak continuity and integration by parts in the terms involving the curl operator.

3 Mathematical Modeling of Smart Structures

The essential technological interest of piezoelectric devices being the monitoring of a deformable body they are bonded to or integrated in, this section is devoted to smart structures. Here we intend to propose various asymptotic models for *the behavior of the body* through the study of the *system* constituted by a very thin linearly piezoelectric flat patch perfectly bonded to or integrated in a linearly elastic or piezoelectric three dimensional body.

3.1 Piezoelectric Patches

A reference configuration for the body is an open set Ω laying in $\{ x_3 < 0 \}$ whose part of its Lipschitz-continuous boundary $\partial\Omega$ is a non-empty domain S in $\{ x_3 = 0 \}$ and such that $S \times (-L, 0)$ is included in Ω for some positive real number L, while the patch occupies $B^\varepsilon := S \times (0, \varepsilon)$, ε being a small real number; let $\mathscr{O}^\varepsilon := \Omega \cup S \cup B^\varepsilon$. The body is clamped on a part Γ_0 of $\partial\Omega \setminus S$ with a positive two-dimensional measure $\mathscr{H}_2(\Gamma_0)$, and subjected to body forces and surface forces on $\Gamma_1 := \partial\Omega \setminus (S \cup \Gamma_0)$ of densities f and F. Moreover, for all δ in $\mathbb{R}$, let S^δ denotes $S + \delta e_3$, $\{ e_1, e_2, e_3 \}$ being a basis of the Euclidean physical space assimilated to $\mathbb{R}^3$, surface forces of density G acts on S^ε whilst the patch is free of mechanical loading and electric charges in B^ε and on its lateral boundary $\partial S \times (0, \varepsilon)$. If u^ε, $e(u^\varepsilon)$, σ^ε denote the fields of displacement, strain and stress in $\mathscr{O}^\varepsilon$ and φ^ε, D^ε stand for the electric potential and the electric displacement, part of the equations describing the electromechanical equilibrium read as:

$$\begin{cases} \operatorname{div} \sigma^\varepsilon = \tilde{f} \text{ in } \mathscr{O}^\varepsilon, \ u^\varepsilon = 0 \text{ on } \Gamma_0, \\ \sigma^\varepsilon n = F \text{ on } \Gamma_1, \ \sigma^\varepsilon n = G^\varepsilon \text{ on } S^\varepsilon, \ \sigma^\varepsilon n = 0 \text{ on } \partial S \times (0, \varepsilon), \\ \operatorname{div} D^\varepsilon = 0 \text{ in } B^\varepsilon, \ D^\varepsilon \cdot n = 0 \text{ on } \partial S \times (0, \varepsilon), \\ \sigma^\varepsilon = a e(u^\varepsilon) \text{ in } \Omega, \ (\sigma^\varepsilon, D^\varepsilon) = \frac{1}{\varepsilon} M\big(e(u^\varepsilon), \nabla\varphi^\varepsilon\big) \text{ in } B^\varepsilon, \end{cases} \tag{23}$$

$\tilde{f}$ is the extension of f to B^ε by 0, n is the unit outward normal and a denotes the elasticity tensor which satisfies

$$a \in L^\infty\big(\Omega; \mathscr{L}(\mathbb{S}^3)\big), \quad \exists c; \ c|e|^2 \le a(x)e \cdot e, \quad \forall e \in \mathbb{S}^3, \text{ a.e. } x \in \Omega, \tag{24}$$

while M is an element of $L^\infty\big(S; \mathscr{L}(\mathbb{H})\big)$ satisfying

$$M = \begin{bmatrix} \alpha & -\beta \\ \beta^T & \gamma \end{bmatrix} \quad , \quad \exists \kappa > 0 ; \quad \kappa|h|^2 \le Mh \cdot h, \quad \forall h \in \mathbb{H}, \text{ a.e. } x \in S. \tag{25}$$

The models will be distinguished according to the additional necessary boundary conditions on S^ε and S, characterized by an index p in $\{1,2\}^2$. Case $p_1 = 1$ corresponds to a condition for the electric displacement on S^ε:

$$D^\varepsilon \cdot n = q^\varepsilon \quad \text{on } S^\varepsilon, \tag{26a}$$

q^ε being a density of electrical charges, while $p_1 = 2$ corresponds to a condition of given electrical potential:

$$\varphi^\varepsilon = \varphi_0^\varepsilon \quad \text{on } S^\varepsilon; \tag{26b}$$

roughly speaking, $p_1 = 1$ deals with patches used as sensors whereas $p_1 = 2$ concerns actuators (see [19, 20]). Index p_2 accounts for the status of the interface between the patch and the body: $p_2 = 1$ corresponds to an insulating interface, $p_2 = 2$ corresponds to a grounded interface:

$$D^\varepsilon \cdot n = 0 \quad \text{on } S, \tag{27a}$$

$$\varphi^\varepsilon = 0 \quad \text{on } S. \tag{27b}$$

Introducing the transverse average of the strain and of the electrical field, it is easy to go to the limit as ε goes to 0 and to show that the limit model corresponds to purely mechanical reinforcement problem along S.

Moreover, when $p = (1,2)$ or $p = (2,1)$, the electric data q or φ_0 does not have any influence on the limit model which corresponds to a purely elastic surface reinforcement of the body. However, the characteristics of this reinforcement may depend on the dielectric or piezoelectric coefficients (see [6]). On the contrary, electrical data q or φ_0 plays a role in models $(1,1)$ or $(2,2)$. More precisely, f, F and G being fixed, there is a one-to-one mapping between the applied electrical potential and the limit displacement. It is thus "theoretically" possible to determine what could be the electrical potential to apply on S^ε in order to get a desired displacement. An approximate procedure may be done easily by finite elements. Another application is that the patch may shift the spectrum of the body in an interesting way, that is why we may regard the patch as an actuator. When $p = (1,1)$ there is also a one-to-one mapping between the limit displacement and the electrical charges. Thus the measurement of the latter may supply the knowledge of the state of displacements: the patch acts as a sensor.

3.2 Piezoelectric Junctions

In this section, we first present our results dealing with smart structures composed of materials whose coefficients are of the same order of magnitude. However, as it is often observed that the electric permeability is very small compared to other

coefficient, next we carry out a general study of piezoelectric junctions whose material coefficients are of different order of magnitude.

3.3 *Piezoelectric Junctions with Material Coefficients of Same Magnitude*

In this section, we present various asymptotic models, indexed by $p = (p_1, p_2) \in \{1, 2, 3, 4\}^2$, for a thin piezoelectric junction between two linearly piezoelectric ($p_2 = 1$) or elastic ($p_2 > 1$) bodies. Index p_1 is relative to the magnitude of the piezoelectric coefficients of the adhesive, characterized by a single parameter μ, with respect to that of the constant thickness 2ε of a layer containing the adhesive. More precisely, we assume that $h := (\varepsilon, \mu)$ takes values in a countable set with a sole cluster point $\bar{h} \in \{0\} \times [0, +\infty]$ so that:

$$\begin{cases} p_1 = 1: \ \bar{\mu}_1 := \lim_{h \to \bar{h}} (\varepsilon\mu) \in (0, +\infty) \\ p_1 = 2: \ \bar{\mu}_1 := \lim_{h \to \bar{h}} (\varepsilon\mu) = 0, \quad \bar{\mu}_2 := \lim_{h \to \bar{h}} (\mu/2\varepsilon) = +\infty \\ p_1 = 3: \ \bar{\mu}_2 := \lim_{h \to \bar{h}} (\mu/2\varepsilon) \in (0, +\infty) \\ p_1 = 4: \ \bar{\mu}_2 := \lim_{h \to \bar{h}} (\mu/2\varepsilon) = 0. \end{cases} \tag{28}$$

As previously said, index p_2 characterizes the status of the adherents but also that of the interfaces between adherents and adhesive:

$$\begin{cases} p_2 = 1: \ \text{the two interfaces are electromechanically perfectly permeable,} \\ p_2 = 2: \ \text{the two interfaces are electrically impermeable,} \\ p_2 = 3: \ \text{one interface is electrically impermeable while the other is electroded,} \\ p_2 = 4: \ \text{the two interfaces are electroded.} \end{cases} \tag{29}$$

Let Ω be a domain, with Lipschitz-continuous boundary, whose intersection S with $\{x_3 = 0\}$ is a domain of $\mathbb{R}^2$ of positive two-dimensional Hausdorff measure $\mathscr{H}_2(S)$. Let $\Omega_\pm := \Omega \cap \{\pm x_3 > 0\}$ and ε be a small positive number, then adhesive and adherents occupy $B^\varepsilon := S \times (-\varepsilon, \varepsilon)$, $\Omega^\varepsilon_\pm := \Omega_\pm \pm \varepsilon e_3$, respectively; let $\Omega^\varepsilon = \Omega^\varepsilon_+ \cup \Omega^\varepsilon_-$, $S^\varepsilon_\pm := S \pm \varepsilon e_3$, $\mathscr{O}^\varepsilon := \Omega^\varepsilon \cup B^\varepsilon \cup_\pm S^\varepsilon_\pm$. Let $(\Gamma_{\mathrm{mD}}, \Gamma_{\mathrm{mN}})$, $(\Gamma_{\mathrm{eD}}, \Gamma_{\mathrm{eN}})$ be two partitions of $\partial\Omega$ with $\mathscr{H}_2(\Gamma_{\mathrm{mD}}), \mathscr{H}_2(\Gamma_{\mathrm{eD}}) > 0$ and $0 < \delta := \mathrm{dist}(\Gamma_{\mathrm{eD}}, S)$. For all Γ in $\{\Gamma_{\mathrm{mD}}, \Gamma_{\mathrm{mN}}, \Gamma_{\mathrm{eD}}, \Gamma_{\mathrm{eN}}\}$, $\Gamma_\pm$, $\Gamma^\varepsilon_\pm$, Γ^ε denotes $\Gamma \cap \{\pm x_3 > 0\}$, $\Gamma_\pm \pm \varepsilon e_3$, $\cup_\pm \Gamma^\varepsilon_\pm$, respectively; if $(\gamma_{\mathrm{D}}, \gamma_{\mathrm{N}})$ is a partition of $\gamma := \partial S$, we denote $\{\gamma_{\mathrm{D}}, \gamma_{\mathrm{N}}, \gamma\} \times (-\varepsilon, \varepsilon)$ by $\left\{\Gamma^\varepsilon_{\mathrm{DI}}, \Gamma^\varepsilon_{\mathrm{NI}}, \Gamma^\varepsilon_{\mathrm{lat}}\right\}$. The structure made of the adhesive and the two adherents, perfectly stuck together along $S^\varepsilon_\pm$, is clamped on $\Gamma^\varepsilon_{\mathrm{mD}}$, subjected to body forces of density f^ε and to surface forces of density F^ε on Γ^ε_{mN} and vanishing on $\Gamma^\varepsilon_{\mathrm{lat}}$. Moreover, a given electric potential $\varphi^h_{p_0}$ is applied on $\Gamma^\varepsilon_{\mathrm{DI}}$ and, when $p_2 = 1$, on $\Gamma^\varepsilon_{\mathrm{eD}}$, while electric charges of density d^ε appear on $\Gamma^\varepsilon_{\mathrm{NI}}$ and, when $p_2 = 1$, on $\Gamma^\varepsilon_{\mathrm{eN}}$.

If $\sigma_p^h, u_p^h, e(u_p^h), D_p^h, \varphi_p^h$ stand for the fields of stress, displacement, strain, electric displacement and electric potential, respectively, the constitutive equations of the structure, for all p_1 in $\{1, 2, 3, 4\}$, read as:

$$\begin{cases} (\sigma_p^h, D_p^h) = \mu M_{\mathrm{I}}\big(e(u_p^h), \nabla\varphi_p^h\big) & \text{in } B^\varepsilon \ \forall\, p_2 \in \{1, 2, 3, 4\}, \\ \begin{cases} (\sigma_p^h, D_p^h) = M_{\mathrm{E}}^\varepsilon\big(e(u_p^h), \nabla\varphi_p^h\big) & \text{in } \Omega^\varepsilon \ \text{ if } p_2 = 1, \\ \sigma_p^h = a_{\mathrm{E}}^\varepsilon e(u_p^h) & \text{in } \Omega^\varepsilon \ \text{ if } p_2 > 1 \end{cases} \end{cases} \tag{30}$$

where

$$(M_{\mathrm{E}}^\varepsilon, a_{\mathrm{E}}^\varepsilon)(x) = (M_{\mathrm{E}}, a_{\mathrm{E}})(x \mp \varepsilon e_3) \quad \forall x \in \Omega_\pm^\varepsilon \tag{31}$$

$$\begin{cases} (M_{\mathrm{I}}, M_{\mathrm{E}}) \in L^\infty\big(S \times \Omega\,;\, \mathscr{L}(\mathbb{H})\big) \text{ such that} \\ M_{\mathrm{P}} = \begin{bmatrix} a_{\mathrm{P}} & -b_{\mathrm{P}} \\ b_{\mathrm{P}}^T & c_{\mathrm{P}} \end{bmatrix}; \\ \exists \kappa > 0, \quad \kappa|k|^2 \le M_{\mathrm{P}}(x)k \cdot k, \quad \forall k \in \mathbb{H} := \mathbb{S}^3 \times \mathbb{R}^3, \ \text{ a.e. } x \in \Omega, \ \forall \mathrm{P} \in \{\mathrm{I}, \mathrm{E}\}. \end{cases} \tag{32}$$

Lastly we have to add the following conditions on $S_\pm^\varepsilon$:

$$\begin{cases} p_2 = 2 & D_p^h \cdot e_3 = 0 \quad \text{on } S_\pm^\varepsilon, \\ p_2 = 3 & D_p^h \cdot e_3 = 0 \quad \text{on } S_+^\varepsilon, \quad \varphi_p^h = \varphi_{p_0}^h \text{ on } S_-^\varepsilon, \\ p_2 = 4 & \varphi_p^h = \varphi_{p_0}^h \quad \text{on } S_\pm^\varepsilon, \end{cases} \tag{33}$$

the electric potential $\varphi_{p_0}^h$ being given on S_+^ε or $S_\pm^\varepsilon$.

The same averaging method through the junction easily leads to our limit models. We are then able to show that in the case of piezoelectric adhesive and adherents ($p_2 = 1$), our results extend those obtained in elasticity (see [1, 5]). The asymptotic behavior of the adhesive strongly depends on the magnitude of the stiffness compared to that of the thickness. When the magnitude of the stiffness is of the order of the inverse of the thickness, the adhesive is replaced by a *material piezoelectric surface* perfectly bonded to the adherents. When it is lesser, the adhesive is replaced by an *electromechanical constraint* between the two adherents which can be perfect adhesion, electromechanical pull-back or free separation, according to the order of magnitude of the stiffness which is, respectively, larger, equal or lower than that of the thickness.

Similarly, in the case of a thin piezoelectric layer embedded between two elastic adherents, depending on the magnitude of the stiffness, the adhesive is replaced by a material elastic surface perfectly bonded to the adherents or by a mechanical constraint between the adherents. In the case of electrically impermeable interfaces, the material surface has a *non local* elastic behavior (see [7]), the constitutive equations being derived from the asymptotic behavior of a thin piezoelectric plate acting as a sensor (case $p = 1$ in [23]). When one interface is electrically impermeable while the other is electroded, the material surface is an elastic membrane. When the two

interfaces are electroded, the material surface is an elastic membrane with residual stress. In these last two cases, the constitutive equations are derived from the asymptotic behavior of a thin piezoelectric plate acting as an actuator (case $p = 2$ in [23]). The mechanical constraint is perfect adhesion, elastic pull-back or free separation according to the order of magnitude of the stiffness. In the case of electrically impermeable interfaces, the elastic pull-back is of non local nature (since the state variable of electric nature ϕ, additional to the relative displacement, can be eliminated). In the two other cases, the elastic pull-back is local. When the two interfaces are electroded, it is similar to the purely elastic case, while, if only one interface is electroded, piezoelectric and dielectric coefficients enter the limit constitutive equations.

3.3.1 Piezoelectric Hybrid Junctions

Due to the wide range of values taken by the elastic, piezoelectric and dielectric coefficients of various devices, it is worthwhile to extend our previous study [7] devoted to thin linearly piezoelectric junctions to the case when the elastic, piezoelectric and dielectric coefficients of the junction *are not of the same order of magnitude*. Our various asymptotic models for a thin piezoelectric junction between two linearly piezoelectric or elastic bodies will be indexed by $p = (p_1, p_2, p_3)$ in $\{1, 2, 3, 4\}^3$. Indices p_1 and p_2 are respectively relative to the magnitude of the elastic and dielectric coefficients of the adhesive with respect to that of the constant thickness 2ε of the layer containing the adhesive. More precisely, we assume that $h := (\varepsilon, \mu) = (\varepsilon, \mu_{mm}, \mu_{ee}, \mu_{me})$ takes values in a countable set with a sole cluster point $\bar{h} \in \{0\} \times [0, +\infty]^3$, so that

$$\begin{cases} p_1 = 1: & \bar{\mu}^1_{mm} := \lim_{h \to \bar{h}} (2\varepsilon \mu_{mm}) \in (0, +\infty) \\ p_1 = 2: & \bar{\mu}^1_{mm} := \lim_{h \to \bar{h}} (2\varepsilon \mu_{mm}) = 0, \\ & \bar{\mu}^2_{mm} := \lim_{h \to \bar{h}} (\mu_{mm}/2\varepsilon) = +\infty \\ p_1 = 3: & \bar{\mu}^2_{mm} := \lim_{h \to \bar{h}} (\mu_{mm}/2\varepsilon) \in (0, +\infty) \\ p_1 = 4: & \bar{\mu}^2_{mm} := \lim_{h \to \bar{h}} (\mu_{mm}/2\varepsilon) = 0 \end{cases} \tag{34}$$

$$\begin{cases} p_2 = 1: & \bar{\mu}^1_{ee} := \lim_{h \to \bar{h}} (2\varepsilon \mu_{ee}) \in (0, +\infty) \\ p_2 = 2: & \bar{\mu}^1_{ee} := \lim_{h \to \bar{h}} (2\varepsilon \mu_{ee}) = 0, \\ & \bar{\mu}^2_{ee} := \lim_{h \to \bar{h}} (\mu_{ee}/2\varepsilon) = +\infty \\ p_2 = 3: & \bar{\mu}^2_{ee} := \lim_{h \to \bar{h}} (\mu_{ee}/2\varepsilon) \in (0, +\infty) \\ p_2 = 4: & \bar{\mu}^2_{ee} := \lim_{h \to \bar{h}} (\mu_{ee}/2\varepsilon) = 0. \end{cases} \tag{35}$$

The parameters $\mu_{mm}, \mu_{ee}, \mu_{me}$ respectively characterize the order of magnitude of the elastic, dielectric and piezoelectric coefficients of the adhesive. The case $p_1 = p_2$, being already treated in [7], in the following we assume $p_1 \neq p_2$. As in [7], index p_3 characterizes the status of the adherents but also that of the interfaces between adherents and adhesive:

$$\begin{cases} p_3 = 1: & \text{the two interfaces are electromechanically perfectly permeable,} \\ p_3 = 2: & \text{the two interfaces are electrically permeable,} \\ p_3 = 3: & \text{one interface is electrically permeable while the other one bears an electrode,} \\ p_3 = 4: & \text{the two interfaces bear an electrode.} \end{cases} \tag{36}$$

Therefore, the constitutive equations of the structure, for all $\hat{p} := (p_1, p_2)$, read as:

$$\begin{cases} (\sigma_p^h, D_p^h) = M_{\mathrm{I}}^{\mu}\big(e(u_p^h), \nabla\varphi_p^h\big) & \text{in } B^{\varepsilon}\ \forall p_3 \in \{1,2,3,4\}, \\ \begin{cases} (\sigma_p^h, D_p^h) = M_{\mathrm{E}}^{\varepsilon}\big(e(u_p^h), \nabla\varphi_p^h\big) & \text{in } \Omega^{\varepsilon}\ \text{ if } p_3 = 1, \\ \sigma_p^h = a_{\mathrm{E}}^{\varepsilon} e(u_p^h) & \text{in } \Omega^{\varepsilon}\ \text{ if } p_3 > 1 \end{cases} \end{cases} \tag{37}$$

where

$$(M_{\mathrm{E}}^{\varepsilon}, a_{\mathrm{E}}^{\varepsilon})(x) = (M_{\mathrm{E}}, a_{\mathrm{E}})(x \mp \varepsilon e_3) \quad \forall x \in \Omega_{\pm}^{\varepsilon} \tag{38}$$

$$\begin{cases} (M_{\mathrm{I}}, M_{\mathrm{E}}) \in L^{\infty}\big(S \times \Omega; \mathscr{L}(\mathscr{H})\big) \text{ such that} \\ M_{\mathrm{I}}^{\mu} := \begin{bmatrix} \mu_{mm} a_{\mathrm{I}} & -\mu_{me} b_{\mathrm{I}} \\ \mu_{me} b_{\mathrm{I}}^T & \mu_{ee} c_{\mathrm{I}} \end{bmatrix}, \quad M_{\mathrm{E}} := \begin{bmatrix} a_{\mathrm{E}} & -b_{\mathrm{E}} \\ b_{\mathrm{E}}^T & c_{\mathrm{E}} \end{bmatrix} \\ M_{\mathrm{P}} := \begin{bmatrix} a_{\mathrm{P}} & -b_{\mathrm{P}} \\ b_{\mathrm{P}}^T & c_{\mathrm{P}} \end{bmatrix}; \exists \kappa > 0 \quad \kappa|k|^2 \le M_{\mathrm{P}}(x)k \cdot k \quad \forall k \in \mathbb{H} \text{ a.e. } x \in \Omega, \ \forall \mathrm{P} \in \{\mathrm{I}, \mathrm{E}\}. \end{cases} \tag{39}$$

Lastly we have to add the following conditions on $S_{\pm}^{\varepsilon}$:

$$\begin{cases} p_3 = 2 & D_p^h \cdot e_3 = 0 \quad \text{on } S_{\pm}^{\varepsilon}, \\ p_3 = 3 & D_p^h \cdot e_3 = 0 \quad \text{on } S_{+}^{\varepsilon}, \quad \varphi_p^h = \varphi_{p_0}^h \text{ on } S_{-}^{\varepsilon}, \\ p_3 = 4 & \varphi_p^h = \varphi_{p_0}^h \quad \text{on } S_{\pm}^{\varepsilon}, \end{cases} \tag{40}$$

the electric potential $\varphi_{p_0}^h$ being given on S_{+}^{ε} or $S_{\pm}^{\varepsilon}$.

Our results show that for piezoelectric adhesive *and* adherents, when the elastic and dielectric coefficients of the adhesive are not of the same order, the piezoelectric coupling remains in the asymptotic model only when $\hat{p} = (1,3)$ or $(3,1)$. More generally, when (necessarily only) one index p_1 or p_2 is equal to 1, the status of the limit model for the adhesive is *hybrid*. When $p_1 = 1$, the adhesive is replaced by both a material surface perfectly bonded to the adherents, from the mechanical point of view, and a constraint, from the electrical point view. On the contrary when $p_2 = 1$, a mechanical constraint appears with an electrical material surface perfectly permeable. The mechanical material surface is an elastic membrane with a possible non-null (only when $\hat{p} = (1,3)$) residual stress *stemming from the possible discontinuity of the electrical potential induced by the limit electrical constraint* which is perfect permeability, electric pull-back or impermeability, according to the magnitude of the dielectric coefficients. The electrical material surface is of lin-

ear conductor type with a possible non-null (only when $\hat{p} = (3, 1)$) residual term *stemming from the possible non-null relative displacement induced by the mechanical constraint* which is perfect adhesion, elastic pull-back or free separation according to the magnitude of the stiffness of the adhesive. When both p_1 and p_2 are greater than 1, the adhesive is replaced by an electromechanical constraint. As the orders of magnitude of the elastic and dielectric coefficients differ, this electromechanical constraint reduces to two *independent* mechanical and electrical constraints of the types previously recalled according to the values of p_1 and p_2, respectively.

For a thin piezoelectric layer embedded between two purely elastic adherents through two electrically impermeable interfaces, the piezoelectric coupling remains in the asymptotic model only when $\hat{p} = (1, 3)$ or $(3, 1)$. When $\hat{p} = (1, 3)$ the adhesive layer is replaced by a piezoelectric material surface; when $\hat{p} = (3, 1)$, it is replaced by a material conductive surface and a mechanical constraint. This constraint is of elastic pull-back type with a residual term *stemming from the electrical potential in the conductive surface*. Actually, when $p_1 = 1$, the adhesive layer is replaced by a material elastic surface perfectly bonded to the adherents. When $p_2 = 3$, the material surface has a non-local elastic behavior since the electrical potential can be eliminated, in the other cases the material surface is a standard elastic membrane. When p_1 ranges from 2 to 4, the adhesive layer is replaced by a mechanical constraint which is perfect adhesion, elastic pull-back or free separation. The elastic pull-back is nonlocal when $p_2 = 1$. When $p_2 = 2$, the electric potential vanishes, in the remaining cases the limit surface is a linear elastic conductor.

The limit models for a thin piezoelectric layer embedded between two elastic adherents, through either two electroded interfaces or one electroded and the other being impermeable, only differ when $\hat{p} = (1, 3)$. In all cases, there is a perfect decoupling between Electricity and Mechanics. When the magnitude of the stiffness is of the order of the inverse of the thickness, the adhesive is replaced by an elastic material membrane perfectly bonded to the adherents; when it is lesser, the adhesive is replaced by a mechanical constraint which is perfect adhesion, elastic pull-back, free separation according to the magnitude of the stiffness. The limit surface is at a given applied potential when $\hat{p} \in \{ 3, 4 \} \times \{ 1 \}$, at a vanishing one in the other cases. Actually when $p = (1, 3, 3)$, the memory of electricity remains because piezoelectric and dielectric coefficients enter in the constitutive equations of the elastic membrane the adhesive layer reduces to.

Eventually the previous method may work when the elastic and dielectric coefficients of the junction are of the same order of magnitude with piezoelectric coefficients of lesser order. Obviously the conclusions of [7] remain but with b_I replaced by 0, so that the piezoelectric coupling disappears in the asymptotic models.

References

1. Aitmoussa A (1989) Modélisation et études des singularités de contraintes d'un joint collé très mince. PhD thesis, Université Montpellier 2, France
2. Bisegna P, Maceri F (1996) A consistent theory of thin piezoelectric plates. J Intell Mater Syst Struct 7:372–389
3. Ciarlet PG (1997) Mathematical Elasticity, vol II. North-Holland, Amsterdam
4. Geymonat G, Licht C, Weller T (2011) Plates made of piezoelectric materials: when are they really piezoelectric? Appl Math Model 35:165–173
5. Licht C (2011) Some new mathematical modelings of junctions. East-West J Math 13(1):23–33
6. Licht C, Orankitjaroen S, Viriyasrisuwattana P, Weller T (2014) Bonding a linearly piezoelectric patch on a linearly elastic body. Comptes Rendus Mécanique 342(4):234–239
7. Licht C, Orankitjaroen S, Viriyasrisuwattana P, Weller T (2015) Thin linearly piezoelectric junctions. Comptes Rendus Mécanique 343(4):282–288
8. Maugin GA, Attou D (1990) An asymptotic theory of thin piezoelectric plates. Q J Mech Appl Math 43:347–362
9. Mead CA (1962) Electron transport mechanism in thin insulating films. Phys Rev 128:2088–2095
10. Mindlin RD (1968) Polarization gradient in elastic dielectrics. Int J Solids Struct 4:637–642
11. Murat F, Sili A (1999) Comportement asymptotique des solutions du système de l'élasticité linéarisée anisotrope hétérogène dans des cylindres minces. Comptes Rendus de l'Académie des Sciences Série I 199:179–184
12. Rahmoune M, Benjeddou A, Ohayon R (1998) New thin piezoelectric plates models. J Intell Mater Syst Struct 9:1017–1029
13. Royer D, Dieulesaint E (1996) Ondes élastiques dans les solides. Masson, Tome I
14. Sène A (2000) Modélisation asymptotique de plaques: contrôlabilité exacte frontière, piezoélectricité. Thèse de l'Université Joseph Fourrier—Grenoble I
15. Toupin RA (1956) The elastic dielectric. J Ration Mech Anal 5:849–915
16. Trabucho L, Viano JM (1996) Mathematical modelling of rods. In: Handbook of numerical analysis, vol IV, Amsterdam, North-Holland
17. Voigt W (1910) Lehrbuch der Kristallphysik (mit Ausschluss der Kristalloptik). Volume 34 of BG Teubners Sammlung von Lehrbchern auf dem Gebiete der mathematischen Wissenschaften mit Einschluss ihrer Anwendungen. Teubner, Leipzig
18. Vrisysrisuwattana D, Licht C, Weller T, Koonprasert S (2007) Mathematical modelling of piezoelectric thin plates and slender beams through functional analysis. In: The 12th annual meeting in mathematics, Burapha University, Chonburi, Thailand
19. Weller T (2004) Étude des symétries et modèles de plaques en piézoélectrictité linéarisée. Thèse de l'Université Montpellier II, France
20. Weller T, Licht C (2002) Analyse asymptotique de plaques minces linéairement piézoélectriques. Comptes Rendus de l'Académie des Sciences Série I 335:309–314
21. Weller T, Licht C (2004) Réponse dynamique asymptotique de plaques minces linéairement piézoélectriques dans l'approximation quasi-électrostatique. Comptes Rendus Mécanique 332:519–524
22. Weller T, Licht C (2007) Modeling of linearly electromagneto-elastic thin plates. Comptes Rendus Mécanique 335:201–206
23. Weller T, Licht C (2010) Asymptotic modeling of thin piezoelectric plates. Ann Solid Struct Mech 1:173–188

Multiplane Cohesive Zone Models Combining Damage, Friction and Interlocking

Elio Sacco, Roberto Serpieri and Giulio Alfano

Abstract The present work describes a number of cohesive zone models (CZMs) developed over the last decade; the models are derived from a simplified approach to the micro-mechanics of the fracture process. The models are able to separately consider damage and frictional dissipation; moreover, the most recent proposed models account also for intelocking and dilatancy. Initially, the model developed by Alfano and Sacco [6], coupling together damage and friction, is reviewed. A damage variable is introduced, evolving from zero for no damage to one when cohesion is lost. The main idea is to assume that friction only acts on the damaged part of the interface. The evolution of damage is governed by a mixed-mode criterion widely used in composite materials. Then, some thermodynamical consideration is presented, which leads in a simplified context to the result that the value of the fracture energy in mode I and II has to be the same [44]. A microstructured interface model is presented, obtained as combination of more inclined planes; this model is named as Representative Multiplane Element (RME) and it shows different fracture energies in mode I and II as result of the interplay between residual adhesion and the frictional slips on the inclined elementary planes, which determines significant frictional dissipation also in pure more II. The RME model is also able to account for interlocking and dilatancy [43]. Numerical applications illustrating the capacity of the proposed models are presented.

E. Sacco (✉)
Dipartimento di Ingegneria Civile e Meccanica, Università di Cassino e del Lazio Meridionale, Cassino, Italy
e-mail: sacco@unicas.it

R. Serpieri
Dipartimento di Ingegneria, Università degli Studi del Sannio, Piazza Roma 21, 82100 Benevento, Italy
e-mail: rserpier@unisannio.it

G. Alfano
Brunel University, School of Engineering and Design, Uxbridge, UK
e-mail: giulio.alfano@brunel.ac.uk

M. Frémond et al. (eds.), *Models, Simulation, and Experimental Issues in Structural Mechanics*, Springer Series in Solid and Structural Mechanics 8,
DOI 10.1007/978-3-319-48884-4_3

1 Introduction

Cohesive-zone models (CZMs) are widely used to simulate the behavior of internal surfaces, which we will generally call 'interfaces', where formation and propagation of cracks are expected, by introducing a nonlinear relationship between a traction and a relative displacement at each point of the interface.

In a general 3D case, the traction and the relative displacement at each point are vectors with three components. Mode I refers to their components in the direction normal to the interface and modes II and III to those in the direction tangential to the interface, orthogonal and parallel, respectively, to the crack front. In 2D problems only modes I and II are defined.

For a monotonically increasing relative displacement in opening mode I or in modes II or III, the corresponding traction component initially has a very rapid (typically linear) increase, for which significant values of the traction are found for extremely small values of the relative displacement. This part simulates the initial undamaged behavior of the interface. At some point, damage starts and results in the slope of the 'traction-relative displacement' curve to reduce from positive to negative, either gradually or suddenly depending on the model. The softening part of the curve simulates the progressive loss of cohesion, i.e. damage, and possibly other inelastic mechanisms occurring during the damage process. At some critical point the traction reduces to zero when cohesion is completely lost. At this point, unilateral contact must be considered in mode I. In a 'mixed-mode' case, more than one component are simultaneously non-zero and their interaction must be considered.

The area under the interface response curve is the energy required to create a new unit crack surface, that is the fracture energy G_c introduced in linear elastic fracture mechanics (LEFM), first by Griffith in his seminal work published almost a century ago [20]. This is the fundamental (and only) conceptual link between CZMs and LEFM. In fact, CZMs were first introduced by Barenblatt [11] and Dugdale [18] as a way of eliminating the physically unjustified stress singularity appearing in LEFM at the crack tip in presence of a sharp crack. Following these pioneering contributions and the first finite-element implementation of a CZM by Hilleborg et al. [22], CZMs have attracted enormous attention, resulting in an immense literature, see [13, 15, 33] for a non-exhaustive account.

CZMs naturally fit a nonlinear finite-element analysis and can also be used when it is not known a priori where the crack can propagate, for example in combination with the X-FEM or meshless methods, see [8, 10, 35, 50] among many others. They can also be easily incorporated within isogeometric analysis [32, 49]. Furthermore, CZMs do not require an initial crack to be present, unlike fracture-mechanics methods.

When the cohesive zone is very small, e.g. on very brittle interfaces, it can be shown that the only parameter which matters is the fracture energy. However, when the size of the cohesive zone is very large and comparable with the dimensions of the structure, results can be strongly affected by the other parameters of the CZM law, such as the peak stress, i.e. the cohesive strength, or the actual shape of the curve

[3, 14, 15]. In these cases, CZMs can be significantly more effective than methods based on LEFM in predicting experimental results.

On the other hand, CZMs are normally computationally expensive, because crack propagation can often result in a highly nonlinear response, particularly if the mesh within and around the cohesive-zone is not refined enough [4]. While a number of remedies to deal with these problems have been proposed [5, 16, 39, 40, 48], the high computational cost of CZMs often makes them less convenient than methods directly based on fracture mechanics.

One advantage of CZMs, with respect to methods based on fracture mechanics, is that they provide a framework where the micro-mechanics of fracture can be accounted for more effectively. One way is to use refined multi-scale methods, such as computational homogenisation [9, 24, 31]. This approach offers potentially unlimited predictivity of the model, as well as deep insight into the physics of fracture. However, it is computationally very expensive. Furthermore, some material parameters are still needed at the smallest scale and are often not easy to determine, unless a number of scales are considered, until the atomistic and sub-atomistic level are reached where *ab initio* simulations are conducted. However, this last option is still too computationally demanding and theoretically challenging for real-life applications.

Instead, this chapter describes a number of CZMs developed by the authors over the last decade [2, 6, 7, 38, 41–44], with a methodology that takes into account the micro-mechanics of the fracture process but without the need for very detailed numerical simulations at the small scale. The models separately consider damage and frictional dissipation and the most recent ones make use of a simplified multi-scale formulation to capture the interplay between these two dissipation mechanisms and the geometry fracture surface at the micro-scale [2, 41, 43, 44].

The first of these models was developed by Alfano and Sacco [6] to combine together damage and friction. In some conceptual aspects the model has some similarity with the work by Raous et al. [36], who also considered adhesion and friction as two separate dissipative processes modelled within a thermodynamic formulation, but it is also rather different in most details. At each point of the interface a damage variable, D, is introduced, evolving from zero for no damage to one when cohesion is lost. Based on a widely accepted damage-mechanics interpretation, each infinitesimal area of interface is then decomposed into a damaged and an undamaged part. The main idea is to assume that friction only acts on the damaged part of the interface, which results in a gradual transition from the undamaged condition, with no frictional dissipation, to the fully damaged condition, at which point all dissipation is due to friction. Adopting a Coulomb frictional law, the kinematic internal variable associated with frictional dissipation is the inelastic slip on the damaged part. The evolution of damage is governed by a mixed-mode criterion widely used in composite materials and previously reformulated in a damage-mechanics framework by Alfano and Crisfield [4]. The effectiveness of the model is demonstrated by the successful calibration and good correlation between numerical and experimental results for the cases of a fibre push-out test [12, 28] and a masonry wall subject to in-plane compression and shear [29].

The model by Alfano and Sacco was then enhanced to account for dilatancy in [7], using a phenomenological approach. To this end, friction and dilatancy angles are both assumed to decrease as a function of the inelastic slip, with a possible recover of the latter in the case of cycling loading. An initial validation of this part of the model was conducted against the experimental test reported by Lee et al. [27]. In order to apply the model to the simulation of cracks propagating at the interface between rock and concrete in a gravity dam [1], the effect of water uplift pressure is introduced as a function of the crack opening.

Sacco and Toti [38] extended the formulation by Alfano and Sacco to model the mechanical behaviour of masonry elements regarded as heterogeneous systems. At the typical point of the interface, a representative elementary volume, characterized by a given thickness, is introduced. The interface thickness is obtained as the sum of the thicknesses of the mortar and brick regions involved in the degradation phenomenon at the interface considering different fracture energies in mode I and II.

With the aim of moving from a rather phenomenological to a more physically-based description of dilatancy, Serpieri and Alfano [41] developed a 2D multi-scale interface model, hereby denominated Multiplane Cohesive-Zone Model (M-CZM) with a smooth interface at the macro-scale, and a simplified representation of the micro-scale through a Representative Multiplane Element (RME) made of 3 elementary-planes, one parallel to the macro-interface and the other two with equal and opposite inclination. On each of the elementary planes, the (non-dilatant) model by Alfano and Sacco is used and the two opposite parts of the RME are assumed to move rigidly with respect to each other. This results in a closed form computation of the stresses and material tangents on each elementary plane, for a given relative displacement at the macro-scale, and therefore of the total macro-stress and related material tangent via equilibrium. Despite the small number of elementary planes considered and the non-dilatant nature of the model on each of them, a dilatant and hysteretic bond-slip response is naturally determined in shear, which was numerically validated against experimental results for pull-out tests of ribbed steel bars from confined concrete [25].

A key feature of the model by Alfano and Sacco [6] is that in modes I and II different fracture energies are assumed, in accordance with the experimental finding that the fracture energy in mode II is significantly greater than in mode I, practically for all materials and interfaces. To fulfill this requirement and avoid the introduction of different damage variables for each mode [30], a non-associate damage evolution law was used, as in [4]. Alternative thermodynamic formulations, which result in different fracture energies in different modes with an associate damage evolution law, have been proposed: for example, Valoroso and Champaney made the threshold energy used in their damage evolution criterion a function of the mode-mixity ratio [47]; very recently, Parrinello et al. introduced an additional internal variable whose evolution governs the additional dissipation required in mode II [34].

On the other hand, if one assumes the adhesion energy only represents the energy of the bonds that have to be broken to create the two faces of the crack, then it would make sense to assume this energy is the same regardless of whether the crack forms and propagates in mode I, II or III. In fact, once the different contributions

to dissipation provided by decohesion and friction are separately modelled, one can expect that the latter may naturally lead to an increase in the dissipated energy with increasing mode II/mode I ratio. This possibility was explored in a recent paper by Serpieri et al. [44], in which the 2D multi-scale model in [41] was recast in a thermodynamic formulation, with an associate type of damage evolution law in which the threshold energy is a function of the damage only, i.e. independent from the mode mixity, and without the introduction of any other internal variable. This resulted automatically in the constraint of having the same decohesion energy dissipated in modes I and II. The capability of the model of naturally predict an increasing total fracture energy with increasing mode II/mode I ratio is demonstrated by the good correlation with available experimental results for a double cantilever beam loaded by uneven bending moments, which vary in way to produce a wide range of mode-mixity ratios, from pure mode I to almost pure mode II [45]. It can be shown that this is the result of the interplay between residual adhesion and the frictional slips on the inclined elementary planes, which determines significant frictional dissipation also in pure more II. It is also worth underlining that the multi-scale model is based on the assumption that the geometry of the RME is independent from the mode mixity. This may be a strong one in some cases, and therefore it will be interesting reconsidering it in future work. However, this assumption may be reasonable in cases where the fracture surface is strongly dictated by the micro-structure, such as in concrete.

In [43] further enhancements of the multi-scale model were made by accounting for the finite-depth of the asperities of the RME, which introduces a further length scale in the model, and by including a degradation law which makes the inclination of the elementary planes a decreasing function of the frictional dissipation.

All the models in [6, 7, 38, 41, 43, 44] were developed for 2D cases. The extension of the multi-scale model to a 3D case was studied in [2], where the sensitivity of the results to the choice of different 3D RMEs was investigated.

2 A Damage-Friction Interface Model

Let Ω_1 and Ω_2 be two bodies in adhesion along an interface $\mathfrak{I}$. The displacement fields in the bodies Ω_1 and Ω_2 are denoted by $\mathbf{u}^1$ and $\mathbf{u}^2$, respectively, so that the relative displacement along $\mathfrak{I}$ is $\mathbf{s} = \mathbf{u}^2 - \mathbf{u}^1$.

A cohesive interface model coupling damage and possible friction, based on the micro-mechanical approach proposed in [6, 7, 38], is presented in this section. The interface model is derived based on a simple micromechanical analysis. With reference to a typical interface zone between two bodies in adhesion, as schematically represented in Fig. 1, three different points are considered on the interface $\mathfrak{I}$:

- at the interface point **A**, the connection between the joined bodies is undamaged,
- at the interface point **B**, partial decohesion between the contacting surfaces of the different bodies has occurred;
- at the interface point **C**, the decohesion phenomenon is complete.

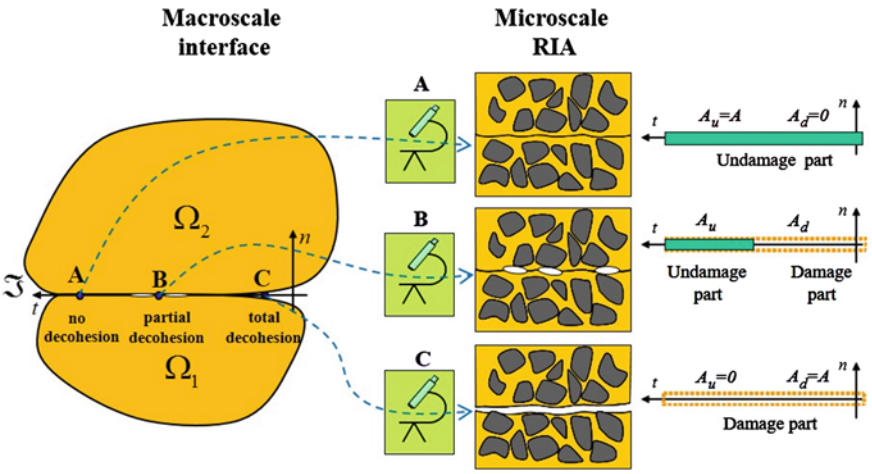

Fig. 1 Multiscale scheme: macroscale interface and microscale representative interface area (RIA)

Considering the Representative Interface Area (RIA) associated with the point A of the interface, the surfaces in adhesion do not present any defect. The RIA associated with point B contains partial dechoesion due to the presence of microcracks. In the RIA corresponding to point C, coalescence of microcracks has occurred and a total dechoesion is present. The RIA can be modelled in a simple manner considering two rigid plates in adhesion; the total area A of the RIA can be split in two parts: an undamaged part A^u and a damaged one A^d, so that $A^u + A^d = A$. To set ideas, in Fig. 1 at point **A** of the interface one has $A^u = A$ and $A^d = 0$, while at point **C** $A^u = 0$ and $A^d = A$, i.e. the representative interface area results completely damaged. Following standard arguments of continuous damage mechanics, the damage parameter D is introduced as ratio between the damaged part and the whole interface area:

$$D = \frac{A^d}{A} \qquad \text{so that} \qquad A^u = (1 - D)\, A\,, \;\; A^u = DA \tag{1}$$

As the RIA is assumed to be composed by two rigid plates in adhesion, the relative displacement on the areas A^u and A^d assumes the same value $\mathbf{s}$. Considering a linear elastic behavior of the undamaged part of the RIA and a constitutive law characterized by unilateral contact and friction for the damaged part of the RIA, the tractions $\boldsymbol{\sigma}^u = \left[\sigma_n^u,\ \sigma_t^u\right]^T$ and $\boldsymbol{\sigma}^d = \left[\sigma_n^d,\ \sigma_t^d\right]^T$ on $A^u = A$ and A^d, respectively, result:

$$\boldsymbol{\sigma}^u = \mathbf{K}\,\mathbf{s} \tag{2}$$

$$\boldsymbol{\sigma}^d = \mathbf{K}\,\mathbf{H}\,\left(\mathbf{s} - \mathbf{s}^{di}\right)\,, \tag{3}$$

where $\mathbf{K} = \text{ diag } [K_n, K_t]$ is a diagonal matrix which collects the stiffness values in the normal and tangential directions to the interface, $\mathbf{H} = \text{ diag } [1 - h(s_n), 1]$, with $h(\bullet)$ being the Heaviside function:

$$h(s_n) = \begin{cases} 1 \text{ if } s_n \geq 0 \\ 0 \text{ if } s_n < 0 \,. \end{cases} \tag{4}$$

The total, i.e. overall homogenized, value of traction on the RIA is obtained by weighting the two stresses determined on A^u and A^d by Eqs. (2) and (3) as:

$$\begin{aligned} \boldsymbol{\sigma} &= (1 - D)\boldsymbol{\sigma}^u + D\,\boldsymbol{\sigma}^d \\ &= \mathbf{K}\left[\mathbf{s} + \mathbf{H}\,\left(\mathbf{s} - \mathbf{s}^{di}\right)\right] . \end{aligned} \tag{5}$$

The evolution of the inelastic slip relative displacement $\mathbf{s}^{di}$, occurring on the damaged part of the RIA, is assumed to be governed by the Coulomb friction with yield function:

$$\phi(\boldsymbol{\sigma}^d) = \mu \left\langle \sigma_n^d \right\rangle_- + \left|\sigma_t^d\right| , \tag{6}$$

where μ is the friction coefficient and the brackets $\langle\bullet\rangle_-$ define the negative part of the argument variable.

A purely tangential slip evolution law is considered for the inelastic relative displacement vector $\mathbf{s}^{di}$, as determined by the non-associated flow rule:

$$\dot{\mathbf{s}}^{di} = \dot{\lambda} \left\{ \begin{array}{c} 0 \\ \dfrac{\sigma_t^d}{\left|\sigma_t^d\right|} \end{array} \right\} , \tag{7}$$

and is completed by the classical loading-unloading (Kuhn-Tucker) conditions:

$$\dot{\lambda} \geq 0 \qquad \phi(\boldsymbol{\sigma}^d) \leq 0 \qquad \dot{\lambda}\,\phi(\boldsymbol{\sigma}^d) = 0 \,. \tag{8}$$

Concerning the evolution of the damage parameter D, a model which accounts for the coupling of mode I of mode II of fracture is considered. Denoting by s_{0n} and s_{cn} the normal relative displacement corresponding to onset and complete damage for pure mode I, respectively, and, in a similar way, with s_{0t} and s_{ct} the tangential relative displacement corresponding to the onset of damage and complete damage for pure mode II, the following ratios are introduced:

$$\chi_n = \frac{s_{0n}}{s_{cn}} \qquad \chi_t = \frac{s_{0t}}{s_{ct}} . \tag{9}$$

Note that the ratios χ_n and χ_t are related to the mode I and mode II fracture energies by:

$$\chi_n = \frac{s_{0n}\sigma_{0n}}{2G_{cI}} , \qquad \chi_t = \frac{s_{0t}\sigma_{0t}}{2G_{cII}} , \tag{10}$$

being σ_{0n} and σ_{0t} the normal and shear peak stresses corresponding to the first cracking relative displacement, and G_{cI} and G_{cII} the specific fracture energies in mode I and mode II, respectively.

An equivalent relative displacement ratio is introduced as:

$$Y = \sqrt{Y_n^2 + Y_t^2} \qquad \text{with} \qquad Y_n = \frac{\langle s_n \rangle_+}{s_{0n}}, \quad Y_t = \frac{s_t}{s_{0t}} \tag{11}$$

being Y_n and Y_t the mode I and mode II relative displacement ratios, respectively, and the brackets $\langle \bullet \rangle_+$ defining the positive part of the number.

The damage parameter is function of the whole history of the equivalent relative displacement ratio Y and of a parameter χ coupling the two modes of fracture:

$$D = \max_{history} \left\{ 0, \min \left\{ 1, \tilde{D} \right\} \right\} \qquad \text{with} \qquad \tilde{D} = \frac{Y - 1}{Y\,(1 - \chi)} \tag{12}$$

whereas χ is defined as:

$$\chi = \frac{1}{\alpha^2} \left[\langle s_n \rangle_+^2 \, \chi_n + s_t^2 \, \chi_n \right], \tag{13}$$

where $\alpha = \sqrt{\langle s_n \rangle_+^2 \, \chi_n + s_t^2 \, \chi_n}$.

The damage evolution equation takes the form originally considered in [6] as function of η by setting $\chi_n = \chi_t = 1 - \eta$ and $\beta = Y - 1$:

$$D = \max_{history} \left\{ 0, \min \left\{ 1, \tilde{D} \right\} \right\} \qquad \text{with} \qquad \tilde{D} = \frac{\beta}{(1 + \beta)\,\eta}. \tag{14}$$

The proposed damage law induces a linear stress-strain softening both in mode I and in mode II, as schematically illustrated in Fig. 2. It can easily proved [38] that the softening remains linear even for mixed mode of the damage evolution.

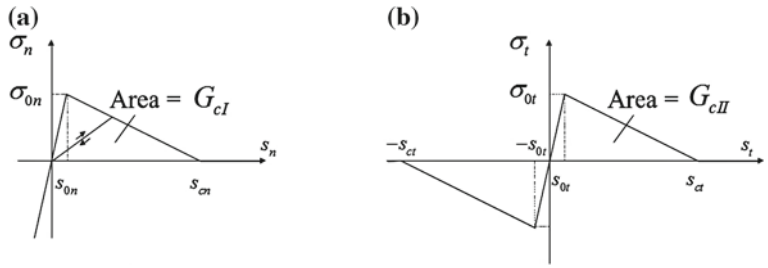

Fig. 2 Stress-strain response in **a** pure mode I and **b** pure mode II

3 Thermodynamic Considerations

It can be observed that, while the use of the nonassociative elastoplastic formulation, provided by Eqs. (5)–(8), represents in some sense an ordinary choice for friction modelling, which finds a foundation in the thermo-mechanics of continua with internal variables [19], the evolution law for damage given in (12) is less standard and has a more phenomenological character. On the other hand, the availability of an evolution law for damage, such as the one in (12), is appealing from a computational point view since it allows to update in decoupled form damage and friction internal variables on a simple kinematic basis.

The possibility of recasting the strategy for combining damage and friction of the previous section, and in particular equation (12), into a more general framework of thermo-mechanics of continua with internal variables has been investigated in [44]. To provide a thermodynamic background to Eq. (12) an Helmholtz free energy function $\Psi = \Psi\left(\mathbf{s},\ \mathbf{s}^{di},\ D\right)$ is introduced with the Ψ-conjugated generalized stress variable associated with D, X, defined as

$$X = -\frac{\partial \Psi}{\partial D}. \tag{15}$$

For damage evolution a rate-independent complementary law is considered and it is assumed that X is independent from frictional displacements $\mathbf{s}^{di}$, viz. $X = X(\mathbf{s}, D)$. Accordingly, a force potential φ is considered which is the indicator function of the interval $P_D = [0,\ X_0]$, [37], with X^0 being the threshold value for damage stress at which damage evolution is triggered. X^0 is assumed to be dependent only on D to account for the property that displacements do not affect the stress damage threshold. These choices determine that, upon introducing the function f

$$f = X(\mathbf{s}, D) - X^0(D), \tag{16}$$

damage increase is governed by the Kuhn-Tucker loading-unloading conditions:

$$\dot{D} \geq 0 \qquad f \leq 0 \qquad \dot{D} f = 0, \tag{17}$$

and that damage is activated only when $X = X^0$. In particular, in a time interval in which damage monotonically evolves, one has $X = X^0$ and $\dot{D} > 0$, and conditions (17) imply that $\dot{f} = 0$ during the whole time interval. In this case, by the chain rule one infers:

$$\dot{f} = \frac{\partial X}{\partial D}\dot{D} + \frac{\partial X}{\partial \mathbf{s}}\dot{\mathbf{s}} - \frac{dX^0}{dD}\dot{D} = 0 \tag{18}$$

and hence:

$$\dot{D} = -\left(\frac{\partial X}{\partial D} - \frac{dX^0}{dD}\right)^{-1} \frac{\partial X}{\partial \mathbf{s}}\dot{\mathbf{s}} \tag{19}$$

This equation can be compared with the rate equation stemming from the *phenomenological* evolution law (12) of Sect. 2 which, instead, for $0 < \tilde{D} < 1$ turns out to be:

$$D = \tilde{D}, \qquad \dot{D} = \dot{\tilde{D}} = \frac{\partial \tilde{D}}{\partial Y} \frac{\partial Y}{\partial \mathbf{s}} \dot{\mathbf{s}} \tag{20}$$

The conditions to be fulfilled by the functions $X(\mathbf{s}, D)$ and $X^0(D)$ in order to retrieve from continuum thermodynamics a damage evolution law of the form postulated in (12) are thus obtained by equating the rate expressions (19) and (20):

$$\frac{\partial \tilde{D}}{\partial Y} \frac{\partial Y}{\partial \mathbf{s}} = -\left(\frac{\partial X}{\partial D} - \frac{dX^0}{dD} \right)^{-1} \frac{\partial X}{\partial \mathbf{s}} \tag{21}$$

Conditions (21) constitute a system of two differential equations. These equations can be viewed either as a constraint to be satisfied when selecting functions $\tilde{D}(Y)$ and $Y(\mathbf{s})$ in order to guarantee thermodynamic consistency, or also as a requirement for identifying functions $X(\mathbf{s}, D)$ and $X^0(D)$ when proceeding from an observed interface response well fitted by the formulation described in the previous section.

Equations (21) are complemented by boundary conditions which have to be satisfied by $\tilde{D}(Y)$ and $Y(\mathbf{s})$, $X(\mathbf{s}, D)$ and $X^0(D)$ at the onset of damage and at complete decohesion, providing additional constraints. In [44] the whole set of constraints constituted by (21) and by the associated boundary conditions is examined, first, in general terms; subsequently, it is specialized to address the possibility of retrieving the interface response detailed in the previous section featuring a linear elastic behavior, linear softening branches in pure modes I and II, and with independent stiffnesses and fracture energies in mode I and mode II. It is proved therein that satisfaction of the whole set of simple and physically reasonable restrictions demanded by thermodynamic consistency is only guaranteed if the following conditions are fulfilled

$$K_{n0} = K_{t0}, \qquad s_{0n} = s_{0t}, \qquad s_{cn} = s_{ct} \tag{22}$$

Equations (22) introduce restrictions to the allowable interface parameters and will be referred to as *thermodynamic constraints*. These constraints are quite severe since they state that the cohesive part of the interface response has to be the same in pure mode I and pure mode II, with the immediate consequence that the fracture energies G_{cI} and G_{cII} have to be the same, that χ_n and χ_t in (9) also share a single value χ, and that similarly $\sigma_{0n} = \sigma_{0t} = \sigma_0$.

The existence of limitations to the describable decohesion responses due to the use of a single damage variable when thermodynamic consistency is maintained has been pointed out also in [17] where it is observed that one single diagonal experiment is sufficient to determine the constitutive behavior of adhesive interfaces when a single damage variable is employed. These limitations conflict with the evidence that the measured response in mode II decohesion in most structural interfaces is typically

stiffer than the one measured in pure mode I, and with a higher energy spent to produce decohesion.

This incapability of discriminating different mode I and mode II responses, when thermodynamic consistency is invoked, is recognized to be the consequence of a fundamental feature of the formulation so far examined: the absence of dilation; in other words, the interface model so far considered is capable of describing only the response of an *ideally flat* interface.

4 Multiplane Interface Formulation

4.1 Indefinitely Dilating Model

In [44] a strategy is devised to build off an enhanced interface model from the formulation of Sect. 2, capable of expanding the class of predicted interface responses so as to simultaneously describe dilation and address a stiffer and tougher response in mode II. This strategy, as shown in [44], is capable of recovering jointly an increased mode II fracture energy and a dilating behavior of the interface element, while preserving a formulation in the framework of the thermomechanics of generalized continua and avoiding the further addition of ad-hoc phenomenological ansatzs.

Such a strategy consists of the use the formulation of Sect. 2 as a component-model in the meso-scale approach proposed in the M-CZM formulation [41], based on the introduction of a microstructured geometry of the interface, in the form of a Representative Multiplane Element (RME). The main features of the M-CZM formulation in 2D are synthesized below in bullet list format:

- The micro-scale geometry is described by a RME (such as the one shown in Fig. 4c), representing a repeating unit made of a finite number N_p of *ideally flat* elementary planes.
- The geometrical irregularities (in short, asperities) are assumed infinitely stiff; accordingly, all the deformation of the interface within the RME is defined by a unique relative-displacement vector $\mathbf{s}$ coincident with the displacement vector on each inclined plane $\mathbf{s}^{(k)}$, i.e. $\mathbf{s}^{(k)} = \mathbf{s}$.
- The interaction within each elementary planes remains governed by the *ideally flat* elementary interface formulation above considered, combining damage-friction, and subjected to restrictions (22). The associated free energy function is denoted by $\Psi^{(k)}$.
- On each elementary plane k the macro-scale relative displacement $\mathbf{s}$ is decomposed into local mode-I and mode-II components depending on the inclination angle θ_k of the microplane, and the corresponding local mode-I and mode-II stress components are computed as determined by $\Psi^{(k)}$.
- The macroscale free energy density Ψ is defined, owing to its extensive character, as the weighted sum of the free energies associated with each microplane $\Psi = \sum_{k=1}^{N_p} \gamma_k \Psi_k$, where $\gamma_k = \frac{A_k}{A_P}$ is the weight coefficient, related to the area fraction

of the k-th microplane, being A_P the overall (projected) area of the RME and A_k the effective area of the k-th microplane.

- Internal variables associated with each k-th plane are the damage variable $D^{(k)}$ and the relevant inelastic slip relative displacement $\mathbf{s}^{di(k)}$ both evolving independently from the inelastic parameters pertaining to the other elementary planes.
- The macro-scale cohesive law, linking the relative displacement vector $\mathbf{s}$ to the interface stress $\boldsymbol{\sigma}$, is determined by resolving the microscale problem for the RME. This law is the one operatively used in finite-element (FE) cohesive zone models at each integration point of interface elements to link the two scales.

An example of 2D RME of trapezoidal shape, with $N_p = 3$, is shown in Figs. 3 and 4d. This RME is also used in all the applications herein presented.

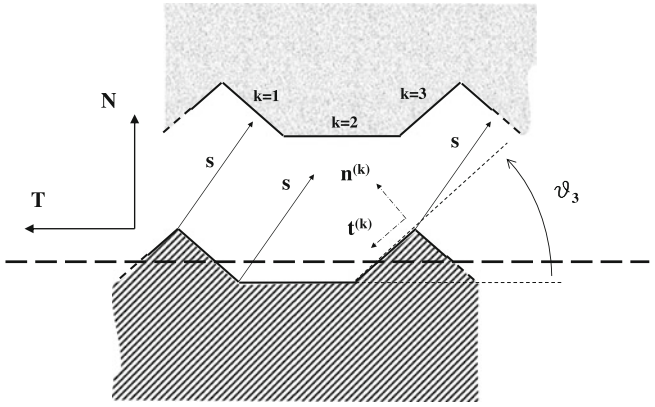

Fig. 3 Trapezoidal representative interface element

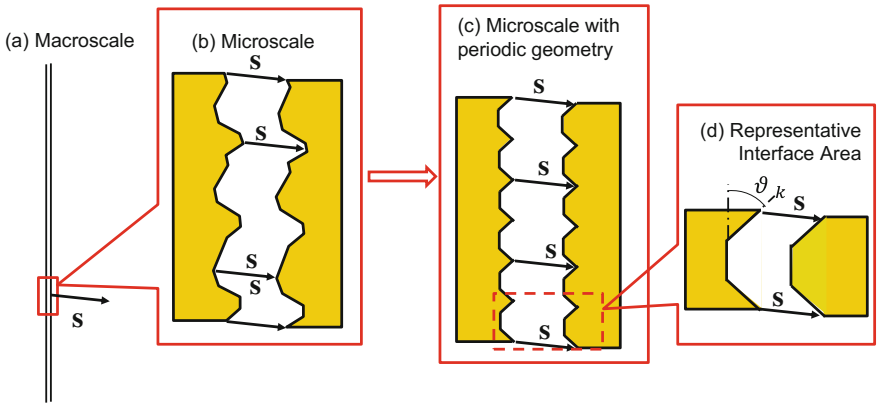

Fig. 4 Multiscale scheme: **a** flat macro-scale geometry; **b** geometry of the asperities accounted for at the micro-scale; **c** micro-scale geometry with simplified periodic pattern; **d** representative interface area (repeating unit)

The macroscopic stress turns out to be expressed as the weighted sum of the contribution of each microplane

$$\boldsymbol{\sigma} = \frac{\partial \Psi}{\partial \mathbf{s}} = \sum_{k=1}^{N_p} \gamma_k \, \boldsymbol{\sigma}_k \qquad \text{where} \qquad \boldsymbol{\sigma}_k = \frac{\partial \Psi_k}{\partial \mathbf{s}}. \tag{23}$$

Distinction is made between global and local reference frames with respective normal and tangential unit vectors ($\mathbf{N}$, $\mathbf{T}$) and ($\mathbf{n}^{(k)}$, $\mathbf{t}^{(k)}$), see Fig. 3. Stress and displacement components in the global frames are denoted by N and T uppercase subscripts while local components are denoted by lowercase n, t subscripts. Accordingly, s_{kn} and s_{kt} denote the relative-displacement components in (local) modes I and II, i.e. the components with respect to the local microplane reference system, while the global components of displacement are indicated by s_N and s_T. Global and local displacement coordinates are related by the rotation matrix $\mathbf{R}_k$:

$$\begin{bmatrix} s_{kn} \\ s_{kt} \end{bmatrix} = \begin{bmatrix} \cos\theta_k & \sin\theta_k \\ -\sin\theta_k & \cos\theta_k \end{bmatrix} \begin{bmatrix} s_N \\ s_T \end{bmatrix} = \mathbf{R}_k \begin{bmatrix} s_N \\ s_T \end{bmatrix} \tag{24}$$

Similarly, for stresses one has the following relation between stress components

$$\begin{bmatrix} \sigma_{kN} \\ \sigma_{kT} \end{bmatrix} = \mathbf{R}_k^t \begin{bmatrix} \sigma_{kn} \\ \sigma_{kt} \end{bmatrix} \tag{25}$$

4.2 Finitely Dilating Model

The above recalled equations constitute a basic version of the M-CZM formulation, which recovers an indefinitely dilating behavior. A response with finite dilation can be also accounted for, by following the strategy proposed in [43]. Therein, interface equilibrium is described considering the current displaced configuration of the interacting elementary planes, by updating the microplane area fraction according to the following relation:

$$\gamma_k = \gamma_{0k} \, \mathscr{A}_g \left(\frac{s_N}{H_N} \right), \tag{26}$$

where γ_{0k} is the initial microplane area fraction, H_N is the height of asperities and $\mathscr{A}_g$ is a function controlling the geometrical contact decay. The analytical expression employed for $\mathscr{A}_g$, inferred on the basis of micromechanical considerations, is:

$$\mathscr{A}_g(x) = \langle 1 - \langle x \rangle \rangle \, . \tag{27}$$

The following regularization of (27) is also alternatively considered

$$\mathscr{A}_g^{(R)}(x) = 1 - \frac{1}{1 + e^{-a(x-\frac{1}{2})}}, \tag{28}$$

with a being a real positive number.

4.3 Modelling of Progressive Interlocking Degradation

Account of degradation of asperities has been included within the M-CZM formulation, and investigated in [43], to capture the decrease of the interlocking effect induced by damage. This effect is addressed by considering the following exponential law for the decrease of the current value θ_k of the inclination angle of microplane k:

$$\theta_k = \left(\theta_{k0} - \theta_{kf}\right) e^{-\frac{\zeta_k}{\zeta_{k0}}} + \theta_{kf}. \tag{29}$$

In (29) ζ_k is the frictional work spent in sliding along the local tangential direction of the k-th plane:

$$\zeta_k = \int_{history} \sigma_{kt}\, ds_{kf}, \tag{30}$$

and ζ_{k0} is a characteristic energy value that controls the degradation rate of asperities, while θ_{k0} is the microplane inclination angle at the beginning of the analysis and θ_{kf} is the angle asymptotically reached in the k-th microplane when $\zeta_k \to \infty$.

5 Numerical Applications of the M-CZM Model

Microstructural computations at the local-point level [2, 41, 43, 44] show that the M-CZM formulation determines, even in purely tangential mode II tests (i.e., with $\sigma_N = 0$), an increase of the energy necessary to produce decohesion compared to pure mode I. This energy is defined in terms of mechanical work spent to produce decohesion as the integral:

$$G_T = \int_0^{+\infty} \boldsymbol{\sigma} \cdot d\mathbf{s}. \tag{31}$$

Figure 5 shows a family of $\sigma_T - s_T$ curves, obtained selecting as RME the 3-planes isosceles trapezoid of Fig. 3 with equal area fractions $\gamma^{(k)} = 1/3$ and employing the basic model (with no finite dilation and no asperity degradation) with the material parameters reported in Table 1.

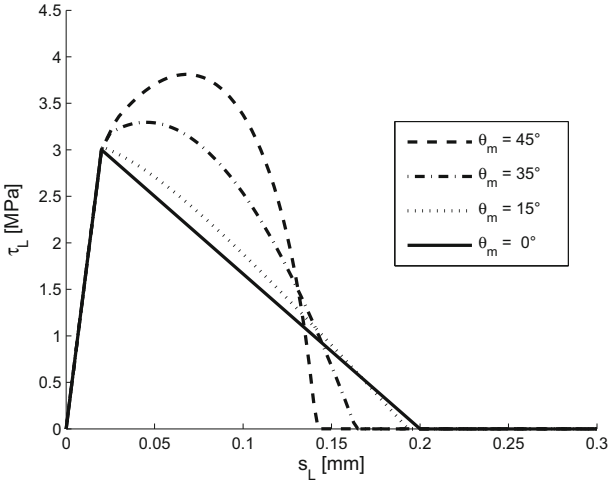

Fig. 5 Tangential stress-slip curves with θ_m spanned in $[0°, 45°]$

Table 1 Interface material parameters employed in the analyses of Fig. 5

σ_0 (MPa)	G_c (kJ/m^2)	η (–)	μ (–)
3.0	0.3	0.9	0.5

The family of curves is generated by spanning the angle of the oblique edge, θ_m, in the interval $[0°, 45°]$ with $\sigma_N = 0$. The figure shows the increase of G_T with the interlocking angle which corresponds to the area underneath the curves. Increase of G_T is detected to be the combined effect of a nonzero friction angle and a nonzero interlocking angle; actually, this increment vanishes when any of friction or interlocking angles are set to zero.

From Fig. 5 it can be also observed that the linear elastic part of the graph is independent of θ_m, and that the tangential stress drops to zero when complete damage is reached, which is a consequence of the enforcement of a zero confining stress, $\sigma_N = 0$.

5.1 Simulations of Pull-Out Test of a Concrete-Anchored Steel Bar

The basic M-CZM formulation has been implemented as a user-defined constitutive law for interface elements in Abaqus [21], version 6.7-1, to perform FE simulations of the pull-out tests on steel anchored bars from a concrete specimen in a triaxial test set-up, reported in [26]. The geometry, loadings and constraints are reported in Fig. 6.

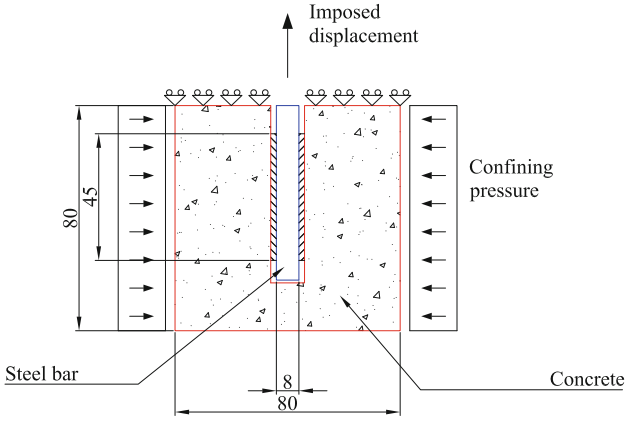

Fig. 6 Geometry, loadings and constraints of the pull-out test

Table 2 Material parameters of the modified Drucker-Prager concrete model

Young Modulus E	30 GPa
Poisson Ratio ν	0.25
Internal Angle of Friction of Concrete φ_{fc}	28°
Dilation Angle of Concrete φ_{dc}	28°
Flow Stress Ratio K	0.8
Uniaxial compressive strength f_c	25 MPa

Steel is modelled as an isotropic linear elastic material with $E = 210{,}000$ MPa and $\nu = 0.2$. For concrete the modified Drucker-Prager plasticity model available in Abaqus is employed adopting the parameters in Table 2. Hardening is defined so as to obtain in uniaxial compression the analytical expression provided in Ref. [23] for ordinary concrete. The parameters of adhesion and friction of the interface model, reported in Table 3, have been calibrated on the basis of the response typically exhibited by a plain bar [46]. The interlocking angle has been set to $\theta_m = 10°$, and calibrated on the basis of the test data reported.

The reader is referred again to [26] for furhter details on the experiments and to [41] to find all data and further details on the constitutive modelling choices and on the employed finite-element model.

Table 3 Material parameters of the interface model used in the bond slip structural simulation

σ_{on} (MPa)	σ_{ot} (MPa)	G_{cn} (kJ/m^2)	G_{ct} (kJ/m^2)	η	μ
3.33	3.33	1.0	1.0	0.99	0.25

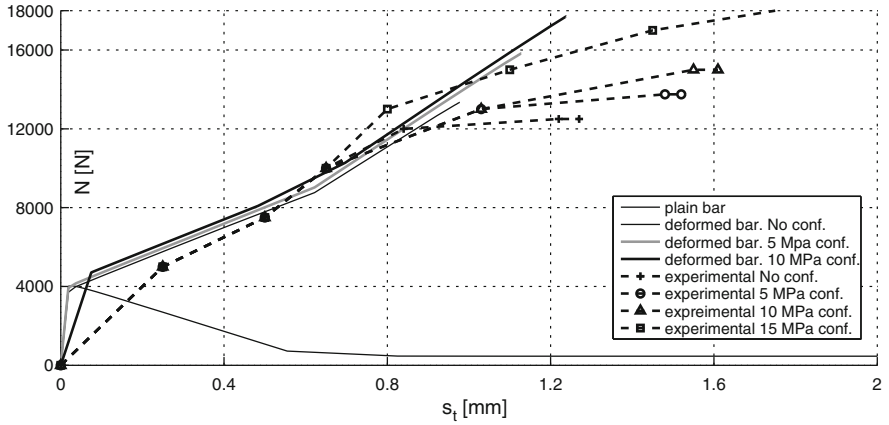

Fig. 7 Pull-out tests: comparison between numerically predicted load-displacement curves at different confining stresses and the experimental results reported in Ref. [26]

A reasonable numerical-experimental agreement is shown by Fig. 7 where the computed load-displacement diagrams are compared with the experimental diagrams reported in [26] for confining pressures of 5 and 10 MPa.

The load-displacement response of the previous set up under cyclic loading paths of variable amplitude is also investigated in [41].

5.2 Simulation of DCB-UBM Tests

The basic M-CZM formulation has been also employed by Serpieri et al. to perform nonlinear dynamic Finite-Element (FE) simulations of the experimental tests reported in [45], consisting of quasi-static delamination of composite beams made of E-glass laminates in a polyester matrix by a Double Cantilever Beam with Uneven Bending Moments (DCB-UBM) [44]. The DCB-UBM test provides mode mixity-dependent experimental measurements of the crack tip fracture growth resistance all through the mode-mixity spectrum. In this set-up, tip bending moments are applied at the free ends of the cantilever by increasing their magnitude while keeping fixed their ratio via a wire and roller arrangement.

The experimental data reported by Sørensen provide a suitable term of comparison to assess the capability of the present interface model in predicting, also at the structural level, the increase in fracture energy under increasing mode II loading.

These experimental measurements, reported in [45] in the form J integral plots against the norm δ of the relative displacement between upper and lower beams at the initial crack tip, are reported by point markers in Fig. 8. A family of plots is obtained associated with several tip-moment ratios $r = M_1/M_2$ enforced by the wire/roller arrangement, with $r = -1$ corresponding to pure mode I delamination, and $r = 1$

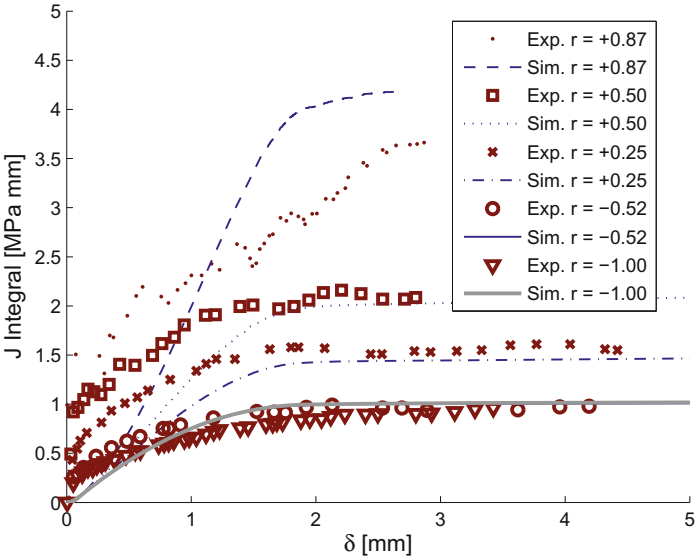

Fig. 8 Numerical-experimental comparison of J-integral fracture resistance plotted versus the norm of relative displacement, obtained under different mode mixity ratios

corresponding to pure mode II delamination. The numerical J-δ responses are plotted in Fig. 8 by solid lines.

The adopted RME is again the one of Fig. 3. Calibration of the interface parameters in the bonded region was performed as follows. For the fracture energy $G_c = G_{cI} = G_{cII}$ the plateau value of the J-δ curve in pure mode I is adopted; σ_o and η are also calibrated based on the pure mode I experimental curves. The remaining parameters μ and θ_m are obtained by curve-fitting the remaining mixed-mode responses. This calibration procedure yields the interface parameters reported in Table 5.

Figure 8 shows that the plateau values for the J-δ curves, corresponding to steady state crack propagation are all well captured, confirming that the model naturally predicts the increase in the steady state values of fracture resistance with increasing mode II component (Table 4).

Table 4 Interface material parameters employed in the DCB-UBM simulations

σ_{on} (MPa)	σ_{ot} (MPa)	G_{cI} (N/mm)	G_{cII} (N/mm)	η (–)	μ (–)	θ_m (deg.)
1.0	1.0	0.97	0.97	0.95	1.0	40°

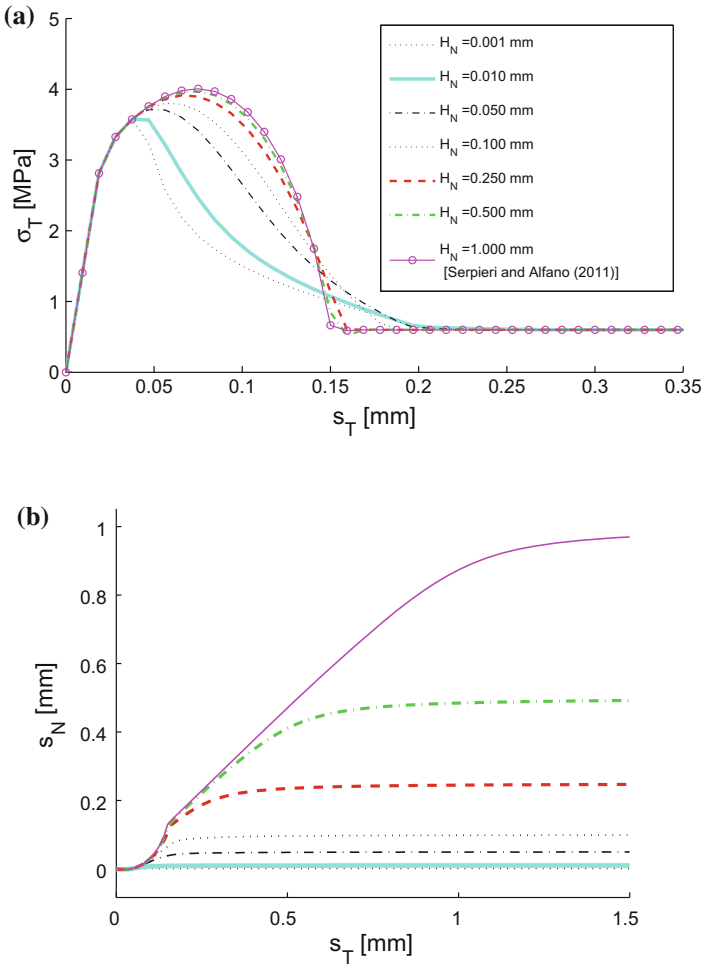

Fig. 9 Response obtained for monotonically increasing slip, constant $\sigma_N = -0.2$ MPa and $\theta_m = 45°$, under different H_N values: **a** shear stress versus slip ($\sigma_T - s_T$); **b** dilation versus slip ($s_N - s_T$). For $\mathscr{A}_g$ expression (27) is used

5.3 *Effects of the Finite Dilatancy*

Figures 9 and 10 illustrate the effect determined when finite dilation is addressed by the treatment of the finite height of interface asperities, described in Sect. 4.2, showing the tangential stress-slip curves and the dilation-slip curves with constant confining stress σ_N when H_N is swept from 1 mm to 0.01 mm. Interface parameters and σ_N are reported in Table 5. The reported value of $\bar{G}_c$ in Table 5 is the overall macroscale fracture energy. This quantity is related to G_c by $A_P \bar{G}_c = \sum_{k=1}^{N_p} A_k G_c$

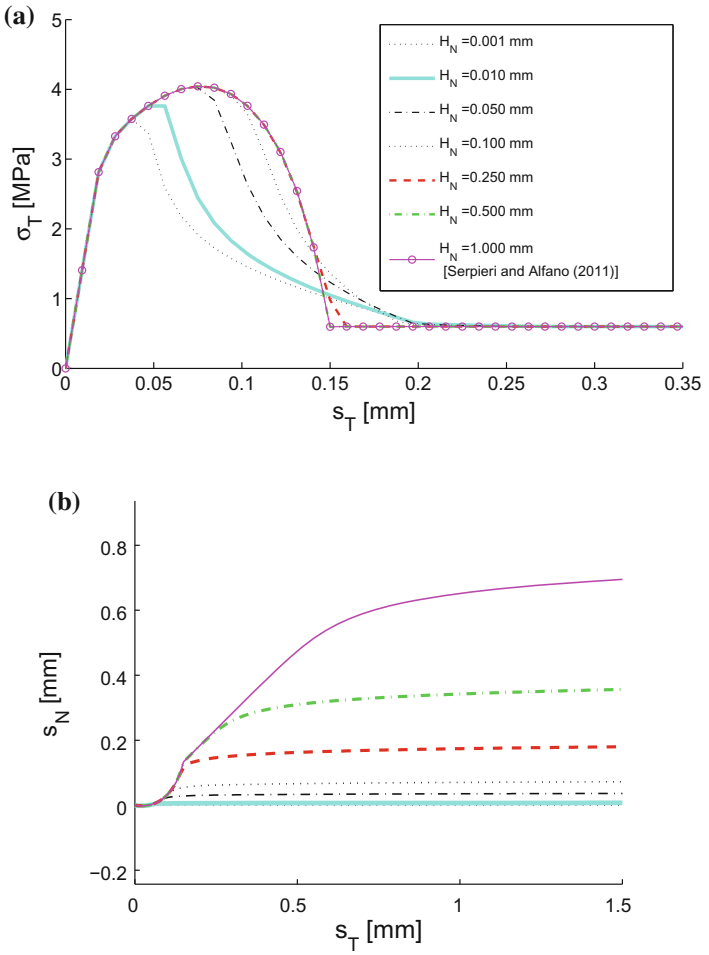

Fig. 10 Response obtained for monotonically increasing slip, constant $\sigma_N = -0.2$ MPa and $\theta_m = 45°$, under different H_N values: **a** shear stress versus slip ($\sigma_T - s_T$); **b** dilation versus slip ($s_N - s_T$). For $\mathscr{A}_g$ the regularized expression (28) is used

Table 5 Material parameters employed in sensitivity analyses to H_N

σ_0 (MPa)	$\bar{G}_c$ (kJ/m^2)	η (–)	μ (–)	θ_m (deg.)	σ_N
3.0	0.3	0.9	0.5	45°	−0.2 MPa

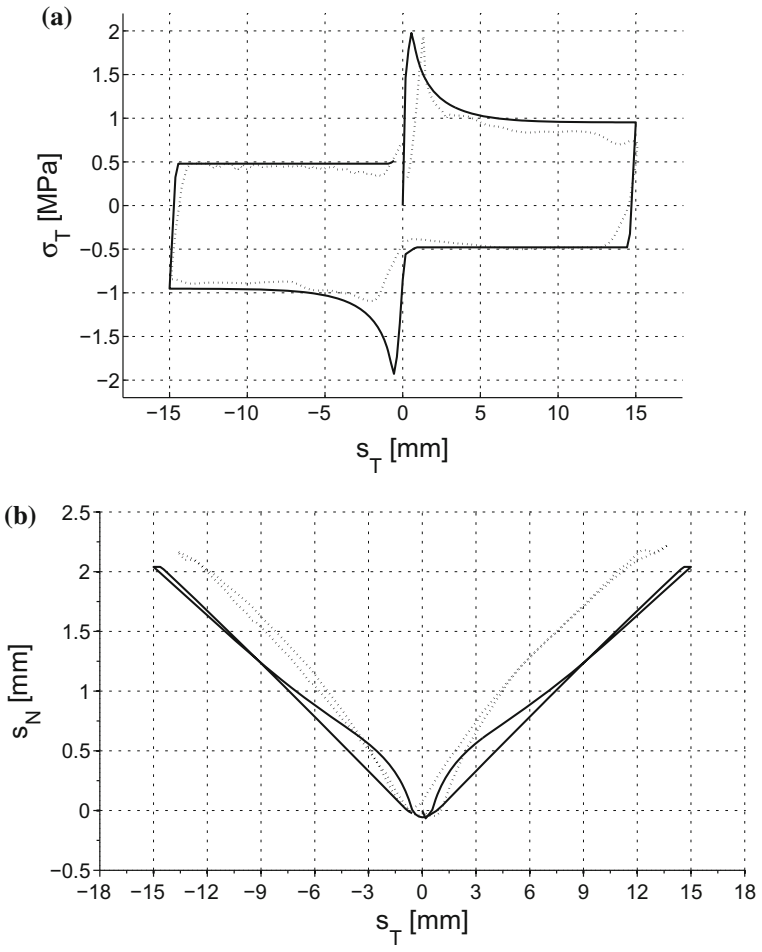

Fig. 11 Experimental (*dotted lines*) and numerical (*solid lines*) shear stress-slip curves (**a**) and dilation-slip curves (**b**) for the rough granite joints tested by Lee et al. [27] during the first loading cycle

where A_k is the area of the k-th elementary plane and A_P is the overall area of the projection of all elementary onto the average surface of the interface.

In particular, the curves of Fig. 9 are obtained adopting for $\mathscr{A}_g$ the expression in (27) while those of Fig. 10 are obtained adopting the regularized expression in (28) for $\mathscr{A}_g$ setting $a = 20$.

Figures 11 and 12 show a numerical-experimental comparison of the tangential stress-slip and dilation-slip curves for the response obtained in the first two cycles of the tests over rough granite joints, reported in [27]. This response is obtained employing the M-CZM formulation combined with the treatment of finite depth of

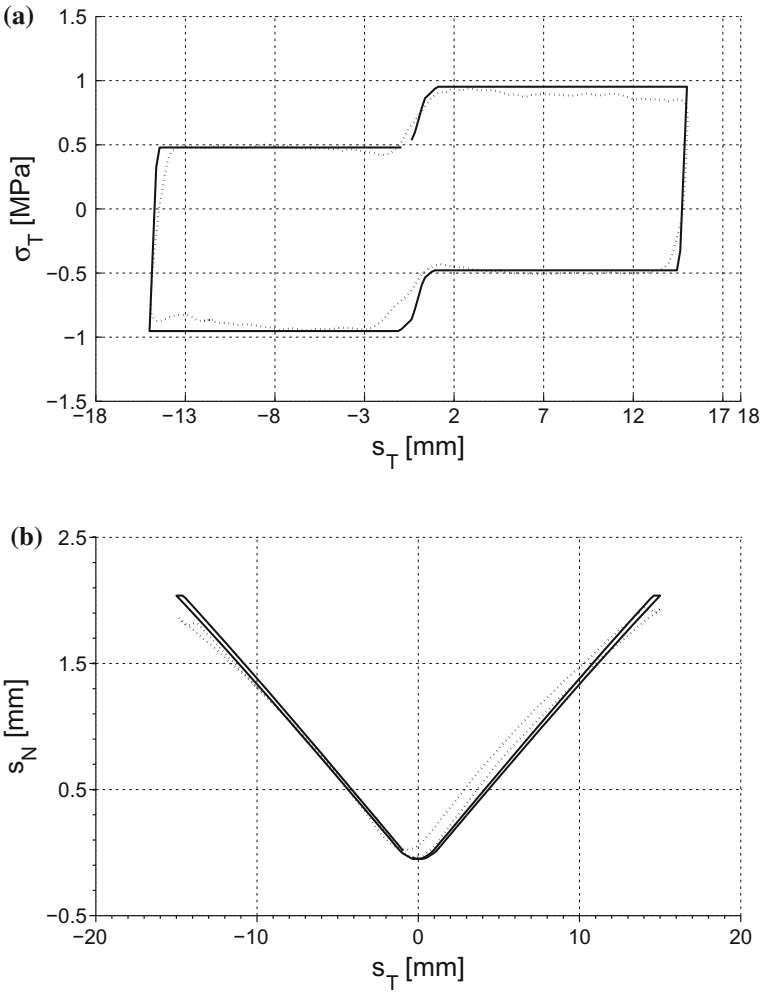

Fig. 12 Experimental (*dotted lines*) and numerical (*solid lines*) shear stress-slip curves (**a**) and dilation-slip curves (**b**) for the rough granite joints tested by Lee et al. [27] during the second loading cycle

asperities and asperity degradation described in Sects. 4.2 and 4.3. The reader is referred to [43] to find all details concerning the calibration procedure adopted to set the material parameters of the M-CZM formulation employed in these analyses.

6 Conclusions

The multiplane cohesive-zone approach for modelling structural interfaces combining damage, unilateral contact, friction, interlocking and dilatancy, developed by the authors over the last decade, has been surveyed.

The basic ideas underlying the M-CZM approach were recalled. The model proceeds by a multiscale analysis considering a microstructured multiplane representative interface area (RME); the RME is characterized by a geometry obtained by assembling a set of elementary planes and each plane is endowed itself with a microstructure. In particular, on each elementary plane the total area is split into a undamaged and a damaged part, the latter accounting for the presence of microcracks. The proposed approach presents several important advantages for structural interface modelling essentially deriving from the adoption of a framework within the thermomechanics of generalized continua and from the use of variables all having well defined physical meaning and microstructural interpretation.

The response of the interface is deduced by following a homogenization procedure, which allows coupling of all linear and nonlinear effects (damage, unilateral contact, friction, interlocking) in a rational and systematic manner. The possibility to treat separately each nonlinear effect in the response of the interface permits a quite viable and reliable way to deduce the values of the material parameters proceeding from standard laboratory tests.

Further desirable features of M-CZM are the following:

- the RME geometry represents the true irregularity of the detachment surfaces arising for fractured cohesive materials;
- the RME is characterized by a number of damage variables depending on the number of elementary planes, each having the physical meaning of the fraction of microcracks present on the relevant space orientation;
- dilatancy and interlocking are solely governed by the inclination the planes, (and from the finite height of asperities when finite dilation is taken into account);
- damage and friction laws for each microplane are uncoupled and can be treated separately, i.e. the evolution laws of damage and friction can be changed independently;
- in each plane the constitutive laws of the undamaged and the damaged parts are also conveniently introduced in separate form;
- other effects like viscoelasticity or viscoplasticty can be introduced in a flexible way into the model by suitably changing the constitutive response of the elementary planes.

Computations developed for the determination of the constitutive response at the single interface point elucidate that interlocking plays a fundamental role in the determination of the total dissipated energy for loading histories involving shear failure. In fact, even for a loading history characterized by zero compressive stress on the interface, the mixed-mode fracture energy depends not only on the pure rupture energy G_c but also from the inclination of the elementary planes.

Numerical applications have been developed to assess the ability of the interface model to correctly reproduce at a structural level several basic interface failure mechanism (pull-out, mixed-mode delamination). In particular, structural simulations of the mixed mode delamination in laminated composite DCB-UBM experiments have shown that the interface model is able to correctly predict the increase of fracture energy when the mode II/mode I ratio increases. The capability of the M-CZM formulation to describe the interaction between steel bars and concrete has been also shown.

The application of the M-CZM approach combined with the possibility of capturing finite dilation and asperity degradation has been also shown, taken from more recent literature, showing a satisfactory predictive capability in the simulation of the mechanical response of rough rock joints.

References

1. Theme ICOLD, A2—imminent failure flood for a concrete gravity dam, (1999) 5th International Benchmark Workshop on Numerical Analysis of Dams. Denver, ICOLD
2. Albarella M, Serpieri R, Alfano G, Sacco E (2015) A 3d multiscale cohesive zone model for quasi-brittle materials accounting for friction, damage and interlocking. Eur J Comput Mech 24(4):144–170
3. Alfano G (2006) On the influence of the shape of the interface law on the application of cohesive-zone models. Compos Sci Technol 66(6):723–730
4. Alfano G, Crisfield MA (2001) Finite element interface models for the delamination analysis of laminated composites: mechanical and computational issues. Int J Numer Methods Eng 50(7):1701–1736
5. Alfano G, Crisfield MA (2003) Solution strategies for the delamination analysis based on a combination of local-control arc length and line searches. Int J Numer Methods Eng 58(7):999–1048
6. Alfano G, Sacco E (2006) Combining interface damage and friction in a cohesive-zone model. Int J Numer Methods Eng 68(5):542–582
7. Alfano G, Marfia S, Sacco E (2006) A cohesive damage-friction interface model accounting for water pressure on crack propagation. Comput Methods Appl Mech Eng 196(1–3):192–209
8. Areias PMA, Belytschko T (2005) Non-linear analysis of shells with arbitrary evolving cracks using XFEM. Int J Numer Methods Eng 62(3):384–415
9. Aubertin P, Rethore J, de Borst R (2010) A coupled molecular dynamics and extended finite element method for dynamic crack propagation. Int J Numer Methods Eng 81(1):7–88
10. Barbieri E, Petrinic N (2014) Three-dimensional crack propagation with distance-based discontinuous kernels in meshfree methods. Comput Mech 53(2):325–342
11. Barenblatt GI (1962) Mathematical theory of equilibrium cracks in brittle fracture. Adv Appl Mech 7(55):55–129
12. Bechel VT, Sottos NR (1998) Application of debond length measurements to examine the mechanics of fiber pushout. J Mech Phys Solids 46(9):1675–1697
13. Camanho PP, Davila CG, de Moura MF (2003) Numerical simulation of mixed-mode progressive delamination in composite materials. J Compos Mater 37:1415–1438
14. Campilho MD, Banea Neto, J.A.B.P., da Silva, L.F.M. (2013) Modelling adhesive joints with cohesive zone models: effect of the cohesive law shape of the adhesive layer. Int J Adhes Adhes 44:48–56
15. Chandra N, Li H, Shet C, Ghonem H (2002) Some issues in the application of cohesive zone models for metal-ceramic interfaces. Int J Solids Struct 39(10):2827–2855

16. Crisfield MA, Alfano G (2002) Adaptive hierarchical enrichment for delamination fracture using a decohesive zone model. Int J Numer Methods Eng 54(9):1369–1390
17. Del Piero G, Raous M (2010) A unified model for adhesive interfaces with damage, viscosity, and friction. Eur J Mech-A/Solids 29(4):496–507
18. Dugdale DS (1960) Yielding of steel sheets containing slits. J Mech Phys Solids 8:100–104
19. Germain P (1973). Cours de mcanique des milieux continus, vol 1. Masson
20. Griffith AA (1920) The phenomena of rupture and flow in solids. Philos Trans R Soc A221:16–198
21. Hibbitt Karlsson, Sorensen, (1977) ABAQUS: theory manual. Hibbitt, Karlsson and Sorensen
22. Hilleborg A, Moder M, Petersson PE (1976) Analysis of crack formation and crack growth in concrete by means of fracture mechanics and finite elements. Cem Concrete Res 6:773–782
23. Kent DC, Park R (1971) Flexural members with confined concrete. J Struct Div 97(7):1969–1990
24. Kulkarni MG, Geubelle PH, Matous K (2009) Multi-scale modeling of heterogeneous adhesives: Effect of particle decohesion. Mech Mater 41(5):573–583
25. La Borderie C, Pijaudier-Cabot G (1992) Influence of the state of the stress in concrete on the behavior of steel concrete interface. In: Bazant ZP (ed) Fracture Mechanics of Concrete Structures. Breckenridge, USA, pp 830–835
26. La Borderie C, Pijaudier-Cabot G (1992) Influence of the state of the stress in concrete on the behaviour of steel concrete interface. Concrete fracture mechanics of structures, Colorado, USA
27. Lee HS, Park YJ, Cho TF, You KH (2001) Influence of asperity degradation on the mechanical behavior of rough rock joints under cyclic shear loading. Int J Rock Mech Min Sci 38(7):967–980
28. Lin G, Geubelle PH, Sottos NR (2001) Simulation of fiber debonding with friction in a model composite pushout test. Int J Solids Struct 38(46–47):8547–8562
29. Loureno PB (1996) Computational strategies for masonry structures. Delft University Press, PhD Dissertation
30. Mi Y, Crisfield MA, Davies GAO, Hellweg HB (1998) Progressive delamination using interface elements. J Compos Mater 32(14):1246–1272
31. Nguyen VP, Lloberas-Valls O, Stroeven M, Sluys LJ (2011) Homogenization-based multiscale crack modelling: from micro-diffusive damage to macro-cracks. Comput Methods Appl Mech Eng 200(9–12):1220–1236
32. Nguyen VP, Kerfriden P, Bordas SPA (2014) Three-dimensional crack propagation with distance-based discontinuous kernels in meshfree methods. Composites: part B -. Engineering 60:193–212
33. Park K, Paulino GH (2011) Cohesive zone models: a critical review of traction-separation relationships across fracture surfaces. Appl Mech Rev 64:060802
34. Parrinello F, Marannano G, Borino G (2016) A thermodynamically consistent cohesive-frictional interface model for mixed mode delamination. Eng Fract Mech 153:61–79
35. Rabczuk T, Areias PMA, Belytschko T (2007) A simplified mesh-free method for shear bands with cohesive surfaces. Int J Numer Methods Eng 69(5):993–1021
36. Raous M, Cangmi L, Cocu M (1999) A consistent model coupling adhesion, friction, and unilateral contact. Comput Methods Appl Mech Eng 177:383–399
37. Rockafellar RT (2015) Convex analysis. Princeton University Press
38. Sacco E, Toti J (2010) Interface elements for the analysis of masonry structures. Int J Comput Methods Eng Sci Mech 11:354–373
39. Samimi M, van Dommelen JAW, Geers MGD (2009) An enriched cohesive zone model for delamination in brittle interfaces. Int J Numer Method Eng 80(5):609–630
40. Samimi M, van Dommelen JAW, Geers MGD (2011) A three-dimensional self-adaptive cohesive zone model for interfacial delamination. Comput Methods Appl Mech Eng 200(49–52):3540–3553
41. Serpieri R, Alfano G (2011) Bond-slip analysis via a thermodynamically consistent interface model combining interlocking, damage and friction. Int J Numer Methods Eng 85(2):164–186

42. Serpieri R, Varricchio L, Sacco E, Alfano G (2014) Bond-slip analysis via cohesive-zone model simulating damage, friction and interlocking. Fract Struct Integrity 29:284–292
43. Serpieri R, Alfano G, Sacco E (2015) A mixed-mode cohesive-zone model accounting for finite dilation and asperity degradation. Int J Solids Struct 67–68:102–115
44. Serpieri R, Sacco E, Alfano G (2015) A thermodynamically consistent derivation of a frictional-damage cohesive-zone model with different mode I and mode II fracture energies. Eur J Mech—A/Solids 49:13–25
45. Sørensen BF, Jacobsen TK (2009) Characterizing delamination of fibre composites by mixed mode cohesive laws. Compos Sci Technol 69(3):445–456
46. Tassios TP (1979) Properties of bond between concrete and steel under load cycles idealizing seismic actions. Bulletin dinformation du CEB 131:65–122
47. Valoroso N, Champaney L (2006) A damage-mechanis-based approach for modelling decohesion in adhesively bonded joints. Eng Fract Mech 73(18):2774–2801
48. Verhoosel CV, Remmers JJC, Gutierrez MA (2009) A dissipation-based arc-length method for robust simulation of brittle and ductile failure. Int J Numer Methods Eng 77(9):1290–1321
49. Verhoosel CV, Scott MA, de Borst R, Hughes TJR (2011) Three-dimensional crack propagation with distance-based discontinuous kernels in mesh free methods. Int J Numer Methods Eng 87(1–5):336–360
50. Wells GN, Sluys LJ (2001) A new method for modelling cohesive cracks using finite elements. Int J Numer Methods Eng 50(12):2667–2682

On Alternative Approaches for Graded Damage Modelling

Michel Frémond and Claude Stolz

Abstract To prevent problem of spurious localization in damage mechanics, the introduction of a quadratic terms in gradient of damage has been used to govern the amplitude of the spatial gradient of damage. In more recent papers based on definition of Thick-Level-Set, the regularization is obtained considering that damage is function of a level-set, then the gradient of damage is bounded in zone where the level-set becomes a signed distance function. Here we consider classical damage modelling with introduction of an internal constraint on the spatial gradient of damage. This point of view produces a new regularization without the introduction of a level-set and signed distance.

1 Introduction

The classical scenario of degradation of solids under mechanical loading is described generally by the progressive loss of stiffness as a function of a damage parameter.

Regularization can be obtained by means of non-local approaches [18] and more effectively by gradient approach [6, 7, 9, 16, 17]. In the same spirit of gradient damage models are the phase-field models. They are motivated by paper [1] approximating the Mumford-Shah segmentation model [14] by an elliptic functional. Based on this idea, paper [2] proposes a numerical strategy, where the fracture energy is distributed on the whole volume of the body.

M. Frémond (✉)
Dipartimento di Ingegneria Civile e Ingegneria Informatica (DICII), Università degli Studi di Roma "Tor Vergata", via Del Politecnico 1, 00133 Rome, Italy
e-mail: michel.fremond@uniroma2.it

C. Stolz
École Centrale Nantes, GeM UMR CNRS 6183, 1 rue de la Noë, BP 92101, 44321 Nantes, France
e-mail: claude.stolz@ec-nantes.fr

C. Stolz
Université Paris Saclay, IMSIA UMR EDF/CNRS/CEA/ENSTA 9219, 828 bd. des Maréchaux, 91762 Palaiseau, France

M. Frémond et al. (eds.), *Models, Simulation, and Experimental Issues in Structural Mechanics*, Springer Series in Solid and Structural Mechanics 8,
DOI 10.1007/978-3-319-48884-4_4

Recently a new approach has been proposed: it is based on the motion of a moving layer associated with propagation of level-sets. This "Thick-Level-Set" (TLS) model is developed in many papers [11, 12, 15, 19] which present analytical solutions and numerical implementations. The model lies between damage and fracture mechanics. Crack opening is allowed across fully damaged zone.

The main idea of the TLS for quasi-brittle fracture is to bound the spatial gradient of the damage variable d, which evolves from 0 to 1, then the crack is located where $d = 1$. The transition layer has a finite thickness l_c. The level-set $\phi = 0$ separates the domain Ω into an undamaged and a damaged zone, this surface is denoted Γ_o. The damage parameter is an increasing function of the level-set ϕ, considering as a signed distance from the surface Γ_o.

The whole body is decomposed in three parts: the undamaged body Ω_o, the zone of transition Ω_c, the fully damaged body Ω_1. Then the boundary $\partial\Omega_c$ is decomposed into Γ_o and $\Gamma_1 : \partial\Omega = \Gamma_o \cup \Gamma_1$.

- For $M_o^t \in \Gamma_o$, $d(M_o^t) = 0$, $\phi(M_o^t, t) = 0$.
- For $M_1^t \in \Gamma_1$, $d(M_1^t) = 1$, $\phi(M_1^t, t) = l_c$.

In the transition layer Ω_c, the damage d is an explicit function of ϕ:

$$\begin{cases} d(\phi) = 0, & \phi(M,t) \le 0, \quad M \in \Omega_o, \\ d'(\phi) \ge 0, & 0 \le \phi(M,t) \le l_c, \quad M \in \Omega_c, \\ d(\phi) = 1, & \phi(M,t) \ge l_c, \quad M \in \Omega_1, \end{cases} \tag{1}$$

where $d'(\phi)$ is the derivative of d with respect to ϕ. The function d is assumed to be continuous. With this definition, the inverse function $\phi(d)$ exists.

In the original model (TLS) [11], the description of damage is essentially described by the motion of a level-set, which describes the position of the boundary Γ_o. The evolution of the damage is then associated with a moving layer. In a more general model [12], local and non local damage interact, the non-local model is used when an internal constraint is reached:

$$\|\nabla d\| \le f(d). \tag{2}$$

The choice of the function f must be discussed. The last condition is related to the level-set ϕ, indeed this condition is equivalent to

$$\|\nabla\phi\| \le 1, \quad d = d(\phi), \tag{3}$$

then $f(d) = d'(\phi(d))$. When the constraint is satisfied, the level-set ϕ becomes a signed distance and the evolution satisfies

$$\|\nabla\phi\| = 1, \quad \nabla\dot{\phi} \cdot \nabla\phi = 0. \tag{4}$$

We propose to analyse the property of the function f and to formulate the problem of evolution of the body without taking into account the definition of a level set ϕ. This new formulation of graded damage modelling combines classical damage model and the internal constraint in Eq. (2). This point of view is discussed in the general framework of non smooth thermodynamics [4]. Finally, approximation and regularization are proposed to solve numerically the problem of damage evolution.

2 Preliminaries and State Equations

Under external loading the body evolves, the local state is described by the strain ε, the quantity of damage d and the spatial gradient ∇d. The strain is associated to the displacement $\mathbf{u}$

$$2\varepsilon(\mathbf{u}) = \nabla \mathbf{u}^t + \nabla \mathbf{u}. \tag{5}$$

It can be noticed that the gradient ∇d of d is necessary a state quantity because it obeys the internal constraint:

$$\|\nabla d\| \leq f(d). \tag{6}$$

2.1 The Free Energy

The local constitutive behaviour is introduced by the local free energy Ψ, function of the strain ε and of the damage parameter d; at this stage any classical model of damage can be used.

The classical state equations associated to the local free energy Ψ are defined as

$$\sigma = \frac{\partial \Psi}{\partial \varepsilon}, \tag{7}$$

$$Y = -\frac{\partial \Psi}{\partial d}. \tag{8}$$

The local stress σ is associated with the equilibrium when no viscosity occurs and the driving force Y is the local energy release rate associated with d.

A Typical Example

In [12], the free energy has the form

$$\Psi(\varepsilon, d) = \frac{1}{2}\varepsilon : \mathbb{C}(d) : \varepsilon, \quad \text{with} \quad \mathbb{C} = (1-d)\mathbb{C}_1 + d\mathbb{C}_2. \tag{9}$$

The undamaged material with elastic moduli $\mathbb{C}_1$ is transformed to partially damaged material with lower stiffness $\mathbb{C}_2$. For fixed strain, the value of the strain energy decreases with d.

2.2 The Pseudo-potential of Dissipation

The evolution of the damage parameter is governed by a normality rule, we assume the existence of a pseudo-potential of dissipation, i.e., convex function $\mathscr{D}(\dot{d}^*)$ [13], satisfying $\mathscr{D}(\dot{d}^*) \geq 0$ and $\mathscr{D}(0) = 0$. It gives the driven force Y

$$Y \in \partial \mathscr{D}(\dot{d}), \tag{10}$$

where $\partial \mathscr{D}(\dot{d})$ is the sub-differential set of $\mathscr{D}$ at state $\dot{d}$, defined by the inequality

$$\forall \dot{d}^*,\ \mathscr{D}(\dot{d}) + Y \cdot (\dot{d} - \dot{d}^*) \leq \mathscr{D}(\dot{d}^*). \tag{11}$$

If $\mathscr{D}$ is differentiable then $Y = \dfrac{\partial \mathscr{D}}{\partial \dot{d}}(\dot{d})$.

Due to convexity of $\mathscr{D}$ the dual formulation is

$$\dot{d} \in \partial \mathscr{D}^*(Y), \tag{12}$$

with

$$\mathscr{D}^*(Y) = \sup_{d^*} \{Y d^* - \mathscr{D}(d^*)\}. \tag{13}$$

Some Examples
For example, consider a power law

$$\mathscr{D}(\dot{d}) = \begin{cases} \eta \dfrac{n+1}{n} (\dot{d})^{\frac{n+1}{n}} + Y_c \dot{d}, & \text{if } \dot{d} \geq 0, \\ +\infty, & \text{otherwise,} \end{cases} \tag{14}$$

with $Y \in \partial \mathscr{D}(\dot{d})$ where $\partial \mathscr{D}$ satisfies

$$\partial \mathscr{D}(\dot{d}) = \begin{cases} Y_c + \eta (\dot{d})^{1/n}, & \text{if } \dot{d} \geq 0, \\ Y_c + \Re^-, & \text{otherwise,} \end{cases} \tag{15}$$

where $\Re^-$ is the set of the non positive numbers.

The relationships (8) or (11) give a kinetic relationship which determines the evolution of the damage, the behaviour is time dependent. They are equivalent to the dual relationship

$$\dot{d} = \frac{\partial \mathscr{D}^*}{\partial Y}, \quad \text{with} \quad \mathscr{D}^*(Y) = \frac{\eta}{n+1}\left(\frac{1}{\eta}\left|Y - Y_c\right|_+\right)^{n+1}, \tag{16}$$

where $\left|x\right|_+ = (x + |x|)/2$.

For a non-smooth function as

$$\mathscr{D}(\dot{d}) = \begin{cases} Y_c \dot{d}, & \text{if } \dot{d} \geq 0, \\ \infty, & \text{otherwise,} \end{cases} \tag{17}$$

we obtain the property

$$Y \leq Y_c, \quad \dot{d} \geq 0, \quad (Y - Y_c)\dot{d} = 0. \tag{18}$$

In this case, the behaviour is time independent. Introducing the convex set $\mathscr{C}_Y = \{Y : Y - Y_c \leq 0\}$, relationship (18) is rewritten as

$$\dot{d} \in \partial I_{\mathscr{C}_Y}(Y), \tag{19}$$

where $I_{\mathscr{C}_Y}$ is the indicator function of convex set $\mathscr{C}_Y$

$$I_{\mathscr{C}_Y}(Y) = \begin{cases} 0, & \text{if } Y \in \mathscr{C}_Y, \\ +\infty, & \text{otherwise.} \end{cases} \tag{20}$$

2.3 The Internal Constraints

The damage variable is submitted to two constraints:

- due to its definition damage d datifies $0 \leq d \leq 1$, or

$$g_1(d) = d(d-1) \leq 0, \tag{21}$$

- the limitation on the gradient:

$$g_2(d, \nabla d) = -f(d) + \|\nabla d\| \leq 0. \tag{22}$$

To take into account these constraints we may use Lagrange's multipliers or convex analysis introducing indicator functions.

The Lagrange Point of View
Consider a convex function $g(d, \nabla d)$ and the rule

$$\lambda \geq 0, \quad g(d, \nabla d) \leq 0, \quad \lambda g(d, \nabla d) = 0. \tag{23}$$

This rule defines an unilateral constraint.

When $g < 0$, then $\lambda = 0$. On the boundary of the convex set $\mathscr{C}_g = \{(d, \nabla d) | g(d, \nabla d) \leq 0\}$ we have $g(d, \nabla d) = 0$, and reaction $\mathbf{R}$ is defined as:

$$\mathbf{R} = \begin{pmatrix} R \\ \mathbf{H} \end{pmatrix} = \lambda \begin{pmatrix} \dfrac{\partial g}{\partial d} \\ \dfrac{\partial g}{\partial \nabla d} \end{pmatrix}. \tag{24}$$

The reaction is normal to the convex set, then $\mathbf{R} \in \partial I_{\mathscr{C}_g}$, where $I_{\mathscr{C}_g}$ is the indicator function of the convex set $\mathscr{C}_g$. We apply this definition to the two constraints.

- Consider function $g_1(d)$. Introducing $\lambda_1 \geq 0$ the multiplier for the constraint $0 \leq d \leq 1$. Then reaction $R_1 = -\lambda_1 \leq 0$ for $d = 0$ and $R_1 = \lambda_1 \geq 0$ for $d = 1$. So $R_1 \in \partial I_{\mathscr{C}_1}$ where
$$\mathscr{C}_1 = \{d | g_1(d) \leq 0\}. \tag{25}$$

- For the second constraint, we must first determine the property of the function $f(d)$ for which
$$\mathscr{C}_2 = \{(d, \nabla d) | g_2(d, \nabla d) = \|\nabla d\| - f(d) \leq 0\} \tag{26}$$
is a convex set in the space spanned by $(d, \nabla d)$.

Theorem 1 *If function f is concave and if there exists d_0 such that $f(d_0) \geq 0$, then set $\mathscr{C}_2$ is non empty and convex.*

Proof Element $(d_0, 0) \in \mathscr{C}_2$, thus $\mathscr{C}_2$ is not empty. Let two elements $(d, \nabla d) \in \mathscr{C}_2$ and $(\bar{d}, \nabla \bar{d}) \in \mathscr{C}_2$ and scalar $\theta \in]0, 1[$. We have

$$\begin{aligned} \left\| \nabla(\theta d + (1-\theta)\bar{d}) \right\| &= \left\| \theta \nabla d + (1-\theta)\nabla \bar{d}) \right\| \\ &\leq \theta \|\nabla d\| + (1-\theta) \left\| \nabla \bar{d} \right\|, \end{aligned}$$

and

$$\theta \|\nabla d\| + (1-\theta) \left\| \nabla \bar{d} \right\| \leq \theta f(d) + (1-\theta) f(\bar{d}),$$

because $(d, \nabla d)$ and $(\bar{d}, \nabla \bar{d})$ are elements of $\mathscr{C}_2$. Because f is concave we have

$$\theta f(d) + (1-\theta) f(\bar{d}) \leq f(\theta d + (1-\theta)\bar{d}).$$

It results

$$\left\|\nabla(\theta d + (1-\theta)\bar{d})\right\| \leq f(\theta d + (1-\theta)\bar{d}),$$

and therefore

$$(\theta d + (1-\theta)\bar{d}) \in \mathscr{C}_2.$$

Thus set $\mathscr{C}_2$ is convex.

Then $\mathbf{R} \in \partial I_{\mathscr{C}_2}$, where $\mathscr{C}_2 = \{(d, \nabla d) | \, \|\nabla d\| - f(d) \leq 0\}$ and

$$\mathbf{R} = \begin{pmatrix} R \\ \mathbf{H} \end{pmatrix} = \lambda_2 \begin{pmatrix} -\dfrac{\mathrm{d}f}{\mathrm{d}d} \\ \dfrac{\nabla d}{\|\nabla d\|} \end{pmatrix}. \tag{27}$$

where λ_2 satisfies

$$\begin{aligned} &\lambda_2 \geq 0, \ \text{if} \ \ \|\nabla d\| - f(d) = 0, \\ &\lambda_2 = 0, \ \text{if} \ \ \|\nabla d\| - f(d) < 0. \end{aligned} \tag{28}$$

It can be noticed that functions f introduced in [12] are concave. This property is important for the theory and the applications.

The Indicator Function Point of View

The constraints (21) and (22) are taken into account by indicator functions, $I_{\mathscr{C}_1}(d)$ and $I_{\mathscr{C}_2}(d, \nabla d)$ of convex sets $\mathscr{C}_1$ and $\mathscr{C}_2$. The reactions are determined by sub-differential sets $\partial(I_{\mathscr{C}_1} + I_{\mathscr{C}_2})$. We have

Theorem 2 *If function f is concave and if $f(d_o)$ is continuous at point d_o with $f(d_o) > 0$, then*

$$\begin{aligned} \partial(I_{\mathscr{C}_1} + I_{\mathscr{C}_2})(d, \nabla d) &= \partial I_{\mathscr{C}_1}(d, \nabla d) + (\partial(I_{\mathscr{C}_2}(d)), 0) \\ &= \begin{pmatrix} \partial I_{\mathscr{C}_1}(d) \\ 0 \end{pmatrix} + \partial I_-\big(\|\nabla d\| - f(d)\big) \begin{pmatrix} -\dfrac{\mathrm{d}f}{\mathrm{d}d}(d) \\ \dfrac{\nabla d}{\|\nabla d\|} \end{pmatrix}, \end{aligned}$$

where ∂I_- is the sub-differential set of $\Re^-$, the set of the non-positive numbers

$$\partial I_-(x) = \begin{cases} 0, & \text{if } \ x < 0, \\ \Re^+, & \text{if } \ x = 0, \\ \emptyset, & \text{if } \ x > 0. \end{cases} \tag{29}$$

Proof Sub-differential set $\partial(I_{\mathscr{C}_1} + I_{\mathscr{C}_2})(d, \|\nabla d\|)$ of the sum $I_{\mathscr{C}_1} + I_{\mathscr{C}_2}$ is the sum of sub-differential sets $\partial I_{\mathscr{C}_2}(d, \nabla d)$ and $(\partial I_{\mathscr{C}_1}(d), 0)$, because set $\mathscr{C}_2$ contains a ball with center $(d_0, \nabla d_0)$ with $\|\nabla d_0\| - f(d_0) < 0$, see [13].

Note that all functions f introduced in [12] satisfy the assumptions of the theorems. It results the reactions, elements of the sub-differential sets are easily computed.

Remark 1 For the internal constraint, the condition $\lambda_i g_i = 0$ implies that reaction $\mathbf{R}_i$ does not work. In other words, we can introduce a potential energy $\Psi_l = \sum_{i=1}^{2} \lambda_i g_i$ for the constraint $\lambda_i \geq 0$.

3 Equilibrium Problem

The external boundary $\partial\Omega$ is decomposed into two complementary parts, $\partial\Omega_u$ where the displacement is imposed ($\mathbf{u}(M, t) = \mathbf{u}^d(t),\ M \in \partial\Omega_u$) and $\partial\Omega_T$ where the traction T^d is prescribed. The unknowns of the problem are displacement $\mathbf{u}$, damage d and reaction $\mathbf{R}$.

To obtain the equations of motion, it is useful to introduce the potential energy:

$$\mathscr{E}(\mathbf{u}, d, \lambda_1, \lambda_2) = \int_\Omega \Psi(\varepsilon, d)\ \mathrm{d}\Omega - \int_{\partial\Omega_T} T^d.\mathbf{u}\ \mathrm{d}S + \int_\Omega \sum_i \lambda_i g_i\ \mathrm{d}\Omega.$$

Displacement $\mathbf{u}$ is admissible with the boundary conditions ($\mathbf{u} = \mathbf{u}^d$, over $\partial\Omega_u$) and Lagrange multipliers λ_i are positive scalars.

Variations with Respect to Displacement
For a given distribution of d at an equilibrium state, the potential energy is minimum on the set of admissible displacement $\mathcal{K}$

$$\mathcal{K} = \{\mathbf{u} \mid \mathbf{u} = \mathbf{u}^d,\ \text{over } \partial\Omega_u\}$$

$$\frac{\partial \mathscr{E}}{\partial \mathbf{u}}.\delta\mathbf{u} = 0, \quad \forall \delta\mathbf{u} \in \{\mathbf{v} | \mathbf{v}(x) = 0, x \in \partial\Omega_u\}. \tag{30}$$

The variations imply

$$0 = \mathrm{div}\sigma, \quad \text{over } \Omega, \quad \mathbf{n}.\sigma = T^d, \ \text{over } \partial\Omega_T. \tag{31}$$

Variations with Respect to Multipliers
The variations with respect to the multipliers give the conditions

$$\frac{\partial \mathscr{E}}{\partial \lambda_1} \cdot \delta\lambda_1 = \int_\Omega d(d-1)\delta\lambda_1 \, \mathrm{d}\Omega = 0. \tag{32}$$

$$\frac{\partial \mathscr{E}}{\partial \lambda_2} \cdot \delta\lambda_2 = -\int_\Omega (f(d) - \|\nabla d\|)\delta\lambda_2 \, \mathrm{d}\Omega = 0. \tag{33}$$

For a given distribution of d which is compatible with ($g_i \leq 0;\ i = 1, 2$) everywhere, the volume Ω is decomposed into three domains $\Omega = \Omega_o \cup \Omega_c \cup \Omega_1$.

- On Ω_o and Ω_1, λ_i takes any value, the variations (Eqs. 32 and 33) imply $g_1 = 0$ and $g_2 = 0$.
- On Ω_c, $\lambda_1 = 0$, then the relationship (32) is also satisfied. This part is decomposed in Ω_c^- where $g_2 < 0$ and Ω_c^o where $g_2 = 0$.
  - On Ω_c^-, $g_2 < 0$ then $\lambda_2 = 0$.
  - On Ω_c^o, $\delta\lambda_2$ takes any value then $g_2 = 0$.

Variations with respect to damage
Consider now the variations with respect to d:

$$\frac{\partial \mathscr{E}}{\partial d} \cdot \delta d = \int_\Omega \frac{\partial \Psi}{\partial d} \cdot \delta d \, \mathrm{d}\Omega + \int_\Omega \lambda_1(2d-1)\delta d \, \mathrm{d}\Omega \tag{34}$$

$$- \int_\Omega \lambda_2 (f'\delta d - \nabla d \cdot \frac{\nabla \delta d}{\|\nabla d\|}) \, \mathrm{d}\Omega \tag{35}$$

$$= -\int_\Omega G \cdot \delta d \, \mathrm{d}\Omega + \int_S \left[\lambda_2 \frac{\nabla d}{\|\nabla d\|}\right]_S \cdot \mathbf{n} \, \delta d \, \mathrm{d}S. \tag{36}$$

These variations contains two terms: a volume term and a surface contribution. The volume term is associated to driving force G.

$$G = -\frac{\partial \hat{\Psi}}{\partial d} + \lambda_2 f' + \mathrm{div}(\lambda_2 \frac{\nabla d}{\|\nabla d\|}) - \lambda_1(2d-1). \tag{37}$$

This relationship is a partial differential equation only in domain Ωo_c where $\lambda_2 \neq 0$, elsewhere it is an algebraic equation.

The surface term shows potential discontinuities of ∇d along surface S where d is continuous, then we obtain:

$$\left[\lambda_2 \frac{\nabla d}{\|\nabla d\|}\right]_S \cdot \mathbf{n} = 0. \tag{38}$$

Similarly, on the external boundary, without external forces:

$$\lambda_2 \nabla d \cdot \mathbf{n} = 0, \ \text{over } \partial\Omega. \tag{39}$$

On the external boundary, the normal derivative of the damage is not necessary null. It is the case, when $\partial\Omega \cap \partial\Omega_c^o \neq$, for which $\lambda_2 = 0$ and $\|\nabla d\| = f(d) \neq 0$.

Due to the pseudo-potential of dissipation, we have

$$G \in \partial\mathscr{D}(\dot{d}), \tag{40}$$

then a state of equilibrium satisfies, $\dot{d} = 0$ and

$$G \in \partial\mathscr{D}(0). \tag{41}$$

4 The Evolution of Damage *d*

The evolution of damage satisfies:

- a kinetic equation *if $\mathscr{D}$ is smooth*:

$$-G + \frac{\partial\mathscr{D}}{\partial\dot{d}}(\dot{d}) = 0. \tag{42}$$

- the classical normality rule *if $\mathscr{D}$ is not smooth*:

$$-G + \partial\mathscr{D}(\dot{d}) \ni 0. \tag{43}$$

For the pseudo-potential defined in Eq. (17) the equation is

$$G - Y_c \leq 0, \quad \dot{d} \geq 0, \quad (G - Y_c)\dot{d} = 0. \tag{44}$$

Non-smooth mechanics

Introducing the formalism used in [4] and the constraint free energy $\hat{\Psi}(\varepsilon, d, \nabla d)$ defined as

$$\hat{\Psi}(\varepsilon, d, \nabla d) = \Psi(\varepsilon, d) + I_{\mathscr{C}_1}(d) + I_{\mathscr{C}_2}(d, \nabla d). \tag{45}$$

We recover the relationship of the constrained constitutive behaviour:

$$(\sigma, B, \mathbf{H}) \in \frac{\partial\Psi}{\partial\varepsilon} + \partial I_{\mathscr{C}_1}(d) + \partial I_{\mathscr{C}_2}(d, \nabla d) + \partial\mathscr{D}(\dot{d}). \tag{46}$$

which corresponds to

$$\sigma = \frac{\partial\Psi}{\partial\varepsilon}(\varepsilon, d), \tag{47}$$

$$B \in -Y(\varepsilon, d) + \partial I_{\mathscr{C}_1}(d) + R + \partial\mathscr{D}(\dot{d}), \tag{48}$$

$$\mathbf{R} = \begin{pmatrix} R \\ \mathbf{H} \end{pmatrix} \in \partial I_{\mathscr{C}_2}(d, \nabla d). \tag{49}$$

It can be noticed the equivalence between the relationships

$$-B + \mathrm{div}\mathbf{H} = 0 \Longleftrightarrow G \in \partial\mathscr{D}(\dot{d}).$$

These relations are valid if we have no damaging external actions. As pointed out in [4] we can take into account such actions which are external damaging works with volume density A and surface density a. They provide damaging power P on the solids Ω without macroscopic motion:

$$P(\dot{d}) = \int_{\Omega} A\,\dot{d}\,\mathrm{d}\Omega + \int_{\partial\Omega} a\,\dot{d}\,\mathrm{d}S. \tag{50}$$

For instance, when damage results from radiative actions, chemical or electrical processes, such damaging forces are active. In this case the equation of evolution of d are modified as

$$-B + \mathrm{div}\mathbf{H} + A = 0, \quad \mathbf{n}.\mathbf{H} = a.$$

Remark 2 It can be noticed that the global value of dissipation is conserved:

$$D_m = \int_{\Omega} G\,\dot{d}\,\mathrm{d}\Omega = \int_{\Omega} Y\,\dot{d}\,\mathrm{d}\Omega. \tag{51}$$

5 An Uniaxial Example

We study now a bar in tension. The domain is defined by $\Omega =]0, L[$, The displacement $\mathbf{u}(x,t) = u(x,t)\mathbf{e}_x$ is prescribed ($u(0,t) = 0, u(L,t) = u^d(t)$), where $u^d(t)$ is an increasing function of time. Initially the state of the bar is stress free, the displacement is uniform ($\mathbf{u}(x,0) = 0$) the damage $d(x,0) = 0$. We assume that there is no external damaging actions The behaviour of the bar is determined by the free energy.

$$\Psi(\varepsilon, d) = (1-d)\,\frac{\mathrm{E}}{2}\varepsilon^2 + \frac{1}{2}\mathrm{H}\,d^2.$$

In this case, the strain is $\varepsilon = \dfrac{\mathrm{d}u}{\mathrm{d}x}$. The gradient of damage is limited by

$$f(d) = \frac{1}{l_c}.$$

During the extension, the equation of quasi-static motion implies the uniformity of the stress $\sigma(X,t) = \Sigma(t)$. The system evolves with successive behaviour.

Phase I: Elastic Response
During this stage $d = 0$, then $g_1 = g_2 = 0$. The driving force $G(x, t)$ satisfies

$$G = \frac{1}{2}\mathrm{E}\,\varepsilon^2 + \lambda_1 \leq Y_c. \tag{52}$$

As $\varepsilon = \dfrac{u^d}{L}$, the response is purely elastic as long as $\dfrac{1}{2}\mathrm{E}\,\varepsilon^2 \leq \dfrac{1}{2}\mathrm{E}\,\varepsilon_c^2 = Y_c$. The state of stress at the end of this phase is: $\Sigma_c = \mathrm{E}\varepsilon_c$.

Phase II: Uniform Damage
During this phase, the damage may evolve, $0 < d(X, t) < 1$ and $g_2 < 0$ then $\lambda_1 = \lambda_2 = 0$. The damage evolves, $\dot{d} \geq 0$ if $G = \dfrac{1}{2}\dfrac{\Sigma^2}{(1-d)^2} - \mathrm{H}d = Y_c$. Then

$$\begin{aligned}
\Sigma &= \sigma(x, t) = (1-d)\mathrm{E}\,\varepsilon,\\
\dot{\Sigma} &= (1-d)\mathrm{E}\,\dot{\varepsilon} - \dot{d}\,\mathrm{E}\,\varepsilon,\\
0 &= \mathrm{E}\,\varepsilon\,\dot{\varepsilon} - \mathrm{H}\,\dot{d}.
\end{aligned}$$

This solution is unique, if $\dot{\Sigma} = M\dot{\varepsilon}$, $M > 0$, that is

$$M = \left(1 - d - \frac{\mathrm{E}}{\mathrm{H}}\varepsilon^2\right)\mathrm{E} > 0.$$

This is true if $\dfrac{\mathrm{E}}{\mathrm{H}}\varepsilon_c^2 < 1$ that is $\mathrm{H} > 2Y_c$. We denote $\mathrm{H} = \alpha Y_c$, $\alpha \geq 0$.

- For $\alpha > 2$. A solution with uniform damage is obtained as long as $\varepsilon \leq \varepsilon_m$. During this phase, the state is uniform $\varepsilon(x, t) = \varepsilon(t), d(x, t) = d(t), \sigma(x, t) = \Sigma$. At the final state of this phase:

$$d_m = 1 - \frac{\mathrm{E}}{\mathrm{H}}\varepsilon_m^2 = \frac{\alpha - 2}{3\alpha}, \tag{53}$$

$$\frac{3}{2}\mathrm{E}\varepsilon_m^2 = \frac{1}{2}\mathrm{E}\varepsilon_c^2 + \mathrm{H} = Y_c(1 + \alpha), \tag{54}$$

$$\frac{\Sigma_m^2}{2\mathrm{E}(1-d_m)^2} = Y_c + \mathrm{H}d_m = Y_c(1 + \alpha d_m). \tag{55}$$

- For $\alpha \leq 2$, the solution is $d_m = 0$, $\varepsilon_m = \varepsilon_c$, the phase II is impossible.

Whatever α is, if the loading u^d is still increasing, the stress Σ decreases from the point (d_m, ε_m), if we consider a homogeneous solution. This solution is unstable, some unloading zones appear with strong discontinuities. The damage is continuous and then the discontinuity of the gradient satisfies $\left[\dot{d}\right]_S + V\left[\nabla d\right]_S \mathbf{e}_x = 0$ where V is the celerity of the discontinuity.

Phase III: Graded Damage

From the state (d_m, ε_m) a solution is obtained considering that a zone where $g_2 = 0$ appears. We assume that damage evolves at point $x = 0$. From $g_2 = 0$ the zone is the segment $]0, l[$, $l \leq l_c$ and

$$d = \frac{l - x}{l_c} + d_m \leq 1, \quad \dot{d} = \frac{\dot{l}}{l_c}. \tag{56}$$

The problem of evolution is governed by

$$G = \frac{\Sigma_l^2}{\mathrm{E}(1-d)^2} - \frac{1}{l_c}\frac{\mathrm{d}\lambda_2}{\mathrm{d}x} - \mathrm{H}d = Y_c. \tag{57}$$

On a point of discontinuity of ∇d we have

$$\left[\lambda_2 \frac{\nabla d}{\|\nabla d\|}\right]_S = 0,$$

then at point $x = l$, $\lambda_2 = 0$. The same is true at $x = 0$ due to the natural boundary condition.

The integration of G between 0 and l, determines the value Σ_l of Σ. and λ_2 is then determined on the set $]0, l[$ by integration of Eq. (57).

In Eq. (57) we replace the derivative with respect to x by the derivative with respect to d

$$G = \frac{1}{2}\frac{\Sigma_l^2}{\mathrm{E}(1-d)^2} + \frac{1}{l_c^2}\frac{\mathrm{d}\lambda_2}{\mathrm{d}d} - \mathrm{H}d = Y_c. \tag{58}$$

By integration from d_m to $d_o = d_m + \dfrac{l}{l_c}$ and taking account of the boundary conditions, we obtain the value of the normal tension Σ_l

$$\frac{\Sigma_l^2}{2\mathrm{E}}\left(\frac{1}{1-d_o} - \frac{1}{1-d_m}\right) = Y_c\left(d_o - d_m + \frac{\alpha}{2}(d_o^2 - d_m^2)\right). \tag{59}$$

The value of the normal force satisfies

$$\frac{1}{2\mathrm{E}}(\Sigma_l^2 - \Sigma_m^2) = -\alpha Y_c\left(\frac{l}{l_c}\right)^2(1 - d_m) \leq 0. \tag{60}$$

Then in the domain $]l, L[$, $Y < Y_c + \mathrm{H}d_m$ and the damage is uniform with value d_m. Σ_l being determined, it is easy to obtain λ_2

$$\frac{1}{l_c^2}\frac{\lambda_2(d)}{d - d_m} = -\frac{d - d_o}{2(1-d)}\left(2\frac{l}{l_c} - \frac{x}{l_c}\right) > 0. \tag{61}$$

then λ_2 is positive on $]0, l[$. The values of G at state d_m and d_o are

$$\frac{\Sigma_l^2}{2\mathrm{E}(1-d_m)^2} + \frac{1}{l_c^2}\frac{\mathrm{d}\lambda_2}{\mathrm{d}d}(d_m) = Y_c(1+\alpha d_m), \tag{62}$$

$$\frac{\Sigma_l^2}{2\mathrm{E}(1-d_o)^2} + \frac{1}{l_c^2}\frac{\mathrm{d}\lambda_2}{\mathrm{d}d}(d_o) = Y_c(1+\alpha d_o). \tag{63}$$

imply that $\lambda_2(d)$ decreases at point d_o and increases at point d_m. This is equivalent to $\lambda_2(x)$ increases at $x = 0$ and decreases at $x = l$.

Consider the local energy release rate Y, we have by definition

$$G = Y + \frac{1}{l_c^2}\frac{\mathrm{d}\lambda_2}{\mathrm{d}d}(d) - \mathrm{H}d = Y_c. \tag{64}$$

The averaging of G between d_m and d_o is equivalent to the definition of the average $\bar{Y}$ of the local energy release rate Y as proposed in [12].

6 Approximation

Contrary to the original TLS approach based on level-set algorithm and equation of evolution of a moving layer, it is proposed here to regularize the position with a gradient theory. Then we give a schematic model giving some properties to the completely damaged zone where $d = 1$. This crude model has the advantage to have a mathematical existence theorem supporting this predictive theory. A more realistic model of the damaged zone is given in [5] where the damaged zone is viscous in compression and does not sustain traction.

6.1 A Smoother Predictive Theory

Let us introduced a smoother free energy which take into account of a quadratic energy in ∇d

$$\hat{\Psi}(\varepsilon, d, \nabla d) = \frac{k}{2}\|\nabla d\|^2 + I_{\mathscr{C}_1}(d) + I_{\mathscr{C}_2}(d, \nabla d) + \Psi(\varepsilon, d),$$

giving

$$\mathbf{H} = k\nabla d + \lambda_2 \frac{\nabla d}{\|\nabla d\|}.$$

This new formalism can be used if the framework using level-set is not implemented into the solver. This new formulation can be used for a comparison with other gradient damage theory like [2, 8, 10], to determine the influence of the internal constraint.

6.1.1 The Damage Equation

It depends on the internal constraint (2).

- In domain where $\|\nabla d\| - f(d) < 0$.
  Reaction $\mathbf{R} = 0$ and the equation is

$$0 \in \frac{\partial \Psi}{\partial d}(\varepsilon, d) + \partial I_{\mathscr{C}_1}(d) - k\Delta d + \partial \mathscr{D}(\dot{d}).$$

- In domain where $f(d) - \|\nabla d\| = 0$.
  The reaction is not null. The damage is given by the eikonal equation

$$\|\nabla d\| = f(d),$$

  and the boundary conditions in this domain. Reaction $\mathbf{R}$ depending on λ_2 is given as usual by an equation of motion

$$\begin{aligned} -\lambda_2 \frac{\mathrm{d}f}{\mathrm{d}d}(d) + \frac{\partial \Psi}{\partial d}(\varepsilon, d) + \partial I_{\mathscr{C}_1}(d) \\ + \partial \mathscr{D}(\dot{d}) - k\Delta d - \operatorname{div}(\lambda_2 \frac{\nabla d}{\|\nabla d\|}) \ni 0, \\ \lambda_2 \geq 0, \end{aligned}$$

  with the boundary conditions

$$0 = \mathbf{H} \cdot \mathbf{n} = k\nabla d \cdot \mathbf{n} + \lambda_2 \frac{\nabla d}{\|\nabla d\|} \cdot \mathbf{n}$$

  allowing $\nabla d \cdot \mathbf{n}$ not to be null.

This set of equations determines λ_2 and then reaction $\mathbf{R}$ in this domain.

We may approximate the indicator functions of convex sets $\mathscr{C}_1$ and $\mathscr{C}_2$ with the Moreau-Yoshida approximation:

$$I^{\eta}(d, \nabla d) = \frac{1}{2\eta}\left|f(d) - \|\nabla d\|\right|_-^2 + \frac{1}{2\eta}\left|d\right|_-^2 + \frac{1}{2\eta}\left|d - 1\right|_+^2,$$

with

$$\left|x\right|_- = \sup\{0, -x\}, \quad \left|x\right|_+ = \sup\{0, x\},$$

and $\eta > 0$, a sufficiently small parameter. The approximated constitutive laws are smooth, defining

$$\frac{\partial I^\eta}{\partial d} = -\frac{1}{\eta}\left|f(d) - \|\nabla d\|\right|_- \frac{\mathrm{d}f}{\mathrm{d}d} - \frac{\left|d\right|_-}{\eta} + \frac{\left|d-1\right|_+}{\eta},$$
$$\frac{\partial I^\eta}{\partial \nabla d} = -\frac{1}{\eta}\left|f(d) - \|\nabla d\|\right|_- (-\frac{\nabla d}{\|\nabla d\|}),$$

we obtain

$$\frac{\partial \Psi}{\partial d}(\varepsilon, d) + \frac{\partial I^\eta}{\partial d}(d, \nabla d)$$
$$-k\Delta d - \mathrm{div}\Big(\frac{\partial I^\eta}{\partial \nabla d}(d, \nabla d)\Big) + \partial \mathscr{D}(\dot{d}) \ni 0.$$

This equation may be used for numerics. Note that the Lagrange multiplier's and some sub-differential are no longer involved. The equations to solve are smooth but non-linear.

6.2 An Even Smoother Predictive Theory

We assume a non-linear elastic material to overcome the lack of cohesion when the solid is completely damaged. For instance,

$$\Psi(\varepsilon, d) = (1-d)\frac{E}{2}\varepsilon : \varepsilon + \frac{k_4}{4}(\varepsilon : \varepsilon)^2, \tag{65}$$

with $k_4 > 0$. This assumption is a different way to prevent a completely lost of rigidity, some authors replace $1-d$ by $(1-d+\alpha)$ with $1 \gg \alpha \geq 0$.

With this assumption, it remains some mechanical stiffness when the solid is completely damaged. Note that we have the same property if we choose the free energy given by formula (9).

The solid is fixed on part $\partial\Omega_{\mathbf{u}}$ where it is not damaged. Traction T^d is prescribed on part $\partial\Omega_T$.

We get the equilibrium positions:

Theorem 3 *The problem*

$$\inf_{(\mathbf{v},\delta)\in\mathcal{A}} \mathscr{E}(\varepsilon(\mathbf{v}), \delta, \nabla\delta)$$
$$\mathcal{A} = \{\delta \in H^1_\Omega, \mathbf{v} \in W^{1,4}_\Omega, \delta = 0, \ on\ \Gamma_o, \ \mathbf{v} = 0, \ on\ \Gamma_o\}$$

with

$$\mathscr{E}(\varepsilon(\mathbf{v}), \delta, \nabla\delta) = \int_\Omega \hat{\Psi}(\varepsilon(\mathbf{v}), \delta, \nabla\delta)\ \mathrm{d}\Omega - \int_{\partial\Omega_T} T^d \cdot \mathbf{v}\ \mathrm{d}S$$

where $\hat{\Psi} = \Psi + I_{\mathscr{C}_1} + I_{\mathscr{C}_2}$, *has solutions.*

Proof Let $(d_n, \mathbf{u}_n)$ a minimizing sequence. This sequence is bounded in $H^1_\Omega \times W^{1,4}_\Omega$ and there exists a subsequence, still denoted $(d_n, \mathbf{u}_n)$, which converges weakly in $H^1_\Omega \times W^{1,4}_\Omega$ to $(d, \mathbf{u})$. We have

$$\lim_{n\to\infty} \int_\Omega (1-d_n)\frac{E}{2}\varepsilon(\mathbf{u}_n)^2 \, \mathrm{d}\Omega = \int_\Omega (1-d)\frac{E}{2}\varepsilon(\mathbf{u})^2 \, \mathrm{d}\Omega,$$

because d_n converges strongly and $\varepsilon(\mathbf{u})^2$ converges weakly in $L^2(\Omega)$. We have also

$$\int_\Omega \frac{k_4}{4}\Big(\varepsilon(\mathbf{u}) : \varepsilon(\mathbf{u})\Big)^2 \, \mathrm{d}\Omega \leq \lim_{n\to\infty} \inf \int_\Omega \frac{k_4}{4}\Big(\varepsilon(\mathbf{u}_n) : \varepsilon(\mathbf{u}_n)\Big)^2 \, \mathrm{d}\Omega,$$

because this norm is weakly semi-continuous. The convex sets $\mathscr{C}_1$ and $\mathscr{C}_2$ are strongly closed. Thus they are weakly closed. It results $d \in \mathscr{C}_1$, $(d, \nabla d) \in \mathscr{C}_2$ and

$$\mathscr{E}(\varepsilon(\mathbf{u}), d, \nabla d) = \inf_{\mathcal{A}} \Big\{\mathscr{E}(\varepsilon(\mathbf{v}), \delta, \nabla\delta)\Big\}$$

Then $(d, \mathbf{u})$ is an equilibrium solution.

Remark 3 There are other ways to have solutions. For instance, it may be assumed a second gradient theory for damage d. The mathematical problem is the limit of the product $(1-d_n)\frac{E}{2}\varepsilon(\mathbf{u}_n)^2$. We need to control $\varepsilon(\mathbf{u}_n)^2$ when the solid becomes completely damaged.

Remark 4 In case, the solid keeps no elasticity in the completely damage domain, it is possible to find solutions, assuming the completely damaged material is a no traction material with viscous and locking properties in compression [5]. The evolution problem with $k_4 > 0$ may also be investigated.

7 Conclusion

The paper proposes new approaches of graded damage modelling. To avoid spurious mode of localization the limitation of the amplitude of the damage gradient is effective in two ways: either the Thick Level Set theory or the convex analysis. The first technique results in surface tracking and solving an eikonal equation. The second use non linear partial differential equation. The two techniques involves only the significant domain.

Approximation and regularization methods are also proposed, which must be solved on the whole domain.

Acknowledgements The support of ERC Advanced Grant XLS no 291102 is greatfully acknowledged.

References

1. Ambrosio L, Tortorelli VM (1990) Approximation of functional depending on jumps by elliptic functional via Γ-convergence. Commun Pure Appl Math 43:999–1036
2. Bourdin B, Francfort GA, Marigo JJ (2008) The variational approach to fracture. J Elast 91:5–148
3. Del Piero G, Lancioni G, March R (2007) A variational model for fracture mechanics: numerical experiments. J Mech Phys Solid 55:2513–2537
4. Frémond M (2002) Non-smooth thermomechanics. Springer, Berlin
5. Frémond M, Kenmochi N (2006) Damage of a viscous locking material. Adv Math Sci Appl 16(2):697–716
6. Frémond M, Nedjar B (1993) Endommagement et principe des puissances virtuelles. Comptes Rendus de l'Académie des Sciences, Paris, II 317(7):857–864
7. Frémond M, Nedjar B (1996) Damage, gradient of damage and principle of virtual power. Int J Solid Struct 33(8):1083–1103
8. Karma A, Kessler D, Levine H (2001) Phase field model in mode III dynamic fracture. Phys Rev Lett 87(4):045501
9. May S, Vignollet J, de Borst R (2015) A numerical assesment of phase-field models for brittle and cohesive fracture: Γ-convergence and stress oscillations. Eur J Mech A/Solid 52:72–89
10. Miehe C, Welschinger F, Hofhacker M (2010) A Thermodynamically consistent phase field models of fracture: variational principles and multifield FE implementation. Int J Numer Methods Eng 83(10):1273–1311
11. Moës N, Stolz C, Bernard P-E, Chevaugeon N (2010) A level set based model for damage growth: the thick level set approach. Int J Numer Methods Eng 86:358–380
12. Moës N, Stolz C, Chevaugeon N (2014) Coupling local and non-local damage evolutions with the thick level set model. Adv Model Simul Eng Sci 2:16
13. Moreau JJ (2003) *Fonctionnelles convexes*. Edizioni del Dipartimento di Ingegneria Civile, Università di Roma "Tor Vergata", Roma, ISBN 978-88-6296-001-4 and Séminaire sur les équations aux dérivées partielles, Collège de France, Paris, 1966
14. Mumford D, Shah J (1989) Optimal approximations by piecewise smooth functions and associated variational problems. Commun Pure Appl Math 42:577–685
15. Parrilla Gómez A, Moës N, Stolz C (2015) Comparison between thick level set (TLS) and cohesive zone models. Adv Model Simul Eng Sci 2:18
16. Peerlings RHJ, de Borst R, Brekelmans WAM, de Vree HPJ (1996) Gradient-enhanced damage for quasi-brittle materials. Int J Numer Methods Eng 39:3391–3403
17. Pham K, Marigo JJ (2013) From the onset of damage until rupture: construction of the responses with damage localization for a general class of gradient damage models. Continuum Mech Thermodyn 25:147–171
18. Pijaudier-Cabot G, Bazant ZP (1987) Non local damage theory. J Eng Mech (ASCE) 113:1512–1533
19. Stolz C, Moës N (2012) A new model of damage: a moving thick layer approach. Int J Fract 174:49–60

Edge Debonding Prediction in Beams Strengthened by FRP Composite Plates

Domenico Bruno, Fabrizio Greco, Stefania Lo Feudo and Paolo Nevone Blasi

Abstract Edge debonding initiation and propagation in beams strengthened with fiber-reinforced composite plates is here studied. The structural system is composed by three physical components, namely the beam, the adhesive layer and the bonded plate, which are modeled by one or several first-order shear deformable layers according to a multi-layer formulation, wherein both strong and weak interface constitutive relations are introduced to model interfaces. Debonding onset is predicted with the aid of a mixed mode coupled stress and energetic criterion, and propagation in different locations across the adhesive thickness is studied by using a mixed mode fracture criterion. The proposed models are implemented according to the 1D finite element technique, allowing accurate evaluation of interlaminar stresses and fracture energies.

1 Introduction

In the repair and strengthening of existing structures, an important role is covered by the Fiber-Reinforced Plastic (FRP) composites, which may be adopted in form of strips, plates, and sheets and bonded externally to the structure to reinforce. An adhesive layer ensures physical adhesion between layers and the load transfer. In this

D. Bruno (✉) · F. Greco · P. Nevone Blasi
Department of Civil Engineering, University of Calabria, Via P. Bucci,
87036 Rende, Italy
e-mail: d.bruno@unical.it

F. Greco
e-mail: f.greco@unical.it

P. Nevone Blasi
e-mail: paolo.nevoneblasi@unical.it

S. Lo Feudo
Université Paris–Saclay, ENSTA ParisTech, IMSIA, CNRS, EDF, CEA,
828 bd. des Maréchaux, 91120 Palaiseau, France
e-mail: stefania.lofeudo@unical.it

M. Frémond et al. (eds.), *Models, Simulation, and Experimental Issues in Structural Mechanics*, Springer Series in Solid and Structural Mechanics 8,
DOI 10.1007/978-3-319-48884-4_5

way, a large improvement in terms of strength and durability of the structural system can be obtained, with small changes in the original weight and dimension. However, the resulting strengthened system may fail due to initiation and propagation of cracks at the interface between the lower face of the beam and the adhesive. In particular, the interfacial debonding is caused by high concentrations of normal and shear stresses at the end of the bonded FRP plate and near cracks within the beam. The ability to predict interfacial stresses becomes a subject of high relevance, increasingly faced in the current scientific literature. Several approximate closed-form analytical solutions based on simplified assumptions for the adhesive layer have been proposed. Generally speaking, a linear elastic behavior is assumed for all materials and the classical beam theory is adopted in order to model each component. For example, in [18] shear and normal stresses are considered to be constants across the adhesive thickness, whereas in [17] the normal stress variation is considered. On the other hand, important numerical analyses were conducted in [19, 20], where existence of stress singularity at the plate end and its mesh dependence is confirmed. Then, in order to analyze debonding of bonded plates, several approaches based on both strength theory and fracture mechanics have been proposed. When fracture mechanics is adopted in order to predict debonding propagation, modal partition of the Energy Release Rate (ERR) may be required. To this end, mixed mode delamination problems were analyzed in [2], where shear deformability is accounted and a multi-layer formulation is used [3–5, 10]. As far as the debonding initiation evaluation is concerned, the stress singularity at the FRP free edges leads to a null applied load for the fulfillment of a stress condition. Moreover, stresses near the plate end are very mesh dependents, and a simple stress criterion may be thus not able to represent properly the damage initiation. To overcome this issue, one way is to consider an average strength evaluated along a small length, which choice is arbitrary and it may depend on both material properties and structural sizes. On the other hand, also the classic Fracture Mechanics fails in predict debonding initiation since ERR vanishes when crack length approaches zero, and consequently an infinite load would be required for the crack initiation. For this reason, the fulfillment of a pure energetic requirement may be considered only in the analysis of crack propagation, i.e. when an initial defect is present and the ERR has a finite value. In this framework, a very innovative criterion for crack initiation was proposed by Leguillon [15], who remarked that both energy and stress criteria are necessary conditions for fracture, although neither one nor the other are sufficient. For this reason, a coupled stress/energy criterion was introduced, consisting in the simultaneous fulfillment of the two failure conditions. A number of applications of such a coupled criterion, which has been adapted to specific loading conditions and damaged systems, may be found [8, 16].

In this paper, onset and propagation of edge debonding in strengthened beams is analyzed numerically by means of a multi-layer formulation and the coupled criterion adapted to the present mixed mode problem. The paper is organized as follows. In the first section the mathematical formulation for the problem is presented. Then, interfacial stresses and fracture energies are evaluated by means of the multi-layer

formulation and a 2D FE continuum model for a three point bending sample. Finally, crack initiation and propagation are predicted according to the proposed mixed mode coupled failure criterion.

2 Governing Equations

A multi-layer formulation able to model beams strengthened by externally bonded fiber-reinforced composite plates is here presented. Interfacial stresses and fracture energies are numerically evaluated, allowing prediction of edge debonding by means of a mixed mode coupled stress and energy criterion. The beam, the adhesive layer and the bonded plate, are modeled by means of one or several first-order shear deformable layers and, for Adhesive/Concrete (AC) and Adhesive/Plate (AP) interfaces both strong and weak interface formulations are adopted, whereas for the mathematical interfaces between layers a strong formulation is used. Among the mathematical interfaces is of particular interest the one placed at the mid-adhesive location, which will be denoted hereafter as (MA). This multi-layer approach provides a refined methodology able to accurately predict the local quantities governing the debonding problem for reinforced beams, and thus overcomes the inaccuracies of the beam based models already proposed in the literature.

2.1 Multi-layer Formulation

A damaged composite laminate composed by several unidirectional fiber reinforced plies is here considered. Each physical layer is modeled by means of one or several mathematical first-order shear deformable layers, assuming both strong and weak interface formulations for the AC and AP interfaces in order to guarantee displacement continuity at the undelaminated interfaces, and a strong formulation for the mathematical interfaces between layers. In case of strong interface formulation, interfacial stresses are represented by Lagrange multipliers, whereas in case of wake formulation a penalty method is adopted. An appropriate calibration of the stiffness parameters, which depend on the geometrical and mechanical properties of the system, allows to take into account for transverse and shear deformability. Moreover, for the sake of simplicity debonding is assumed to take place at the AC interface.

A variational formulation is adopted, and the following energy functional Π (for unit width) is introduced:

$$\Pi = U + \Lambda + I - W \tag{1}$$

where U is the strain energy of the structural system, Λ is the Lagrange functional imposing displacement continuity for the strong interfaces, I the strain energy of the weak interface representing the penalty functional, and W is the work done by the applied loads. The stationarity of Π with respect to a variation of the generalized

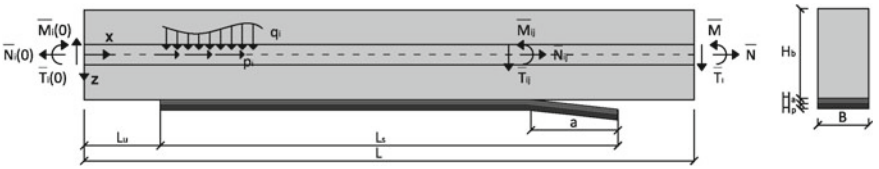

Fig. 1 Mathematical notation and conventions for loads and stress resultants

displacements of the layers and of the Lagrange multipliers, allows to obtain the governing equations for the problem:

$$\delta U + \delta \Lambda + \delta I - \delta W = 0 \tag{2}$$

where δ is the variational operator. An elastic beam of length L and of thickness H_b is reinforced over the length $L_u \leq x \leq L_u + L_s$ by an elastic *FRP* plate of thickness H_p. All components width is equal to B. Therefore, two unstregthened regions may be identified at $0 \leq x \leq L_u$ and $L_u + L_s \leq x \leq L$, whereas debonding takes place at the region $L_u + L_s - a \leq x \leq L_u + L_s$, as shown in Fig. 1. Either distributed or concentrated loads act only on the beam, and on the upper and lower side of the delamination n_b and $n_a + n_p$ mathematical layers are considered, where n_b, n_a and n_p are the number of layers for the base beam, the adhesive layer and the *FRP* plate, respectively. The first layer is the lowest one and the i-th layer thickness is t_i, whereas the horizontal axis x is oriented from left to right and the vertical axis z is oriented downwards. For a generic layer, membrane strain at the reference surface, curvature and transverse shear strain may be expressed as:

$$\varepsilon_i = u_i', \quad \kappa_i = \psi_i', \quad \gamma_i = \psi_i + w_i' \tag{3}$$

where $u_i(x)$ and $w_i(x)$ are the mid-surface in-plane and transverse displacements, respectively, $\psi_i(x)$ are the rotations of transverse normals, and prime denotes derivative with respect to x. The first variation of the strain energy is:

$$\delta U = \int_{L_u}^{L_u+L_s} \sum_{i=1}^{n_p+n_a} [\boldsymbol{\sigma}_i \cdot \delta \boldsymbol{\varepsilon}_i]\, dx + \int_0^L \sum_{i=n_p+n_a+1}^{n_p+n_a+n_b} [\boldsymbol{\sigma}_i \cdot \delta \boldsymbol{\varepsilon}_i]\, dx \tag{4}$$

where $\boldsymbol{\sigma}_i = \{N_i, M_i, T_i\}$ and $\boldsymbol{\varepsilon}_i = \{\varepsilon_i, \kappa_i, \gamma_i\}$ are the vectors containing stress resultants and strains for the i-th layer, respectively, and dot denotes the scalar product. In particular, N_i is the membrane force resultant, M_i the moment resultant and T_i the transverse shear force resultant. In case of strong interface formulation, the variation of the Lagrange functional related to interface displacement continuity between adjacent layers is:

$$\delta \Lambda = \int_{L_u}^{L_u+L_s} \sum_{j=1}^{n_p+n_a-1} [\boldsymbol{\lambda}_j \cdot \delta \Delta \mathbf{u}_j]\, dx + \int_0^{L} \sum_{j=n_p+n_a+1}^{n_p+n_a+n_b-1} [\boldsymbol{\lambda}_j \cdot \delta \Delta \mathbf{u}_j]\, dx \tag{5}$$

where $\Delta \mathbf{u}_j = \{\Delta u_j, \Delta w_j\}$ is the vector of the relative displacements at the j-th interface between the j-th and the $j+1$-th mathematical layer,

$$\begin{cases} \Delta u_j &= u_j - \dfrac{t_j}{2}\psi_j - u_{j+1} - \dfrac{t_{j+1}}{2}\psi_{j+1} \\ \Delta w_j &= w_j - w_{j+1} \end{cases} \tag{6}$$

and $\boldsymbol{\lambda}_j = \{\lambda_{zxj}, \lambda_{zj}\}$ is the Lagrange multipliers vector, which represents the interfacial stresses at the j-th interface. A weak formulation is now assumed where debonding occurs, that is at the $(n_p + n_a)$-th interface, i.e. AC in the present formulation. In this case, the variation of the strain energy is:

$$\delta I = \int_{L_u}^{L_u+L_s} \delta \Omega\, dx, \quad \Omega = \frac{1}{2}\mathbf{t}_{z,\, n_p+n_a} \cdot \Delta \mathbf{u}_{n_p+n_a} \tag{7}$$

where $\Delta \mathbf{u}_{n_p+n_a} = \{\Delta u_{n_p+n_a}, \Delta w_{n_p+n_a}\}$ contains the relative displacements at the $(n_p + n_a)$-th interface and $\mathbf{t}_{z\, n_p+n_a} = \{\sigma_{zx,\, n_p+n_a}, \sigma_{z,\, n_p+n_a}\}$ contains the interlaminar shear $(\sigma_{zx,\, n_p+n_a})$ and normal $(\sigma_{z,\, n_p+n_a})$ stresses that, in the weak interface formulation, assume the following expressions:

$$\sigma_{z,\, n_p+n_a} = \bar{k}_z \Delta w_{n_p+n_a}, \quad \sigma_{zx,\, n_p+n_a} = \bar{k}_{zx} \Delta u_{n_p+n_a} \tag{8}$$

$$\bar{k}_z = (1-d)k_z, \quad \bar{k}_{zx} = (1-d)k_{zx} \tag{9}$$

where d is a damage variable, which is equal to 1 in the damaged zone, and to 0 in the bonded region, and k_z and k_{zx} are the interface stiffness parameters (having dimensions FL^{-3}). It is worth noting that the penalty formulation is equivalent to the Lagrange method when the stiffness parameters approach infinity. The variation of external load work is:

$$\delta W = \int_0^{L} \sum_{i=n_p+n_a-1}^{n_p+n_a+n_b} [p_i \delta u_i + q_i \delta w_i]\, dx + \delta \bar{W}^c + \delta \bar{W} \tag{10}$$

where p_i and q_i are the distributed axial and transverse external loads applied to the i-th layer, $\delta \bar{W}^c$ is the variation of the work of concentrated external loads and

bending moments, and $\delta\bar{W}$ is the variation of the work of external concentrated loads and bending moments at the two ends of each layer. Each i-th mathematical homogeneous layer is modeled as orthotropic by means of the classical extensional, bending–extensional coupling, bending and shear stiffness, see [5] for further details.

The constraint equations used to ensure displacement continuity at the strong interfaces are obtained by the variation of Π with respect to Lagrange multipliers and are given by:

$$\begin{cases} \Delta u_j & = 0 \\ \Delta w_j & = 0 \end{cases}, \quad j = 1, ...n_p + n_a + n_b - 1, \; j \neq n_p + n_a \tag{11}$$

Thus, the independent displacement variables may be reduced to $n_p + n_a + n_b + 4$ and are:

$$\{w_{n_p+n_a}, w_{n_p+n_a+1}, u_{n_p+n_a}, u_{n_p+n_a+1}, \psi_i\}, \quad i = 1, ..., n_p + n_a + n_b \tag{12}$$

The fundamental lemma of variational calculus, together with the appropriate continuity conditions for the generalized displacement variables, leads to a boundary value problem. Two equations for the translational equilibrium in the x-direction and in the z-direction of the layer assemblies at the two sides of the interface crack, and one equation for rotational equilibrium of each mathematical layer are obtained. Moreover, the boundary conditions are specified at $x = 0$ and $x = L$ for the layers above the debonded interface, and at $x = L_u$ and $x = L_u + L_s$ for the layers below, whereas the matching conditions are specified at $x = Lu$ and $x = L_u + L_s$ above the debonded interface, and at $x = L_u + L_s - a$ for the two sets of layers at the two sides of the debonding interface. The following result is also obtained for the Lagrange multipliers, i.e. the interfacial stresses:

$$\begin{aligned} \sigma_{zx,\,i} &= \sum_{j=1}^{i} N_j', \quad i = 1, ..., n_p + n_a - 1 \\ \sigma_{z,\,i} &= \sum_{j=1}^{i} T_j', \quad i = 1, ..., n_p + n_a - 1 \end{aligned} \tag{13}$$

The matching conditions are compatible with concentrated interfacial forces, which dimension are force/length, arising from the constraint equations at the strong interfaces, i.e. for $j = 1, ..., n_p + n_a - 1, n_p + n_a + 1, ..., n_p + n_a + n_b - 1$. For instance, at the crack tip, $x = L_u + L_s - a$, and for the layer assembly below the debonded interface, the matching force conditions are:

$$\begin{aligned}
&\left[\!\left[\sum_{j=1}^{n_p+n_a} N_j\right]\!\right]_{L_u+L_s-a} = 0, \qquad \left[\!\left[\sum_{j=1}^{n_p+n_a} T_j\right]\!\right]_{L_u+L_s-a} = 0,\\
&\left[\!\left[M_1 + N_1\frac{t_1}{2}\right]\!\right]_{L_u+L_s-a} = 0,\\
&\left[\!\left[M_i - \left(\sum_{j=1}^{i} N_j + \sum_{j=1}^{i-1} N_j\right)\frac{t_i}{2}\right]\!\right]_{L_u+L_s-a} = 0, \quad i = 2, ..., n_p + n_a - 1,\\
&\left[\!\left[M_{n_p+n_a} + \sum_{j=1}^{n_p+n_a-1} N_j\frac{t_j}{2}\right]\!\right]_{L_u+L_s-a} = 0
\end{aligned} \tag{14}$$

where the double square brackets stand for the jump of the enclosed quantities ahead and behind the crack tip. The concentrated forces at the i-th strong interface are given by:

$$\begin{gathered}
\Sigma_{zx,i} = \sum_{j=1}^{i} N_j^+ - \sum_{j=1}^{i} N_j^-, \quad \Sigma_{z,i} = \sum_{j=1}^{i} T_j^+ - \sum_{j=1}^{i} T_j^-\\
i = 1, ..., n_p + n_a - 1, n_p + n_a + 1, ..., n_p + n_a + n_b - 1
\end{gathered} \tag{15}$$

Moreover, the boundary conditions at the plate end, $x = L_u$, and at the end of the delaminated interface, $x = L_u + L_s$, for the lower layer assembly, i.e. $i = 1, ..., n_p + n_a$, are imposed according to the free edge conditions, for additional details please see [5].

In conclusion, when a weak formulation with finite stiffness parameters is assumed, stress singularities are excluded since interfacial concentrated forces are not compatibles with the formulation. On the other hand, for stiffness parameters approaching infinity, stress singularities appear, and the limit process leads to the concentrated interfacial forces. These interfacial concentrated forces are helpful to evaluate the individual components of the ERR since the in-plane and out-of-plane interfacial forces are directly related to the Mode II and Mode I of fracture, respectively. In this way, the non-convergent behavior of mode partition of the continuum FE models, which is due to the oscillatory singularities at the bi-material interfaces, is avoided.

2.2 *Fracture Energies*

One major advantages with the use of the coupled multi-layer and interface elements models are related as stated above to the ERRs evaluation. In fact, in case of strong interface it was proved by Greco et al. [10] that the total ERR does not decrease rapidly to zero for vanishing cracks, but has a smooth continuous behavior. On the

other hand, when a weak interface is adopted, since interface stiffness and relative displacements have a finite value, stresses singularities are excluded and the ERRs may be computed also for a zero crack from these stresses, see [9]. In addition, also the individual model components of the ERR may be well defined, in both cases of strong or weak interface. In the former case from the vertical and horizontal interface concentrated forces, and in the latter by carrying out the penalty procedure. In fact, as proved by Bruno et al. [3], a good convergence of the individual ERRs can be also obtained by refining the layer subdivision, which however may reflect the physical layer thicknesses. Although the numerical evaluation of ERRs could be in theory easily obtained in terms of displacement variables calculated at the interface crack tip in the context of a weak interface, since the ERRs must be computed in the limit as the interface stiffness parameters approach infinity, a very fine finite element mesh is required in proximity of the crack tip. Alternatively, it is possible to take advantage of the strong interface formulation and to compute the energy release rate components as half the work of interfacial concentrated forces at the crack tip through corresponding displacement jumps occurring after the delamination is extended by an small (in theory infinitesimal) length da, according to the Virtual Crack Closure Technique (VCCT). For a sufficiently small da, the displacement jumps can be also evaluated at a distance da ahead the delamination tip, thus obtaining ERR and mode components by means of one stress analysis. Therefor, the Mode I and Mode II components of the ERR at the delamination tip may be expressed as:

$$\begin{aligned} G_I &= \lim_{k_{zx},k_z\to\infty} k_z \Delta w^2 = \frac{1}{2da}\Sigma_z \Delta w^+ \\ G_{II} &= \lim_{k_{zx},k_z\to\infty} k_{zx} \Delta u^2 = \frac{1}{2da}\Sigma_{zx} \Delta u^+ \end{aligned} \tag{16}$$

where the left side is valid for the weak interface formulation, and Δw and Δu are the displacement jumps at the delamination tip, whereas the right side refers to the strong interface formulation, and Δw^+ and Δu^+ are the displacement jumps at a distance da from the delamination tip.

2.3 Debonding Initiation and Propagation in Mixed Mode Problems

The coupled energetic/stress criterion introduced by Leguillon [15] for the prediction of crack onset consists in the simultaneous fulfillment of two failure conditions. Therefore, the criterion is here adapted to the case of mixed mode problems and employed to predict the edge debonding initiation. Basically, both a stress and an energy failure criterion must be satisfied simultaneously, leading to a system of two equations for two unknowns, which are the critical load level required for the crack onset β_c (seen as a multiplier of unit load) and the corresponding crack length a_c.

The stress criterion may be adopted in an integral or a point-wise form according to [1, 8], and the following non-linear equations system must be solved iteratively. In particular, the coupled mixed mode failure criteria can be expressed as:

$$\begin{cases} \dfrac{\beta^2 \int_0^a G_T(1,l)\, dl}{\int_0^a G_c\, dl} = 1 \\ \left(\dfrac{\beta \langle \int_0^a \sigma_y(1,l)\, dl \rangle}{\sigma_c\, a}\right)^2 + \left(\dfrac{\beta \langle \int_0^a \tau_x(1,l)\, dl \rangle}{\tau_c\, a}\right)^2 = 1 \end{cases} \tag{17}$$

$$\begin{cases} \dfrac{\beta^2 \int_0^a G_T(1,l)\, dl}{\int_0^a G_c\, dl} = 1 \\ \left(\dfrac{\beta \langle \sigma_y(1,l) \rangle}{\sigma_c}\right)^2 + \left(\dfrac{\beta \langle \tau_x(1,l) \rangle}{\tau_c}\right)^2 = 1 \end{cases} \tag{18}$$

where σ_c and τ_c denote the tensile and shear strengths, respectively, $G_T(1,l)$ is the total *ERR* for a unit load at the distance l from the plate end, $\sigma_y(1,l)$ and $\tau_x(1,l)$ are the normal and tangential interlaminar stresses for a unit load at a distance l behind the plate end, $<>$ are the Macaulay brackets and G_c is the fracture toughness. In particular, the proposed equations take into account that in linear elasticity stresses are directly proportional to load ($(\sigma_y, \tau_x) \sim \beta$), whereas *ERR* has a quadratic proportionality ($G_T \sim \beta^2$) [13]. For a given a it is possible to calculate the load levels that guarantee the satisfaction of the stress and energy criterion. When the obtained load levels coincide, although within a small tolerance, the set of critical load and critical length is obtained (see [11, 12] for additional details). For the mixed mode fracture toughness, a function reported in [14] may be adopted, that is $\Gamma(\rho) = G_{IC}\{1 + \tan^2[(1-\alpha)\rho]\}$, where G_{IC} is the Mode *I* interface toughness, α is a sensitivity parameter which takes into account mode mixity, and $\rho = \tan^{-1}(G_{II}/G_I)$ is the mode mixity angle.

Once that the debonding onset length a_c is determined, the subsequent propagation starting from a_c may be computed by using only the energetic criterion introduced in Eqs. (17) and (18), with the debonding length assumed to be a-priori known.

$$\beta^2 \frac{G_T}{G_c(\rho,\alpha)} = 1\,. \tag{19}$$

3 Numerical Analyses

In this Section, numerical evaluation of interfacial stresses and fracture energy for a simply supported beam reinforced with a bonded plate and subjected to a point load are presented. The 2D FE and the proposed multi-layer model are implemented by using the commercial finite element software Comsol Multiphysics 4.4 [7], and three

section locations across the adhesive thickness are studied, namely the AC and the AP interfaces and the MA section (en extended version of the study may be found in [5]).

3.1 Interfacial Stresses Prediction

A concrete beam strengthened by a CFRP plate is here considered, the structural system properties are reported in Table 1 and a Three Point Bending (TPB) scheme is analyzed. A 2D FE model with a mapped distributed mesh defined as in [19] and several multi-layer models have been developed. They differ for the number of layers adopted to model the adhesive and the concrete beam, their thickness distribution, and for the type of interface formulation assumed to simulate the adhesion between components. In the developed FE models, a maximum size of the finite element equal to 0.5 mm is adopted, with a mesh refinement near the plate end. Two-noded straight elements with an Hermitian formulation are used for each layers, considering the Timoshenko beam formulation in order to take into account the shear deformation. In particular 3, 4 or 6 mathematical layers are used in the formulation leading respectively to the $1/1/1$, the $1/2/1$ and the $3/2/1$ multi-layer models, for which the first number indicates the layers accounted for the concrete beam (n_b), the second one those for the adhesive physical layer (n_a) and the last one those for the bonded plate (n_p). The layers thickness (t_i for the i-th layer) varies depending on the chosen assembly and according to Table 2.

Displacements continuity at the bonded region is ensured by either a strong or a weak interface. In particular, three formulations are adopted for the physical interfaces AC and AP, as shown in Fig. 2:

- in the (a) multi-layer models, a strong interface formulation is assumed in both vertical and horizontal directions;

Table 1 Geometrical and material properties of the TPB sample

Component	Width (mm)	Thickness (mm)	Length (mm)	Young modulus (MPa)	Shear modulus (MPa)	Poisson's ratio
Concrete beam	1,000	300	3,000	30,000	12,820.5	0.17
Adhesive layer	1,000	2	2,400	2,000	740.74	0.35
CFRP laminate	1,000	4	2,400	$E_1 = E_2 = E_3 =$ 160,000	$G_{12} = G_{23} = G_{13} =$ 5,333.3	$\nu_{12} = \nu_{13} =$ 0.3 $\nu_{23} = 0.4$

Table 2 Layers assembly and thickness distribution

Model	Concrete beam	Adhesive layer	CFRP laminate
1/1/1	H_b	H_a	H_p
1/2/1	H_b	$H_a/2$ $H_a/2$	H_p
3/2/1	$H_b/3$ $H_b/3$ $H_b/3$	$H_a/2$ $H_a/2$	H_p

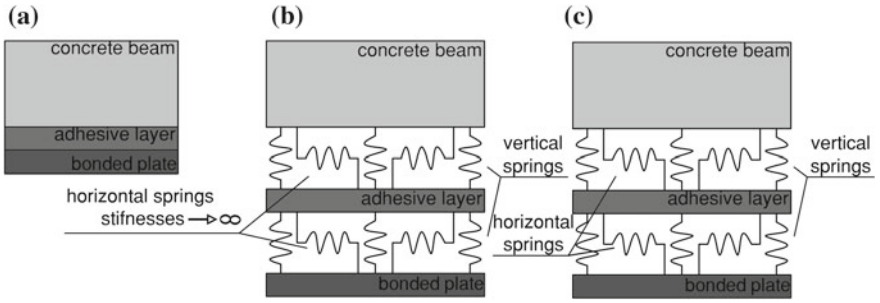

Fig. 2 **a** Strong, **b** coupled strong/weak and **c** weak interface formulation

- in the (b) multi-layer models, a strong interface formulation is assumed for the horizontal direction, whereas in the vertical direction a weak interface formulation is implemented through elastic springs whose stiffness represents the interface stiffness parameter;
- in the (c) multi-layer models, a weak interface formulation is assumed in both vertical and horizontal directions;

The above interface formulations are considered as constraint conditions in the FE models. In particular, in case of a strong interface a prescribed displacement is assigned on the lower of the two adjacent layers at the interface, and the displacement variables of the upper one are extruded on the lower one. Therefore, the displacements continuity is obtained by imposing vanishing interface relative displacements, see Eq. (11).

On the other hand, in case of weak interface, a continuous distribution of linear normal and tangent springs is considered, see Cornetti et al. [9]. Therefore, an edge load, which is linearly related to the interface relative displacements through the interface stiffness parameters, is assigned in the required direction on the adjacent layers but with opposite sign. In addition, in order to obtain a load system equivalent to an edge load acting on the interface between layers, an edge distributed moment is also considered since the edge load assigned in the x direction is applied on the central axis of the layer.

As far as the weak formulation is concerned, the interface stiffness coefficients in the vertical direction are obtained from the adhesive thickness and elastic moduli, E_a, thus allowing to recover the vertical compliance of the adhesive neglected by the structural model. Conversely, when the weak interface is considered also in the

horizontal direction, the stiffness parameters are obtained from the shear modulus of the adhesive layer, G_a, and from a fraction of its thickness, which may be determined by a parametric study through a parameter η. This issue is due to the fact that, although the adopted the multi-layer first order shear deformation theory takes into account the shear deformability of each component, for an accurate evaluation of the interface shear stress distribution, an enrichment of the kinematic formulation is required.

$$K_{j,v} = \frac{E_a B_a}{H_a/2}, \quad K_{j,h} = \frac{G_a B_a}{\beta \eta H_{ai}/2} \tag{20}$$

where H_{ai} denotes the thickness of the sub-layer representing the adhesive and adjacent to the interface.

Comparisons in terms of normal and shear interfacial stresses, between a 2*D FE* continuum model and the proposed multi-layer formulation, are illustrated in Figs. 3, 4 and 5. In particular, when a weak interface formulation is accounted, Eq. (20) is assumed, and the horizontal stiffness adopted for the (*c*) models are $K_{j,h} = G_a B_a/(0.25 H_a/2)$, $K_{j,h} = G_a B_a/(0.05 H_a/2)$ and $K_{j,h} = G_a B_a/(0.05 H_a/2)$ for the 1/1/1 (*c*), the 1/2/1 (*c*) and the 3/2/1 (*c*) assembly, respectively.

From the presented figures, it is possible to conclude that the interface formulation plays a stronger role in the interfacial stresses behavior with respect to the number of layers considered in the multi-layer model. In particular, when a strong interface formulation is considered at AC and AP, i.e. (a) models, the interfacial normal stresses are compressive in all the analyzed locations, which is in contrast with the 2D result, and they do not contribute to the debonding initiation. However, the inaccuracy of the (a) multi-layer models is within a small zone near the plate end, and it will be shown to have a scarce influence on debonding onset.

On the other hand, when in the vertical direction the elastic springs are introduced, i.e. (b) models, the normal stress distribution becomes in good agreement with the 2D FE continuum solution, with a large improvement in the prediction of the normal stresses. In particular, results show how near the edge of the bonded plate the AC interface is subjected to tensile stresses, whereas the AP interface is subjected to compressive stresses. Moreover, in the (b) multi-layer models, the shear stress vanishes at the plate end at the physical interfaces, which is in good agreement with Rabinovitch and Frostig [17]. On the contrary, when the weak interface formulation is accounted in both vertical and horizontal directions, the obtained shear stress is not equal to zero and approaches result obtained by means of the used 2D FE model.

3.2 Fracture Energies Computation

In this Section, the computation of the energy release rate at the different analyzed locations is presented. The ERRs evaluation is obtained by means of the modified VCCT, which needs evaluation of the nodal forces at the crack tip and of the relative displacements at a small distance *da* from the tip. A strong interface formulation in

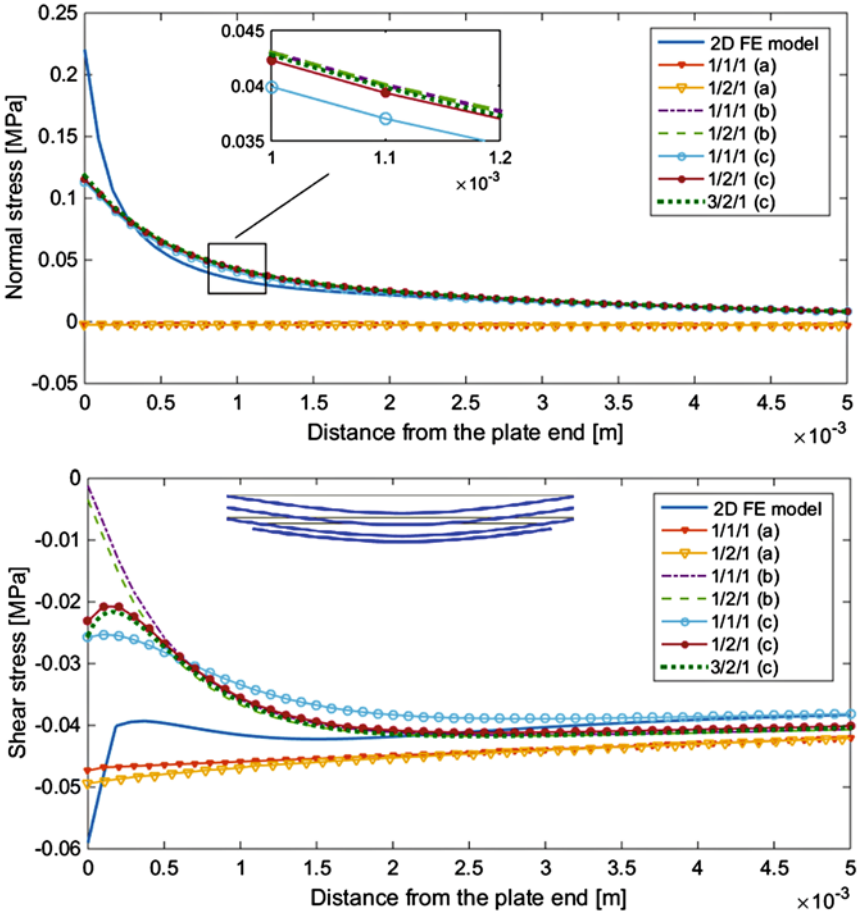

Fig. 3 Interfacial stresses near the plate end at the AC interface: comparison between the 2D FE continuum model and the proposed multi-layer formulation (TPB sample)

both vertical and horizontal directions is assumed, so that the individual ERRs can be evaluated from concentrated forces at the crack tip, which arise from the stress discontinuities and can be expressed in term of Lagrangian multipliers as in Eq. (16).

Regarding the 2D FE model, two types of mesh are implemented. When the ERRs are evaluated at the AC and the AP interfaces, a mapped mesh refined near the crack tip, with the minimum element size equal to 1 mm, is used. Conversely, when ERRs are investigated in the MA position, a free triangular mesh is adopted everywhere except around the crack tip, where a mapped mesh of four quadrilateral elements with a size of 0.1 mm is used. For the multi-layer models, two-noded straight elements with an Hermitian formulation are used for each layer, the mesh size is equal to 0.1 mm and the Timoshenko beam formulation is adopted.

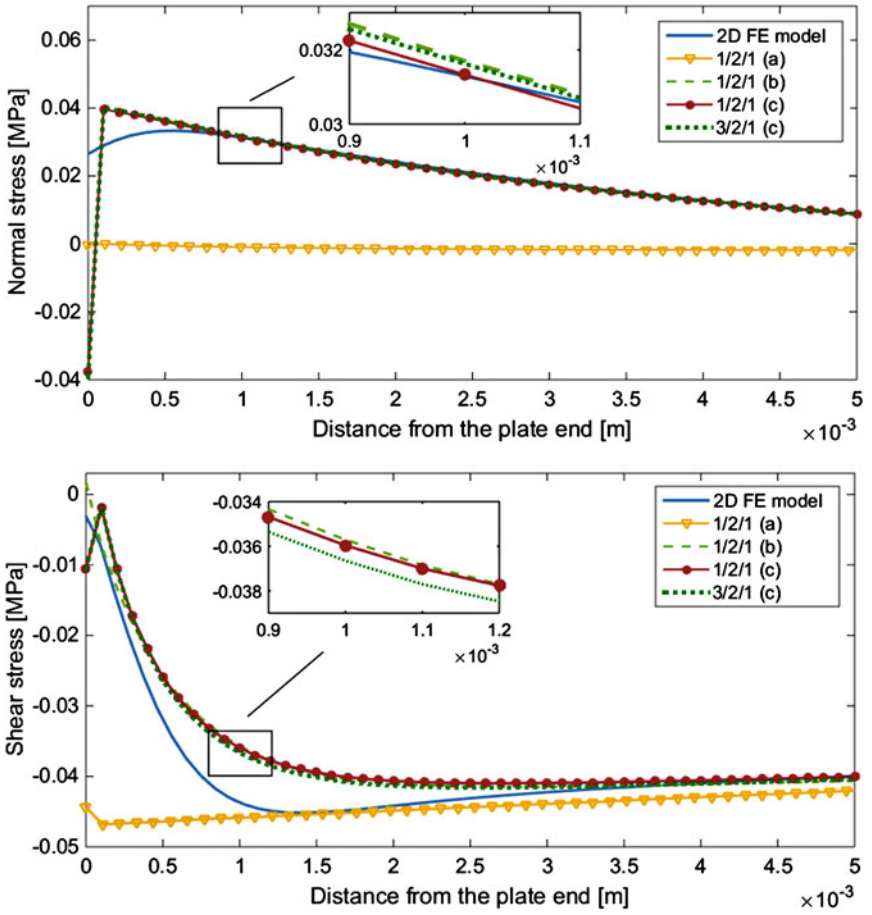

Fig. 4 Interfacial stresses near the plate end at the MA section: comparison between the 2D FE continuum model and the proposed multi-layer formulation (TPB sample)

In Table 3, individual and total ERRs normalized by using the factor $E_b H_b/(F/B)^2$ at the considered locations and for a fixed delamination length are reported. Results show a very good agreement between the 2D and the multi-layer models in terms of the total ERR. On the other hand, mode partition between the 2D FE and the multi-layer models does not agree everywhere, which is due to the fact that 2D FE solution involves an intrinsic oscillatory behavior in the evaluation of individual ERR components for an interface crack between two dissimilar layers. Conversely, when the oscillatory singularities do not occur as in the case of the MA section, a reasonable agreement with the 2D FE results is obtained also in terms of individual ERR mode components in spite of the small number of layers adopted in the multi-layer models.

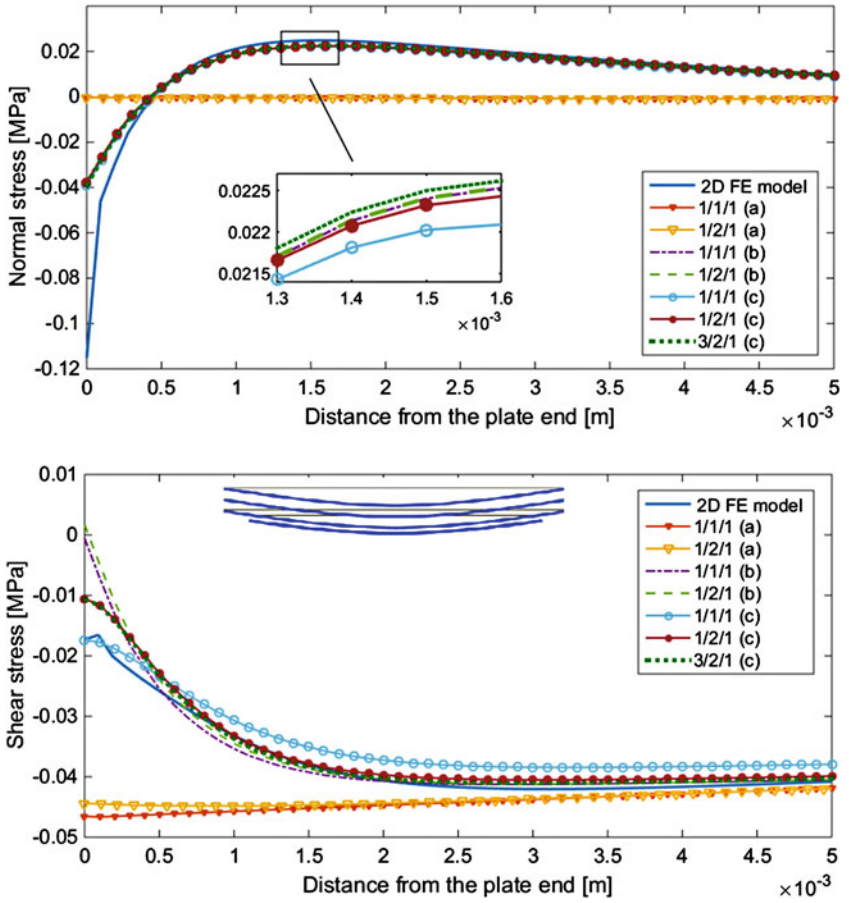

Fig. 5 Interfacial stresses near the plate end at the AP i interface: comparison between the 2D FE continuum model and the proposed multi-layer formulation (TPB sample)

Table 3 Normalized ERRs at different locations for a delamination length of 400 mm

FE model	$G_{I,AC}$	$G_{II,AC}$	$G_{Tot,AC}$	$G_{I,MA}$	$G_{II,MA}$	$G_{Tot,MA}$	$G_{I,AP}$	$G_{II,AP}$	$G_{Tot,AP}$
1/1/1 (a)	0.49	1.10	1.59	/	/	/	0.13	1.44	1.58
1/2/1 (a)	0.47	1.12	1.59	0.24	1.34	1.58	0.13	1.45	1.58
3/2/1 (a)	0.48	1.14	1.62	0.24	1.37	1.61	0.13	1.48	1.60
2*D*	0.66	0.97	1.63	0.31	1.30	1.61	0.13	1.48	1.61

4 Debonding Onset and Propagation

In order to predict crack initiation at interfaces of the strengthened system, the coupled criterion defined in Sect. 2.3 is here adopted. In particular, such a criterion was introduced in order to overcome difficulties in the onset evaluation due to the singularity of the stress field at plate end, and to the impossibility to apply the LEFM for vanishing cracks. Indeed, the present criterion, which is here adapted to mixed mode cases, requires a simultaneous fulfillment of an energetic and a tensional (integral or point-wise) condition according to Eqs. (17) and (18). The critical parameters considered in the numerical simulations are taken from [4, 6] and are summarized in the Table 4, where σ_c and τ_c are the tensile and the shear strengths, respectively.

The effectiveness of the proposed multi-layer modelling technique is verified in terms of predictions of debonding onset load, F_c for both integral and point-wise coupled criteria at the MA section, where also the 2D FE model gives reliable results in term of ERR components. Results are shown in Fig. 6, where subscript ML denotes multi-layer models and the arrangements are referred to the multi-layer models adopted for the interface stresses predictions, since ERRs are always calculated by using a strong interface formulation.

Numerical analyses conducted at all locations show that the point-wise criterion compared to the integral one leads to higher values for the critical load and, consequently, to lower critical lengths. Onset load errors between the multi-layer and 2D FE, which is the reference solution, is of low magnitude, but larger errors are

Table 4 Critical parameters adopted for the coupled stress–energy criterion

Location	σ_c (MPa)	τ_c (MPa)	G_{Ic}	α
AC	7.2	7.2	100	0.2
MA	7.2	7.2	500	0.2
AP	7.2	7.2	500	0.2

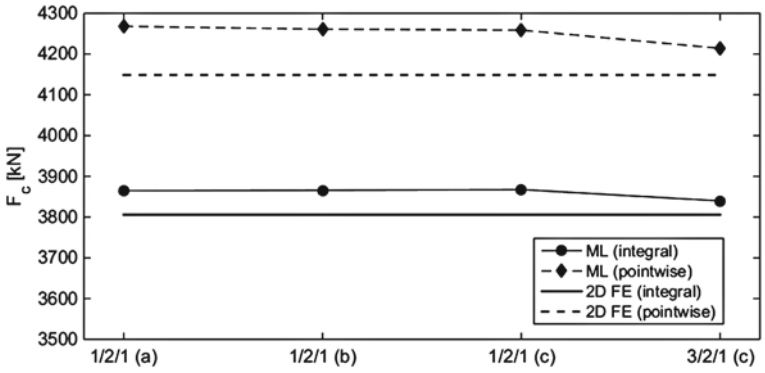

Fig. 6 Critical load at the MA section: comparison between 2D FE and multi-layer results

Table 5 Critical onset load for the 3/2/1 layer assembly (the 3/2/1 (*c*) model is adopted for interfacial stresses)

Stress condition	$F_{c,AC}$ (kN)	$F_{c,MA}$ (kN)	$F_{c,AP}$ (kN)
Integral	1939.849	3839.684	3932.603
Point-wise	2002.365	4213.965	4348.327

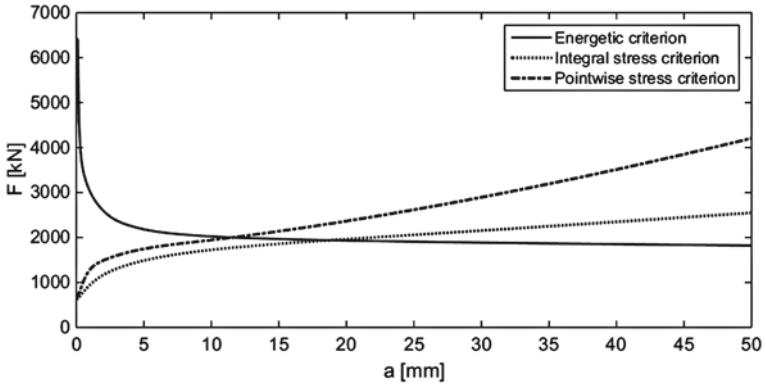

Fig. 7 Critical load and critical length according to the mixed mode coupled criterion at the AC interface for the 3/2/1 layer assembly (the 3/2/1 (*c*) model is adopted for interfacial stresses)

Table 6 Debonding onset load (F_c) for various multi-layer assemblies and different debonding locations across the adhesive layer

(Location) stress condition	$F_{c,1/2/1\ (a)}$	$F_{c,1/2/1\ (b)}$	$F_{c,1/2/1\ (c)}$	$F_{c,3/2/1\ (c)}$
(AC) Integral	1946.68	1958.10	1963.39	1939.85
(AC) Point-wise	2020.83	2016.61	2022.85	2002.37
(MA) Integral	3864.62	3865.68	3867.54	3839.68
(MA) Point-wise	4268.01	4261.02	4258.77	4213.97
(AP) Integral	3957.21	3958.14	3959.82	3932.60
(AP) Point-wise	4406.93	4398.55	4394.66	4348.33

obtained in term of onset length. However, the onset length is small compared to the FRP plate size. Numerical simulations show also that the most favorable location for crack initiation is the AC interface (see Table 5). In fact, a lowest load is required, which is true independently of the interface formulation adopted to capture interfacial stresses.

Therefore, in Fig. 7 load-delamination length curves satisfying the energetic and the stress (point-wise and integral) criteria are reported, respectively, when debonding occurs at the AC interface. The critical pair of crack onset load and length values can be obtained at the intersection between the two curves associated to the energetic and stress criteria. Finally, results given in Table 6 point out that the delamination

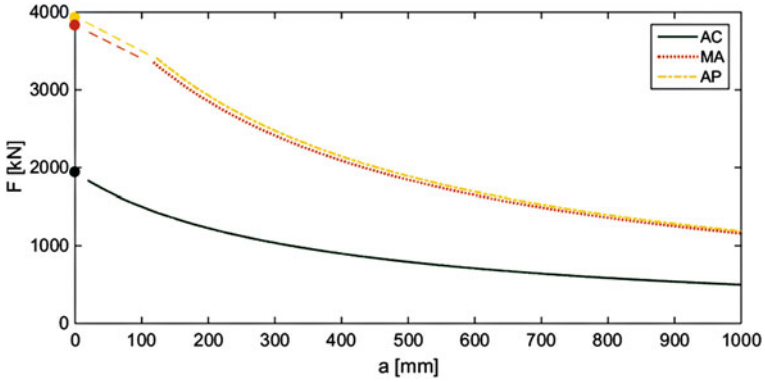

Fig. 8 Crack propagation for the 3/2/1 multi-layer assembly (the 3/2/1 (*c*) model is adopted for interfacial stresses)

prediction obtained by the different multi-layer models are in a reasonable agreement, whatever interface formulation is adopted for the stress distribution evaluation. Indeed, the error in interfacial normal stresses of the strong interface models is confined within a small zone near the plate end, and interfacial shear stresses, which are overestimated by the (a) models, play a more significant role in the fulfillment of the crack onset coupled criterion.

Once that edge debonding initiation of FRP in strengthened systems is predicted, the damage propagation can be studied with the aid of the mixed-mode fracture energy criterion. In Fig. 8 debonding propagation is illustrated for the three analyzed locations across the adhesive layers, by evaluating for each value of the debonding length a the associated load satisfying Eq. (19). In particular, the point at $a = 0$ corresponds to the critical load at the crack onset, which is attributed to a zero debonding length and evaluated with the proposed coupled criterion, while the onset length corresponds to the first point of the curves. Also during propagation, debonding at the AC interface takes place at lower loads than those required at MA and AP.

Then, in Fig. 9 the post-peak response of the strengthened system is shown, in which the mid-span deflection is measured at the lower beam sub-layer, being the axis origin taken at the AC interface. In particular: from point 1–2, the FRP is perfectly bonded to the reinforced concrete beam, and the load-displacement relationship is linear; at point 2, debonding starts at the AC interface; from point 2–3, debonding propagates along the interface until the mid-span, corresponding to a softening behavior of the load-displacement curve and finally, from point 3–4 debonding is beyond the mid-span, the whole system loses stiffness returning to that of the unstrengthened system.

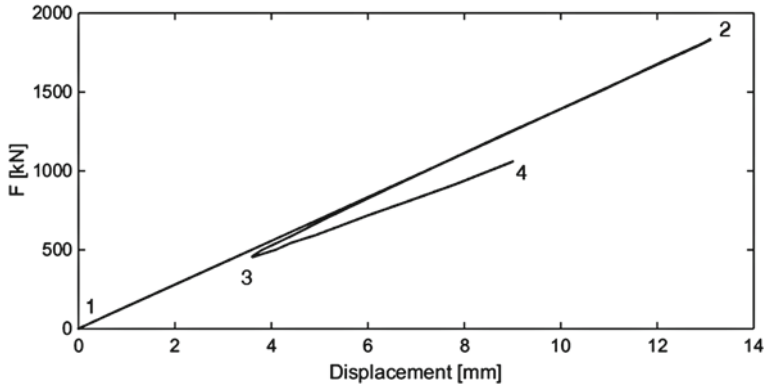

Fig. 9 Load-displacement curve for the 3/2/1 multi-layer assembly (the 3/2/1 (*c*) model is adopted for interfacial stresses) when debonding occurs at the AC interface

5 Conclusions

Edge debonding onset and propagation of beams strengthened with externally bonded FRP composite plates is here investigated numerically. A multi-layer model with first-order shear deformable mathematical layers is adopted for the structural system, with both strong and weak interface constitutive relations for the two physical interfaces, and strong interface constitutive relations for the mathematical interfaces. Numerical models are implemented by using a 1D finite element formulation, which allows evaluation of interfacial normal and shear stresses and of modal components of the ERR. Then, debonding initiation of a three point bending scheme is evaluated by means of a mixed mode coupled criterion accounting for both fracture energies and interfacial stresses, whereas debonding propagation is studied with the aid of a mixed mode energetic criterion.

In terms of interfacial stresses, multi-layers greatly reduce computational costs with respect to 2D FE models. Moreover, although a strong interface formulation does not allow to catch the actual behavior of stresses near the plate end, the error is confined in a small zone compared to the plate length. For this reason, multi-layer models with different interface formulation and mathematical layers lead to an accurate prediction of the load at debonding onset. The AC interface is the most favorite location for debonding initiation and propagation, and the load-displacement representation shows a softening behavior during debonding. Therefore, the proposed multi-layer models, together with the coupled criterion, are able to predict edge debonding initiation, and may be adapted to other geometries and debonding mechanisms, such as debonding in correspondence of intermediate flexural or shear crack within the base beam.

References

1. Anderson J, Tarasovs S, Spārņinš E (2010) Finite fracture mechanics analysis of crack onset at a stress concentrations in a UD glass/epoxy composite in off-axis tension. Compos Sci Technol 70(9):1380–1385
2. Bruno D, Greco F (2001) Mixed mode delamination in plates: a refined approach. Int J Solid Struct 38:9149–9177
3. Bruno D, Greco F, Lonetti P (2003) A coupled interface-multilayer approach for mixed mode delamination and contact analysis in laminated composites. International Journal of Solids and Structures 40:7245–7268
4. Bruno D, Carpino R, Greco F (2007) Modelling of mixed mode debonding in externally FRP reinforced beams. Compos Sci Technol 67(7–8):1459–1474
5. Bruno D, Greco F, Lo Feudo S, Nevone Blasi P (2016) Multi-layer modeling of edge debonding in strengthened beams using interface stresses and fracture energies. Eng Struct 109:26–42
6. Carpinteri A, Cornetti P, Pugno N (2009) Edge debonding in FRP strengthened beams: stress versus energy failure criteria. Eng Struct 31:2436–2447
7. COMSOL–AB (2014) COMSOL multiphysics reference manual
8. Cornetti P, Pugno N, Carpinteri A, Taylor D (2006) Finite fracture mechanics: a coupled stress and energy failure criterion. Eng Fract Mech 73:2021–2033
9. Cornetti P, Mantič V, Carpinteri A (2012) Finite fracture mechanics at elastic interfaces. Int J Solid Struct 49(7–8):1022–1032
10. Greco F, Lonetti P, Nevone Blasi P (2007) An analytical investigation of debonding problems in beams strenghtened using composite plates. Eng Fract Mech 74:346–372
11. Greco F, Leonetti L, Nevone Blasi P (2012) Non-linear macroscopic response of fiber-reinforced composite materials due to initiation and propagation of interface cracks. Eng Fract Mech 80:90–113
12. Greco F, Leonetti L, Lonetti P (2013) A two-scale failure analysis of composite materials in presence of fiber/matrix crack initiation and propagation. Int J Solid Struct 95:582–597
13. Hell S, Weißgraeber P, Felger J, Becker W (2014) A coupled stress and energy criterion for the assessment of crack initiation in single lap joints: a numerical approach. Eng Fract Mech 117:112–126
14. Hutchinson JW, Suo Z (1992) Mixed mode cracking in layered materials. Adv Appl Mech 29:63–191
15. Leguillon D (2002) Strength or toughness? A criterion for crack onset at a notch. Eur J Mech A/Solid 21:61–72
16. Mantič V (2009) Interface crack onset at a circular cylindrical inclusion under a remote transverse tension. Application of a coupled stress and energy criterion. Int J Solid Struct 46:1287–1304
17. Rabinovitch O, Frostig Y (2000) Closed-form high–order analysis of RC beams strengthened with FRP strips. J Compos Constr 4(2):65–74
18. Smith ST, Teng JG (2001) Interfacial stresses in plated beams. Eng Struct 23:857–871
19. Teng J, Zhang L, Smith S (2002) Interfacial stresses in reinforced concrete beams bonded with a soffit plate: a finite element study. Constr Build Mater 16:1–14
20. Zhang L, Teng J (2010) Finite element prediction of interfacial stresses in structural members bonded with a thin plate. Eng Struct 32:459–471

A Concurrent Multiscale Model for Crack Propagation Analysis in Composite Materials

Domenico Bruno, Fabrizio Greco, Lorenzo Leonetti and Paolo Lonetti

Abstract An innovative concurrent multiscale model is proposed for simulating transverse crack propagation in fiber-reinforced composite materials, based on a domain decomposition technique equipped with an adaptive zooming-in strategy. Under general loading, the crack path is not a priori known, as both fiber/matrix interface debonding and matrix cracking are involved. Therefore, a suitable crack path tracking strategy is proposed, based a moving mesh approach coupled with a shape optimization method. A number of numerical experiments have been carried out for assessing the validity of the proposed model, with reference to the complete failure analysis of a single notched fiber-reinforced composite beam subjected to both mode-I and mixed-mode crack propagation conditions.

1 Introduction

Composite materials are usually affected by a variety of damage mechanisms originating from pre-existing defects. In particular, fiber-reinforced composite laminates experience both intralaminar (such as matrix cracking and fiber/matrix interface debonding) and interlaminar mechanisms (i.e. inter-ply delamination). Such damage mechanisms are multiscale in nature; indeed, they initially take place at the microscopic level, but strongly influence the overall (macroscopic) behavior of composite

D. Bruno (✉) · F. Greco · L. Leonetti · P. Lonetti
Department of Civil Engineering, University of Calabria,
via P. Bucci, 87036 Rende (cs), Italy
e-mail: d.bruno@unical.it

F. Greco
e-mail: f.greco@unical.it

L. Leonetti
e-mail: lorenzo.leonetti@unical.it

P. Lonetti
e-mail: lonetti@unical.it

M. Frémond et al. (eds.), *Models, Simulation, and Experimental Issues in Structural Mechanics*, Springer Series in Solid and Structural Mechanics 8,
DOI 10.1007/978-3-319-48884-4_6

materials, leading to a highly nonlinear mechanical response associated with a progressive loss in strength and stiffness during the deformation history [5].

As a matter of fact, a proper analysis of damage mechanisms in composite materials would require a complete description of their microstructural details, leading to full-scale microscopic problems, whose numerical solution is inevitably unpractical due to the associated huge computational effort. Therefore, a large set of simplified strategies have been proposed in the literature for the failure analysis of composites, including micromechanical approaches; however, classical homogenization methods [6, 12, 20] are only effective when the micro- and the macro-scales are well separated. Such hypothesis ceases to hold when strain localization phenomena occur in locally periodic structures; moreover, the softening behavior cannot be properly accounted for, because of the ill-posedness of the macroscopic boundary value problem, as shown in [11]. In order to overcome such limitations, more sophisticated methods have been introduced, belonging to the wide class of multiscale methods; following [2], three groups of multiscale methods can be identified, depending on the nature of the micro-to-macro coupling: hierarchical, semi-concurrent and concurrent methods.

In hierarchical (or sequential) methods, a "one-way" coupling is established between the microscopic and macroscopic sub-problems, i.e. the information is only passed from lower to higher scales; classical micromechanical and homogenization approaches belong to this group. In semi-concurrent methods, also named as computational homogenization approaches, a microscopic boundary value problem is associated with each integration point of the discretized macroscopic domain, in order to obtain the local governing equation at the macroscopic level; this group of methods allows one to determine a microscopically informed constitutive response, thus avoiding the use of a phenomenological stress-strain relationship at the macro-scale. Finally, concurrent methods abandon the concept of scale transition in favor of the concept of scale embedding, according to which sub-problems exhibiting different spatial resolution are simultaneously solved, in the spirit of domain decomposition methods (DDMs).

In this work, a novel concurrent multiscale method is presented, able to simulate the transverse crack propagation in fiber-reinforced composite materials, taking advantage of a non-overlapping domain decomposition method, used in conjunction with an adaptive model refinement technique able to continuously update the finely resolved subdomain around a macroscopic crack propagating along a non-prescribed path. The competition between fiber/matrix interface debonding and kinking phenomena from and towards the matrix is taken into account, as well the continuous matrix cracking, by employing ad-hoc formulated fracture criteria. Matrix cracking is numerically predicted by using an innovative shape optimization method based on the synergistic application of a moving mesh technique and an optimization strategy; such an ingredient makes the present approach different form existing concurrent multiscale methods, which usually adopt damage models or cohesive zone models to simulate damage propagation (see, for instance, [10]). The paper can be regarded as an extension of the previous authors' work [13], since it incorporates enhancements in the crack propagation modeling technique and proposes original simplified

comparison models in order to assess the validity of the multiscale approach. The related numerical experiments have been carried out with reference to a single notched composite beam subjected to different loading conditions involving both mode-I and mixed-mode crack propagation.

2 Theoretical Framework

In this section, the main theoretical concepts forming the base for our numerical approach, are discussed. In Sect. 2.1, the general framework of concurrent multiscale modeling is illustrated, by extending the multiscale non-overlapping domain decomposition scheme to the case of damaging composite materials, whereas in Sect. 2.2, the attention is paid to fracture modeling in composite materials, with reference to the competition between different damage mechanisms including matrix cracking and fiber/matrix interface debonding.

2.1 A Multiscale Domain Decomposition Scheme for Damaging Fiber-Reinforced Composites

Let us consider a cracked composite structure occupying the open set $\Omega \in \mathbb{R}^3$, as depicted in Fig. 1a, subjected to general external loads in a quasi-static manner; its boundary $\partial\Omega$ is assumed to be Lipschitz continuous, such that $\partial_N\Omega \cup \partial_D\Omega = \partial\Omega$ and $\partial_N\Omega \cap \partial_D\Omega = \emptyset$, $\partial_N\Omega$ and $\partial_D\Omega$ being the portions subjected to Neumann and Dirichlet boundary conditions, respectively; moreover, $\partial_D\Omega \neq \emptyset$ in order to avoid rigid-body motions. Such a heterogeneous body is composed of a doubly periodic distribution of unit cells, whose microstructure is the same as for a reference cell, denoted as repeating unit cell (RUC). The given crack set Γ_c, at which strong

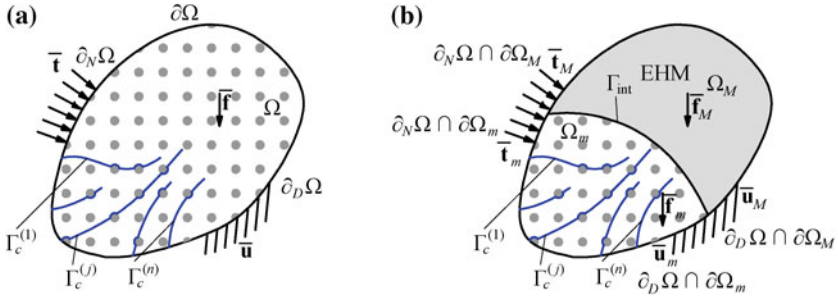

Fig. 1 Crack propagation problem in a periodic composite structure: (**a**) full-scale microscopic formulation; (**b**) multiscale formulation, coupling a fine-scale and a coarse-scale subdomain, the latter being filled with an equivalent homogenized material (EHM)

discontinuities (displacement jumps) occur, is represented by a number of physical surfaces, denoted by $\Gamma_c^{(i)}$ with $i = 1, \ldots, n$. If all the micro-constituents are assumed to be made of linearly hyperelastic material, the elasticity problem at fixed crack set under small deformation and contact-free crack assumptions can be mathematically stated as a classical elliptic PDE system with associated boundary conditions. The related weak form can be written as:

$$\int_{\Omega\setminus\Gamma_c} [\boldsymbol{C} : \boldsymbol{\varepsilon}(\boldsymbol{u})] : \boldsymbol{\varepsilon}(\boldsymbol{v}) d\Omega = \int_{\Omega\setminus\Gamma_c} \bar{\boldsymbol{f}} \cdot \boldsymbol{v} d\Omega + \int_{\partial_N\Omega} \bar{\boldsymbol{t}} \cdot \boldsymbol{v} d\Gamma \quad \forall \boldsymbol{v} \in V(\Omega\setminus\Gamma_c) \,, \tag{1}$$

where $\boldsymbol{u} \in H^1(\Omega\setminus\Gamma_c)$, $\boldsymbol{u} = \bar{\boldsymbol{u}}$ on $\partial_D\Omega$, $\boldsymbol{u}$ being the (actual) unknown displacement field, $\bar{\boldsymbol{u}}$ the prescribed displacement on $\partial_D\Omega$, and $H^1(\Omega\setminus\Gamma_c)$ denoting the usual Hilbert space of order 1 on $\Omega\setminus\Gamma_c$; moreover $V(\Omega\setminus\Gamma_c) = \left\{\boldsymbol{v} \in H^1(\Omega\setminus\Gamma_c), \boldsymbol{v} = \boldsymbol{0} \text{ on } \partial_D\Omega\right\}$ is the set of virtual displacement fields, $\bar{\boldsymbol{f}}$ and $\bar{\boldsymbol{t}}$ are the external body and surface forces, respectively, and $\boldsymbol{C}$ is the fourth-order elasticity tensor. The latter one is assumed to be rapidly varying with respect to the macro-variable $\boldsymbol{X}$, and thus the elasticity problem (1) is rather complex to solve without a suitable modeling strategy.

In the presence of evolving defects, classical homogenization techniques inevitably fail due to the loss of macro-homogeneity and periodicity assumptions; therefore, here a different approach is proposed, based on a multiscale domain decomposition scheme [18]. Without loss of generality, let us partition the original domain Ω into only two non-overlapping subdomains Ω_M and Ω_m. As $\boldsymbol{C}$ is assumed to be periodic only in Ω_M, it follows that:

$$\boldsymbol{C}(\boldsymbol{X}) = \begin{cases} \boldsymbol{C}_M^{\varepsilon}(\boldsymbol{X}), & \text{if } \boldsymbol{X} \in \Omega_M \\ \boldsymbol{C}_m(\boldsymbol{X}), & \text{if } \boldsymbol{X} \in \Omega_m, \end{cases} \tag{2}$$

where the superscript ε indicates the dependence on a small period, identified by the RUC size. After this position, the problem (1) can be rewritten in the following equivalent multi-domain form, involving an additional boundary Γ_{int} generated by the considered partition:

$$\begin{cases} \int_{\Omega_M} [\boldsymbol{C}_M^{\varepsilon} : \boldsymbol{\varepsilon}(\boldsymbol{u}_M^{\varepsilon})] : \boldsymbol{\varepsilon}(\boldsymbol{v}_M) d\Omega = \\ \qquad = \int_{\Omega_M} \bar{\boldsymbol{f}}_M \cdot \boldsymbol{v}_M d\Omega + \int_{\partial\Omega_M\cap\partial_N\Omega} \bar{\boldsymbol{t}}_M \cdot \boldsymbol{v}_M d\Gamma \quad \forall \boldsymbol{v}_M \in V(\Omega_M) \\ \int_{\Omega_m\setminus\Gamma_c} [\boldsymbol{C}_m : \boldsymbol{\varepsilon}(\boldsymbol{u}_m)] : \boldsymbol{\varepsilon}(\boldsymbol{v}_m) d\Omega = \\ \qquad = \int_{\Omega_m\setminus\Gamma_c} \bar{\boldsymbol{f}}_m \cdot \boldsymbol{v}_m d\Omega + \int_{\partial\Omega_m\cap\partial_N\Omega} \bar{\boldsymbol{t}}_m \cdot \boldsymbol{v}_m d\Gamma \quad \forall \boldsymbol{v}_m \in V(\Omega_m\setminus\Gamma_c) \\ \int_{\Omega_M} [\boldsymbol{C}_M^{\varepsilon} : \boldsymbol{\varepsilon}(\boldsymbol{u}_M^{\varepsilon})] : \boldsymbol{\varepsilon}(\tilde{\boldsymbol{w}}_M) d\Omega + \int_{\Omega_m\setminus\Gamma_c} [\boldsymbol{C}_m : \boldsymbol{\varepsilon}(\boldsymbol{u}_m)] : \boldsymbol{\varepsilon}(\tilde{\boldsymbol{w}}_m) d\Omega = \\ \qquad = \int_{\Omega_M} \bar{\boldsymbol{f}}_M \cdot \tilde{\boldsymbol{w}}_M d\Omega + \int_{\Omega_m\setminus\Gamma_c} \bar{\boldsymbol{f}}_m \cdot \tilde{\boldsymbol{w}}_m d\Omega \quad \forall \boldsymbol{w} \in V_\Gamma \end{cases} \tag{3}$$

where $\boldsymbol{u}_M^{\varepsilon} \in H^1(\Omega_M)$, $\boldsymbol{u}_M^{\varepsilon} = \bar{\boldsymbol{u}}_M$ on $\partial\Omega_M \cap \partial_D\Omega$ and $\boldsymbol{u}_m \in H^1(\Omega_m\setminus\Gamma_c)$, $\boldsymbol{u}_m = \bar{\boldsymbol{u}}_m$ on $\partial\Omega_m \cap \partial_D\Omega$; moreover, $V(\Omega_M)$ and $V(\Omega_m\setminus\Gamma_c)$ are the sets of test functions belonging to $H^1(\Omega_M)$ and $H^1(\Omega_m\setminus\Gamma_c)$, respectively, and vanishing on $\left\{\Gamma_{\text{int}} \cup \partial_D\Omega\right\} \cap$

$\partial\Omega_M$ and $\left\{\Gamma_{\text{int}} \cup \partial_D\Omega\right\} \cap \partial\Omega_m$, respectively; finally, V_Γ denotes the set of test functions $\boldsymbol{w}$ defined on Γ_{int}, which are traces of functions of V, whereas $\tilde{\boldsymbol{w}}_M$ and $\tilde{\boldsymbol{w}}_m$ are arbitrary continuous extensions of $\boldsymbol{w}$ to Ω_M and $\Omega_m \backslash \Gamma_c$, respectively, such that $\tilde{\boldsymbol{w}}_M = \boldsymbol{0}$ on $\partial\Omega_M \backslash \Gamma_{\text{int}}$ and $\tilde{\boldsymbol{w}}_m = \boldsymbol{0}$ on $\partial\Omega_m \backslash \Gamma_{\text{int}}$, respectively.

The sub-problem defined over Ω_M, where the periodicity assumption is assumed to hold, can be successfully tackled by replacing the original microstructure with an equivalent homogenized material (see Fig. 1b), whose effective moduli tensor is obtained by a first-order periodic homogenization scheme applied to the given repeating RUC. It follows that an inherent separation of scales exists between Ω_M and Ω_m; as a matter of fact, the adopted subscripts M and m stand for macro- and micro-scale, respectively.

2.2 Competition Between Damage Mechanisms in Transversely Loaded Fiber-Reinforced Composites

In this section, the competition between different damage mechanisms in fiber-reinforced composite materials is discussed, with exclusive attention to the case of transverse cracking. To this end, let us consider a multiphase solid containing a single propagating crack of finite length l; thus, an energy-based crack advancing criterion can be formulated in a quasi-static rate-independent setting by means of classical Karush–Kuhn–Tucker (KKT) conditions:

$$\begin{cases} \dot{l} \geq 0 \\ G(l) - G_c \leq 0 \\ \left(G(l) - G_c\right)\dot{l} = 0, \end{cases} \tag{4}$$

$\dot{l}$ being the rate of the crack length, G the strain energy release rate associated with l, and G_c the fracture toughness, regarded as a material constant for crack tips embedded in an isotropic homogeneous phase or as a function of the mode mixity for interface cracks. A crack length control scheme [7] is used, allowing to reformulate the nonsmooth and highly nonlinear crack propagation problem as a sequence of linear problems.

Furthermore, a proper simulation of damage phenomena at the microscopic scale should require additional criteria for tracking the crack path; here, a new crack propagation algorithm is proposed, accounting for the competition between matrix cracking, fiber/matrix interface debonding and crack kinking in/out of the interface.

2.2.1 Matrix Micro-Cracking

Matrix micro-cracking usually leads to the nucleation of macroscopic cracks via coalescence phenomena, and therefore it is one of the most relevant damage mechanisms

for transverse loading conditions. In this case, the crack path is not known a priori, thus classical fracture approaches require the adoption of additional kinking criteria able to find the current crack direction, such as the maximum strain energy release rate (MSERR) criterion. Such a criterion is here enforced in a variational setting, by considering the following expression for G, written as a function of both the total crack length l and the kink angle θ:

$$G(l,\theta) = -\frac{\partial \Pi^\star}{\partial l}(l,\theta) \approx -\frac{\Pi^\star(l+\Delta l,\theta) - \Pi^\star(l)}{\Delta l} \,, \tag{5}$$

where Δl is the crack length increment, and $\Pi^\star$ indicates the total potential energy at equilibrium:

$$\Pi^\star(l) = \Pi(\boldsymbol{u}(l), l) = \inf_{\boldsymbol{u}\in U_a(l)} \Pi(\boldsymbol{u}, l) \,, \tag{6}$$

U_a being the set of admissible displacement fields. By inserting Eq. (6) into Eq. (5), the MSERR criterion can be reformulated as the double minimization of Π with respect to both the displacement field and the crack direction:

$$\sup_\theta G(l,\theta) \Rightarrow \inf_\theta \Pi^\star(l+\Delta l,\theta) \Rightarrow \inf_\theta \left[\inf_{\boldsymbol{u}\in U_a(l+\Delta l,\theta)} \Pi(\boldsymbol{u}, l+\Delta l, \theta) \right] , \tag{7}$$

which is numerically performed by testing a number of different trial crack directions. Classically, this problem has been tackled by performing a remeshing operation for each tested direction, thus leading to a highly time consuming solution. In order to reduce the computational cost, the moving mesh strategy proposed in the previous authors' work [13] is here used. In this context, the geometry update needed for determining the actual crack direction is performed by means of a nodal relocation technique, without any topological change of the mesh, within the ALE (Arbitrary Lagrangian-Eulerian) framework; classical remeshing is only used for updating the geometry after each crack advance.

Accordingly, the minimization problem (7) at fixed crack length is solved by adopting a loop-in-loop algorithm requiring the definition of two nested optimization sub-steps; in the inner loop, the BVP associated with the minimization of Π with respect to $\boldsymbol{u}$ at fixed θ is solved, in order to find the equilibrium state for the given external loads; in the outer loop, the minimization with respect to θ is performed, devoted to the search for the crack direction maximizing the strain energy release rate (see [13] for further details).

2.2.2 Crack Kinking In/Out of a Fiber/Matrix Interface

Transverse cracking in fiber-reinforced composite materials often involves a strong interaction between the main propagating crack and the preexistent (undamaged or partially damaged) material interfaces: in the case of inclusions stiffer than the

surrounding matrix, a crack growing inside the matrix tends to be deflected away from the interface, possibly experiencing an arrest event, due to the well-known vanishing behavior of the strain energy release rate at fixed external load as the crack tip approaches an interface [17]. This crack arrest can be avoided by accounting for the competition between matrix crack propagation and crack nucleation at the fiber/matrix interface, here enforced by using the following stress- and energy-based criterion, introduced in the previous authors' work [13]:

$$\begin{cases} \beta_c^2 \hat{G}(l_c) = G_c \\ \beta_c^2 \left[\left(\frac{\langle \hat{\sigma}(l_c) \rangle}{\sigma_c} \right)^2 + \left(\frac{\hat{\tau}(l_c)}{\tau_c} \right)^2 \right] = 1, \end{cases} \tag{8}$$

where β_c is the critical load factor, l_c is the critical crack ligament, $\hat{G}$ is the strain energy release rate per unit load factor for the main propagating crack, $\hat{\sigma}$ and $\hat{\tau}$ are the normal and tangential stress per unit load factor, σ_c and τ_c are the corresponding strengths, and $\langle \cdot \rangle$ denotes the Macaulay brackets; this hybrid criterion is found by combining the classical Griffith's criterion for the matrix crack and a stress-based failure criterion for the interface, under the hypothesis of abrupt rupture of the crack ligament.

Conversely, a crack propagating along a fiber/matrix interface tends to kink out for sufficiently high values of the mode mixity, according a suitably established criterion measuring this tendency; according to [14], kinking is favored over continuous interface debonding if

$$\frac{G_{\max}^{(m)}}{G_c^{(m)}} > \frac{G^{(\Gamma)}}{G_c^{(\Gamma)}(\psi)}, \tag{9}$$

where $G_{\max}^{(m)}$ is the maximum strain energy release rate of the matrix crack with respect to the kink angle, $G_c^{(m)}$ is the mode I fracture energy of the matrix, $G^{(\Gamma)}$ is the interfacial strain energy release rate, and $G_c^{(\Gamma)}(\psi)$ denotes the toughness function of the interface, depending on the mode mixity ψ according to a properly identified phenomenological law; in this work, the same law as in [16] is adopted.

3 Description and Numerical Implementation of the Concurrent Multiscale Strategy

In this section, the proposed multiscale strategy is described, together with the needed details for its numerical implementation within a standard displacement-based finite element setting. The principal attention is devoted to the adaptive model refinement strategy, allowing the above-discussed theoretical aspects to be incorporated in an efficient numerical model able to continuously adjust itself during the damage growth.

3.1 *Adaptive Model Refinement Strategy for Crack Propagation in Periodic Composite Materials*

The proposed adaptive model refinement strategy adopted within the above-discussed multiscale framework is here illustrated. Adaptivity plays a key role in the present work, assuring for the adopted multiscale model the same accuracy as the full-scale microscopic models and the same efficiency as the purely macroscopic models; in fact, under general loading conditions, the crack trajectory is not known a priori, so that the zone of interest, i.e. the region directly influenced by the presence of micro-cracks and thus requiring a fine-scale discretization, has to be continuously updated following the propagating crack tip.

Several model refinement (zooming-in) criteria have been proposed in the literature for determining the extension of the zone of interest, usually involving either periodicity or macro-homogeneity indicators (see, for instance, [10]); in this work, a simple heuristic criterion is proposed, which is valid only for periodic microstructures and only depends on the current crack geometry. The point of departure is the construction of a regular grid by which the original domain is discretized in macro-elements, whose size is identified by the RUC size; given an initial crack configuration, the macro-elements affected by the model refinement (or zooming-in) procedure are those intersected by the crack path, plus the cells adjacent to the one containing the crack tip; the remaining macro-elements are equipped with equivalent material properties computed by performing a first-order homogenization on the RUC prototype. This adaptive model refinement strategy is sketched in Fig. 2, for different crack propagation steps; the aim of the proposed approach is to push the micro-to-macro interface far enough to avoid spurious effects related to the influence on the gluing condition between nonmatching meshes on the composite's overall mechanical behavior.

If used in conjunction with the crack length control scheme, such a strategy can be implemented within a dedicated multiscale algorithm for the automatic simulation of transverse crack propagation in fiber-reinforced composite materials. This algorithm

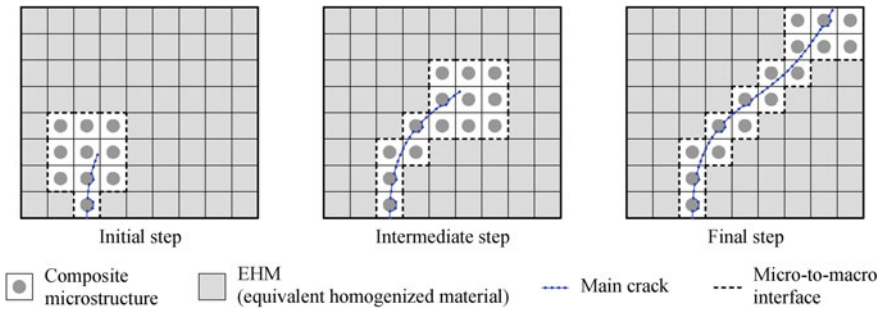

Fig. 2 Heuristic adaptive model refinement strategy for the crack propagation analysis in composite materials

is composed of two separated macro-step. In the first one, a classical first-order periodic homogenization scheme is used to determine the macroscopic elastic moduli of the equivalent homogenized material to be assigned outside of the zone of interest; in the latter one, an incremental-iterative methodology is adopted to perform the above-discussed adaptive model refinement.

The entire algorithm has been implemented within the commercial finite element environment COMSOL Multiphysics [8], chosen for its extended scripting capabilities for pre-processing, model manipulation and post-processing; in this work, a MATLAB code linked to the finite element software has been developed in order to automatically perform the main loop, responsible for the model adaptation stage during the numerical simulation.

4 Numerical Examples

The validity of the proposed multiscale approach for the crack propagation analysis in transversely loaded composite structures is assessed in this section, with reference to simple tests involving both mode I and mixed-mode loading conditions. The related numerical results are compared with those obtained from different models, including analytical solutions, purely homogenized solutions and fully-meshed solutions. A complete failure analysis has been carried out for each considered case, in order to evaluate both the peak and the post-peak response of a periodic composite structure with evolving damage configuration.

4.1 Description of the Reference Specimen

A 2D periodic fiber-reinforced composite structure is considered, obtained from the doubly periodic repetition of a square unit cell, playing the role of representative volume element (RVE), made of a centered circular fiber embedded in a softer matrix, as shown in Fig. 3a; the side of such a unit cell is set as 30 μm, whereas the fiber diameter is taken equal to 15 μm unless otherwise stated, leading to a fiber/matrix volume ratio

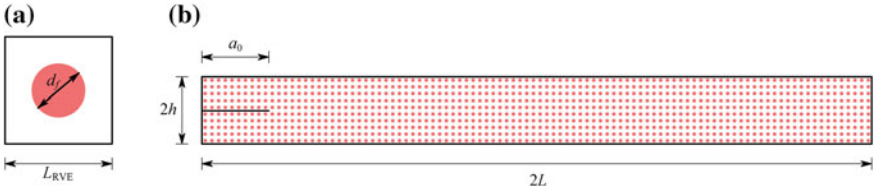

Fig. 3 Geometric configuration of the reference fiber-reinforced microstructure: (**a**) RUC prototype; (**b**) geometry of the macroscopic specimen

Table 1 Elastic properties of the bimaterial system

Component	Material	E (GPa)	ν	G_c (N/m)
Matrix	Epoxy	2.79	0.33	100
Fiber	Glass	70.8	0.22	–

Table 2 Mechanical properties of the fiber/matrix interface

σ_c (MPa)	τ_c (MPa)	G_{Ic} (N/m)	λ
150	200	25	0.3

of about 20%. The elastic properties of the considered bimaterial system are listed in Table 1; in addition, the fiber/matrix interface, which is assumed undamaged at the beginning of analysis, is characterized by the four strength/toughness properties shown in Table 2. Moreover, the reference length l_{ref} necessary to compute the mode mixity angle, expressed as angular distance along the circular interface with respect to the crack tip, is set as 0.1° (see [16] for additional details).

The reference specimen is the pre-notched composite beam shown in Fig. 3b subjected to transverse loading conditions; its half-length L is set as 1.5 mm, whereas each arm's height h is equal to 0.15 mm; moreover, the initial crack length a_0 is set as 0.3 mm. All the present numerical simulations have been carried out assuming plane strain conditions and considering a thickness of 1 mm.

For the numerical simulations performed by using the proposed multiscale method, referred to as multiscale numerical simulations (MNS), the macroscopic and the microscopic subdomains are meshed differently; a coarse mapped mesh composed of four-node square elements (here named as macro-elements) is used for discretizing the macroscopic subdomain, whereas an unstructured mesh made of three-node triangular elements is adopted for the zone of interest (see Fig. 4a). Moreover, a suitable mesh refinement is performed along the fiber/matrix interfaces and the contours on which the J-integral (used for determining the strain energy release rate) is computed; the entire mesh with reference to the initial crack configuration is composed of 48,394 elements, resulting in 50,326 DOFs. Conversely, the numerical model used for the direct numerical simulation (DNS) has been represented by using the same fine mesh as in the zone of interest of the multiscale model (see Fig. 4b). In detail, this mesh at the beginning of simulation is made of 617,782 elements, resulting in 619,996 DOFs.

4.2 Numerical Results: The Double Cantilever Beam (DCB) Test

In this section, the numerical results obtained via the proposed multiscale approach are presented, with reference to a classical double cantilever beam (DCB) test per-

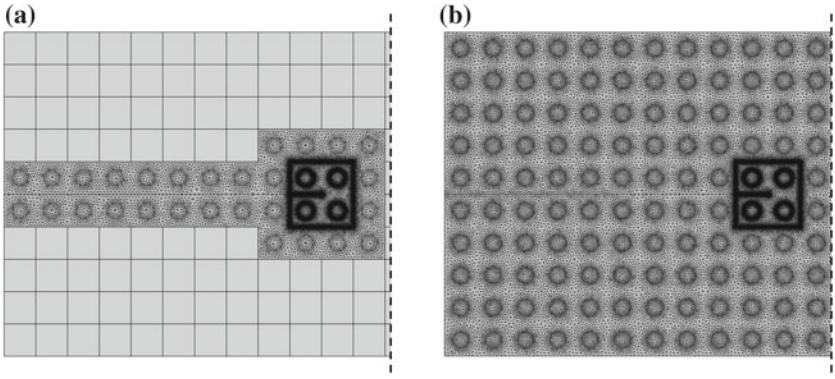

Fig. 4 Left end portion of the adopted mesh for the reference composite structure: (**a**) nonconforming mesh for the multiscale numerical simulation; (**b**) fine resolution mesh for the direct numerical simulation

formed on the specimen of Fig. 3b, involving a pure mode I (see, for instance, [1]). It is work noting that the considered combination of material and geometric parameters does not lead to the onset of fiber/matrix interface debonding, and therefore, during the entire numerical simulation, the crack runs straight within the matrix. The macroscopic mechanical behavior in terms of force-displacement curve is shown in Fig. 5; please note that the external load is applied as a prescribed crack mouth opening displacement Δ. Each point represents an equilibrium state for quasi-static propagation conditions, corresponding to a crack configuration obtained by extending the previous crack by a prescribed length increment, here chosen equal to 3 μm.

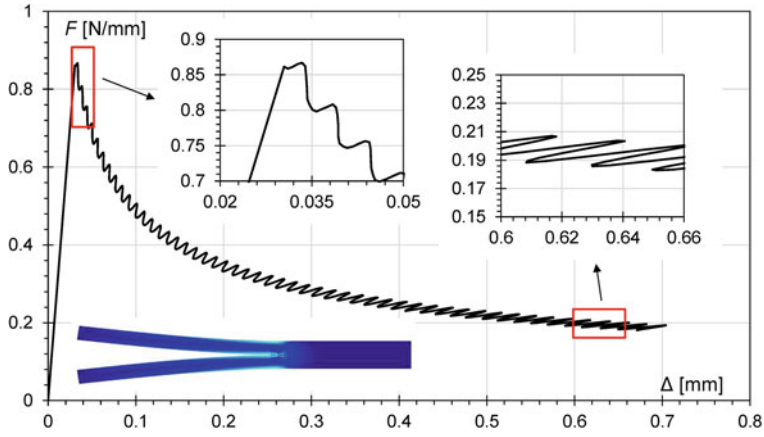

Fig. 5 Force versus imposed displacement for the DCB test by means of a multiscale numerical simulation

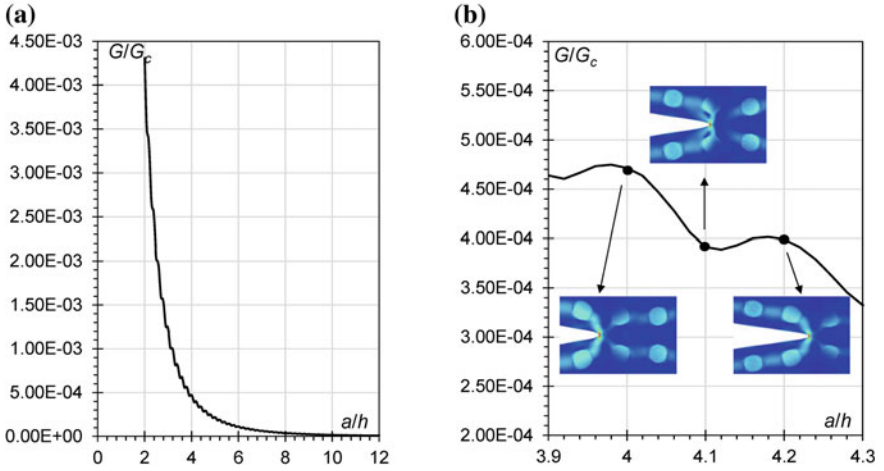

Fig. 6 Dimensionless strain energy release rate per unit prescribed displacement as a function of the dimensionless crack length for the DCB test by means of a multiscale numerical simulation: **a** global behavior; **b** local behavior

As expected, the overall structural response is globally stable, experiencing a progressive loss in stiffness and strength for increasing values of the crack length; such a behavior is coherent with the strain energy release rate curve, shown in Fig. 6a, whose trend is globally descending. However, the local behavior of Figs. 5 and 6a appears to be oscillating with a small period directly depending on the RUC size; this is due to the microstructural effects, and specifically, to the local strengthening provided by the rigid inclusions, as highlighted in Fig. 6b.

The numerical results obtained via the proposed multiscale strategy have been validated by comparing them with those referring to direct numerical simulations (DNS) performed by using a full-scale microscopic problem, regarded as our reference model. Moreover, additional comparisons with two simplified models have been considered; the first one is a purely homogenized model, obtained by applying everywhere a first-order homogenization scheme; the latter one is the analytical model proposed in [3, 4], i.e. a two-layer plate model based on the first-order shear theory.

In Fig. 7 all the considered solutions are superposed, in terms of force-displacement curves. A very good accordance between the different models can be observed; obviously, only the multiscale numerical simulation (MNS) is able to capture the oscillating behavior of the structural response, being a distinct feature of fully meshed models (see DNS curve in Fig. 7), whereas the other comparison models provide only an averaged structural behavior, which is however globally matching with the previously considered numerical results.

The analytical model provides a slightly overestimated stiffness with respect to the other considered models, owing to approximated kinematic assumptions for the plate theory; in fact, especially for short crack lengths, the plate models (also considering

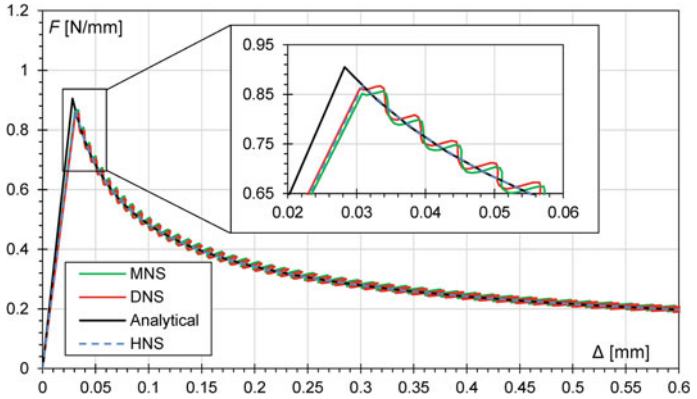

Fig. 7 Comparisons between the multiscale numerical simulation (MNS), the direct numerical simulation (DNS), the homogenized numerical simulation (HNS), and the analytical solution from [3], in terms of load-displacement curve for the DCB test

the shear deformability) are no longer valid. The numerical errors of the considered models with respect to the reference one are listed in Table 3, in terms of critical load, apparent stiffness and strain energy release rate for two different values of the dimensionless crack length a/h, i.e. 2 and 10. The multiscale numerical simulation

Table 3 Comparison between the direct numerical simulation (DNS), the multiscale numerical simulation (MNS), the homogenized numerical simulation (HNS) and the analytical solution from [3] in terms of critical load, stiffness and strain energy release rate for two values of the crack length: $a/h = 2$ and $a/h = 10$

		Critical load		Stiffness		Energy release rate	
		F (N/mm)	Error$_F$ (%)	K (N/mm^2)	Error$_K$ (%)	G(N/mm)	Error$_G$ (%)
$a/h = 2$	DNS (reference)	0.851	–	27.65	–	4.218e−3	–
	MNS (present model)	0.862	1.20	28.28	2.28	4.309e−3	2.15
	HNS	0.868	2.01	28.07	1.52	4.179e−3	−0.943
	Analytical solution [3]	0.905	6.30	32.03	15.8	5.010e−3	18.8
$a/h = 10$	DNS (reference)	0.212	–	0.440	–	1.727e−5	–
	MNS (present model)	0.214	1.16	0.450	2.25	1.765e−5	2.16
	HNS	0.219	3.23	0.447	1.60	1.673e−5	−3.13
	Analytical solution [3]	0.221	4.29	0.461	4.78	1.743e−5	0.939

is associated with very small percentage errors with respect to the direct numerical simulation, especially in terms of critical load, being overestimated by a little more than 1%; the homogenized numerical simulation also leads to a little deviation from the reference solution, providing a small underestimation of the strain energy release rate.

4.3 Numerical Results: The Mixed Mode Bending (MMB) Test

In this section, the mixed-mode bending (MMB) test, introduced in [19], has been considered for the given end-notched composite beam, for investigating the transverse micro-cracking along a non-prescribed path. The test apparatus is depicted in Fig. 8, with reference to a generic eccentricity e of the force F with respect to the beam's midsection; however, in the following computations, only the case $e = L$ is considered, characterized by a mode II dominated fracture.

Figure 9 shows the overall structural behavior in terms of force-displacement curve, obtained by assuming a crack length increment of 1 μm; the differently marked equilibrium branches represents either the crack propagation within the matrix or the fiber/matrix interface debonding. After a severe snap-back phenomenon associated with the crack propagation along the nearest interface to the initial crack tip, a number of alternating stable/unstable equilibrium branches can be identified during the matrix crack propagation, leading to a post-peak behavior more irregular than in the DCB test.

In addition, three notable points have been highlighted in Fig. 9, i.e. the turning points characterized by the increment of the residual strength and/or the related displacement; this recover in strength essentially arises from the fact that the crack is constrained to rum along the interface; in fact, while turning around the fiber, the

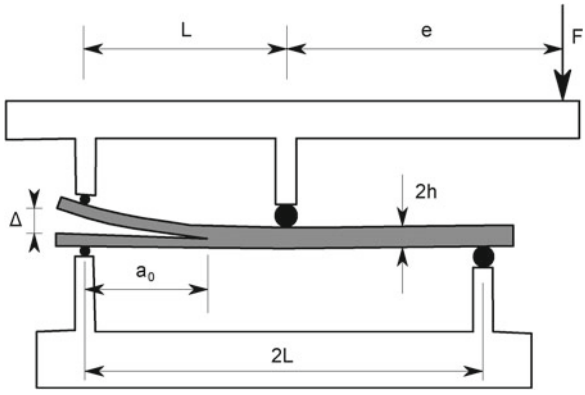

Fig. 8 Mixed-mode bending (MMB) test: geometry and boundary conditions

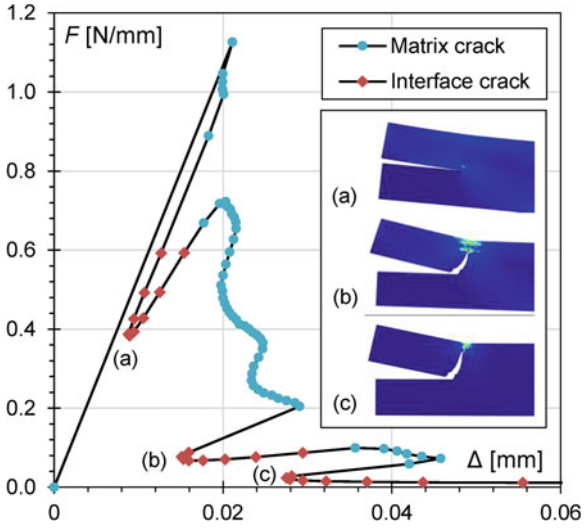

Fig. 9 Force versus displacement for the mixed mode bending test (MMB) by means of a multiscale numerical simulation (MNS)

interface debonding has the tendency to be more energetically costly than the matrix crack propagation, thus promoting the crack kinking out of the interface.

As in the previous case, in order to assess the accuracy of the proposed multiscale method, a comparison with a direct numerical simulation (DNS) is carried out. The numerical results show a very good estimation of the overall structural behavior,

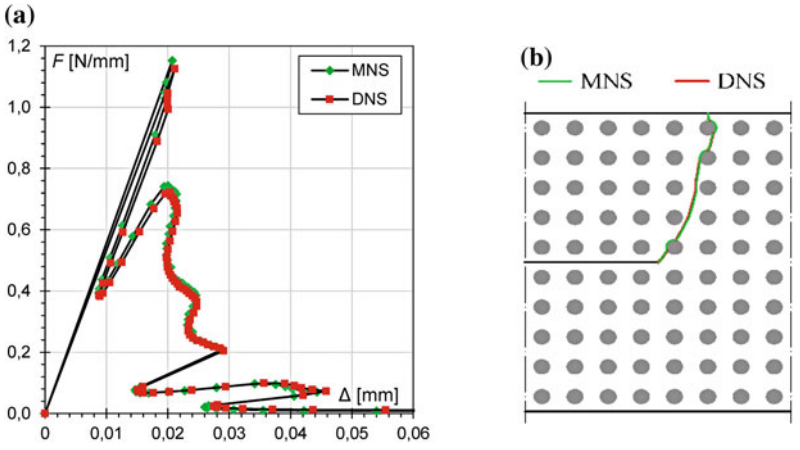

Fig. 10 Comparisons between the multiscale numerical simulation (MNS) and the direct numerical simulation (DNS) for the MMB test: **a** load-displacement curve; **b** final crack trajectories

Table 4 Comparison between the direct numerical simulation (DNS) and the multiscale numerical simulation (MNS) in terms of peak load and initial stiffness

	Peak load		Initial stiffness	
	F_0 (N/mm)	Error$_F$ (%)	K_0 (N/mm^2)	Error$_K$ (%)
DNS (reference)	1.13	–	53.3	–
MNS (present model)	1.15	2.31	55.6	4.30

in terms of both the load-displacement curves and the related crack trajectories, reported in Figs. 10a, b, respectively. Moreover, by analyzing the related percentage errors reported in Table 4, it can be observed that the peak load and the initial stiffness are only slightly overestimated, due to the non-negligible discretization error at the beginning of simulation.

5 Concluding Remarks

In the present work, an innovative adaptive multiscale model for crack propagation analyses in fiber-reinforced composite materials has been proposed. The main aim of our approach is to simulate complete failure of composite materials accounting for the influence of the microstructural details on their overall mechanical response, assuring the same accuracy as the purely microscopic models and the same computational efficiency as the macroscopic ones. In detail, a concurrent two-scale model has been developed, based on a two-level domain decomposition method equipped with an adaptive strategy, able to continuously update the zone of interest following the crack trajectories.

The attention is restricted to the case of transverse cracking, including the competition between matrix cracking along a non-prescribed path and fiber/matrix interface debonding; in addition, ad hoc fracture criteria have been introduced into the multiscale model, in order to handling the crack kinking in/out of a material interface. The quasi-static crack propagation has been numerically simulated via a strong discontinuity approach in the Linear Elastic Fracture Mechanics (LEFM) setting; to this end, a novel crack propagation algorithm has been proposed, based on the synergistic application of a crack length continuation scheme, allowing to follow the unstable branches of the equilibrium path, together with a moving mesh approach, enforcing in an efficient manner the maximum strain energy release rate criterion for a crack propagating within the matrix phase.

Numerical experiments have been carried out in order to assess the capability of the proposed multiscale model to predict the failure event in fiber-reinforced composite materials due to the quasi-static application of transverse loads. Two numerical tests (DCB and MMB tests) have been performed on a pre-notched composite beam, involving both mode I and mixed-mode loading conditions; for such tests, the influ-

ence of microscopic details on the overall mechanical behavior has been investigated, with reference to both the peak and the post-peak response.

Furthermore, suitable comparisons with reference solutions and simplified models have been reported is order to assess the accuracy of the numerical predictions found via the proposed multiscale method. For the DCB test, such comparison models include an analytical plate model, a homogenized model, and a direct numerical model, for which all the microstructural details have been explicitly accounted for; the numerical results obtained by the present multiscale model are in perfect agreement with those obtained via all the comparison models, especially the direct numerical model, regarded as our reference model (with percentage errors of about 1% in terms of peak load and of about 2% in terms of the maximum value reached by the strain energy release rate during the entire crack propagation process). For the MMB test, the only considered comparison model is the direct numerical one; the percentage error in terms of peak load between the two analyses is of about 2%, whereas no significant deviation are observed in terms of crack path numerical prediction. It is worth noting that for all the considered tests, the comparison between the multiscale (MNS) and the direct (DNS) numerical simulations highlights a systematic slight overestimation of the apparent stiffness, which is however acceptable for engineering purposes, being less than 5%.

In conclusion, the proposed adaptive multiscale strategy may be regarded as an efficient tool for investigating the nonlinear behavior of fiber-reinforced composite materials subjected to different damage mechanisms, also taking into account the effects of the underlying microstructure. Nevertheless, some limitations may be encountered when solving practical structural problems, first of all the implicitly supposed negligibility of the process zone. Therefore, a future extension of the present work could be the introduction of a more general multiscale framework for dealing with strain localization, more complex crack propagation phenomena, contact and boundary layer effects in a unified manner. According to these perspectives, the following possible improvements are indicated: the use of nonlinear constitutive behaviors for both bulk phases and material interfaces; the extension to the case of multiple-site crack initiation and propagation; and finally, the development of more sophisticated switching criteria incorporating zooming-out strategies for already damaged regions exhibiting unloading, in order to increase the overall computational efficiency of the present multiscale method.

References

1. Alfano G, Crisfield A (2001) Finite element interface models for the delamination analysis of laminated composites: mechanical and computational issues. Int J Num Methods Eng 50:1701–1736
2. Belytschko T, Song JH (2010) Coarse-graining of multiscale crack propagation. Int J Num Methods Eng 81:537–563
3. Bruno D, Greco F (2001) Delamination in composite plates: influence of shear deformability on interfacial debonding. Cem Concr Compos 23:33–45

4. Bruno D, Greco F (2001) Mixed mode delamination in plates: a refined approach. Int J Solids Struct 38:9149–9177
5. Bruno D, Greco F, Lonetti P (2008) Influence of micro-cracking and contact on the effective properties of composite materials. Simul Model Pract Theor 8:861–884
6. Caporale A, Luciano R, Sacco E (2006) Micromechanical analysis of interfacial debonding in unidirectional bre-reinforced composites. Comput Struct 84:2200–2211
7. Carpinteri A, Monetto I (1999) Snap-back analysis of fracture evolution in multi-cracked solids using boundary element method. Int J Fract 98:225–241
8. COMSOL-AB (2013) COMSOL multiphysics reference manual
9. Farhat C, Lesoinne M, LeTallec P, Pierson K, Rixen D (2001) FETI-DP: a dual-primal unified FETI method part I: a faster alternative to the two-level FETI method. Int J Num Methods Eng 50:1523–1544
10. Ghosh F, Bai J, Raghavan P (2007) Concurrent multi-level model for damage evolution in microstructurally debonding composites. Mech Mater 39:241–266
11. Gitman IM, Askes H, Sluys LJ (2007) Representative volume: existence and size determination. Eng Fract Mech 74:2518–2534
12. Greco F, Leonetti L, Nevone Blasi P (2012) Non-linear macroscopic response of ber-reinforced composite materials due to initiation and propagation of interface cracks. Eng Fract Mech 80:92–113
13. Greco F, Leonetti L, Nevone Blasi P (2014) Adaptive multiscale modeling of ber-reinforced composite materials subjected to transverse microcracking. Compos Struct 113:249–263
14. Hutchinson JW, Suo Z (1992) Mixed mode cracking in layered materials. Adv Appl Mech 29:64–187
15. Lloberas-Valls O, Rixen DJ, Simone A, Sluys LJ (2012) On micro-to-macro connections in domain decomposition multiscale methods. Comput Methods Appl Mech Eng 225–228:177–196
16. Mantič V (2009) Interface crack onset at a circular cylindrical inclusion under a remote transverse tension. Application of a coupled stress and energy criterion. Int J Solids Struct 46:1287–1304
17. Martin E, Leguillon D, Lacroix C (2001) A revisited criterion for crack deection at an interface in a brittle bimaterial. Compos Sci Tech 61:1671–1679
18. Mobasher Amini A, Dureisseix D, Cartraud P (2009) Multi-scale domain decomposition method for large-scale structural analysis with a zooming technique: application to plate assembly. Int J Num Methods Eng 79:417–443
19. Reeder JR, Crews JH (1990) Mixed-mode bending method for delamination testing. Am Inst Aeronaut Astronaut 28:1270–1276
20. Yuan FJ, Pagano NJ, Cai X (1997) Elastic moduli of brittle matrix composites with interfacial debonding. Simul Model Pract Theor 34:177–201

Quasi-static Evolution, Variational Principles and Implicit Scheme in Gradient Plasticity

Quoc-Son Nguyen

Abstract This paper is devoted to the theory of gradient plasticity. Our attention is focussed on the description of the constitutive equations, on the formulation of the governing equations in terms of the energy potential and the dissipation potential of the solid. The evolution equation is discussed for quasi-static responses. A time-discretization by the implicit scheme of the evolution equation leads to the study of the incremental problem which is different from the rate problem. The incremental problem and associated incremental variational principles are discussed in relation with some existing results of the literature.

1 Introduction

Since two last decades, gradient theories have been much discussed in elasticity, in plasticity as in damage mechanics, see for example [2, 3, 5–7, 9]. This paper is devoted to the study of gradient plasticity. A general and consistent description of the theory of gradient plasticity is considered. Our attention is focussed on the formulation of the constitutive equations and the derivation of the governing equations for the response of a solid under a loading path **in terms of the expression of the energy potential and the dissipation potential of the solid**. Such a synthetic description, still lacking in the literature, appears to be interesting for an overview on the subject. It enables us to include in the same framework all general statements which result from the basic ingredients of the theory such as the evolution equation in quasi-statics and the associated variational principles. In particular, the discretization of the evolution equation by the implicit scheme leads to the formulation of the incremental response which is interesting for the numerical simulation and the stability analysis.

Q.-S. Nguyen (✉)
École Polytechnique-ParisTech, Laboratoire de Mécanique des Solides,
91128 Palaiseau Cedex, France
e-mail: son@lms.polytechnique.fr

M. Frémond et al. (eds.), *Models, Simulation, and Experimental Issues in Structural Mechanics*, Springer Series in Solid and Structural Mechanics 8,
DOI 10.1007/978-3-319-48884-4_7

2 Standard Theory of Gradient Plasticity

In an isothermal transformation, the mechanical response of a solid V is described by the fields of displacement $\boldsymbol{u}$, of internal parameter Φ. The internal parameter is a scalar or a tensor and represent physically hidden parameters such as micro-displacements or phase proportions or anelastic strains, etc. The set of state variables $(\nabla u, \phi, \nabla\phi)$ describes the material behaviour and the governing equations can be given in the following way (see [4, 5, 7]).

It is accepted that the rates $(\nabla\dot{u},\ \dot{\phi},\ \nabla\dot{\phi})$ of the state variables are associated with the generalized forces (σ, X, Y) such that a generalized virtual work equation holds

$$\begin{cases} P_i + P_j = P_e \quad \forall\ \delta u,\ \delta\Phi \\ P_i = \int_V (\sigma \cdot \nabla\delta u + X \cdot \delta\phi + Y \cdot \nabla\delta\phi)\, dV, \\ P_j = \int_V \rho\ddot{u} \cdot \delta u\, dV, \\ P_e = \int_V (F_{uv} \cdot \delta u + F_{\phi v} \cdot \delta\phi)\, dV + \int_{\partial V} (F_{us} \cdot \delta u + F_{\phi s} \cdot \delta\phi)\, da \end{cases} \tag{1}$$

where (F_{uv}, F_{us}) and $(F_{\phi v}, F_{\phi s})$ are respectively external body and surface forces associated with the displacement and the internal parameter. It follows that: *a*

$$\nabla \cdot \sigma + F_{uv} = \rho\ddot{u} = 0 \quad \text{in} \quad V, \qquad \sigma \cdot n = F_{us} \quad \text{on} \quad \partial V_f \tag{2}$$

$$X + \nabla \cdot Y + F_{\phi v} = 0 \qquad \text{in} \quad V, \qquad Y \cdot n = F_{\phi s} \quad \text{on} \quad \partial V \tag{3}$$

Standard gradient models of plasticity also assume that there exists per unit volume an energy potential which is a smooth function $W(\nabla u, \phi, \nabla\phi)$ associated with the energy forces σ, X_e, Y_e:

$$\sigma = W_{,\nabla u}\ , \qquad X_e = W_{,\phi}\ , \qquad Y_e = W_{,\nabla\phi} \tag{4}$$

and a dissipation potential $D(\dot{\phi}, \nabla\dot{\phi})$ which is a convex and positively homogeneous function of degree 1

$$D(a\dot{\phi}, a\nabla\dot{\phi}) = aD(\dot{\phi}, \nabla\dot{\phi}) \qquad \forall\ \ a \geq 0 \tag{5}$$

associated with the dissipative forces

$$X_d = \partial_{\dot{\phi}}\ D(\dot{\phi}, \nabla\dot{\phi})\,, \qquad Y_d = \partial_{\nabla\dot{\phi}}\ D(\dot{\phi}, \nabla\dot{\phi}) \tag{6}$$

such that the following equations hold:

$$X = X_e + X_d\,, \qquad Y = Y_e + Y_d. \tag{7}$$

In Eq. (6), the derivative must be understood in the sense of sub-gradients of a convex function, see for example [4, 10]. The dissipation potential can be state-dependent, for exampe via the history of the state variable ϕ.

2.1 Standard Models of Gradient Plasticity

For example, the following model has been discussed by Fleck et al. [2] with $\phi = \epsilon^p$ and

$$\begin{cases} W(\nabla u, \epsilon^p) = \frac{1}{2}(\epsilon - \epsilon^p) : L : (\epsilon - \epsilon^p), \\ D(\dot{\epsilon}^p, \nabla\dot{\epsilon}^p) = R(\gamma)\sqrt{\|\dot{\epsilon}^p\|^2 + \ell^2\|\nabla\dot{\epsilon}^p\|^2}, \\ \gamma = \int_0^t \sqrt{\|\dot{\epsilon}^p\|^2 + \ell^2\|\nabla\dot{\epsilon}^p\|^2)}\, d\tau, \end{cases} \tag{8}$$

with $\epsilon = (\nabla u)_s$ and the notation $\|\dot{\epsilon}^p\| = \sqrt{\dot{\epsilon}^p_{ij}\dot{\epsilon}^p_{ij}}$ and $\|\nabla\dot{\epsilon}^p\| = \sqrt{\dot{\epsilon}^p_{ij,k}\dot{\epsilon}^p_{ij,k}}$.

Here, the dissipation potential is state-dependent via the expression of γ. As in classical plasticity, the model leads to a plastic criterion $f(X^p_d, Y^p_d) \le 0$ which defines the set of physically admissible forces and to the normality law:

$$\begin{cases} f = (\|X^p_d\|^2 + \frac{1}{\ell^2}\|Y^p_d\|^2)^{1/2} - R(\gamma) \le 0, \\ \dot{\epsilon}^p = \lambda\frac{\partial f}{\partial X^p_d}, \quad \nabla\dot{\epsilon}^p = \lambda\frac{\partial f}{\partial Y^p_d}, \quad \lambda \ge 0, \qquad f\lambda = 0 \\ \dot{\gamma} = \lambda. \end{cases} \tag{9}$$

The dissipation is

$$d = X^p_d \cdot \dot{\epsilon}^p + Y^p_d \cdot \nabla\dot{\epsilon}^p = R(\gamma)\lambda = \frac{d}{dt}W_d(\gamma) \quad \text{with} \quad R = W'_d(\gamma), \tag{10}$$

$W_d(\gamma)$ being the dissipated energy.

This model can be easily modified to obtain a state-independent dissipation potential. For this, the following model is introduced with $\phi = (\epsilon^p, \gamma)$

$$\begin{cases} W(\nabla u, \epsilon^p, \gamma) = \frac{1}{2}(\epsilon - \epsilon^p) : L : (\epsilon - \epsilon^p) + H(\gamma), \\ D(\dot{\epsilon}^p, \dot{\gamma}, \nabla\dot{\epsilon}^p) = k\sqrt{\|\dot{\epsilon}^p\|^2 + \ell^2\|\nabla\dot{\epsilon}^p\|^2} + \Psi_o(\dot{\gamma} - \sqrt{\|\dot{\epsilon}^p\|^2 + \ell^2\|\nabla\dot{\epsilon}^p\|^2}) \end{cases} \tag{11}$$

where k is a constant and Ψ_o the indicator function

$$\Psi_o(a) = 0 \quad \text{if} \quad a = 0 \quad \text{and} \quad \Psi_o(a) = +\infty \quad \text{if} \quad a \ne 0 \tag{12}$$

which ensures the constraint

$$\dot{\gamma} = \sqrt{\|\dot{\epsilon}^p\|^2 + \ell^2\|\nabla\dot{\epsilon}^p\|^2}.$$

From Eq. (11), the considered model leads to the plastic criterion

$$f(X^p_d, X^\gamma_d, Y^p_d) = (\|X^p_d\|^2 + \frac{1}{\ell^2}\|Y^p_d\|^2)^{1/2} + X^\gamma_d - k \le 0 \tag{13}$$

and the normality law

$$\begin{cases} \dot{\epsilon}^p = \lambda \frac{\partial f}{\partial X_d^p}, \qquad \dot{\gamma} = \lambda \frac{\partial f}{\partial X_d^\gamma} = \lambda, \qquad \nabla \dot{\epsilon}^p = \lambda \frac{\partial f}{\partial Y_d^p}, \\ f \le 0, \qquad \lambda \ge 0, \qquad f\lambda = 0. \end{cases} \tag{14}$$

The dissipation is

$$d = X_d^p \cdot \dot{\epsilon}^p + X_d^\gamma \, \dot{\gamma} + Y_d^p \cdot \nabla \dot{\epsilon}^p = k\lambda = k\dot{\gamma} = k\sqrt{\|\dot{\epsilon}^p\|^2 + \ell^2 \|\nabla \dot{\epsilon}^p\|^2}$$

which gives here the physical interpretation of $k\gamma$ as the dissipated energy.

Since $X_d^\gamma = -X_e^\gamma = H'(\gamma)$, the constitutive equation (8) is recovered with $H'(\gamma) + k = R(\gamma)$. In this model, W_d is the work done by plastic deformation and consists of the dissipated energy $k\gamma$ and the stored energy $H(\gamma)$.

In the same spirit, an interesting model of isotropic hardening is given by

$$\begin{cases} W(\nabla u, \epsilon^p, \gamma, \nabla\gamma) = \frac{1}{2}(\epsilon - \epsilon^p) : L : (\epsilon - \epsilon^p) + H(\gamma) + \frac{g}{2}\nabla\gamma^2, \\ D(\dot{\epsilon}^p, \dot{\gamma}, \nabla\dot{\gamma}) = k\|\dot{\epsilon}^p\| + \kappa\|\nabla\dot{\gamma}\| + \Psi_o(\dot{\gamma} - \|\dot{\epsilon}^p\|). \end{cases} \tag{15}$$

The plastic criterion is given by two inequalities

$$f(X_d^p, X_d^\gamma) = \|X_d^p\| + X_d^\gamma - k \le 0, \qquad \varphi(Y_d^\gamma) = \|Y_d^\gamma\| - \kappa \le 0 \tag{16}$$

and the normality law is

$$\begin{cases} \dot{\epsilon}^p = \lambda \frac{\partial f}{\partial X_d^p}, \quad \dot{\gamma} = \lambda \frac{\partial f}{\partial X_d^\gamma} \quad \text{with} \quad f \le 0, \quad \lambda \ge 0, \quad \lambda f = 0, \\ \nabla\dot{\gamma} = \tau \frac{\partial \varphi}{\partial Y_d^\gamma} \quad \text{with} \quad \varphi \le 0, \quad \tau \ge 0, \quad \tau\varphi = 0. \end{cases} \tag{17}$$

The reader can also refer to [6, 8, 9] for interesting discussions on a model of energy $W = \frac{1}{2}(\epsilon - \epsilon^p) : L : (\epsilon - \epsilon^p) + \frac{1}{2}\text{curl}(\epsilon^p) : E : \text{curl}(\epsilon^p)$. Here the energy potential depends on the gradient of the plastic strain via the operator 'curl'.

3 Evolution Equation

3.1 Governing Equations for a Solid Under a Loading Path

In the sequel, the assumption of state-independent dissipation is accepted. The conditions $F_{\phi v} = 0$ and $F_{\phi s} = 0$, although not essential, are also admitted. For a solid

submitted to a classical loading path, defined by the body forces $F_{uv}(x,t)$, $F_{\phi v}(x,t)$, the surface forces $F_{us}(x,t)$, $F_{\phi,s}(x,t)$ and the imposed displacement $u_g(x,t)$, the response of the solid must satisfy the local equations

$$
\begin{aligned}
&\forall \quad t \in [0,T]: \\
&\qquad \sigma = W_{,\nabla u}\,, \quad X_e = W_{,\phi}\,, \quad Y_e = W_{,\nabla\phi}\,, \\
&\qquad X = X_e + X_d\,, \quad Y = Y_e + Y_d\,, \quad (X_d,\, Y_d) = \partial D(\dot\phi, \nabla\dot\phi)\,, \\
&\qquad \nabla\cdot\sigma + F_{uv} = \rho\ddot u\,, \quad X + \nabla\cdot Y = 0 \quad \text{in} \quad V\,, \\
&\qquad \sigma\cdot n = F_{us} \quad \text{on} \quad \partial V_f\,, \quad u = u_g \quad \text{on} \quad \partial V_u\,, \\
&\qquad Y\cdot n = 0 \quad \text{on} \quad \partial V \\
&\text{at} \quad t = 0: \\
&\qquad \boldsymbol{u}(0) = \boldsymbol{u}_o\,, \quad \Phi(0) = \Phi_o, \quad \dot{\mathbf{u}}(0) = \boldsymbol{v}_o\,.
\end{aligned}
\tag{18}
$$

These equations describe the response of the solid from an initial position of state and velocity.

3.2 The Quasi-static Response

It is convenient to introduce as a condensed notation the general displacement $\boldsymbol{U} = (\boldsymbol{u}, \Phi)$ to write simply the energy and dissipation potentials of the solid as :

$$
\boldsymbol{W}(U) = \int_V W(\nabla u, \phi, \nabla\phi)\, dV\,, \qquad \boldsymbol{D}(\dot U) = \int_V D(\dot\phi, \nabla\dot\phi)\, dV. \tag{19}
$$

In quasi-static transformation, a variational and condensed form of the evolution equation for the solid can be introduced as in classical plasticity (see [10]).

Evolution Equation. *For all* $t \in [0,T]$, *the quasi-static response* $\boldsymbol{U}(t)$ *of the solid submitted to a given loading path* $\boldsymbol{F}_g(t)$, $u_g(t)$ *satisfies the following variational inequality:*

$$
\boldsymbol{W}_{,U}\,(U)\cdot(\dot U^* - \dot U) + D(\dot U^*) - D(\dot U) - \boldsymbol{F}_g\cdot(\dot U^* - \dot U) \geq 0 \tag{20}
$$

for all response $\boldsymbol{U}^*(t)$ *satisfying the imposed condition* $\boldsymbol{u}^*(t) = u_g(t)$ *on* ∂V_u.

This variational inequality means explicitly that

$$
\begin{cases}
\int_V \sigma : \nabla(\dot u^* - \dot u)\, dV - \int_V F_{vu}\cdot(\dot u^* - \dot u)\, dV - \int_{\partial V_F} F_{gsu}\cdot(\dot u^* - \dot u)\, dS \\
+ \int_V (X_e\cdot(\dot\phi^* - \dot\phi) + Y_e\cdot(\nabla\dot\phi^* - \nabla\dot\phi) + D(\dot\phi^*, \nabla\dot\phi^*) - D(\dot\phi, \nabla\dot\phi))\, dV \geq 0
\end{cases}
\tag{21}
$$

for all Φ^* and for all $\boldsymbol{u}^*$ admissible.

Thus for all t, it follows from the evolution variational inequality that the equilibrium equation holds

$$\boldsymbol{W}_{,u}(U)\cdot\delta u - F_{gu}\cdot\delta u = 0 \quad \forall \quad \delta u = 0 \quad \text{on} \quad \partial V_u$$

and that $\dot{\Phi}$ must satisfy the following minimum principle:

$$\begin{cases} \boldsymbol{I}(\dot{\Phi}) = \min_{\delta\Phi} \ \boldsymbol{I}(\delta\Phi), \\ \boldsymbol{I}(\delta\Phi) = \int_V (X_e\cdot\delta\phi + Y_e\cdot\nabla\delta\phi + D(\delta\phi,\nabla\delta\phi)\,dV \end{cases} \tag{22}$$

which is the minimum principle I in Fleck & Willis [2].

The force-flux relationships (4), (6), (7) follows from the minimum principle (22).

Indeed, the minimum principle holds only if for almost t, $m = \min_{\delta\Phi} \ \boldsymbol{I} = 0$ since $\mathbf{I}$ is the sum of a linear and a positive homogeneous functionals. Moreover, the rate $\dot{\Phi}$ must be found among the solutions of (22). Such a solution will be denoted as *compatible* rate. The set of compatible rates has the structure of a convex cone since

(i) if $\Phi^* \neq 0$ is compatible then $a\,\Phi^*$ is also compatible for all number $a > 0$;
(ii) if ϕ_1^* and ϕ_2^* are two different compatible rates, then $\alpha\Phi_1^* + (1-\alpha)\Phi_2^*$ is also compatible for $0 \leq \alpha \leq 1$ since D is a convex function.

If there is no gradient term in the dissipation potential, the proof is very simple. The condition $m = 0$ implies that $\nabla\cdot Y_e - X_e = X_d$ must satisfy the plastic criterion since $m = -\infty$ otherwise. It is also straightforward that an compatible rate Φ^* has the following expression

$$\phi^* = \lambda^* f_{,X_d} \quad \text{with} \quad \lambda^* \geq 0\,, \qquad \lambda^* f = 0, \qquad X_d = -W_{,\phi} + \nabla\cdot W_{,\nabla\phi}\,.$$

When the gradient term does figure in the dissipation potential, the set of compatible rates cannot be easily generated although its definition is mathematically clear.

The question of existence of a solution of (20) has been much discussed in classical plasticity. In gradient plasticity, many discussions have been recently proposed for the existence, regularity and the numerical analysis of a solution (see [1, 3, 6, 9]).

Finally, the evolution equation (20) can be also schematically condensed as

$$\begin{cases} W_{,u} = \ F_u \\ -\boldsymbol{W}_{,\Phi} \in \ \partial\boldsymbol{D}(\dot{\Phi}). \end{cases} \tag{23}$$

This discussion shows in particular that higher gradients can also be included in the same framework. The force-flux relation is still given by Biot equation for the solid and the response of the solid is governed by the evolution equation (20).

4 Time-Discretization by the Implicit Scheme

4.1 Implicit Scheme and Incremental Problem

The numerical analysis of the quasi-static response of a solid to a given loading path is considered in this section. In a time-like discretization, the present value $\boldsymbol{U}$ is assumed at a current step. The incremental problem consists in determining the incremental response $\Delta \boldsymbol{U}$ to an increment of load $(\Delta \boldsymbol{F}_g,\ \Delta \boldsymbol{u}_g)$.

A time discretization of the evolution variational inequality (20) following the implicit scheme consists in replacing $\dot{\mathbf{U}},\ \dot{\mathbf{U}}^*,\ \dot{\mathbf{F}}$ respectively by $\frac{\Delta \boldsymbol{U}}{\Delta t},\ \frac{\Delta \boldsymbol{U}^*}{\Delta t},\ \frac{\Delta \boldsymbol{F}}{\Delta t}$ and $\boldsymbol{U}$ by $\boldsymbol{U}_+ = \boldsymbol{U} + \Delta \boldsymbol{U},\ \ \boldsymbol{F}$ by $\boldsymbol{F}_+ = \boldsymbol{F} + \Delta \boldsymbol{F}$ in the expression (20).

Since the dissipation potential is positively homogeneous of degree 1, it follows that the incremental response $\Delta \boldsymbol{U}$ must be a solution of the incremental problem i.e. satisfy the following variational inequality

$$\begin{aligned} &\boldsymbol{W}_{,U}(\boldsymbol{U} + \Delta \boldsymbol{U}) \cdot (\Delta \boldsymbol{U}^* - \Delta \boldsymbol{U}) + \boldsymbol{D}(\Delta \boldsymbol{U}^*) - \boldsymbol{D}(\Delta \boldsymbol{U}) \\ &\qquad - \boldsymbol{F}_g + \Delta \boldsymbol{F}_g \cdot (\Delta \boldsymbol{U}^* - \Delta \boldsymbol{U}) \geq 0 \quad \forall \quad \Delta \boldsymbol{U}^* \quad \text{admissible.} \end{aligned} \tag{24}$$

The implicit scheme ensures that the equilibrium equation and the normality law are satisfied by the increments of the displacement and the internal parameter at the next step.

Conversely, an incremental process $\Delta \boldsymbol{U}(t_n)$, with $t_n = n\Delta t,\ n = 1, 2, \ldots N$, $N\Delta t = T$ defined by the increment variational inequality (24) and starting from $\boldsymbol{U}_o$ must satisfy at each current increment

$$\begin{cases} \boldsymbol{W}_{,U}(\boldsymbol{U}) \cdot (\frac{\Delta \boldsymbol{U}^*}{\Delta t} - \frac{\Delta \boldsymbol{U}}{\Delta t}) + \boldsymbol{D}(\frac{\Delta \boldsymbol{U}^*}{\Delta t}) - \boldsymbol{D}(\frac{\Delta \boldsymbol{U}}{\Delta t}) - \boldsymbol{F}_g \cdot (\boldsymbol{U}) \cdot (\frac{\Delta \boldsymbol{U}^*}{\Delta t} - \frac{\Delta \boldsymbol{U}}{\Delta t}) \\ +\Delta t \ \{\frac{\Delta \boldsymbol{U}}{\Delta t} \cdot \boldsymbol{W}_{,UU}(\boldsymbol{U}) - \frac{\Delta \boldsymbol{F}_g}{\Delta t}\} \cdot (\frac{\Delta \boldsymbol{U}^*}{\Delta t} - \frac{\Delta \boldsymbol{U}}{\Delta t}) \\ +o(\Delta t) \geq 0 \quad \forall \quad \Delta \boldsymbol{U}^* \quad \text{admissible.} \end{cases} \tag{25}$$

At the limit, when $\Delta t \to 0$, then $\frac{\Delta \boldsymbol{F}}{\Delta t} \to \dot{\mathbf{F}}$, $\frac{\Delta \boldsymbol{U}}{\Delta t} \to \dot{\mathbf{F}}$ and $\frac{\Delta \boldsymbol{U}^*}{\Delta t} \to \dot{\mathbf{U}}^*$ and the evolution equation (20) is recovered since the term of order zero in Δt must be non negative for all $\dot{\mathbf{U}}^*$ admissible.

Moreover, with the choice $\dot{\Phi}^*$ compatible, the term of order zero is zero at the limit. It follows that the term of order Δt in (25) must be non negative at the limit and a variational inequality is obtained for the rate $\dot{\mathbf{U}}$ [10]:

$$\begin{aligned} &\dot{\mathbf{U}} \cdot W_{,UU} \cdot (\dot{U}^* - \dot{U}) - \dot{\mathbf{F}}_g \cdot (\dot{U}^* - \dot{U}) \geq 0 \\ &\forall \quad \dot{\mathbf{U}}^* \quad \text{such that } \dot{\mathbf{u}}^* \text{ is admissible and } \dot{\Phi}^* \text{ compatible.} \end{aligned} \tag{26}$$

4.2 Incremental Minimum Principle

If the energy potential is a convex function (as in the models (11) and (15)), a solution $\Delta \boldsymbol{U}$ of the variational inequality (24) is also a solution of the following minimization problem.

Incremental Minimum Principle. *The increment $\Delta \boldsymbol{U}$ minimizes the functional*

$$\boldsymbol{K}(\Delta \boldsymbol{U}^*) = \boldsymbol{W}(\boldsymbol{U} + \Delta \boldsymbol{U}^*) + \boldsymbol{D}(\Delta \boldsymbol{U}^*) - (\boldsymbol{F}_g + \Delta \boldsymbol{F}_g) \cdot \Delta \boldsymbol{U}^* \qquad (27)$$

among the set of admissible increments $\Delta \boldsymbol{U}^*$.

Indeed, the minimum principle (27) results from the variational inequality (24) since the convexity of the energy potential ensures that

$$\boldsymbol{W}(\boldsymbol{U} + \Delta \boldsymbol{U}^*) - \boldsymbol{W}(\boldsymbol{U} + \Delta \boldsymbol{U}) \geq \boldsymbol{W}_{,U}(\boldsymbol{U}_+) \cdot (\Delta \boldsymbol{U}^* - \Delta \boldsymbol{U}) \,.$$

The same conclusion also holds if the energy potential is only locally convex. In this case the solution $\Delta \boldsymbol{U}$ of (24) is a local minimum of the functional $\boldsymbol{K}(\Delta \boldsymbol{U}^*)$.

Conversely, a local minimum $\Delta \boldsymbol{U}$ of the functional $\boldsymbol{K}$ is necessarily a local solution of the variational inequality (24) for any smooth energy potential. Indeed, for any $\Delta \boldsymbol{U}^* \in \mathcal{N}$, a neighborhood of $\Delta \boldsymbol{U}$

$$\left\{ \begin{array}{l} \boldsymbol{K}(\Delta \boldsymbol{U}) \leq \boldsymbol{K}(1-\alpha)\Delta \boldsymbol{U} + \alpha \Delta \boldsymbol{U}^*) \leq \boldsymbol{W}(\boldsymbol{U}_+ + \alpha(\Delta \boldsymbol{U}^* - \Delta \boldsymbol{U}))+ \\ (1-\alpha)\boldsymbol{D}(\Delta \boldsymbol{U}) + \alpha \boldsymbol{D}(\Delta \boldsymbol{U}^*) - \boldsymbol{F}_{g+} \cdot (\Delta \boldsymbol{U} + \alpha(\Delta \boldsymbol{U}^* - \Delta \boldsymbol{U}) \quad \forall \ \alpha \in [0,1] \end{array} \right.$$

since $\boldsymbol{D}$ is a convex function. It follows that

$$\frac{1}{\alpha}(\boldsymbol{W}(\boldsymbol{U}_+ + \alpha(\Delta \boldsymbol{U}^* - \Delta \boldsymbol{U})) - \boldsymbol{W}(\boldsymbol{U}_+) - \boldsymbol{F}_{g+} \cdot (\Delta \boldsymbol{U}^* - \Delta \boldsymbol{U}) + \boldsymbol{D}(\Delta \boldsymbol{U}^*) - \boldsymbol{D}(\Delta \boldsymbol{U}) \geq 0$$

thus (24) results for vanishing α.

The minimum principle (27) deals with stable solutions of the variational inequality (24). The stability is understood here in the sense of a positive external work in any perturbation of the equilibrium $\boldsymbol{U}_+$ (see [10, 11]). In detail, an equilibrium $\boldsymbol{U}_+ = \boldsymbol{U} + \Delta \boldsymbol{U}$ under the applied force $\boldsymbol{F}_+$ and imposed displacement $\boldsymbol{u}_{g+}$ is stable if in any perturbation of this equilibrium, defined by a perturbed path in function of a kinematic time τ

$$\boldsymbol{U}[\tau], \tau \in [0,1] \,, \qquad \boldsymbol{U}[0] = \boldsymbol{U}_+ \,, \qquad \boldsymbol{U}[1] = \boldsymbol{U}_+^* \in \mathcal{N} \,,$$

under the action of some perturbation forces, the work provided by these forces is non-negative.

Indeed, in such a perturbation the energy balance, which results from the constitutive equations (1)–(7) of the solid, shows that the amount of work provided by the

perturbed forces is

$$W_{per} = \boldsymbol{W}(\boldsymbol{U}_+^*) - \boldsymbol{W}(\boldsymbol{U}_+) + \int_0^1 \boldsymbol{D}(\frac{d\phi}{d\tau}[\tau])d\tau - \boldsymbol{F}_{g+} \cdot (\boldsymbol{U}_+^* - \boldsymbol{U}_+). \tag{28}$$

From the fact that the dissipation potential is a kind of norm

$$\int_0^1 \boldsymbol{D}(\frac{d\phi}{d\tau}[\tau])d\tau \geq \boldsymbol{D}(\Delta\boldsymbol{U}^* - \Delta\boldsymbol{U}) \geq \boldsymbol{D}(\Delta\boldsymbol{U}^*) - \boldsymbol{D}(\Delta\boldsymbol{U}), \tag{29}$$

it follows that

$$W_{per} \geq \boldsymbol{W}(U_+^*) - W(U_+) + \boldsymbol{D}(\Delta\boldsymbol{U}^*) - \boldsymbol{D}(\Delta\boldsymbol{U}) - \boldsymbol{F}_{g+} \cdot (\Delta\boldsymbol{U}^* - \Delta\boldsymbol{U}) \geq 0. \tag{30}$$

The incremental minimum principle can also written as the following minimum principle concerning the response at the next step $\boldsymbol{U}_+$.

Displacement Minimum Principle. *At time $t + \Delta t$, the generalized displacement $\boldsymbol{U}_+$ minimizes the functional*

$$\bar{\boldsymbol{K}}(U_+^*) = \boldsymbol{W}(U_+^*) + D(U_+^* - U) - \boldsymbol{F}_{g+} \cdot U_+^* \tag{31}$$

among the set of admissible displacements $\boldsymbol{U}_+^*$.

In particular, if the current state is the natural state and if the load increment is the final load, the implicit scheme gives the response of the associated deformation model under the final load.

The reader can refer to [1, 3, 6] for an original mathematical formulation on stable responses. In their approach, the starting point is the displacement minimum principle (31) instead of the evolution equation (20) and the implicit scheme. Their results show in particular that the convergence of the implicit scheme is ensured under the assumption of convexity of the energy potential.

5 Conclusions

Within the framework of standard plasticity, the theory of gradient plasticity is discussed. The governing equations of the response of a solid under a loading path are written in terms of the energy and the dissipation potentials. It is shown that the quasi-static response of the solid is a solution of a variational inequality as in classical plasticity and that higher gradients can also be included in the same spirit. A time-discretization by the implicit scheme of the evolution equation leads to the

study of the incremental problem. The increment of the response under a load increment must satisfy a variational inequality and, if the energy potential is convex, an incremental minimum principle. In particular, a local minimum of the incremental minimum principle is a stable solution of the variational inequality.

References

1. Dal Maso G, De Simone A, Mora MG (2006) Quasistatic evolution problems for linearly elastic-perfectly plastic materials. Arch Ration Mech Anal 180:237–291
2. Fleck NA, Willis JR (2009) A mathematical basis for strain-gradient plasticity theory, part II. J Mech Phys Solids 57:1045–1057
3. Francfort G, Mielke A (2006) Existence results for a class of rate-independent material models with nonconvex elastic energies. Journal für die Reine und Angewandte Mathematik 595:55–91
4. Frémond M (2012) Phase change in mechanics. Lecture notes UMI, Berlin, Springer
5. Frémond M, Nedjar B (1996) Damage, gradient of damage and principle of virtual power. Int J Solids Struct 33:1083–1103
6. Giacomini A, Lussardi L (2008) Quasi-static evolution for a model in strain gradient plasticity. SIAM J Math Anal 40:1201–1245
7. Gurtin ME (1996) Generalized Ginzburg-Landau and Cahn-Hilliard equations based on a microforce balance. Physica D 92:178–192
8. Gurtin ME, Anand L (2005) A theory of strain-gradient plasticity for isotropic, plastically irrotational materials. J Mech Phys Solids 53:1624–1649
9. Neff P, Sydov A, Wieners C (2009) Numerical approximation of incremental infinitesimal gradient plasticity. Int J Numer Methods Eng 77(3):414–436
10. Nguyen QS (2000) Stability and nonlinear solid mechanics. Wiley, Chichester
11. Nguyen QS, Radenkovic D (1975) Stability of an equilibrium in elastic-plastic solids. In: IUTAM symposium applications of methods of functional analysis to problems of mechanics. Springer, Berlin
12. Nielson KL, Niordson CF, Hutchinson JW (2014) Strain gradient effects in periodic flat punch indenting at small scales. Int J Solids Struct 51:3549–3556

Deviatoric Strength of Nanoporous Materials: A Limit Analysis Approach

Stella Brach, Luc Dormieux, Djimédo Kondo and Giuseppe Vairo

Abstract In this paper, deviatoric strength properties of nanoporous materials are investigated by addressing the limit state of a hollow sphere undergoing axisymmetric deviatoric strain-rate based loading conditions. The hollow sphere is assumed to be comprised of a rigid ideal-plastic matrix obeying to a von Mises strength criterion. Void-size effects are consistently described by introducing a coherent-imperfect homogeneous interface at the cavity boundary. In the framework of a kinematic approach, the limit-analysis problem on the hollow sphere is solved by referring to a particular trial velocity field, expressed in terms of some free model parameters, chosen as a result of an optimization strategy. A closed-form expression for estimating the macroscopic deviatoric strength is obtained and successfully compared with available benchmarking data.

1 Introduction

Nanoporous materials have been characterised by a fast-growing development in the last two decades, attracting a world-wide interest in both industrial and academic domains [1, 16, 17]. As a matter of fact, owing to their good properties in terms of

S. Brach (✉) · G. Vairo
DICII, Università degli Studi di Roma "Tor Vergata", Via del Politecnico 1, 00133 Rome, Italy
e-mail: brach@ing.uniroma2.it

G. Vairo
e-mail: vairo@ing.uniroma2.it

S. Brach · G. Vairo · D. Kondo
Institut D'Alembert, Université Pierre et Marie Curie, 4, Place Jussieu,
75252 Paris, France

D. Kondo
e-mail: djimedo.kondo@upmc.fr

L. Dormieux
Ecole des Ponts ParisTech, UR Navier, 6-8 av. Blaise Pascal,
77455 Marne-la-vallée, France
e-mail: dormieux@lmsgc.enpc.fr

M. Frémond et al. (eds.), *Models, Simulation, and Experimental Issues in Structural Mechanics*, Springer Series in Solid and Structural Mechanics 8,
DOI 10.1007/978-3-319-48884-4_8

stiffness and strength, nanoporous materials open towards groundbreaking applications in several technical fields, involving ultra-high performance devices and challenging multifunctional uses. In order to fulfil to these promising applications, one of the most fundamental aspects consists in describing, into an effective engineering design framework, strength properties of these materials as dependent on the size of voids. Recent nano-mechanical experiments (e.g., [2, 3, 15]) have shown that, for a fixed porosity value, a reduction in the length-scale of nanovoids induces an increase in the material yield strength. Similarly, Molecular-Dynamics simulations carried out on in-silico nanoporous samples [4, 18, 25, 31] have proven that the predicted strength decreases towards asymptotic values when the size of voids increases. The physical origin of such a phenomenon has been related by Needs et al. [21] to the presence of self-equilibrated surface stresses at the cavity surface, induced by a local perturbation in the atomic arrangement close to the nanovoids and usually negligible for classical porous materials. In the framework of a continuum approach, void-size effects have been generally addressed by introducing coherent-imperfect interface laws at the cavity boundaries (e.g., [9, 10, 13, 14, 23], that is accounting for surface stresses by prescribing the discontinuity of the stress vector across the interface.

Strength models for classical porous materials [12, 22] are able to account for porosity effects only, thereby resulting in void-size independent yield functions. Void-size dependent strength criteria have been recently proposed in [5, 8, 11, 20, 28–30], by referring to non-linear homogenization techniques. As regards limit analysis approaches, the well-established criterion proposed by Gurson [12] for porous media has been extended to nanoporous materials in [7], via a plastic generalization of interface stress models [19]. However, as it will be also shown in the following, the novel strength criterion proposed in [7] overrates available numerical evidence [26]. In this light, and with reference to deviatoric axisymmetric states only, present paper aims to furnish a more effective estimate for the macroscopic deviatoric strength of nanoporous materials, properly accounting for void-size effects. In detail, the limit analysis problem on a hollow sphere domain is solved by referring to the parametric trial velocity field introduced in [6] (see also [32]), allowing for an optimization procedure.

The paper is organized as follows. In Sect. 2 basic elements of the limit-analysis theoretical framework are presented. In Sect. 3 the adopted trial velocity field is introduced. The estimate of the macroscopic strength of a hollow sphere with interface effects and undergoing an axisymmetric deviatoric loading is determined in Sect. 4, discussing effectiveness and accuracy of the proposed model. Finally, some conclusions are traced in Sect. 5.

2 Problem Statement

Let the hollow sphere in Fig. 1 be considered, whose internal and external radii are denoted as R_i and R_e, respectively. Moreover, let $\partial\Omega_\mathrm{i}$ and $\partial\Omega_\mathrm{e}$ be the corresponding internal and external surfaces, the total boundary of the system resulting in $\partial\Omega =$

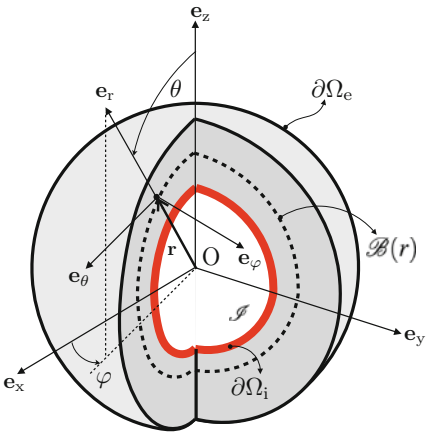

Fig. 1 Problem statement. Notation

$\partial\Omega_i \cup \partial\Omega_e$. Denoting as $|\Omega_s|$ and $|\Omega_v|$ the volume measures of the solid region (namely, Ω_s) and of the spherical void (Ω_v), respectively, the total volume of the system (namely, $\Omega = \Omega_s \cup \Omega_v$) is $|\Omega| = |\Omega_s| + |\Omega_v|$, and the porosity p is equal to $p = |\Omega_v|/|\Omega|$. The solid matrix Ω_s is assumed to be homogeneous and comprised of an isotropic material with a rigid ideal-plastic behaviour.

In agreement with continuum-based descriptions [10, 13, 14, 27] and strength models for nanoporous materials [7, 8], the influence of non-negligible surface stresses induced by the presence of a possibly-nanosized void is herein addressed by introducing a coherent and imperfect homogeneous interface $\mathscr{I}$ at the void boundary $\partial\Omega_i$ (Fig. 1). In particular, the velocity field (resp., the stress vector) is prescribed to be continuous (resp., discontinuous) through $\partial\Omega_i$. In the framework of a plastic generalization of the Gurtin-Murdoch stress-interface model [13], the material comprising the homogeneous interface is assumed to be itself isotropic and rigid ideal-plastic.

Let the Cartesian reference system $(\mathbf{e}_x, \mathbf{e}_y, \mathbf{e}_z)$ be introduced, with the origin O at the sphere center. For what follows, and referring to the notation in Fig. 1, it is useful to consider the spherical coordinate system (r, θ, φ) and the local orthonormal basis $(\mathbf{e}_r, \mathbf{e}_\theta, \mathbf{e}_\varphi)$, r being the radial coordinate, $\theta \in [0, \pi]$ and $\varphi \in [0, 2\pi]$ the zenith and the azimuth angular coordinates, respectively. Accordingly, the position of a point in Ω (resp., at the interface $\mathscr{I}$ and at the exterior boundary $\partial\Omega_e$) with respect to O is identified by $\mathbf{r} = r\,\mathbf{e}_r(\theta, \varphi)$ (resp., $\mathbf{r}_i = R_i\,\mathbf{e}_r(\theta, \varphi)$ and $\mathbf{r}_e = R_e\,\mathbf{e}_r(\theta, \varphi)$).

As a notation rule, vector and second-order tensor quantities are denoted by bold letters; symbols $\cdot$, $:$, and $\otimes$ indicate inner, double-dot, and tensor product operators, respectively; ∇ and $\nabla^{\mathscr{I}}$ are the nabla operators in Ω_s and along the interface, $\widetilde{\nabla}$ and $\widetilde{\nabla}^{\mathscr{I}}$ identifying the symmetric parts of the corresponding gradient operators. Notation $\mathscr{B}(r^*)$ is also introduced to indicate the spherical surface identified by the radial coordinate $r = r^*$.

Let the fourth-order projector tensor $\mathbb{T} = \mathbf{P} \overline{\otimes} \mathbf{P}$ be introduced, where the operator $\overline{\otimes}$ is component-wise defined by $\mathbb{T}_{ijkl} = (P_{ik}P_{jl} + P_{il}P_{jk})/2$, and where the second-

order tensor $\mathbf{P}$ is defined as $\mathbf{P} = (\mathbf{1} - \mathbf{e}_\mathrm{r} \otimes \mathbf{e}_\mathrm{r})$ with $\mathbf{1}$ the identity tensor. Accordingly, $\mathbf{A}_\mathbb{T} = \mathbb{T} : \mathbf{A}$ identifies the projection on planes orthogonal to $\mathbf{e}_\mathrm{r}$ of a second-order tensor $\mathbf{A}$. In the following, $\mathbf{A}$ is referred to as a planar tensor if $\mathbf{A} = \mathbf{A}_\mathbb{T}$.

Neglecting the influence of body forces, sets of statically-admissible ($\mathscr{S}_\sigma$) and plastically-admissible ($\mathscr{P}_\sigma$) stress fields are introduced as

$$\mathscr{S}_\sigma = \left\{ (\boldsymbol{\sigma}, \boldsymbol{\tau}) \quad \text{s.t.} \quad \begin{array}{l} \nabla \cdot \boldsymbol{\sigma} = \mathbf{0} \quad \text{in } \Omega_\mathrm{s}\,, \\ (\boldsymbol{\sigma}^+ - \boldsymbol{\sigma}^-) \cdot \mathbf{e}_\mathrm{r} + (\boldsymbol{\tau} : \mathbf{K})\mathbf{e}_\mathrm{r} = \nabla^{\mathscr{I}} \cdot \boldsymbol{\tau} \quad \text{on } \partial\Omega_\mathrm{i} \end{array} \right\} \tag{1a}$$

$$\mathscr{P}_\sigma = \left\{ (\boldsymbol{\sigma}, \boldsymbol{\tau}) \quad \text{s.t.} \quad f^\mathrm{s}(\boldsymbol{\sigma}) = 0 \quad \text{in } \Omega_\mathrm{s} \quad \text{and} \quad f^{\mathscr{I}}(\boldsymbol{\tau}) = 0 \quad \text{on } \partial\Omega_\mathrm{i} \right\} \tag{1b}$$

where $\boldsymbol{\sigma}$ (resp., $\boldsymbol{\tau}$) denotes the microscopic second-order stress tensor (resp., the planar surface stress tensor at $\mathscr{I}$), f^s (resp., $f^{\mathscr{I}}$) indicates the yield function of the solid matrix (resp., of the interface), $\mathbf{K}$ is the curvature tensor, and $\boldsymbol{\sigma}^\pm = \boldsymbol{\sigma}(r \to R_\mathrm{i}^\pm)$. It is worth pointing out that the equilibrium equation at $\mathscr{I}$ in Eq. (1a) is expressed via a generalized form of the Young-Laplace equation [9, 13], and set $\mathscr{P}_\sigma$ prescribes that the material is everywhere yielding.

The exterior boundary $\partial\Omega_\mathrm{e}$ of the system is assumed to undergo to strain rate-based conditions, expressed in terms of the following second-order axisymmetric deviatoric tensor:

$$\mathbf{D} = \widetilde{D}\left[\frac{1}{2}\left(\mathbf{e}_\mathrm{x} \otimes \mathbf{e}_\mathrm{x} + \mathbf{e}_\mathrm{y} \otimes \mathbf{e}_\mathrm{y}\right) - \mathbf{e}_\mathrm{z} \otimes \mathbf{e}_\mathrm{z}\right] \tag{2}$$

$\widetilde{D}$ being a constant strain-rate parameter, and whose second-order deviatoric and third-order deviatoric stress invariants are denoted as $J_2^\mathrm{d} = \mathrm{tr}(\mathbf{D}^2)/2$ and $J_3^\mathrm{d} = \mathrm{tr}(\mathbf{D}^3)/3$, respectively. The strain-rate deviatoric measure D_eq, as well as the strain-rate Lode angle θ_D are also introduced

$$D_\mathrm{eq} = 2\sqrt{\frac{J_2^\mathrm{d}}{3}}, \qquad \theta_\mathrm{D} = \frac{1}{3}\arccos\frac{3\sqrt{3}J_3^\mathrm{d}}{2(J_2^\mathrm{d})^{3/2}} \tag{3}$$

The set of kinematically-admissible ($\mathscr{K}_d$) strain-rate fields is defined as:

$$\mathscr{K}_d = \left\{ (\mathbf{d}, \mathbf{d}^{\mathscr{I}}) \quad \text{s.t.} \quad \begin{array}{l} \mathbf{d} = \widetilde{\nabla}\mathbf{v} \quad \text{in } \Omega_\mathrm{s}, \\ \mathbf{d}^{\mathscr{I}} = \mathbf{d}(\mathbf{r}_\mathrm{i}) \quad \text{on } \partial\Omega_\mathrm{i}, \\ \text{with } \mathbf{v} = \mathbf{D} \cdot \mathbf{r} \quad \text{on } \partial\Omega_\mathrm{e} \end{array} \right\} \tag{4}$$

with $\mathbf{d}$ (resp., $\mathbf{d}^{\mathscr{I}}$) denoting the microscopic second-order strain-rate tensor in Ω_s (resp., on $\partial\Omega_\mathrm{i}$), and where $\mathbf{v}$ is the local velocity field.

When statically-admissible stress (i.e., $(\boldsymbol{\sigma}, \boldsymbol{\tau}) \in \mathscr{S}_\sigma$) and kinematically-admissible strain-rate (i.e., $(\mathbf{d}, \mathbf{d}^{\mathscr{I}}) \in \mathscr{K}_\mathrm{d}$) local fields are considered, the Hill's theorem holds (e.g., [24])

$$|\Omega|\boldsymbol{\Sigma} : \mathbf{D} = \int_{\Omega^{\mathrm{s}}} \boldsymbol{\sigma} : \mathbf{d}\, d\Omega + \int_{\partial\Omega_{\mathrm{i}}} \boldsymbol{\tau} : \mathbf{d}_{\mathbb{T}}^{\mathscr{I}}\, dA \tag{5}$$

the macroscopic stress tensor $\boldsymbol{\Sigma}$ and the macroscopic strain-rate tensor $\mathbf{D}$ having to comply with relationships $\boldsymbol{\Sigma} = \overline{\boldsymbol{\sigma}}$ and $\mathbf{D} = \overline{\mathbf{d}}$, respectively, where $\overline{\mathbf{a}}$ identifies the Ω-based average of a certain space-dependent field $\mathbf{a}(\mathbf{r})$ (i.e., $\overline{\mathbf{a}} = |\Omega|^{-1} \int_{\Omega} \mathbf{a}\, d\Omega$). The exterior power has to be lower or at the most equal to the maximum plastic dissipation $\mathscr{P}_{\mathrm{rm}}$ that can be afforded in Ω

$$|\Omega|\boldsymbol{\Sigma} : \mathbf{D} \leq \mathscr{P}_{\mathrm{rm}}, \quad \text{with } \mathscr{P}_{\mathrm{rm}}(\mathbf{d}) = \int_{\Omega_{\mathrm{s}}} \pi^{\mathrm{s}}(\mathbf{d})\, d\Omega + \int_{\partial\Omega_{\mathrm{i}}} \pi^{\mathscr{I}}(\mathbf{d}^{\mathscr{I}})\, dA\,, \tag{6}$$

where

$$\pi^{\mathrm{s}}(\mathbf{d}) = \sup_{\boldsymbol{\sigma}\in\mathscr{G}^{\mathrm{s}}} (\boldsymbol{\sigma} : \mathbf{d}), \qquad \text{with} \quad \mathscr{G}^{\mathrm{s}} = \left\{\boldsymbol{\sigma} \text{ s.t. } f^{\mathrm{s}}(\boldsymbol{\sigma}) \leq 0\right\} \tag{7}$$

$$\pi^{\mathscr{I}}(\mathbf{d}^{\mathscr{I}}) = \sup_{\boldsymbol{\tau}\in\mathscr{G}^{\mathscr{I}}} (\boldsymbol{\tau} : \mathbf{d}_{\mathbb{T}}^{\mathscr{I}}), \quad \text{with} \quad \mathscr{G}^{\mathscr{I}} = \left\{\boldsymbol{\tau} \text{ s.t. } f^{\mathscr{I}}(\boldsymbol{\tau}) \leq 0\right\} \tag{8}$$

with $\mathbf{d}_{\mathbb{T}}^{\mathscr{I}} = \mathbb{T} : \mathbf{d}^{\mathscr{I}}$, and where the equality sign in Eq. (6) holds at the limit state. Function π^{s} (resp., $\pi^{\mathscr{I}}$) is the support function for the local strength domain $\mathscr{G}^{\mathrm{s}}$ (resp., $\mathscr{G}^{\mathscr{I}}$). It has the meaning of the maximum volume (resp., surface) density of the resisting power that can be locally achieved by the material, when the local strain-rate field $\mathbf{d}$ (resp., $\mathbf{d}^{\mathscr{I}}$) is considered.

Accordingly, the macroscopic limit stress $\boldsymbol{\Sigma}^{\ell}$ results from

$$\boldsymbol{\Sigma}^{\ell} = \frac{\partial \Pi_{\mathrm{hom}}(\mathbf{D})}{\partial \mathbf{D}} \tag{9}$$

where $\Pi_{\mathrm{hom}}(\mathbf{D})$ is the macroscopic support function, defined as [7]

$$\Pi_{\mathrm{hom}}(\mathbf{D}) = \inf_{(\mathbf{d},\mathbf{d}^{\mathscr{I}})\in\mathscr{K}_d} \left\{\Pi_{\mathrm{hom}}^{\mathrm{s}}(\mathbf{d}) + \Pi_{\mathrm{hom}}^{\mathscr{I}}(\mathbf{d}^{\mathscr{I}})\right\} \tag{10}$$

with

$$\Pi_{\mathrm{hom}}^{\mathrm{s}} = \overline{\pi^{\mathrm{s}}(\mathbf{d})}, \qquad \Pi_{\mathrm{hom}}^{\mathscr{I}} = \frac{1}{|\Omega|} \int_{\partial\Omega_{\mathrm{i}}} \pi^{\mathscr{I}}(\mathbf{d}^{\mathscr{I}})\, dA \tag{11}$$

In the case of an isotropic local plastic behaviour and since for the case under investigation $\mathrm{tr}(\mathbf{D}) = 0$, the macroscopic support function Π_{hom} in Eq. (10) is expressed in terms of the isotropic strain-rate invariants D_{eq} and θ_{D} only, resulting in the macroscopic limit deviatoric stress tensor

$$\boldsymbol{\Sigma}^{\ell} = \frac{2}{3D_{\mathrm{eq}}} \frac{\partial \Pi_{\mathrm{hom}}}{\partial D_{\mathrm{eq}}} \mathbf{D} + \frac{\partial \Pi_{\mathrm{hom}}}{\partial \theta_{\mathrm{D}}} \frac{\partial \theta_{\mathrm{D}}}{\partial \mathbf{D}} \tag{12}$$

Correspondingly, the deviatoric strength measure $\Sigma^{\ell}_{\mathrm{eq}} = \sqrt{3J^{\sigma}_2}$ is introduced, with $J^{\sigma}_2 = \mathrm{tr}(\boldsymbol{\Sigma}^{\ell})^2/2$.

In the following, instead of seeking the infimum in Eq. (10) over all the kinematically-admissible strain-rate states, a particular microscopic velocity field $\widehat{\mathbf{v}}$, such that $\widehat{\mathbf{v}} = \mathbf{D}\cdot\mathbf{r}$ on $\partial\Omega_{\mathrm{e}}$ and yielding to the local strain-rate fields $(\widehat{\mathbf{d}}, \widehat{\mathbf{d}}^{\mathscr{I}}) \in \mathscr{K}_{\mathrm{d}}$, is chosen furnishing an estimate of the macroscopic support function and thereby an upper bound of the macroscopic limit stress.

3 Trial Velocity Field

In agreement with the strategy originally derived in [6] and also adopted in [32], the local kinematics at the collapse state is estimated by assuming a trial velocity field $\widehat{\mathbf{v}} = \widehat{v}_{\mathrm{r}}\,\mathbf{e}_{\mathrm{r}} + \widehat{v}_{\theta}\,\mathbf{e}_{\theta} + \widehat{v}_{\varphi}\,\mathbf{e}_{\varphi}$ in the form

$$\begin{aligned}
\widehat{v}_{\mathrm{r}} &= -\frac{1}{r^2\sin\theta}\frac{\partial}{\partial\theta}\big[\zeta(r,\theta)\sin\theta\big]\\
\widehat{v}_{\theta} &= \frac{1}{r}\frac{\partial}{\partial r}\big[\zeta(r,\theta)\big]\\
\widehat{v}_{\varphi} &= 0
\end{aligned} \tag{13}$$

where function $\zeta(r,\theta)$ is defined by

$$\zeta(r,\theta) = D_{\mathrm{eq}}\left[\frac{r^3}{4} + \chi(r)\right]\sin(2\theta) \tag{14}$$

$\chi(r)$ being a regular function such that

$$\chi(R_{\mathrm{e}}) = \chi^{I}(R_{\mathrm{e}}) = 0 \tag{15}$$

where Roman numerals are used to indicate derivatives with respect to r. Relationships (15) allow the velocity field in Eq. (13) to comply with the strain-rate boundary condition expressed in Eq. (4), and thereby resulting in a kinematically-admissible strain-rate field $(\widehat{\mathbf{d}}, \widehat{\mathbf{d}}^{\mathscr{I}}) \in \mathscr{K}_{\mathrm{d}}$. In detail, it is simple to prove that the adopted trial velocity field under the constrain (15) satisfies the boundary requirement $\widehat{\mathbf{v}} = \mathbf{D}\cdot\mathbf{r}$ on $\partial\Omega_{\mathrm{e}}$, that is

$$\begin{aligned}
\widehat{v}_{\mathrm{r}}(\mathbf{r}_{\mathrm{e}}) &= -D_{\mathrm{eq}}\frac{R_{\mathrm{e}}}{4}\left[1 + 3\cos(2\theta)\right]\\
\widehat{v}_{\theta}(\mathbf{r}_{\mathrm{e}}) &= D_{\mathrm{eq}}\frac{3}{4}R_{\mathrm{e}}\sin(2\theta)\\
\widehat{v}_{\varphi}(\mathbf{r}_{\mathrm{e}}) &= 0
\end{aligned} \tag{16}$$

It is worth observing that condition $\chi(r) = 0$ straight yields the velocity field classically adopted in kinematic limit-analysis approaches [7, 12]. Furthermore, assumptions (13) and (14) correspond to a local strain-rate field verifying the incompressibility condition

$$\operatorname{tr}\widehat{\mathbf{d}} = \frac{\partial}{\partial r}\left(r^2\widehat{v}_r \sin\theta\right) + \frac{\partial}{\partial\theta}\left(r\widehat{v}_\theta \sin\theta\right) = 0 \tag{17}$$

everywhere in the hollow sphere, irrespective of the particular form assumed for $\chi(r)$.

4 Strength Estimate

The solid matrix Ω_s and the interface $\mathscr{I}$ are assumed to obey to a von Mises strength criterion, whose yield (f^s and $f^\mathscr{I}$) and support (π^s and $\pi^\mathscr{I}$) functions are respectively expressed as [24]

$$f^\mathrm{s}(\boldsymbol{\sigma}) = \frac{3}{2}\boldsymbol{\sigma}_\mathrm{d} : \boldsymbol{\sigma}_\mathrm{d} - \sigma_0^2 \tag{18a}$$

$$f^\mathscr{I}(\boldsymbol{\tau}) = \frac{3}{2}\boldsymbol{\tau}_\mathrm{d} : \boldsymbol{\tau}_\mathrm{d} - k_\mathscr{I}^2 \tag{18b}$$

$$\pi^\mathrm{s}(\mathbf{d}) = \begin{cases} \sigma_0\sqrt{\frac{2}{3}\mathbf{d} : \mathbf{d}} & \text{if } \operatorname{tr}\mathbf{d} = 0 \\ +\infty & \text{if } \operatorname{tr}\mathbf{d} \neq 0 \end{cases} \tag{18c}$$

$$\pi^\mathscr{I}(\mathbf{d}^\mathscr{I}) = \begin{cases} k_\mathscr{I}\sqrt{\frac{2}{3}\mathbf{d}^\mathscr{I} : \mathbf{d}^\mathscr{I}} & \text{if } \operatorname{tr}\mathbf{d}^\mathscr{I} = 0 \\ +\infty & \text{if } \operatorname{tr}\mathbf{d}^\mathscr{I} \neq 0 \end{cases} \tag{18d}$$

where $\boldsymbol{\sigma}_\mathrm{d} = \boldsymbol{\sigma} - (\operatorname{tr}\boldsymbol{\sigma}/3)\mathbf{1}$ is the deviatoric part of the stress tensor $\boldsymbol{\sigma}$ in Ω_s, $\boldsymbol{\tau}_\mathrm{d} = \boldsymbol{\tau} - (\operatorname{tr}\boldsymbol{\tau}/3)\mathbf{1}$ is the deviatoric part of the planar stress tensor $\boldsymbol{\tau}$ at $\mathscr{I}$, with $\mathbf{1}$ the second-order identity tensor, and where σ_0 and $k_\mathscr{I}$ are the deviatoric strength parameters of the solid matrix and the interface, respectively, the latter having the dimensions of a membrane stress (namely, a force per unit length).

Kinematically-admissible strain-rate fields $(\widehat{\mathbf{d}}, \widehat{\mathbf{d}}^\mathscr{I}) \in \mathscr{K}_\mathrm{d}$, computed via the velocity field $\widehat{\mathbf{v}}$ introduced in Sect. 3, allows to determine, through Eqs. (18c) and (18d), the following estimate for the macroscopic support function introduced in Eq. (11)

$$\widehat{\Pi}_\mathrm{hom}(D_\mathrm{eq}, \theta_\mathrm{D}) = \sqrt{\frac{2}{3}}\frac{\sigma_0}{|\Omega|}\left[\int_{\Omega_\mathrm{s}} \sqrt{\widehat{\mathbf{d}} : \widehat{\mathbf{d}}}\, d\Omega + \kappa R_\mathrm{i}\int_{\partial\Omega_\mathrm{i}} \sqrt{\widehat{\mathbf{d}}^\mathscr{I} : \widehat{\mathbf{d}}^\mathscr{I}}\, dA\right] \tag{19}$$

where the dimensionless parameter

$$\kappa = \frac{k_{\mathscr{I}}}{R_{\mathrm{i}}\sigma_0} \tag{20}$$

is introduced aiming to account for the influence of void-size effects. As a matter of fact, when strength values for the interface (namely, $k_{\mathscr{I}}$) and for the solid matrix (σ_0) are considered as fixed, a reduction in the void size R_{i} corresponds to increase κ. The case of porous materials comprising cavities with large values of R_{i} is thereby recovered simply by considering $\kappa = 0$, namely by assuming as negligible surface-induced effects.

In order to obtain an explicit analytical estimate of Π_{hom}, the Cauchy-Schwartz inequality leads:

$$\int_{\mathscr{B}(r)} \sqrt{\widehat{\mathbf{d}} : \widehat{\mathbf{d}}}\, dA \leq \sqrt{4\pi r^2}\sqrt{\int_{\mathscr{B}(r)} \widehat{\mathbf{d}} : \widehat{\mathbf{d}}\, dA} \tag{21}$$

and therefore, it results in

$$\widehat{\Pi}_{\mathrm{hom}}(D_{\mathrm{eq}}, \theta_{\mathrm{D}}) \leq \breve{\Pi}_{\mathrm{hom}}(D_{\mathrm{eq}}) \tag{22}$$

with

$$\breve{\Pi}_{\mathrm{hom}}(D_{\mathrm{eq}}) = \sqrt{\frac{2}{3}}\frac{\sigma_0}{|\Omega|}\left[\int_{R_{\mathrm{i}}}^{R_{\mathrm{e}}}\left(\sqrt{4\pi r^2}\sqrt{\int_{\mathscr{B}(r)} \widehat{\mathbf{d}} : \widehat{\mathbf{d}}\, dA}\right) dr + 3\kappa p|\Omega|\sqrt{\lambda_{\mathscr{I}}}\right] \tag{23}$$

where

$$\lambda_{\mathscr{I}} = \frac{1}{4\pi R_{\mathrm{i}}^2}\int_{\partial\Omega_{\mathrm{i}}} \widehat{\mathbf{d}}^{\mathscr{I}} : \widehat{\mathbf{d}}^{\mathscr{I}}\, dA \tag{24}$$

A further use of the Cauchy-Schwartz inequality for the radial-coordinate integral in Eq. (22) produces

$$\breve{\Pi}_{\mathrm{hom}}(D_{\mathrm{eq}}) \leq \widetilde{\Pi}_{\mathrm{hom}}(D_{\mathrm{eq}}) \tag{25}$$

with

$$\widetilde{\Pi}_{\mathrm{hom}}(D_{\mathrm{eq}}) = \sqrt{\frac{2}{3}}\sigma_0\left[(1-p)\sqrt{\lambda_{\mathrm{s}}} + 3\kappa p\sqrt{\lambda_{\mathscr{I}}}\right] \tag{26}$$

and where

$$\lambda_{\mathrm{s}} = \frac{1}{|\Omega_{\mathrm{s}}|}\int_{\Omega_{\mathrm{s}}} \widehat{\mathbf{d}} : \widehat{\mathbf{d}}\, d\Omega \tag{27}$$

It is worth observing that both λ_s and $\lambda_{\mathscr{J}}$ depend on the choice of function $\chi(r)$. Moreover, as proven in [12], $\widetilde{\Pi}_{\text{hom}}$ and thereby $\widetilde{\Pi}_{\text{hom}}$ do not depend on the strain-rate Lode angle θ_D. Accordingly, the corresponding macroscopic stress estimate results in (see Eq. (12))

$$\widetilde{\boldsymbol{\Sigma}}^{\ell} = \frac{2}{3}\frac{1}{D_{\text{eq}}}\frac{\partial \widetilde{\Pi}_{\text{hom}}}{\partial D_{\text{eq}}}\mathbf{D} = \frac{2}{3}\frac{1}{D_{\text{eq}}}\widetilde{\Sigma}^{\ell}_{\text{eq}}\mathbf{D} \tag{28}$$

where $\widetilde{\Sigma}^{\ell}_{\text{eq}}$ is an upper-bound deviatoric macroscopic strength measure.

Aiming to furnish a consistent and effective estimate for the macroscopic support function in Eq. (10), function $\chi(r)$ has to minimise $\lambda_s(\chi)$ and $\lambda_{\mathscr{J}}(\chi)$, as well as it has to comply with kinematic admissibility conditions (15). The first requirement results in a standard problem of variational calculus and leads to the following differential equation

$$\chi^{IV}(r) - \frac{12}{r^2}\chi^{II}(r) + \frac{24}{r^3}\chi^{I}(r) = 0 \tag{29}$$

whose solution is:

$$\chi(r) = C_1 + C_2\frac{R_e^2}{r^2} + C_3\frac{r^3}{R_e^3} + C_4\frac{r^5}{R_e^5} \tag{30}$$

where C_1, C_2, C_3 and C_4 are some integration constants. These latter, due to the kinematic admissibility in Eq. (15), have to satisfy

$$C_1 = -\frac{1}{2}(5C_3 + 7C_4), \qquad C_2 = \frac{1}{2}(3C_3 + 5C_4) \tag{31}$$

Therefore, C_3 and C_4 can be considered as free model parameters to employ for seeking the best possible estimate for the infimum in Eq. (10). In detail, by replacing Eqs. (30) and (31) into Eq. (26), function $\widetilde{\Pi}_{\text{hom}} = \widetilde{\Pi}_{\text{hom}}(C_3, C_4)$ can be minimized with respect to C_3 and C_4.

It is worth remarking that such an optimization strategy can not be performed with classical trial velocity fields, which result to be completely defined via strain-rate boundary conditions only, such the one proposed by Gurson [12] and used in [7] (namely, Eq. (13) with $\chi(r) = 0$).

Accordingly, the optimal values C_3^{opt} and C_4^{opt} are obtained as

$$\begin{aligned} C_3^{\text{opt}} &= -R_i^3\frac{100 - 84p^{2/3} + 19p^{7/3}}{2\Delta} \\ C_4^{\text{opt}} &= 30R_i^3\frac{1 - p^{2/3}}{\Delta} \end{aligned} \tag{32}$$

where $\Delta = 48 + 225p^{2/3} - 336p^{5/3} + 200p + 38p^{10/3}$.

By replacing Eqs. (32) into Eq. (28) and in the framework of small values of p, the following closed-form upper bound of the macroscopic deviatoric strength measure (denoted as BDKV) is obtained

$$\frac{\widetilde{\Sigma}^{\ell}_{\mathrm{eq}}}{\sigma_0} = 1 - \left(\frac{4}{3} - \kappa\sqrt{15}\right)p + \left(\frac{41}{12} - \frac{25}{6}\kappa\sqrt{15}\right)p^2 + \\ - \left(\frac{35}{6} - \frac{28}{3}\kappa\sqrt{15}\right)p^{8/3} + \mathrm{O}(p^3) \tag{33}$$

With reference to the proposed result, the following observations can be stated:

- By enforcing $\chi = 0$ in the estimate $\widetilde{\Pi}_{\mathrm{hom}}$ of Eq. (22), the upper-bound strength measure proposed by Dormieux and Kondo in [7] (denoted in the following as DK) is recovered, resulting in

$$\frac{\Sigma^{\mathrm{DK}}_{\mathrm{eq}}}{\sigma_0} = 1 - \left(1 - \frac{3\sqrt{15}}{5}\kappa\right)p \tag{34}$$

  that, in the case of negligible interface effects (namely, $\kappa = 0$) corresponds to the Gurson's description [12];
- Equation (33), truncated at the first order in p and for $\kappa = 0$, recovers the strength estimate obtained via a variational procedure by Ponte-Castaneda [22].

Model sensitivity to porosity p and void-size effect parameter κ is addressed in Figs. 2 and 3. As expected, results shown in Fig. 2 highlight that the macroscopic deviatoric strength estimate reduces when p increases. The influence of void-size effects is addressed in Figs. 2b and 3, resulting in an improvement of the material strength when the size of void reduces (that is, for large values of κ). Such an occurrence is qualitatively in agreement with well-established experimental [2, 3, 15] and numerical (e.g., [4, 31]) evidence.

Aiming to assess the effectiveness of the proposed strength estimate, comparisons with both theoretical and numerical benchmarks are also provided for different values of parameters p and κ. In detail, reference is made to the theoretical predictions obtained via Eq. (34) [7, 12] and to finite-element-based static and kinematic limit-analysis computations provided in [26] (these latter, available only in the case of $\kappa = 0$ and denoted as TP data). It is observed that, although the proposed deviatoric strength is an upper bound of the exact one, BDKV-based results improve the DK estimate, resulting in lower values and thereby in a more accurate estimate of deviatoric strength properties for porous ($\kappa = 0$) and nanoporous ($\kappa > 0$) materials.

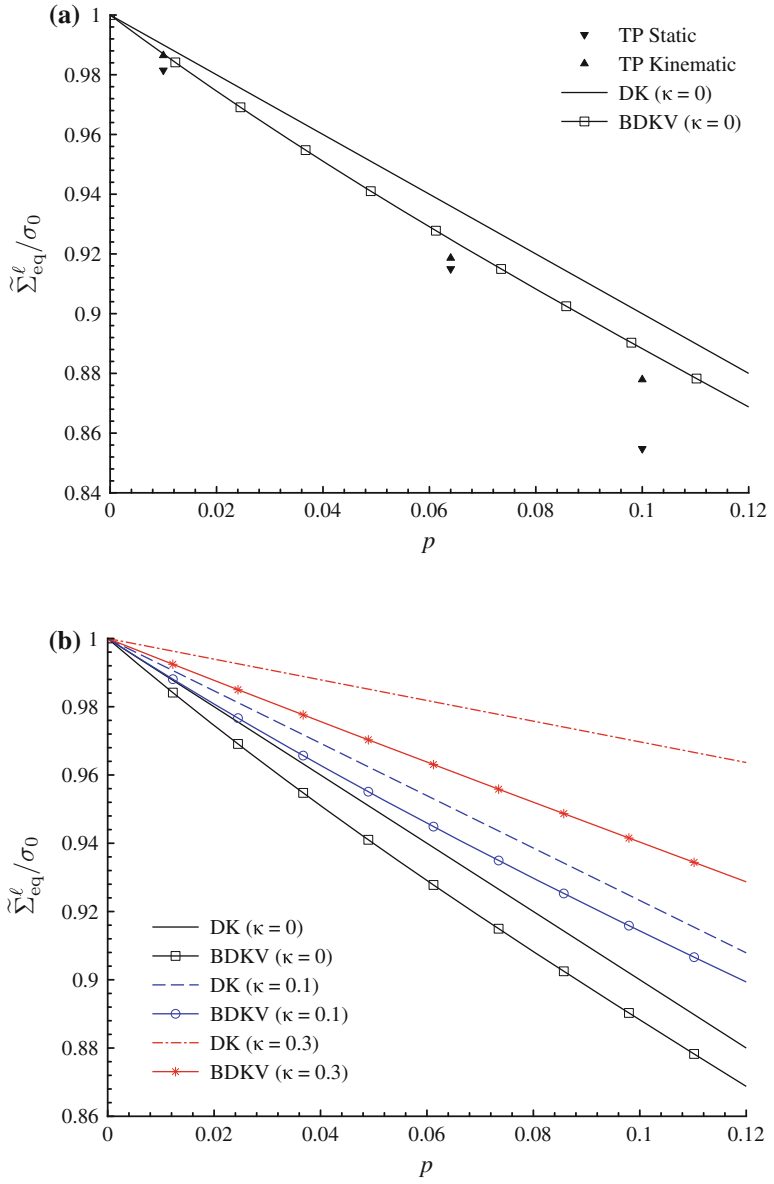

Fig. 2 Normalised deviatoric strength estimate $\widetilde{\Sigma}^{\ell}_{\mathrm{eq}}/\sigma_0$ as a function of the porosity p for different values of κ. (**a**) Assessment with respect to ($\kappa = 0$): static and kinematic numerical bounds (TP [26]); DK model [7, 12]. (**b**) Void-size effects and comparison with respect to the DK model

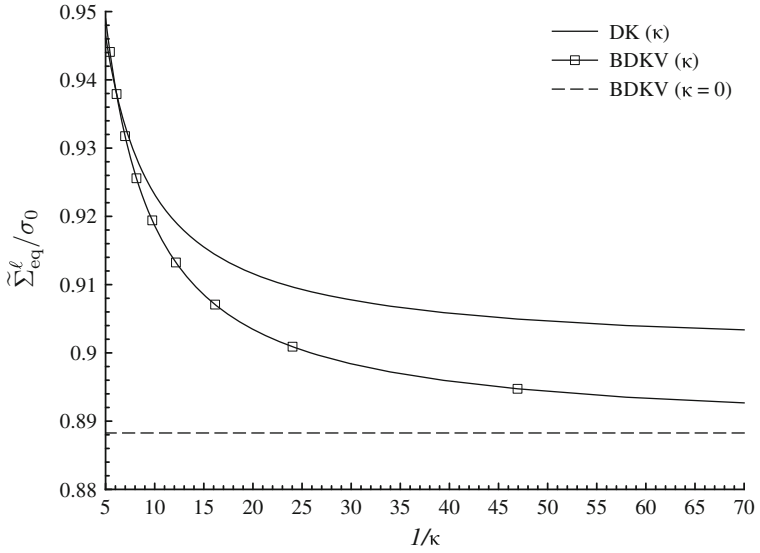

Fig. 3 Normalised deviatoric strength estimate $\widetilde{\Sigma}^{\ell}_{\mathrm{eq}}/\sigma_0$ as a function of the void-size parameter κ ($1/\kappa$ resulting proportional to the void radius R_{i}) for $p = 0.1$. Comparison with respect to the DK model [7, 12].

5 Concluding Remarks

In this paper, an upper-bound estimate of the macroscopic deviatoric strength of a hollow sphere, representative of a particular microstructure for porous and nanoporous materials, has been determined in the case of an axisymmetric deviatoric strain-rate condition and via a kinematic limit analysis approach. The hollow sphere has been assumed to be comprised of a rigid ideal-plastic material, obeying to a von Mises strength criterion. Void-size effects associated to the possible void nanoscale [2, 3, 15] have been accounted for via a coherent and imperfect homogeneous interface at the cavity boundary. The local kinematics at the limit state has been estimated by introducing a suitable trial velocity field, in agreement with findings in [6] (see also [32]) and allowing for an optimization procedure.

With respect to the current state-of-the-art, proposed results furnish the following novel and original contributions:

- an effective description of void-size effects, resulting in an increase of the predicted macroscopic deviatoric strength as the void radius decreases, qualitatively in agreement with available experimental [2, 3, 15] and and numerical [4, 31] evidence;
- an improvement of limit-analysis based estimates [7, 12], resulting in a more effective description of the macroscopic deviatoric strength for porous and nanoporous materials.

Acknowledgements This work was developed within the framework of the Lagrange Laboratory, a European French-Italian research group. Present research study was supported by Sorbonne Universits, in the framework of the PACHA program 2015 (Programme d'Accueil de Chercheurs de HAut niveau).

References

1. Arico AS, Bruce P, Scrosati B, Tarascon JM, Van Schalkwijk W (2005) Nanostructured materials for advanced energy conversion and storage devices. Nature Mater 4:366–377
2. Biener J, Hodge AM, Hamza AV, Hsiung LM, Satcher JH (2005) Nanoporous Au: a high yield strength material. J Appl Phys 97:024301
3. Biener J, Hodge AM, Hayes JR, Volkert CA, Zepeda-Ruiz LA, Hamza AV, Abraham FF (2006) Size effects on the mechanical behaviour of nanoporous Au. Nano Lett 6:2379–2382
4. Brach S, Dormieux L, Kondo D, Vairo G (2016) A computational insight into void-size effects on strength properties of nanoporous materials. Mech Mater 101:102–117
5. Brach S, Dormieux L, Kondo D, Vairo G (2016) Strength properties of nanoporous materials: a 3-layered based non-linear homogenization approach with interface effects, submitted
6. Budiansky B, Hutchinson JW, Slutsky S (1982) Void growth and collapse in viscous solids. In: Hopkins HG, Sewell MJ (eds) Mechanics of solids, The Rodney Hill 60th anniversary volume. Pergamon Press, Oxford, pp 13–45
7. Dormieux L, Kondo D (2010) An extension of Gurson model incorporating interface stress effects. Int J Eng Sci 48:575–581
8. Dormieux L, Kondo D (2013) Non linear homogenization approach of strength of nanoporous materials with interface effects. Int J Eng Sci 71:102–110
9. Duan HL, Wang J, Huang ZP, Karihaloo BL (2005) Size-dependent effective elastic constants of solids containing nano-inhomogeneities with interface stress. J Mech Phys Solids 53:1574–1596
10. Duan HL, Wang J, Huang ZP, Luo ZY (2005) Stress concentration tensors of inhomogeneities with interface effects. Mech Mater 37:723–736
11. Goudarzi T, Avazmohammadi R, Naghdabadi R (2010) Surface energy effects on the yield strength of nanoporous materials containing nanoscale cylindrical voids. Mech Mater 42:852–862
12. Gurson AL (1977) Continuum theory of ductile rupture by void nucleation and growth: Part I.—Yield criterion and flow rules for porous ductile media. J Eng Mater Technol 99:2–15
13. Gurtin ME, Murdoch AI (1975) A continuum theory of elastic material surfaces. Arch Ration Mech Anal 57:291–323
14. Gurtin ME, Murdoch AI (1978) Surface stress in solids. Int J Solids Struct 14:431–440
15. Hakamada M, Mabuchi M (2007) Mechanical strength of nanoporous gold fabricated by dealloying. Scr Mater 56:1003–1006
16. Jenkins SB (2010) Nanoporous materials: types, properties, and uses. Nova Science Publishers, New York
17. Lu GQ, Zhao XS (2004) Nanoporous materials: science and engineering. Imperial College Press, London
18. Mi C, Buttry DA, Sharma P, Kouris DA (2011) Atomistic insights into dislocation-based mechanisms of void growth and coalescence. J Mech Phys Solids 59:1858–1871
19. Monchiet V, Bonnet G (2010) Interfacial models in viscoplastic composites materials. Int J Eng Sci 48:1762–1768
20. Moshtaghin AF, Naghdabadi R, Asghari M (2008) Effects of surface residual stress and surface elasticity on the overall yield surfaces of nanoporous materials with cylindrical nanovoids. Mech Mater 51:74–87

21. Needs RJ, Godfrey MJ, Mansfield M (1991) Theory of surface stress and surface reconstruction. Surf Sci 242:215–221
22. Ponte Castañeda P (1991) The effective mechanical properties of nonlinear isotropic composites. J Mech Phys Solids 39:45–71
23. Povstenko YuZ (1993) Theoretical investigation of phenomena caused by heterogeneous surface tension in solids. J Mech Phys Solids 41:1499–1514
24. Salençon J (1983) Calcul la rupture et analyse limite (in French). Presses de lÉcole Nationale des Ponts et Chaussées, Paris
25. Traiviratana S, Bringa EM, Benson DJ, Meyers MA (2008) Void growth in metals: atomistic calculations. Acta Mater 56:3874–3886
26. Trillat M, Pastor J (2005) Limit analysis and Gursons model. Eur J Mech A/Solids 24:800–819
27. Wang J, Huang Z, Duan H, Yu S, Feng X, Wang G, Zhang W, Wang T (2011) Surface stress effect in mechanics of nanostructured materials. Acta MechSolida Sinica 52–82
28. Zhang W, Wang TJ, Chen X (2008) Effect of surface stress on the asymmetric yield strength of nanowires. J Appl Phys 103:123527
29. Zhang W, Wang TJ, Chen X (2010) Effect of surface/interface stress on the plastic deformation of nanoporous materials and nanocomposites. Int J Plast 26:957–975
30. Zhang W, Wang TJ (2007) Effect of surface energy on the yield strength of nanoporous materials. Appl Phys Lett 90:063104
31. Zhao KJ, Chen CQ, Shen YP, Lu TJ (2009) Molecular dynamics study on the nano-void growth in face-centered cubic single crystal copper. Comput Mater Sci 46:749–754
32. Zhu HT, Zbib HM (1993) A continuum model for flow strength of metal-matrix composites. Scripta Metallurgica et Materialia 28:1323–1328

On Melan's Theorem in Temperature-Dependent Viscoplasticity

Michaël Peigney

Abstract In plasticity, Melan's theorem is a well-known result that is both of theoretical and practical importance. That theorem applies to elastic-plastic structures under time-dependent loading histories, and gives a sufficient condition for the plastic dissipation to remain bounded in time. That situation is classically referred to as shakedown. Regarding fatigue, shakedown corresponds to the most favorable case of high-cycle fatigue. The original Melan's theorem rests on the assumption that the material properties remain constant in time, independently on the applied loading. Extending Melan's theorem to time fluctuating elastic moduli is a long standing issue. The main motivation is to extend the range of applications of Melan's theorem to thermomechanical loading histories with large temperature fluctuations: In such case, the variation of the elastic properties with the temperature cannot be neglected. In this contribution, an extension of Melan's theorem to elastic-viscoplastic materials with time-periodic elastic moduli is presented. Such a time-dependence may for instance result from time-periodic temperature variations. An illustrative example is presented and supported by numerical results obtained from incremental analysis.

1 Introduction

For elastic-perfectly plastic structures under prescribed loading histories, the well-known Melan's theorem [11, 16, 26] gives a sufficient condition for the evolution to become elastic in the large-time limit. That situation is classically referred to as *shakedown*. Intuitively, shakedown means that the plastic strain tends to a limit as time tends to infinity. The Melan's theorem has the distinctive property of being path-independent, i.e. independent on the initial state of the structure. For a parametrized loading history, Melan's theorem gives bounds on the domain of load parameters for which shakedown occurs. Regarding fatigue design, shakedown corresponds to the

M. Peigney (✉)
Laboratoire Navier (UMR 8205), CNRS, Ecole des Ponts ParisTech, IFSTTAR, Université Paris-Est, 77455 Marne la Vallée, France
e-mail: michael.peigney@polytechnique.org

M. Frémond et al. (eds.), *Models, Simulation, and Experimental Issues in Structural Mechanics*, Springer Series in Solid and Structural Mechanics 8,
DOI 10.1007/978-3-319-48884-4_9

most beneficial regime of high-cycle fatigue, as opposed to the regime of low-cycle fatigue which typically occurs if the plastic strain does not converge towards a stabilized value [5]. The shakedown theory has been the object of numerous developments, regarding both extensions of the original theorem to various nonlinear behaviors [1, 17, 20, 21, 23, 27] and numerical methods for assessing the shakedown limits in the space of load parameters [4, 15, 18, 19, 24, 25, 28].

This chapter is concerned with extensions of the Melan's theorem to situations in which the elastic moduli are fluctuating in time, for instance as a result of imposed temperature variations. Whereas the case of temperature-dependent yield limits is well understood [2], the case of temperature-dependent elastic moduli remains a long standing issue and has been the object of several conjectures [8–10, 12]. The main difficulty is that the proof used in the original Melan's theorem—as well as in most of its knows extensions—crucially relies on some monotonicity properties that are lost when the elastic moduli are allowed to vary in time. For instance, in the case of constant elastic moduli, the distance between two solutions (as measured by the energy norm) is always decreasing with time [17], which is no longer true when the elastic moduli vary in time (see [22] for some example). A shakedown theorem has recently been proposed for elastic-perfectly plastic materials with time-periodic elastic properties [22]. The statement and proof of that theorem differ significantly from the case of constant material properties. A salient result is that time fluctuations of the elastic moduli need to be not too large for shakedown to occur in a path-independent fashion.

In this contribution, we aim at extending the result of [22] to elastic-viscoplastic materials with time fluctuating elastic moduli. The proof presented in [22] for elastic-perfectly plastic materials used the fact that the stress remains in the elasticity domain, which is not necessarily the case in viscoplasticity. In particular, the initial residual stress can be chosen as arbitrarily large, so that the stress is expected to remain outside (and possibly far away from) the elasticity domain—at least on some time interval. This chapter is organized as follows: In Sect. 2, starting from the local constitutive relations and the equilibrium equations, we derive the differential equation that governs quasistatic evolutions of the residual stress. We comment on the special (and important) case of elastic solutions. Section 3 is devoted to the statement and proof of a shakedown theorem for elastic-viscoplastic materials with time-periodic material properties, that is the main result of this chapter. An illustrative example is presented in Sect. 4 and supported by numerical results provided by incremental analysis. Some concluding remarks follow.

2 Quasistatic Evolutions of an Elastic-Viscoplastic Medium

Consider an elastic-viscoplastic body occupying a domain Ω in the reference configuration. Under the assumption of infinitesimal strains, the strain tensor $\boldsymbol{\varepsilon}$ is derived from the displacement $\boldsymbol{u}$ by

$$\boldsymbol{\varepsilon} = \frac{1}{2}(\nabla \boldsymbol{u} + \nabla^T \boldsymbol{u}).$$

The total strain $\boldsymbol{\varepsilon}$, stress $\boldsymbol{\sigma}$ and plastic strain $\boldsymbol{\varepsilon}^p$ at position $\boldsymbol{x}$ and time t satisfy the constitutive equations

$$\boldsymbol{\varepsilon}(\boldsymbol{x}, t) = \boldsymbol{L}(\boldsymbol{x}, t) : \boldsymbol{\sigma}(\boldsymbol{x}, t) + \boldsymbol{\varepsilon}^\theta(\boldsymbol{x}, t) + \boldsymbol{\varepsilon}^p(\boldsymbol{x}, t), \tag{1}$$

$$\dot{\boldsymbol{\varepsilon}}^p(\boldsymbol{x}, t) = \phi'(\boldsymbol{\sigma}(\boldsymbol{x}, t), \boldsymbol{x}, t), \tag{2}$$

where ϕ is the dissipation potential, taken in the form

$$\phi(\boldsymbol{\sigma}, \boldsymbol{x}, t) = \frac{\alpha}{2}|\boldsymbol{\sigma} - P_{\mathscr{C}(\boldsymbol{x},t)}\boldsymbol{\sigma}|^2. \tag{3}$$

In (1), $\boldsymbol{L}$ is the (symmetric positive definite) elastic moduli tensor and $\boldsymbol{\varepsilon}^\theta$ is the thermal strain tensor. The double product: in (1) denotes contraction with respect to the last two indexes, i.e. $(\boldsymbol{L} : \boldsymbol{\sigma})_{ij} = \sum_{k,l} \boldsymbol{L}_{ijkl}\boldsymbol{\sigma}_{lk}$.

In (3), $\mathscr{C}(\boldsymbol{x}, t)$ is the elasticity domain of the material (assumed to be closed and convex), $\alpha > 0$ is a viscosity parameter (assumed to be independent on $(\boldsymbol{x}, t)$ for simplicity) and $P_{\mathscr{C}(\boldsymbol{x},t)}$ denotes the projection of $\mathscr{C}(\boldsymbol{x}, t)$. The norm $|\cdot|$ in (3) is defined by $|\boldsymbol{\sigma}| = \sqrt{\sum_{i,j} \boldsymbol{\sigma}_{ij}^2}$ for any symmetric tensor $\boldsymbol{\sigma}$.

As mentioned in Sect. 1, the space and time dependence of $\boldsymbol{L}$, $\boldsymbol{\varepsilon}^\theta$ and $\mathscr{C}$ may reflect imposed variations of the temperature. For instance, the elastic moduli $\boldsymbol{L}$ of most materials depend on the temperature θ, what can be written as $\boldsymbol{L} = \boldsymbol{L}(\theta)$. For imposed variations $\theta(\boldsymbol{x}, t)$ of the temperature, the elastic moduli tensor vary as $\boldsymbol{L}(\theta(\boldsymbol{x}, t))$ and can thus be regarded as a function of space and time.

Assuming quasi-static evolutions, the stress field $\boldsymbol{\sigma}$ satisfies the equilibrium equations

$$\text{div } \boldsymbol{\sigma} + \boldsymbol{f} = 0 \text{ in } \Omega, \ \boldsymbol{\sigma} \cdot \boldsymbol{n} = \boldsymbol{T} \text{ on } \partial\Omega_T, \tag{4}$$

where $\boldsymbol{f}(\boldsymbol{x}, t)$ are body forces imposed in the domain Ω and $\boldsymbol{T}(\boldsymbol{x}, t)$ are tractions prescribed on a part $\partial\Omega_T$ of the boundary $\partial\Omega$. Prescribed displacements $\boldsymbol{v}(\boldsymbol{x}, t)$ are imposed on $\partial\Omega_u = \partial\Omega - \partial\Omega_T$.

2.1 Evolution Equation for the Residual Stress

We now use Eqs. (1–4) to derive the equation governing the evolution of the stress field. The space $\mathcal{E}$ of stress fields is chosen as a subspace of symmetric second-order tensor fields with square-integrable components, which is known to be a Hilbert space for the scalar product

$$\langle \boldsymbol{\sigma}, \boldsymbol{\sigma}' \rangle = \int_\Omega \boldsymbol{\sigma}(\boldsymbol{x}) : \boldsymbol{\sigma}'(\boldsymbol{x}) d\omega.$$

The associated norm is denoted by $\| \ \|$, i.e. $\|\boldsymbol{\sigma}\| = \sqrt{\langle \boldsymbol{\sigma}, \boldsymbol{\sigma} \rangle}$.

Consider the so-called *fictitious elastic response* $(\boldsymbol{u}^E, \boldsymbol{\sigma}^E)$, i.e. the response of the system if it were purely elastic, defined by

$$\begin{aligned} \boldsymbol{\varepsilon}^E &= \boldsymbol{L} : \boldsymbol{\sigma}^E + \boldsymbol{\varepsilon}^\theta, \\ \boldsymbol{\varepsilon}^E &= \frac{1}{2}(\nabla \boldsymbol{u}^E + \nabla^T \boldsymbol{u}^E), \\ \text{div } \boldsymbol{\sigma}^E + \boldsymbol{f} &= 0 \text{ in } \Omega, \\ \boldsymbol{\sigma}^E \cdot \boldsymbol{n} &= \boldsymbol{T} \text{ on } \partial\Omega_T, \\ \boldsymbol{u}^E &= \boldsymbol{v} \text{ on } \partial\Omega_u. \end{aligned} \tag{5}$$

The stress field $\boldsymbol{\sigma}$ can be written as $\boldsymbol{\sigma} = \boldsymbol{\sigma}^E + \boldsymbol{\rho}$ where $\boldsymbol{\rho}$ is the residual stress field and belongs to the vectorial space $\mathcal{H} \subset \mathcal{E}$ of self-equilibrated fields, defined by

$$\mathcal{H} = \{\boldsymbol{\rho} \in \mathcal{E} : \text{div } \boldsymbol{\rho} = 0 \text{ in } \Omega, \ \boldsymbol{\rho} \cdot \boldsymbol{n} = 0 \text{ on } \partial\Omega_T\}. \tag{6}$$

Let $\mathcal{K}_0(t)$ and $\mathcal{K}(t)$ be the convex subsets of $\mathcal{E}$ defined as

$$\mathcal{K}_0(t) = \{\boldsymbol{\sigma} \in \mathcal{E} : \boldsymbol{\sigma}(\boldsymbol{x}, t) \in \mathscr{C}(\boldsymbol{x}, t) \ \forall \boldsymbol{x} \in \Omega\}, \ \mathcal{K}(t) = \mathcal{K}_0(t) - \boldsymbol{\sigma}^E(t). \tag{7}$$

The set $\mathcal{K}_0(t)$ is the set of stress fields that are everywhere in the elasticity domain of the material. The set $\mathcal{K}(t)$ is the translated of $\mathcal{K}_0$ by $-\boldsymbol{\sigma}^E(t)$. Note that $\mathcal{K}_0$ is independent on time t if the yield parameters are. Under suitable regularity assumptions on $(\boldsymbol{f}, \boldsymbol{T}, \boldsymbol{v})$, it can proved that the sets $\mathcal{H}$ and $\mathcal{K}(t)$ are closed in $\mathcal{E}$ [13].

For an arbitrary $\boldsymbol{\rho}' \in \mathcal{K}(t)$, it follows from (1) that

$$\begin{aligned} \int_\Omega (\boldsymbol{\rho}' - \boldsymbol{\rho}) : \frac{d(\boldsymbol{\varepsilon} - \boldsymbol{\varepsilon}^E)}{dt} d\omega = \int_\Omega (\boldsymbol{\rho}' - \boldsymbol{\rho}) : \frac{d}{dt}(\boldsymbol{L} : \boldsymbol{\rho}) \, d\omega \\ + \int_\Omega (\boldsymbol{\rho}' - \boldsymbol{\rho}) : \phi'(\boldsymbol{\sigma}) \, d\omega \, . \end{aligned} \tag{8}$$

Using (5–6) together with the principle of virtual power shows that the left-hand side of (8) is equal to zero. Hence

$$-\int_\Omega (\boldsymbol{\rho}' - \boldsymbol{\rho}) : \frac{d}{dt}(\boldsymbol{L}(\boldsymbol{x}, t) : \boldsymbol{\rho}) \, d\omega = \int_\Omega (\boldsymbol{\rho}' - \boldsymbol{\rho}) : \phi'(\boldsymbol{\sigma}, \boldsymbol{x}, t) \, d\omega. \tag{9}$$

The function

$$\Phi(\boldsymbol{\sigma}, t) = \int_\Omega \phi(\boldsymbol{\sigma}, \boldsymbol{x}, t) \, d\omega$$

is convex, positive, and vanishes on $\mathcal{K}_0(t)$. It is a classical result [3] that

$$\Phi(\boldsymbol{\sigma}, t) = \frac{\alpha}{2}\|\boldsymbol{\sigma} - P_{\mathcal{K}_0(t)}\boldsymbol{\sigma}\|^2, \quad \Phi'(\boldsymbol{\sigma}, t) = \alpha(\boldsymbol{\sigma} - P_{\mathcal{K}_0(t)}\boldsymbol{\sigma}) \tag{10}$$

where $P_{\mathcal{K}_0(t)} : \mathcal{E} \mapsto \mathcal{E}$ denotes the projection on $\mathcal{K}_0(t)$ (for the scalar product $\langle \cdot, \cdot \rangle$). It follows from (10) that

$$\int_\Omega (\boldsymbol{\rho}' - \boldsymbol{\rho}) : \phi'(\boldsymbol{\sigma})\, d\omega = \langle \boldsymbol{\rho}' - \boldsymbol{\rho}, \Phi'(\boldsymbol{\sigma}) \rangle = \langle \boldsymbol{\rho}' - \boldsymbol{\rho}, \alpha(\boldsymbol{\sigma} - P_{\mathcal{K}_0(t)}\boldsymbol{\sigma}) \rangle.$$

Further observing that $\boldsymbol{\sigma} - P_{\mathcal{K}_0(t)}\boldsymbol{\sigma} = \boldsymbol{\rho} - P_{\mathcal{K}(t)}\boldsymbol{\rho}$, we obtain from (9) that $\boldsymbol{\rho}$ satisfies

$$-\frac{d}{dt}(\boldsymbol{L}(\boldsymbol{x}, t)\boldsymbol{\rho}) : \in \alpha(\boldsymbol{\rho} - P_{\mathcal{K}(t)}\boldsymbol{\rho}) + \mathcal{H}^\perp \tag{11}$$

where $\mathcal{H}^\perp$ is the orthogonal of $\mathcal{H}$ in $\mathcal{E}$.

Equation (11) can be simplified by projecting it on $\mathcal{H}$. To that purpose, set $\mathcal{L}(t) = \boldsymbol{\pi}\boldsymbol{L}$: where $\boldsymbol{\pi} : \mathcal{E} \mapsto \mathcal{H}$ is the orthogonal projector on $\mathcal{H}$. Equation (11) becomes

$$-\frac{d}{dt}(\mathcal{L}(t)\boldsymbol{\rho}) = \alpha(\boldsymbol{\rho} - \boldsymbol{\pi} P_{\mathcal{K}(t)}\boldsymbol{\rho}). \tag{12}$$

Since the elastic moduli tensor $\boldsymbol{L}(\boldsymbol{x}, t)$ is symmetric positive definite, it can easily be verified that $\mathcal{L}(t)$ is self-adjoint and positive definite. Starting from a given initial state $\boldsymbol{\rho}(t = 0)$, the evolution of the stress field in $\mathcal{H}$ is governed by the ordinary differential equation (12). The uniqueness of the stress rate $\dot{\boldsymbol{\rho}}$ has been proved in [7].

2.2 *Elastic Solutions*

In the following we study the asymptotic behavior of solutions to (12) as $t \to \infty$. We only consider the case where $\mathcal{L}(t), \mathcal{K}(t)$ are periodic in time (with the same period T) and the dimension of $\mathcal{H}$ is finite. A central role is played by elastic solutions of (12), i.e. solutions without any plastic yielding. Such an elastic solution $\boldsymbol{\rho}^*(t)$ necessarily lies in $\mathcal{K}(t)$ at each time t, and therefore satisfies

$$\frac{d}{dt}(\mathcal{L}(t)\boldsymbol{\rho}^*(t)) = 0, \quad \boldsymbol{\rho}^*(t) \in \mathcal{K}(t) \cap \mathcal{H}\ \forall t \in [0, T] \tag{13}$$

Our main objective is to examine conditions under which *every* solution of (12) converges towards an elastic solution in the large time limit. A first requisite is obviously that elastic solutions do exist, i.e. that

$$\bigcap_{0\leq t\leq T} \mathcal{L}(t)\mathcal{K}(t) \neq \emptyset. \tag{14}$$

Even when the elastic moduli are time-independent, the condition (14) is not sufficient to obtain results on the asymptotic behavior. Loosely speaking, a minimal requirement is the existence of an elastic solution that remains 'strictly inside' the elastic domain. In the case of time-independent elastic moduli, that notion of 'strictly inside' is captured by the Melan's condition defined as follows

Melan's condition (standard form): There exists an elastic solution $\boldsymbol{\rho}^*$ and some $m > 1$ such that $\boldsymbol{\rho}^*(\boldsymbol{x}, t) + m\boldsymbol{\sigma}^E(\boldsymbol{x}, t) \in \mathscr{C}(\boldsymbol{x}, t)\ \forall(\boldsymbol{x}, t) \in \Omega \times [0, T]$.

Let $B(\boldsymbol{\rho}^*, r)$ denotes the ball of center $\boldsymbol{\rho}^*$ and radius r in $\mathcal{E}$ (for the norm $\|\cdot\|$). In the following, we consider a strong version of Melan's condition, defined as follows:

Melan's condition (strong version): There exists an elastic solution $\boldsymbol{\rho}^*$ and some $r > 0$ such that $\mathcal{H} \cap B(\boldsymbol{\rho}^*(t), r) \in \mathcal{K}(t)\ \forall t \in \times[0, T]$.

When the dimension of $\mathcal{H}$ is finite, the strong and standard versions of Melan's condition are equivalent. This is no longer true in infinite dimension (the strong version, as its names suggests, is more restrictive).

3 Shakedown Theorem

Let us fix some notations and assumptions to be used in the remainder:

- $\mu(t)$ denotes an arbitrary non-negative differentiable function such that $\inf_t \mu(t) > 0$. We set
$$\mathcal{L}_0(t) = \mathcal{L}(t)/\mu(t),\ \mathcal{M}_0(t) = \mathcal{L}_0^{-1}(t) = \mu(t)\mathcal{M}(t). \tag{15}$$
with $\mathcal{M}(t) = \mathcal{L}(t)^{-1}$.
- The set $\boldsymbol{\pi}\mathcal{K}(t)$ remains bounded[1] i.e. there exists a constant M such that
$$\|\boldsymbol{\pi}\boldsymbol{\rho}'\| \leq M \ \text{ for all } t \text{ and } \boldsymbol{\rho}' \in \mathcal{K}(t). \tag{16}$$
- The elastic operator $\mathcal{L}(t)$ is assumed to remain bounded in $\mathcal{H}$, i.e. there exists a constant C such that
$$|||\mathcal{L}(t)||| \leq C \tag{17}$$
for all $t \in [0, T]$. In (17), $|||\cdot|||$ denotes the norm operator in $\mathcal{H}$, i.e. $|||\mathcal{L}(t)||| = \sup_{\boldsymbol{\rho}'\in\mathcal{H}, \|\boldsymbol{\rho}'\|=1} \|\mathcal{L}(t)\boldsymbol{\rho}'\|$. We note that (17) is satisfied if the local elastic moduli $\boldsymbol{L}(\boldsymbol{x}, t)$ remain bounded [22]. Similarly, the operator $\mathcal{M}(t)$ is assumed to be bounded.

[1] It can observed that $\boldsymbol{\pi}\mathcal{K}(t)$ is bounded if the $\mathscr{C}(\boldsymbol{x}, t)$ is.

- We introduce a measure $\gamma(0,T)$ of the time-fluctuations of the elastic moduli, defined as

$$\gamma(0,T)=\int_0^T |||\dot{\mathcal{M}}_0(t)|||\,dt=\int_0^T |||\mu(t)\dot{\mathcal{M}}(t)+\dot{\mu}(t)\mathcal{M}(t)|||\,dt. \tag{18}$$

The objective of this section is to prove Theorem 1 below.

Theorem 1 *If*

(i) the Melan's condition is satisfied by some $(\boldsymbol{\rho}^*, r)$*;*

(ii) the elastic moduli are such that

$$\frac{\gamma(0,T)}{\inf\mu}<\frac{r}{2CM};$$

then the residual stress converges towards an elastic solution, whatever the initial state is.

In that theorem, condition (ii) sets a restriction on the time variations of the elastic moduli. Setting such a restriction is necessary to obtain global convergence results: One can indeed find counter examples in which condition (i) is fulfilled and some solutions of (12) do not become elastic in the large time limit [22].

The statement of Theorem 1 above is quite similar to that obtained in perfect plasticity [22]. The proof, however, is more complicated and detailed in the following. To clarify the exposition, the proof is broken down in 3 separate steps, covered by Sects. 3.1–3.3 below. Compared to perfect plasticity, an additional difficulty is that the stress is not restricted to remain in the elasticity domain. For instance, the initial stress can be chosen as arbitrarily large. It can be proved, however, that the stress is bounded at large time: This is the object of Lemma 1, Sect. 3.1. The next step consists in proving that, for large time, the variation of some elastic energy is controlled by the plastic dissipation, in a sense that is defined in Lemma 2, Sect. 3.2. The claimed result follows from those two lemmas, as detailed in Sect. 3.3.

In all that follows, $\boldsymbol{\rho}(t)$ denotes an arbitrary solution of (12).

3.1 Bound on the Stress Field

Let $\boldsymbol{\eta}(t)=\mathcal{L}(t)\boldsymbol{\rho}(t)$. The object of the following lemma is to prove that, for large time, $\boldsymbol{\eta}(t)$ is bounded by some constant M' that can be chosen as arbitrarily close to CM.

Lemma 1 *For any* $M'>CM$*, there exists* $t_0\geq 0$ *such that* $\|\boldsymbol{\eta}(t)\|\leq M'$ *for all* $t\geq t_0$.

Proof We have

$$\begin{aligned}\frac{d}{dt}\|\boldsymbol{\eta}(t)\|^2 &= -2\alpha\langle\boldsymbol{\rho}-\boldsymbol{\pi}\,P_{\mathcal{K}(t)}\boldsymbol{\rho},\,\boldsymbol{\eta}(t)\rangle \\ &= -2\alpha\langle\boldsymbol{\eta}(t),\,\mathcal{M}(t)\boldsymbol{\eta}(t)\rangle + 2\alpha\langle\boldsymbol{\pi}\,P_{\mathcal{K}(t)}\boldsymbol{\rho},\,\boldsymbol{\eta}(t)\rangle.\end{aligned} \tag{19}$$

Since $\mathcal{L}(t)$ is symmetric positive definite, we have $|||\mathcal{L}(t)||| = \max_i \lambda_i$ where $\{\lambda_i\}$ are the eigenvalues of $\mathcal{L}(t)$. The relation (17) implies that $\lambda_i \le C$ for all i. Since $\mathcal{M}(t)$ is positive definite with eigenvalues $\{1/\lambda_i\}$, it follows that

$$\langle\boldsymbol{\eta}(t),\,\mathcal{M}(t)\boldsymbol{\eta}(t)\rangle \ge \min_i \frac{1}{\lambda_i}\|\boldsymbol{\eta}(t)\|^2 \ge \frac{\|\boldsymbol{\eta}(t)\|^2}{C}.$$

Moreover, using Cauchy-Schwartz inequality together with (16), we find

$$2\alpha\langle\boldsymbol{\pi}\,P_{\mathcal{K}(t)}\boldsymbol{\rho},\,\boldsymbol{\eta}(t)\rangle \le 2\alpha\|\boldsymbol{\pi}\,P_{\mathcal{K}(t)}\boldsymbol{\rho}\|\cdot\|\boldsymbol{\eta}(t)\| \le 2\alpha M\|\boldsymbol{\eta}(t)\|.$$

Substituting in (19) gives

$$\frac{d}{dt}\|\boldsymbol{\eta}(t)\|^2 \le -2\frac{\alpha}{C}\|\boldsymbol{\eta}(t)\|^2 + 2\alpha M\|\boldsymbol{\eta}(t)\|. \tag{20}$$

Setting $G(t) = \max(M^2C^2, \|\boldsymbol{\eta}(t)\|^2)$, Eq. (20) implies that G is decreasing with time t. It can indeed easily be verified from (20) that G is right-differentiable and satisfies $G'_+(t) \le 0$ for all t, where $G'_+(t)$ is the right-derivative of G.

If $\|\boldsymbol{\eta}(t_0)\| \le CM$ for some time t_0, then it directly follows from the monotonicity of G that $\|\boldsymbol{\eta}(t)\| \le CM$ for any $t \ge t_0$, which proves the claim. Now consider the case where $\|\boldsymbol{\eta}(t)\| > CM$ for all time t. Dividing (20) by $\|\boldsymbol{\eta}(t)\|$, we have

$$\frac{1}{\|\boldsymbol{\eta}(t)\|}\frac{d}{dt}\|\boldsymbol{\eta}(t)\|^2 = 2\frac{d}{dt}\|\boldsymbol{\eta}(t)\| \le -2\frac{\alpha}{C}\|\boldsymbol{\eta}(t)\| + 2\alpha M. \tag{21}$$

Using the differential form of Gronwall's lemma, (21) implies that

$$\|\boldsymbol{\eta}(t)\| \le \|\boldsymbol{\eta}(t_0)\|e^{-\alpha t/C} + CM(1-e^{-\alpha t/C}). \tag{22}$$

The right-hand side of (22) varies between $\|\boldsymbol{\eta}(t_0)\|$ and CM in a monotonic fashion. Choosing for instance

$$t_0 = \frac{C}{\alpha}|\log\frac{\|\boldsymbol{\eta}(0)\| - CM}{M' - CM}|,$$

Equation (22) implies that $\|\boldsymbol{\eta}(t)\| \le M'$ for all $t \ge t_0$, which proves the claim. □

3.2 Variation of the Elastic Energy

Consider the positive function f defined as

$$f(t) = \frac{1}{2}\langle \boldsymbol{\tau}(t), \mathcal{L}_0(t)\boldsymbol{\tau}(t)\rangle \tag{23}$$

where $\boldsymbol{\tau}(t) = \mu(t)(\boldsymbol{\rho}(t) - \boldsymbol{\rho}^*(t))$. The function f is referred to as the elastic energy. The aim of this section is to establish Lemma 2 below, which bounds the variation $f(a+T) - f(a)$ for large time a.

Lemma 2 *Let (M', t_0) satisfying Lemma 1. For any $a \geq t_0$ we have*

$$f(a+T) - f(a) \leq \left(2M'\gamma(0,T) - r \inf \mu\right) \int_a^{a+T} \|\dot{\boldsymbol{\eta}}(t)\| dt. \tag{24}$$

Proof We have

$$\dot{f}(t) = \langle \boldsymbol{\tau}(t), \mathcal{L}_0(t)\dot{\boldsymbol{\tau}}(t)\rangle + \frac{1}{2}\langle \boldsymbol{\tau}(t), \dot{\mathcal{L}}_0(t)\boldsymbol{\tau}(t)\rangle. \tag{25}$$

Recalling that $d(\mathcal{L}(t)\boldsymbol{\rho}^*(t))/dt = 0$, Eq. (25) can be rewritten as $\dot{f}(t) = \langle \boldsymbol{\tau}(t), \dot{\boldsymbol{\eta}}(t)\rangle + H(t)$ with

$$H(t) = -\frac{1}{2}\langle \boldsymbol{\tau}(t), \dot{\mathcal{L}}_0(t)\boldsymbol{\tau}(t)\rangle. \tag{26}$$

Integrating on the time interval $[a, a+T]$, we obtain

$$f(a+T) - f(a) = \int_a^{a+T} \langle \boldsymbol{\tau}(t), \dot{\boldsymbol{\eta}}(t)\rangle \, dt + \int_a^{a+T} H(t)\, dt. \tag{27}$$

In the right-hand side of (27), the first term is an irreversible contribution associated with the plastic dissipation whereas the second term is a reversible contribution associated with the time fluctuations of the elastic moduli. In the following, we bound those two terms separately, starting with the irreversible contribution $-\int_a^{a+T} \langle \boldsymbol{\tau}(t), \dot{\boldsymbol{\eta}}(t)\rangle \, dt$. To that purpose, we use a reasoning that is quite similar to that used in [22] for perfect plasticity.

We first note from (12) that $\dot{\boldsymbol{\eta}}(t) = -\boldsymbol{\pi}\Phi'(\boldsymbol{\rho}(t) + \boldsymbol{\sigma}^E(t), t)$. Since Φ is convex, positive and vanishes in $\mathcal{K}_0(t)$, we have

$$0 \leq \Phi(\boldsymbol{\rho}(t) + \boldsymbol{\sigma}^E(t), t) \leq \langle \dot{\boldsymbol{\eta}}(t), \boldsymbol{\rho}'(t) - \boldsymbol{\rho}(t)\rangle \quad \text{for all } \boldsymbol{\rho}' \in \mathcal{K}(t) \cap \mathcal{H}. \tag{28}$$

The strong Melan's condition implies that $\boldsymbol{\rho}^*(t) - r\dot{\boldsymbol{\eta}}/\|\dot{\boldsymbol{\eta}}\|$ is in $\mathcal{K}(t) \cap \mathcal{H}$. Hence (28) gives

$$0 \leq \langle \dot{\boldsymbol{\eta}}(t), \boldsymbol{\rho}^*(t) - r\frac{\dot{\boldsymbol{\eta}}}{\|\dot{\boldsymbol{\eta}}\|} - \boldsymbol{\rho}(t)\rangle = \langle \dot{\boldsymbol{\eta}}(t), \boldsymbol{\rho}^*(t) - \boldsymbol{\rho}(t)\rangle - r\|\dot{\boldsymbol{\eta}}(t)\|,$$

i.e., $\langle \dot{\boldsymbol{\eta}}(t), \boldsymbol{\rho}(t) - \boldsymbol{\rho}^*(t)\rangle \leq -r\|\dot{\boldsymbol{\eta}}(t)\|$. Hence

$$\int_a^{a+T} \langle \boldsymbol{\tau}(t), \dot{\boldsymbol{\eta}}(t)\rangle \, dt \leq -r(\inf \mu) \int_a^{a+T} \|\dot{\boldsymbol{\eta}}\| \, dt. \tag{29}$$

Bounding the reversible contribution $\int_a^{a+T} H(t)\, dt$ requires a little more effort. We have

$$\boldsymbol{\tau}(t) = \mathcal{L}_0^{-1}(t)(\boldsymbol{\eta}(t) - \boldsymbol{\eta}(a) + \boldsymbol{s}) \tag{30}$$

where

$$\boldsymbol{s} = \mathcal{L}(a)(\boldsymbol{\rho}(a) - \boldsymbol{\rho}^*(a)) \tag{31}$$

is independent on t. Substituting the expression (30) in (26) and using the fact that $\mathcal{L}_0(t)$ is self-adjoint, we find

$$H(t) = -\frac{1}{2}\langle (\boldsymbol{\eta}(t) - \boldsymbol{\eta}(a) + \boldsymbol{s}), \mathcal{L}_0^{-1}(t)\dot{\mathcal{L}}_0(t)\mathcal{L}_0^{-1}(t)(\boldsymbol{\eta}(t) - \boldsymbol{\eta}(a) + \boldsymbol{s})\rangle.$$

Observing that $\mathcal{L}_0^{-1}(t)\dot{\mathcal{L}}_0(t)\mathcal{L}_0^{-1}(t) = -\dot{\mathcal{M}}_0(t)$ yields

$$H(t) = \frac{1}{2}\langle (\boldsymbol{\eta}(t) - \boldsymbol{\eta}(a) + \boldsymbol{s}), \dot{\mathcal{M}}_0(t)(\boldsymbol{\eta}(t) - \boldsymbol{\eta}(a) + \boldsymbol{s})\rangle. \tag{32}$$

Since $\boldsymbol{s}$ does not depend on t and $\mathcal{M}_0(t)$ is T-periodic, the integration of (32) on the time interval $[a, a+T]$ gives

$$\int_a^{a+T} H(t)dt = \frac{1}{2}\int_a^{a+T} \langle \boldsymbol{\eta}(t) - \boldsymbol{\eta}(a), \dot{\mathcal{M}}_0(t)(\boldsymbol{\eta}(t) - \boldsymbol{\eta}(a) + 2\boldsymbol{s})\rangle dt. \tag{33}$$

Using now the Cauchy-Schwartz inequality and the definition of the norm operator, we obtain

$$\langle \boldsymbol{\eta}(t) - \boldsymbol{\eta}(a), \dot{\mathcal{M}}_0(t)(\boldsymbol{\eta}(t) - \boldsymbol{\eta}(a) + 2\boldsymbol{s})\rangle \leq \|\boldsymbol{\eta}(t) - \boldsymbol{\eta}(a)\| \cdot |||\dot{\mathcal{M}}_0(t)||| \cdot \|\boldsymbol{\eta}(t) - \boldsymbol{\eta}(a) + 2\boldsymbol{s}\|.$$

Since $\boldsymbol{\eta}(t) - \boldsymbol{\eta}(a) + 2\boldsymbol{s} = \boldsymbol{\eta}(t) + \boldsymbol{\eta}(a) - 2\mathcal{L}(a)\boldsymbol{\rho}^*(a)$, we have

$$\|\boldsymbol{\eta}(t) - \boldsymbol{\eta}(a) + 2\boldsymbol{s}\| \leq \|\boldsymbol{\eta}(t)\| + \|\boldsymbol{\eta}(a)\| + 2\|\mathcal{L}(a)\boldsymbol{\rho}^*(a)\|.$$

Lemma 1 gives $\|\boldsymbol{\eta}(t)\| \leq M'$ and $\|\boldsymbol{\eta}(a)\| \leq M'$. Since $\boldsymbol{\rho}^*(a) \in \mathcal{K}(a) \cap \mathcal{H}$, we have $\|\mathcal{L}(a)\boldsymbol{\rho}^*(a)\| \leq CM$ as a consequence of (16–17). Hence

$$\|\boldsymbol{\eta}(t) - \boldsymbol{\eta}(a) + 2\boldsymbol{s}\| \leq 2M' + 2CM \leq 4M'. \tag{34}$$

We also have, for $t \in [a, a+T]$,

$$\|\boldsymbol{\eta}(t) - \boldsymbol{\eta}(a)\| = \|\int_a^t \dot{\boldsymbol{\eta}}(t')dt'\| \leq \int_a^t \|\dot{\boldsymbol{\eta}}(t')\|dt' \leq \int_a^{a+T} \|\dot{\boldsymbol{\eta}}(t')\|dt'. \tag{35}$$

Substituting (34–35) in (33) and using the definition (18) of $\gamma(0, T)$, we obtain

$$\int_a^{a+T} H(t)dt \leq 2M'\gamma(0, T) \int_a^{a+T} \|\dot{\boldsymbol{\eta}}(t)\|dt \tag{36}$$

Replacing (29) and (36) in (24) gives the desired result. □

3.3 *Proof of the Theorem*

We are now in a position to prove Theorem 1. By condition (i), one can pick $M' > CM$ such that $\frac{\gamma(0,T)}{\inf \mu} < \frac{r}{2M'}$. Using Lemma 1 we such M', there exists t_0 such that $\|\boldsymbol{\eta}(t)\| \leq M'$ for $t \geq t_0$. Let now $N_0 \in \mathbb{N}$ be such that $N_0 T \geq t_0$. For $i \geq N_0$, Lemma 2 gives

$$f((i+1)T) - f(iT) \leq -m \int_{iT}^{(i+1)T} \|\dot{\boldsymbol{\eta}}(t)\|\, dt$$

where $m = r(\inf \mu) - 2M'\gamma(0, T)$ is non-negative by (ii). Summing over $i = N_0, \ldots, N$ and recalling that f is positive, we find

$$\int_{N_0 T}^{NT} \|\dot{\boldsymbol{\eta}}(t)\|\, dt \leq \frac{1}{m} f(N_0 T).$$

Taking the limit $N \to \infty$ shows that the integral $\int_0^S \|\dot{\boldsymbol{\eta}}(t)\|dt$ converges as $S \longrightarrow +\infty$. Since $\mathcal{E}$ is a Hilbert space, it follows that $\boldsymbol{\eta}(t)$ also converges towards a limit $\boldsymbol{\eta}_\infty$ as $t \longrightarrow +\infty$. That limit $\boldsymbol{\eta}_\infty$ is in $\mathcal{H}$ because $\mathcal{H}$ is closed in $\mathcal{E}$. Setting $\boldsymbol{\rho}_\infty(t) = \mathcal{M}(t)\boldsymbol{\eta}_\infty$ and recalling that $\mathcal{M}(t)$ is bounded, we have $\boldsymbol{\rho}(t) - \boldsymbol{\rho}_\infty(t) \longrightarrow 0$ as $t \to \infty$. We now check that $\boldsymbol{\rho}_\infty(t)$ is an elastic solution, i.e. satisfies (13). The definition of $\boldsymbol{\rho}_\infty(t)$ rightly gives $d(\mathcal{L}(t)\boldsymbol{\rho}_\infty(t))/dt = 0$, but the fact that $\boldsymbol{\rho}_\infty(t) \in \mathcal{K}(t)$ calls for some justification. Noting by (12) that $\dot{\boldsymbol{\eta}}(t) = -\alpha(\boldsymbol{\rho}(t) - \boldsymbol{\pi} P_{\mathcal{K}(t)}\boldsymbol{\rho}(t))$, we have

$$\|\boldsymbol{\rho}_\infty(t) - \boldsymbol{\pi} P_{\mathcal{K}(t)}\boldsymbol{\rho}_\infty(t)\| \leq \frac{1}{\alpha}\|\dot{\boldsymbol{\eta}}(t)\| + \|\boldsymbol{\rho}(t) - \boldsymbol{\rho}_\infty(t)\| + \|\boldsymbol{\pi} P_{\mathcal{K}(t)}\boldsymbol{\rho}(t) - \boldsymbol{\pi} P_{\mathcal{K}(t)}\boldsymbol{\rho}_\infty(t)\|.$$

It is a classical result that the projection operator on a closed convex set is a contractive mapping [3], hence $\|\boldsymbol{\pi} P_{\mathcal{K}(t)}\boldsymbol{\rho}(t) - \boldsymbol{\pi} P_{\mathcal{K}(t)}\boldsymbol{\rho}_\infty\| \leq \|\boldsymbol{\rho}(t) - \boldsymbol{\rho}_\infty(t)\|$ and

$$\|\boldsymbol{\rho}_\infty(t) - \boldsymbol{\pi} P_{\mathcal{K}(t)}\boldsymbol{\rho}_\infty(t)\| \leq \frac{1}{\alpha}\|\dot{\boldsymbol{\eta}}(t)\| + 2\|\boldsymbol{\rho}(t) - \boldsymbol{\rho}_\infty(t)\|.$$

Recall that $\boldsymbol{\rho}(t) - \boldsymbol{\rho}_\infty(t) = \mathcal{M}(t)(\boldsymbol{\eta}(t) - \boldsymbol{\eta}_\infty)$. Since $\mathcal{M}(t)$ is bounded, there is a constant K such that $\|\boldsymbol{\rho}(t) - \boldsymbol{\rho}_\infty(t)\| \leq K\|\boldsymbol{\eta}(t) - \boldsymbol{\eta}_\infty\|$. Therefore,

$$\|\boldsymbol{\rho}_\infty(t) - \boldsymbol{\pi} P_{\mathcal{K}(t)}\boldsymbol{\rho}_\infty(t)\| \leq \frac{1}{\alpha}\|\dot{\boldsymbol{\eta}}(t)\| + 2K\|\boldsymbol{\eta}(t) - \boldsymbol{\eta}_\infty(t)\|.$$

Integrating on the time interval $[iT, (i+1)T]$ and observing that $\boldsymbol{\rho}_\infty(t)$ and $\mathcal{K}(t)$ are T-periodic, we obtain

$$\int_0^T \|\boldsymbol{\rho}_\infty(t) - \boldsymbol{\pi} P_{\mathcal{K}(t)}\boldsymbol{\rho}_\infty(t)\|\, dt \leq \frac{1}{\alpha}\int_{iT}^{(i+1)T} \|\dot{\boldsymbol{\eta}}(t)\|\, dt + 2K\int_{iT}^{(i+1)T} \|\boldsymbol{\eta}(t) - \boldsymbol{\eta}_\infty\|\, dt.$$

Since $\int_0^\infty \|\dot{\boldsymbol{\eta}}(t)\|\, dt < \infty$, we have

$$\int_{iT}^{(i+1)T} \|\dot{\boldsymbol{\eta}}(t)\|\, dt \longrightarrow 0 \text{ as } i \longrightarrow \infty.$$

Moreover, since $\boldsymbol{\eta}(t)$ converges towards $\boldsymbol{\eta}_\infty$, we also have

$$\int_{iT}^{(i+1)T} \|\boldsymbol{\eta}(t) - \boldsymbol{\eta}_\infty\|\, dt \longrightarrow 0 \text{ as } i \longrightarrow \infty.$$

It follows that $\|\boldsymbol{\rho}_\infty(t) - \boldsymbol{\pi} P_{\mathcal{K}(t)}\boldsymbol{\rho}_\infty(t)\| = 0$ on $[0, T]$, i.e. $\boldsymbol{\rho}_\infty(t) = \boldsymbol{\pi} P_{\mathcal{K}(t)}\boldsymbol{\rho}_\infty(t)$ on $[0, T]$. Therefore, we have $P_{\mathcal{K}(t)}\boldsymbol{\rho}_\infty(t) = \boldsymbol{\rho}_\infty(t) + \boldsymbol{q}$ with $\boldsymbol{q} \in \mathcal{H}^\perp$. By the definition of the projection it follows that

$$\langle \boldsymbol{\rho}_\infty(t) - P_{\mathcal{K}(t)}\boldsymbol{\rho}_\infty(t),\, \boldsymbol{\rho}' - P_{\mathcal{K}(t)}\boldsymbol{\rho}_\infty\rangle \leq 0$$

for any $\boldsymbol{\rho}' \in \mathcal{K}(t)$. In particular, choosing $\boldsymbol{\rho}' = \boldsymbol{\rho}^*(t) \in \mathcal{K}(t) \cap \mathcal{H}$ we find

$$-\langle \boldsymbol{q},\, \boldsymbol{\rho}^*(t) - \boldsymbol{\rho}_\infty(t) - \boldsymbol{q}\rangle = \|\boldsymbol{q}\|^2 \leq 0$$

hence $\boldsymbol{q} = 0$, i.e. $P_{\mathcal{K}(t)}\boldsymbol{\rho}_\infty(t) = \boldsymbol{\rho}_\infty(t)$ or equivalently $\boldsymbol{\rho}_\infty(t) \in \mathcal{K}(t)$. This completes the proof that $\boldsymbol{\rho}_\infty(t)$ is an elastic solution. Since $\boldsymbol{\rho}_\infty(t) - \boldsymbol{\rho}(t) \longrightarrow 0$ as $t \to \infty$, the convergence of $\boldsymbol{\rho}(t)$ towards an elastic solution is obtained.

Remark 1 It is interesting to compare Theorem 1 with the analog result obtained in [22] for elastic-perfectly plastic materials. In [22], a condition analog to (ii) was formulated, with the factor 2 in (ii) replaced by a factor 3. That factor 3 results from Eq. (46) in [22], which—using the present notations—states that

$\|\boldsymbol{\eta}(t) - \boldsymbol{\eta}(a) + 2\boldsymbol{s}\| \leq 6CM$. Using a reasoning similar to that used in Eq. (34), one can actually observe that $\|\boldsymbol{\eta}(t) - \boldsymbol{\eta}(a) + 2\boldsymbol{s}\| \leq 4CM$, which leads to an improved factor 2 instead of a factor 3.

There is also a more subtle difference between Theorem 1 above and the results in [22], regarding the definition of the constant M. In Theorem 1, M is a bound on $\boldsymbol{\pi}\mathcal{K}(t)$ whereas in [22] M is a bound on $\mathcal{K}(t) \cap \mathcal{H}$. We have $\mathcal{K}(t) \cap \mathcal{H} \subset \boldsymbol{\pi}\mathcal{K}(t)$ but the inclusion is generally strict.

4 Illustrative Example

As an illustration of Theorem 1, consider the problem of an elastic-viscoplastic plate under cyclic thermal loading. The plate is stress-free in the $\boldsymbol{e}_3$ direction and is in frictionless contact with rigid walls in the $(\boldsymbol{e}_1, \boldsymbol{e}_2)$ directions (Fig. 1). Length units are chosen such that the plate has unit volume. The constitutive material is homogeneous and the dissipation potential ϕ of the Perzyna type

$$\phi(\boldsymbol{\sigma}) = \frac{1}{\alpha}\langle J_2 - \sigma_y\rangle_+^2 \tag{37}$$

where α is a viscosity parameter, σ_y is the yield strength, $J_2 = \sqrt{3/2}|\boldsymbol{\sigma} - (\operatorname{tr}\boldsymbol{\sigma}/3)\boldsymbol{I}|$ is the second invariant of the deviatoric stress, and $\langle x\rangle_+ = \max(0, x)$ denotes the positive part of a scalar x. The potential (37) can be put in the format (3) by setting $\mathscr{C}(\boldsymbol{x}, t) = \{\boldsymbol{\sigma} : J_2 \leq \sigma_y\}$.

Because of the rigid walls in the $\boldsymbol{e}_1$ and $\boldsymbol{e}_2$ directions, thermal dilatation may result in high compressive stress and plastic flow. In the following we are interested in bounding the temperature fluctuations θ for which shakedown occurs.

4.1 Temperature-Independent Elastic Moduli

Using the plane stress assumption, we consider a 2-dimensional model of the problem. If the imposed temperature field θ as well as the initial state $\boldsymbol{\varepsilon}^p(t = 0)$ are uniform—which is assumed in the following—then the fields $\boldsymbol{\varepsilon}^p$, $\boldsymbol{\varepsilon}$ and $\boldsymbol{\sigma}$ remain

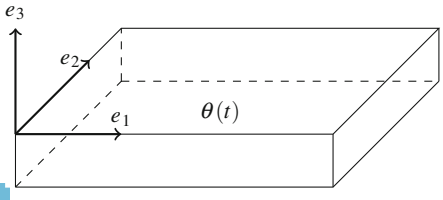

Fig. 1 An elastic-viscoplastic plate under a cyclic temperature $\theta(t)$. The plate is constrained in the $\boldsymbol{e}_1$ and $\boldsymbol{e}_2$ direction

uniform at all time. The space $\mathcal{E}$ is thus chosen as the 3-dimensional space of tensors $\boldsymbol{\sigma}$ with a matrix representation of the form

$$\boldsymbol{\sigma} = \begin{pmatrix} \sigma_{11} & \sigma_{12} & 0 \\ \sigma_{12} & \sigma_{22} & 0 \\ 0 & 0 & 0 \end{pmatrix} \tag{38}$$

in the basis $(\boldsymbol{e}_1, \boldsymbol{e}_2, \boldsymbol{e}_3)$. The space $\mathcal{H}$ of residual stresses is the subspace of $\mathcal{E}$ constituted by uniform fields $\boldsymbol{\rho}$ of the form

$$\boldsymbol{\rho} = \begin{pmatrix} \rho_1 & 0 & 0 \\ 0 & \rho_2 & 0 \\ 0 & 0 & 0 \end{pmatrix}. \tag{39}$$

The purely elastic stress response $\boldsymbol{\sigma}^E(t)$ of the plate is given by

$$\boldsymbol{\sigma}^E = \begin{pmatrix} f^E(t) & 0 & 0 \\ 0 & f^E(t) & 0 \\ 0 & 0 & 0 \end{pmatrix} \tag{40}$$

where $f^E(t) = -E(t)\boldsymbol{\varepsilon}^\theta(t)/(1-\nu(t))$. It can easily be verified that

$$\mathcal{K}_0 = \{\boldsymbol{\sigma} \in \mathcal{E} : \sigma_{11}^2 + \sigma_{22}^2 - \sigma_{11}\sigma_{22} + 6\sigma_{12}^2 \leq \sigma_y^2\}, \tag{41}$$

$$\boldsymbol{\pi}\mathcal{K}_0 = \{\boldsymbol{\rho} \in \mathcal{H} : \rho_1^2 + \rho_2^2 - \rho_1\rho_2 \leq \sigma_y^2\}. \tag{42}$$

Let $(\mathbf{E}_1, \mathbf{E}_2)$ be the orthonormal basis of $\mathcal{H}$ defined by $\mathbf{E}_1 = \mathrm{diag}(1,0,0)$ and $\mathbf{E}_2 = \mathrm{diag}(0,1,0)$. The set $\boldsymbol{\pi}\mathcal{K}_0$ in (42) is a solid ellipsoid with axes $\mathbf{E}_1 + \mathbf{E}_2$ and $\mathbf{E}_1 - \mathbf{E}_2$. The set $\boldsymbol{\pi}\mathcal{K}(t) = \boldsymbol{\pi}(\mathcal{K}_0 - \boldsymbol{\sigma}^E(t))$ is obtained by a time-dependent translation of $\boldsymbol{\pi}\mathcal{K}_0$ in the $\mathbf{E}_1 + \mathbf{E}_2$ direction (Fig. 2).

Setting $\sigma^\theta = \sup_t |\sigma^E(t)|$, it can easily be verified that $\cap_t \boldsymbol{\pi}\mathcal{K}(t)$ is non empty as long as $\sigma^\theta \leq \sigma_y$. More precisely, $\cap_t \boldsymbol{\pi}\mathcal{K}(t)$ contains $B(0,r) \cap \mathcal{H}$ where $B(0,r)$ is the ball centered at the origin with a radius r given by

$$r = \begin{cases} \sigma_y \sqrt{\dfrac{2}{3} - \left(\dfrac{\sigma^\theta}{\sigma_y}\right)^2} & \text{if } 0 \leq \dfrac{\sigma^\theta}{\sigma_y} \leq \dfrac{2}{3}, \\ \sigma_y \sqrt{2}\left(1 - \dfrac{\sigma^\theta}{\sigma_y}\right) & \text{if } \dfrac{2}{3} \leq \dfrac{\sigma^\theta}{\sigma_y} \leq 1. \end{cases} \tag{43}$$

Since $\boldsymbol{\rho} = 0$ is an elastic solution to the evolution problem, it can be deduced from Theorem 1 (or from the standard form of Melan's theorem) that shakedown occurs if $\sigma^\theta \leq \sigma_y$.

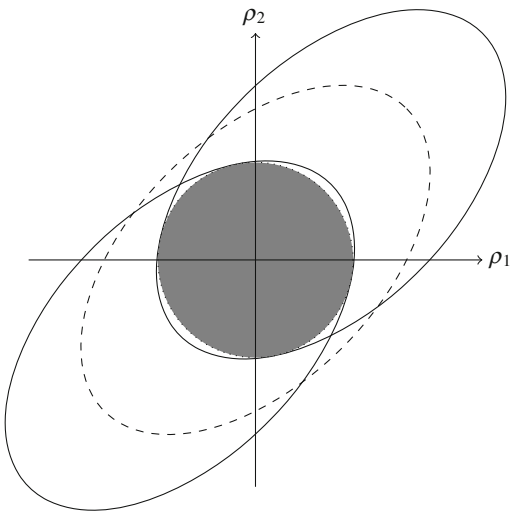

Fig. 2 The set $\boldsymbol{\pi}\mathcal{K}(t)$ is a solid ellipsoid obtained by translation of the ellipsoid $\boldsymbol{\pi}\mathcal{K}_0$ (shown in *dotted lines*) in the (1,1) direction. Shown in *solid lines* are the extreme locations of $\boldsymbol{\pi}\mathcal{K}(t)$, corresponding to $f^E(t) = \pm\sigma^\theta$. The filled ball centered at the origin is included in $\boldsymbol{\pi}\mathcal{K}(t)$ for all t

4.2 Temperature-Dependent Elastic Moduli

Let us now use Theorem 1 to estimate the shakedown limit in the case of non constant elastic moduli. Applying Theorem 1 requires to evaluate the constants M, C in (16–17) as well as the scalar $\gamma(0, T)$ defined in (18).

It can be verified from (42) that any $\boldsymbol{\sigma}$ in $\boldsymbol{\pi}\mathcal{K}_0$ satisfies $\|\boldsymbol{\sigma}\| \leq \sqrt{2}\sigma_y$. Hence any $\boldsymbol{\sigma}$ in $\boldsymbol{\pi}\mathcal{K}(t)$ satisfies

$$\|\boldsymbol{\sigma}\| \leq \sqrt{2}\sigma_y + \|\boldsymbol{\sigma}^E(t)\| \leq \sqrt{2}(\sigma_y + \sigma^\theta).$$

The constant M in (16) can thus be chosen as

$$M = \sqrt{2}(\sigma_y + \sigma^\theta). \tag{44}$$

Recall that $\mathcal{L}(t)\boldsymbol{\rho}$ is defined as the projection of $\boldsymbol{L}(t) : \boldsymbol{\rho}$ on $\mathcal{H}$. In the present case, we have

$$\mathcal{L}(t)\boldsymbol{\rho} = \frac{1}{E(t)} \begin{pmatrix} \rho_1 - \nu\rho_2 & 0 & 0 \\ 0 & \rho_2 - \nu\rho_1 & 0 \\ 0 & 0 & 0 \end{pmatrix}.$$

Hence the matrix representation of $\mathcal{L}$ in the basis $(\mathbf{E}_1, \mathbf{E}_2)$ is given by

$$\mathcal{L}(t) = \frac{1}{E(t)} \begin{pmatrix} 1 & -\nu \\ -\nu & 1 \end{pmatrix}.$$

The operator $\mathcal{L}(t)$ being symmetric, its norm operator $|||\mathcal{L}(t)|||$ is equal to $\max_i |\lambda_i|$ where $\{\lambda_i\}$ are the eigenvalues of $\mathcal{L}(t)$. A simple calculation gives

$$|||\mathcal{L}(t)||| = \frac{1+\nu(t)}{E(t)}. \tag{45}$$

Set

$$\nu_{min} = \inf_t \nu(t),\ \nu_{max} = \sup_t \nu(t),\ E_{min} = \inf_t E(t),\ E_{max} = \sup_t E(t).$$

From (45) we have $|||\mathcal{L}(t)||| \leq \frac{1+\nu_{max}}{E_{min}}$ for all t. Hence the constant C in (17) can be chosen as

$$C = \frac{1+\nu_{max}}{E_{min}}. \tag{46}$$

In order to calculate $\gamma(0, T)$, we note that

$$\mathcal{M}(t) = \mathcal{L}^{-1}(t) = \frac{E(t)}{1-\nu^2(t)} \begin{pmatrix} 1 & \nu \\ \nu & 1 \end{pmatrix}.$$

Choosing $\mu(t) = 1/\operatorname{tr} \mathcal{M}(t)$ as suggested in [22], we get

$$\mu(t) = \frac{1-\nu^2(t)}{2E(t)},\ \mathcal{M}_0(t) = \frac{1}{2}\begin{pmatrix} 1 & \nu \\ \nu & 1 \end{pmatrix},\ \dot{\mathcal{M}}_0(t) = \frac{1}{2}\begin{pmatrix} 0 & \dot{\nu} \\ \dot{\nu} & 0 \end{pmatrix}.$$

It follows that $|||\dot{\mathcal{M}}_0(t)||| = \frac{1}{2}|\dot{\nu}|$ and

$$\gamma(0, T) = \frac{1}{2}\int_0^T |\dot{\nu}| dt.$$

Using the values of M and C defined in (44) and (46) respectively, we obtain from Theorem 1 that shakedown occurs if

$$\frac{1+\nu_{max}}{E_{min}} \frac{\int_0^T |\dot{\nu}| dt}{\inf_t \frac{1-\nu^2(t)}{E(t)}} \leq \frac{r}{\sqrt{2}(\sigma_y + \sigma^\theta)} \tag{47}$$

where r is the function of σ^θ defined in (43). The left-hand side of (47) is a function of the fluctuations of the elastic moduli, whereas the right-hand side is a function of the loading σ^θ. Observing that $(1-\nu^2(t))/E(t) \geq (1-\nu_{max}^2)/E_{max}$, it can be seen that a sufficient condition for Eq. (47) to be satisfied is

$$\frac{1}{1-\nu_{max}} \frac{E_{max}}{E_{min}} \int_0^T |\dot{\nu}| dt \leq \frac{r}{\sqrt{2}(\sigma_y + \sigma^\theta)}. \tag{48}$$

Assume that $\dot{\nu}$ vanishes only when $\nu(t) = \nu_{min}$ or $\nu(t) = \nu_{max}$, i.e. $\nu(t)$ grows monotonically from ν_{min} to ν_{max} and then decreases monotonically from ν_{max} to ν_{min}, in a periodic fashion. In such case, we have

$$\int_0^T |\dot{\nu}| dt = 2(\nu_{max} - \nu_{min})$$

and the inequality (48) reduces to

$$\frac{(\nu_{max} - \nu_{min})}{1 - \nu_{max}} \frac{E_{max}}{E_{min}} \leq \frac{r}{2\sqrt{2}(\sigma_y + \sigma^\theta)}. \tag{49}$$

For fixed values of E_{max}/E_{min}, the shakedown limit σ^θ_{SD} is defined at the largest value of σ^θ that satisfies (49). The shakedown limit σ^θ_{SD} is plotted in Fig. 3 as a function of E_{max}/E_{min}, for several values of $\nu_{max} - \nu_{min}$. The maximum value ν_{max} is set to 0.3 for all the curves in Fig. 3. First consider the case $\nu_{max} - \nu_{min} = 0$: Whatever the value of E_{max}/E_{min}, the shakedown limit is equal to σ_y and thus coincides with the value obtained in Sect. 4.1 for temperature-independent elastic moduli. When $\nu_{max} - \nu_{min}$ increases, the shakedown limit decreases rapidly. For instance, the shakedown limit is approximatively equal to $0.6\sigma_y$ in the case of a 20 % variation of E and ν around nominal values (E_0, $\nu_0 = 0.3$). For common metals, the Young modulus E decreases with the temperature, while the Poisson ratio increases [14]. The Young modulus is more sensitive to temperature variations than the Poisson ratio. To put things in perspective, a 20 % variation of the Young modulus E in steels would typically correspond to temperatures fluctuating between 0 and 500 °C [6].

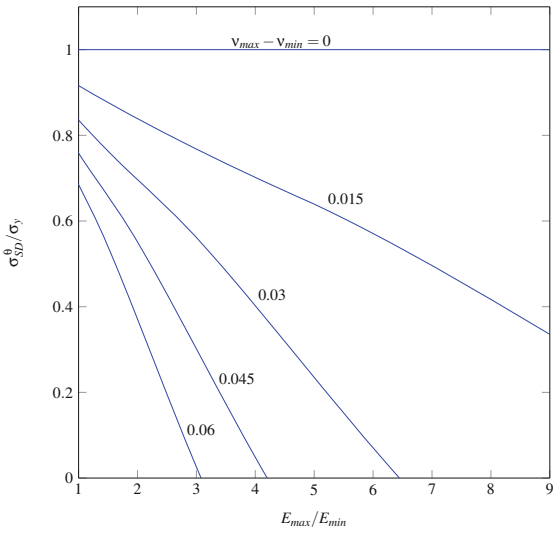

Fig. 3 Shakedown limit as a function of E_{max}/E_{min}, plotted for several values of $\nu_{max} - \nu_{min}$. Case $\nu_{max} = 0.3$

4.3 Incremental Analysis

As a further illustration of Theorem 1, we use incremental analysis to solve (12) for given loading history and fluctuations of the elastic moduli. The functions $f^E(t)$, $E(t)$ and $\nu(t)$ are taken as $f^E(t) = \sigma^\theta \sin \omega t$, $E(t) = E_0(1 - 0.2 \sin^2 \omega t)$, $\nu(t) = \nu_0(1 + 0.2 \sin^2 \omega t)$ with $E_0/\sigma_y = 10$ and $\nu_0 = 0.3$. For such parameters, the shakedown limit σ^θ_{SD} as provided by Eq. (49) is approximatively equal to $0.6\sigma_y$. The differential equation (12) is solved numerically using a Runge-Kutta scheme with variable step size. In Fig. 4 is shown the evolution of the plastic strain in the case $\sigma^\theta = 0.5\sigma_y$, i.e. below the shakedown limit. The initial state is taken as $\rho_1(t = 0) = \sigma_y$, $\rho_2(t = 0) = 2\sigma_y$. In accordance with the results of Sect. 4.2, the plastic strain converges towards a limit as $t \to \infty$. Theorem 1 ensures that such behavior occurs for *all* initial states $\rho_1(t = 0)$, $\rho_2(t = 0)$. In Fig. 5 is plotted the evolution of $\|\boldsymbol{\varepsilon}^p(t)\|$ (solid line). A fast

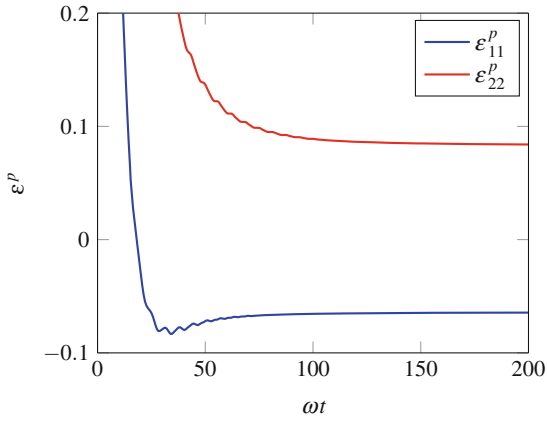

Fig. 4 Evolution of the plastic strain for a loading below the shakedown limit. Case $\rho_1(t = 0) = \sigma_y$, $\rho_2(t = 0) = 2\sigma_y$

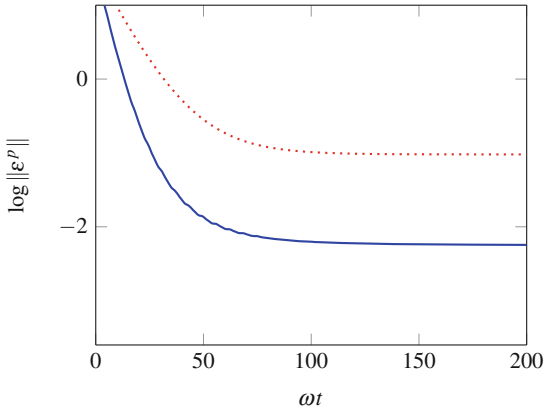

Fig. 5 Evolution of $\|\boldsymbol{\varepsilon}^p(t)\|$ (blue solid line) and comparison with the exponential upper bound provided by Eq. (22) (*red dotted line*)

decrease is observed for small time: This is the meaning of Lemma 1 introduced in Sect. 3.1. In dashed line is plotted the exponential upper bound on $\|\boldsymbol{\varepsilon}^p(t)\|$ that is deduced from Eq. (22).

5 Concluding Remarks

The shakedown theorem presented in this chapter gives a sufficient condition for the evolution to become elastic in the large time limit, whatever the initial state is. Loosely speaking, that theorem states that if the loading is not too large (in the sense of condition (i)) *and* the time-fluctuations of the elastic moduli are not too large (in the sense of condition (ii)), then shakedown occurs immaterial of the initial state. We emphasize again that setting a restriction on the time-fluctuations of the elastic moduli is essential to ensure that shakedown occurs in a path-independent fashion.

It can be observed that Theorem 1 is independent on the viscosity parameter α. This is consistent with the case of constant elastic moduli: the shakedown behavior is essentially determined by the elasticity domain of the material (as long as the dissipation ϕ satisfies standard assumptions such as convexity).

For the sake of simplicity, the viscosity parameter α has been assumed to be independent on $(\boldsymbol{x}, t)$ but there is no difficulty in extending Theorem 1 to non constant viscosities. It could be interesting to investigate whether Theorem 1 could be extended to other viscoplastic potentials than those of the form (3).

In practice, the shakedown theorem that has been presented could be useful for the fatigue design of structures submitted to large temperature variations. As illustrated in Sect. 4, that theorem gives lower bounds on the shakedown limit. It would be interesting to investigate whether the kinematic shakedown theorem of [11] could be extended to the case of temperature-dependent elastic moduli, so as to obtain upper bounds.

References

1. Ahn YJ, Bertocchi E, Barber J (2008) Shakedown of coupled two-dimensional discrete frictional systems. J Mech Phys Solids 56:3433–3440
2. Borino G (2000) Consistent shakedown theorems for materials with temperature dependent yield functions. Int J Solid Struct 37:3121–3147
3. Brézis H (1972) Opérateurs maximaux monotones et semigroupes de contractions dans les espaces de Hilbert. North-Holland, Amsterdam
4. Carvelli C, Cen Z, Liu Y, Maier G (1999) Shakedown analysis of defective pressure vessels by a kinematic approach. Arch Appl Mech 69:751–764
5. Dang Van K, Papadopoulos IV (1999) Introduction to fatigue analysis in mechanical design by the multiscale approach. In: High-cycle metal fatigue. Springer, Vienna, pp 57–88
6. European Committee for Standardization (1995) Eurocode 3: design of steel structures, ENV 1993-1-2: general rules—structural fire design. Brussels, Belgium

7. Halphen B (2005) Elastic perfectly plastic structures with temperature dependent elastic coefficients. Comptes Renuds Mécanique 333:617–621
8. Halphen B, Di Domizio S (2005) Evolution des structures élastoplastiques dont les coefficients d'élasticité dépendent de la température. In: Actes du 17ème congrès français de mécanique. Troyes, France
9. Hasbroucq S, Oueslati A, de Saxcé G (2010) Inelastic responses of a two-bar system with temperature-dependent elastic modulus under cyclic thermomechanical loadings. Int J Solid Struct 47:1924–1932
10. Hasbroucq S, Oueslati A, de Saxcé G (2012) Analytical study of the asymptotic behavior of a thin plate with temperature-dependent elastic modulus under cyclic thermomechanical loadings. Int J Mech Sci 54:95–104
11. Koiter WT (1960) General theorems for elastic-plastic solids. North-Holland, Amsterdam
12. König J (1969) A shakedown theorem for temperature dependent elastic moduli. Academie Polonaise des Sciences, Bulletin, Serie des Sciences Techniques 17(3):161–165
13. Lanchon H (1974) Elastic-plastic torsion of a cylindrical shaft with simply or multiply connected cross section. J de Mecanique 13:267–320
14. Ledbetter HM, Naimon ER (1974) Elastic properties of metals and alloys. II. Copper. J Phys Chem Ref Data 3:897–935
15. Maitournam H, Pommier B, Thomas JJ (2002) Détermination de la réponse asymptotique d'une structure anélastique sous chargement cyclique. Comptes Rendus Mécanique 330:703–708
16. Melan E (1936) Theorie statisch unbestimmter systeme aus ideal-plastischen baustoff. Sitzungsberichte der Deutschen Akademie der Wissenschaften 145:195–218
17. Nguyen QS (2003) On shakedown analysis in hardening plasticity. J Mech Phys Solid 51:101–125
18. Peigney M, Stolz C (2001) Approche par contrôle optimal des structures élastoviscoplastiques sous chargement cyclique. Comptes Rendus de l'Académie des Sciences II 329:643–648
19. Peigney M, Stolz C (2003) An optimal control approach to the analysis of inelastic structures under cyclic loading. J Mech Phys Solid 51:575–605
20. Peigney M (2010) Shakedown theorems and asymptotic behaviour of solids in non-smooth mechanics. Eur J Mech A/Solid 29:784–793
21. Peigney M (2014) On shakedown of shape memory alloys structures. Ann Solid Struct Mech 6:17–28
22. Peigney M (2014) Shakedown of elastic-perfectly plastic materials with temperature-dependent elastic moduli. J Mech Phys Solid 71:112–131
23. Pham DC (2008) On shakedown theory for elastic-plastic materials and extensions. J Mech Phys Solid 56:1905–1915
24. Simon JW, Weichert D (2012) Shakedown analysis of engineering structures with limited kinematical hardening. Int J Solid Struct 49:2177–2186
25. Spiliopoulos KV, Panagiotou KD (2012) A direct method to predict cyclic steady states of elastoplastic structures. Comput Methods Appl Mech Eng 223:186–198
26. Symonds PS (1951) Shakedown in continuous media. J Appl Mech 18:85–89
27. Weichert D, Ponter A (2014) A historical view on Shakedown theory. In: The history of theoretical, material and computational mechanics-mathematics meets mechanics and engineering. Springer, Berlin, pp 169–193
28. Zarka J, Frelat J, Inglebert G (1988) A new approach to inelastic analysis of structures. Martinus Nijhoff Publishers, Dordrecht

Incompressibility and Large Deformations

Elena Bonetti and Michel Frémond

Abstract We present a new point of view on the motion of an incompressible solid with large deformations. The description of the shape changes of the solid involves the stretch matrix $\mathbf{W}$ of the classical polar decomposition. The incompressibility condition is $\det \mathbf{W} \geq 1$, accounting for possible cavitation or phase change. The reaction to the incompressibility condition is a pressure which is positive. There is cavitation or phase change when the pressure is null. The motion of a three-dimensional solid is investigated between time 0 and a final time $T > 0$. It is possible to prove that the model is coherent in terms of mechanics and mathematics. Let us note that the pressure is a measure allowing possible internal collisions due to cavitation.

1 Introduction

Predictive theories of the motion of a solid with large deformations is still under investigation. Research on this topic is active, see for instance the books [1, 5] where the classical theories for the equilibrium are investigated. We present an other point of view taking into account an internal constraint on some kinematic quantity and upgrading the angular momentum equation of motion. We recall the results for the elastic and viscoelastic behaviours [2–4, 8, 9, 11] and extend the theory to incompressible materials.

The motion of a dimension 3 solid is investigated between time 0 and a final time $T > 0$. At time $t = 0$, the solid occupies smooth domain $\mathscr{D}_a$.

E. Bonetti (✉)
Dipartimento "F. Enriques", Università di Milano, via Saldini 50,
20133 Milano, Italy
e-mail: elena.bonetti@unimi.it

M. Frémond
Dipartimento di Ingegneria Civile e Ingegneria Informatica (DICII),
Università degli Studi di Roma "Tor Vergata", via del Politecnico 1,
00133 Roma, Italy
e-mail: michel.fremond@uniroma2.it

M. Frémond et al. (eds.), *Models, Simulation, and Experimental Issues in Structural Mechanics*, Springer Series in Solid and Structural Mechanics 8,
DOI 10.1007/978-3-319-48884-4_10

1.1 The System and the Position Function

We consider a solid which moves with respect to an immobile obstacle. The system we consider is made of the solid and the obstacle. A frame is attached to the obstacle, it is the initial frame with points denotes $a = (a_\alpha)$. The indices of the components are Greek letters.

The motion is described by function

$$\begin{aligned} &(a, t) \to \Phi(a, t) \in \mathbb{R}^3, \\ &(a, t) \in \mathscr{D}_a \times [0, T], \\ &a = \Phi(a, 0). \end{aligned}$$

Position function Φ gives the position at time t of the point which is at initial time 0 at point a. Position may be measured in a frame, the position frame assumed to be Galilean, $\Phi = (\Phi_i)$ with components denoted with Latin indices.

We consider kinematically admissible position functions which satisfy: Φ is differentiable and, letting $\mathbf{F} = \text{grad}\Phi$ be the gradient matrix, the following property is satisfied

$$\det \mathbf{F} > 0.$$

Thus there are neither local interpenetration or flattening. We assume also that there are no self-collision nor collision with an obstacle during the motion. The theory may be upgraded [11] to account for these motions. For the sake of simplicity, we assume also there is neither smooth self-contact nor smooth contact with an obstacle.

We denote by $\mathscr{M}$ the space of 3×3 matrices, endowed with scalar product

$$\mathbf{A} : \mathbf{B} = A_{ij} B_{ij} = \text{tr}(\mathbf{A}\mathbf{B}^T).$$

The subspaces $\mathscr{S} \subset \mathscr{M}$ of the symmetric matrices and $\mathscr{A} \subset \mathscr{M}$ of the antisymmetric matrices are orthogonal. In $\mathscr{M}$ we introduce the set

$$\begin{aligned} C_\alpha = \{&\mathbf{B} \in \mathscr{M} \mid i_1(\mathbf{B}) = \text{tr}\mathbf{B} \geq 3\alpha, \\ &i_2(\mathbf{B}) = \text{tr}(\text{cof}(\mathbf{B})) \geq 3\alpha^2,\ i_3(\mathbf{B}) = \det \mathbf{B} \geq \alpha^3 \big\}, \quad 0 < \alpha < 1. \end{aligned}$$

Note that $\mathbf{I} \in C_\alpha$ ($\mathbf{I}$ being the identity matrix). The set $C_\alpha \cap \mathscr{S}$ is the set of symmetric matrices with eigenvalues which are positive and not too small. For the sake of simplicity, we assume that the values of all the physical constants, except α, are equal to 1.

1.2 The Polar Decomposition

The classical polar decomposition of the gradient matrix of a kinematically admissible position function reads

$$\mathbf{F} = \text{grad}\Phi = \mathbf{RW},$$

for a unique $\mathbf{W} \in \mathscr{S}$ with $\det \mathbf{W} > 1$ and a unique $\mathbf{R}$, which is an unique direct orthogonal matrix ($\mathbf{RR}^T = \mathbf{I}$ and $\det \mathbf{R} = 1$).

Matrix $\mathbf{W}$ is the stretch matrix. It describes the stretches at point a whereas matrix $\mathbf{R}$, the rotation matrix describes the rotation with respect to the initial frame. Usually the orientation of the solid with respect to the initial frame, the orientation of the solid with respect to the obstacle, has not much physical properties. It measures the shape change of the system made of the solid and the immobile obstacle. There may be cases where the solids are connected by hair springs to the obstacle giving importance to the orientation. Actually, the variation of this orientation with respect to space is an element to characterize the shape change of the system.

1.3 The State Quantities

They are the quantities which are needed to describe how the shape of the system evolves. The elongation at a point of the solid is quantified by $\mathbf{W}$. Rotation matrix $\mathbf{R}$ accounts for the orientation of the solid with respect to the obstacle. It describes, as we have already pointed out, a shape change of the system.

We do not choose $\text{grad}\Phi = \mathbf{RW}$ as state quantity of the system but matrices $\mathbf{W}$ and $\mathbf{R}$ which have clear physical meaning. The variation of the rotation matrix $\mathbf{R}$ with respect to space is also useful to describe the shape change of the system. As explained in [2–4, 11] we add also a third gradient quantity describing local interactions to take into account external actions applied by curvilinear beams or cables. Thus, we choose the state quantities to be

$$E = (\mathbf{W}, \mathbf{R}, (\text{grad}\mathbf{R})\,\mathbf{R}^T, \text{grad}\Delta\Phi),$$

with

$$\left((\text{grad}\mathbf{R})\,\mathbf{R}^T\right)_{ij\alpha} = R_{i\beta,\alpha} R_{j\beta}.$$

Moreover for the sake of simplicity, we will assume the free energy depends on

$$\|\text{grad}\mathbf{R}\|^2 = \left\|(\text{grad}\,\mathbf{R})\,\mathbf{R}^T\right\|^2.$$

Remark 1 Let us also note that if stretch matrix function, $a \to \mathbf{W}(a,t)$ is known in domain $\mathscr{D}_a$, it is possible to compute rotation matrix $\mathbf{R}$ provided a compatibility relationship is satisfied, [6, 17, 18]. But if the numbers, entries of matrix $\mathbf{W}$, are known at a point, rotation matrix at this point is not known.

2 The Velocities and the Evolution Quantities

The velocity at a point is

$$\overrightarrow{U} = \frac{d\Phi}{dt} = \dot{\Phi}.$$

Because we have chosen matrices $\mathbf{W}$ and $\mathbf{R}$ to describe the shape change, it is natural and useful to choose their velocities $\dot{\mathbf{W}}$ and $\dot{\mathbf{R}}$ to describe the shape change velocity, i.e., the velocity of deformation. We choose $\dot{\mathbf{R}}\mathbf{R}^T = \boldsymbol{\Omega}$, the angular velocity, which has a good physical property instead of $\dot{\mathbf{R}}$. Actually, the two choices are equivalent.

We choose also $\mathrm{grad}\boldsymbol{\Omega}$ and $\mathrm{grad}\Delta\overrightarrow{U}$ (Δ is the Laplacian operator) as velocities of deformation accounting for local interactions [2–4, 11]. Let us note that there holds

$$\mathrm{grad}\,\overrightarrow{U} = \mathbf{R}\dot{\mathbf{W}} + \dot{\mathbf{R}}\mathbf{W} = \mathbf{R}\dot{\mathbf{W}} + \boldsymbol{\Omega}\boldsymbol{F}. \tag{1}$$

This relationship relates quantities which appear in the velocities of deformation. It may be used to make choices among these velocities. We choose not to have $\dot{\mathbf{W}}$, but we take into account $\mathrm{grad}\,\overrightarrow{U}$ which is the velocity of deformation in classical theories [5, 16]. The final set of velocities of deformation of the system is

$$\mathrm{grad}\,\overrightarrow{U},\ \mathrm{grad}\Delta\overrightarrow{U},\ \boldsymbol{\Omega},\ \mathrm{grad}\boldsymbol{\Omega}.$$

There are two velocities at point a, $\overrightarrow{U}(a,t)$ and $\boldsymbol{\Omega}(a,t)$. They are independent because we do not know $\dot{\mathbf{W}}$. We may think of virtual linear velocities $\hat{V}$ and of virtual angular velocities $\hat{\boldsymbol{\Omega}}$. Thus the virtual velocities of deformation are

$$\mathrm{grad}\hat{V},\ \mathrm{grad}\Delta\hat{V},\ \hat{\boldsymbol{\Omega}},\ \mathrm{grad}\hat{\boldsymbol{\Omega}}.$$

The quantities which describe the evolution are

$$\dot{\mathbf{W}},\ \mathrm{grad}\boldsymbol{\Omega}.$$

We do not choose $\boldsymbol{\Omega}$ and $\mathrm{grad}\Delta\dot{\Phi}$ which are not objective quantities to describe the evolution assuming there is no interaction between the obstacle and the solid [11].

Remark 2 We have already mention that rotation matrix may be a state quantity when the orientation of the solid with respect to the solid intervenes in the motion.

2.1 The Angular Velocity and the Spin Velocity

We have chosen angular velocity $\boldsymbol{\Omega}$ to describe rotation properties. We could have chosen the spin velocity [16] $\mathbf{O}$, the antisymmetric part of the Eulerian gradient of the velocity

$$\frac{\partial \overrightarrow{U}}{\partial \Phi} = \frac{\partial \overrightarrow{U}}{\partial a}\frac{\partial a}{\partial \Phi} = (\text{grad}\,\overrightarrow{U})\mathbf{F}^{-1} = \mathbf{R}\dot{\mathbf{W}}\mathbf{W}^{-1}\mathbf{R}^T + \boldsymbol{\Omega},$$

which is the instantaneous angular velocity of the material [16]

$$\mathbf{O} = \boldsymbol{\Omega} + \frac{\mathbf{R}(\dot{\mathbf{W}}\mathbf{W}^{-1} - \mathbf{W}^{-1}\dot{\mathbf{W}})\mathbf{R}^T}{2}. \tag{2}$$

It is a linear function of the angular velocity, $\boldsymbol{\Omega}$, and of the stretch velocity, $\dot{\mathbf{W}}$. The two choices are equivalent for what concerns the internal and external powers and of course the angular momentum equation of motion.

Because the stretch produces a rotation of the material, the spin matrix mix the stretch matrix velocity, $\dot{\mathbf{W}}$, and the rotation matrix velocity, $\boldsymbol{\Omega}$. Matrices $\mathbf{W}$ and $\mathbf{R}$ are basic distinct elements of the deformation. Thus it is natural to choose their velocities as the basic distinct elements to account for the evolution. In case an external moment is applied with spin velocity, the external power is a linear function of $\boldsymbol{\Omega}$ and of $\dot{\mathbf{W}}$. This external action produces both a rotation and a stretch as seen in experiments. Note that it is easy to experiment and measure angular velocity $\boldsymbol{\Omega}$ with an external action applied by a rigid device, for instance a rigid screwdriver, as explained in [11].

3 The Principle of Virtual Power

The either actual or virtual power of the internal forces is a linear function of the either actual or virtual velocities. This linear function involves derivatives of the velocities. Let us recall that when the power of the internal forces involves order n derivatives of the velocities, we have an nth gradient theory. We have to choose which gradient theory is convenient for large deformations. Our choice is based on observing the different ways to apply external actions, i.e., the different ways to load a solid. The dimension 3 solid may be loaded by curvilinear beams which are in bilateral contact with the solid on lines of its surface. The velocities in the beams

are equal to the traces on the lines of the body velocities of the solid (the body is the interior of the solid). Principle of virtual power for beams requires the second space derivatives on the lines of the surface. Thus it is convenient to have a third gradient body theory which insures that the trace of the body second gradient is defined on lines of the surface of the solid.

Note also that the dimension 3 solid may also be loaded by needles, wires, membranes, curvilinear rods, curvilinear beams and shells (rods, beams and plates on a flat surface). Column hooping is an example of such a loading. The velocities of the hoop points are equal to the velocities of the points of the surface of the column they are in contact with.

Power of the internal forces involves third order space derivatives introducing a new internal force $\mathbf{Z}$. It is a stress taking into account the effects of the spatial variation of the Laplacian of the velocity

$$\mathscr{P}_{int}(\overrightarrow{V}, \widehat{\boldsymbol{\Omega}}) = -\int_{\mathscr{D}_a} \left\{ \boldsymbol{\Pi} : \operatorname{grad} \overrightarrow{V} + \mathbf{Z} : \operatorname{grad} \Delta \overrightarrow{V} \right\} da + \int_{\mathscr{D}_a} \frac{1}{2} \left\{ \mathbf{M} : \widehat{\boldsymbol{\Omega}} - \Lambda_\alpha : \widehat{\boldsymbol{\Omega}}_{,\alpha} \right\} da,$$

with

$$\mathbf{Z} : \operatorname{grad} \Delta \overrightarrow{V} = \mathbf{Z}_{i\delta} V_{i,\beta\beta\delta} = \mathbf{Z} : \Delta(\operatorname{grad} \overrightarrow{V}),$$

where $\boldsymbol{\Pi}$ is the Piola-Kirchhoff-Boussinesq stress, $\mathbf{M}$ is an internal moment and Λ an internal moment flux. The virtual velocities $\overrightarrow{V}$ and virtual angular velocities $\widehat{\boldsymbol{\Omega}}$ are independent. Quantity

$$\operatorname{grad} \Delta \overrightarrow{V} = \operatorname{grad}(\operatorname{div}(\operatorname{grad} \overrightarrow{V})),$$

quantifies the variation of the Laplacian of velocity of deformation $\Delta \overrightarrow{V}$ with respect to space. One may say it quantifies the diffusion of the velocity of deformation. The dual quantity is a stress, matrix $\mathbf{Z}_{i\delta}$, the physical meaning of which is given by the equations of motion.

The virtual powers of the acceleration forces and external forces are

$$\mathscr{P}_{acc}(\overrightarrow{V}, \widehat{\boldsymbol{\Omega}}) = \int_{\mathscr{D}_a} \frac{d^2 \Phi}{dt^2} \cdot \overrightarrow{V} \, da,$$

$$\mathscr{P}_{ext}(\overrightarrow{V}, \widehat{\boldsymbol{\Omega}}) = \int_{\mathscr{D}_a} \overrightarrow{f} \cdot \overrightarrow{V} + \mathbf{M}^{\mathbf{ext}} : \widehat{\boldsymbol{\Omega}} \, da + \int_{\partial \mathscr{D}_a} \mathbf{m}^{\mathbf{ext}} : \widehat{\boldsymbol{\Omega}} \, d\Gamma_a,$$

assuming no external forces on surface, where $\overrightarrow{f}$ is the body force, $\mathbf{M}^{\mathbf{ext}}$ and $\mathbf{m}^{ext}$ are the body and surface moments applied by the exterior.

3.1 The Linear Momentum Equation

The linear momentum equation of motion results from the principle of virtual power with $\widehat{\boldsymbol{\Omega}} = 0$. It is in domain $\mathscr{D}_a$

$$\frac{d\overrightarrow{U}}{dt} = \mathrm{div}\boldsymbol{\Pi} + \mathrm{div}(\Delta\mathbf{Z}) + \overrightarrow{f},$$

with boundary conditions on $\partial\mathscr{D}_a$ we do not detail for the sake of simplicity.

3.2 The Angular Momentum Equation

The angular momentum equation results from the principle of virtual power with $\overrightarrow{V} = 0$. By a classical computation, we get

$$\mathrm{div}\Lambda + \mathbf{M} + \mathbf{M}^{\mathbf{ext}} = 0, \quad \text{in } \mathscr{D}_a,$$

with boundary condition

$$\Lambda\overrightarrow{N} = \mathbf{m}^{ext}, \quad \text{on } \partial\mathscr{D}_a.$$

4 Free Energy and Pseudo-Potential of Dissipation

We derive the constitutive laws from the schematic free energy where, as already said, the physical constants have value 1 to have simple formulas

$$\Psi(\mathbf{B}, \mathrm{grad}\Delta\hat{\Phi}, \left\|\mathrm{grad}\widehat{\mathbf{R}}\right\|^2) = \frac{1}{2}\left\|\mathbf{B}-\mathbf{I}\right\|^2 + \frac{1}{2}\left\|\mathrm{grad}\Delta\hat{\Phi}\right\|^2 + \hat{\Psi}(\mathbf{B}) + I_{\mathscr{S}}(\mathbf{B}) + \frac{1}{4}\left\|\mathrm{grad}\widehat{\mathbf{R}}\right\|^2, \tag{3}$$

where $\hat{\Phi}$ is a position function, $\mathbf{B}$ is a matrix of $\mathscr{M}$, $\widehat{\mathbf{R}}$ is a matrix of $\mathscr{M}$, and

$$\left\|\mathbf{B}\right\|^2 = \mathbf{B}:\mathbf{B}, \quad \left\|\mathrm{grad}\Delta\hat{\Phi}\right\|^2 = \hat{\Phi}_{i,\alpha\beta\beta}\hat{\Phi}_{i,\alpha\delta\delta},$$

and from the pseudo-potential of dissipation

$$D(\dot{\mathbf{B}}, \mathrm{grad}\widehat{\boldsymbol{\Omega}}) = \frac{1}{2}\left\|\dot{\mathbf{B}}\right\|^2 + \frac{1}{4}\left\|\mathrm{grad}\widehat{\boldsymbol{\Omega}}\right\|^2, \tag{4}$$

The function $I_{\mathscr{S}}$ is the indicator function of subspace $\mathscr{S}$ of $\mathscr{M}$. It insures the internal constraint: the stretch matrix $\mathbf{W}$ is symmetric.

Remark 3 Free energy we have chosen is schematic in order to focus on its properties: $\Psi(\mathbf{B}, \mathrm{grad}\Delta\hat{\Phi}, \left\|\mathrm{grad}\widehat{\mathbf{R}}\right\|^2) - \hat{\Psi}(\mathbf{B})$ is convex [13, 15] with respect to $\mathbf{B}$, $\mathrm{grad}\Delta\hat{\Phi}$, $\left\|\mathrm{grad}\widehat{\mathbf{R}}\right\|^2$. Free energy is coercive and goes to infinite if $\mathbf{B}$ goes to the boundary of set C_α. It is easy to have more realistic free energies, for instance

$$\Psi(\mathbf{B}, \mathrm{grad}\Delta\hat{\Phi}, \left\|\mathrm{grad}\widehat{\mathbf{R}}\right\|^2) = \frac{1}{4}\left(\mathrm{tr}(\mathbf{B}^2-\mathbf{I})\right)^2 + \frac{1}{2}\left\|\mathbf{B}^2-\mathbf{I}\right\|^2 + \frac{1}{2}\left\|\mathrm{grad}\Delta\hat{\Phi}\right\|^2 + \hat{\Psi}(\mathbf{B}) + I_{\mathscr{S}}(\mathbf{B}) + \frac{1}{4}\left\|\mathrm{grad}\widehat{\mathbf{R}}\right\|^2,$$

giving stress

$$\boldsymbol{\Pi} = \mathbf{R}\left\{\mathbf{W}\mathrm{tr}(\mathbf{W^2}-\mathbf{I}) + 2(\mathbf{W}^3-\mathbf{W}) + \frac{\partial\hat{\Psi}}{\partial\mathbf{B}}(\mathbf{W}) + \mathbf{A}\right\}$$
$$= \mathrm{tr}(\mathbf{W^2}-\mathbf{I})\mathbf{F} + 2\mathbf{F}(\mathbf{W}^2-\mathbf{I}) + \mathbf{R}\frac{\partial\hat{\Psi}}{\partial\mathbf{B}}(\mathbf{W}) + \mathbf{RA}.$$

The first two terms are the Saint Venant-Kirchhoff large deformation stress [5]. Within the small perturbation assumption, $\mathbf{F} = \mathbf{I}$, $\mathbf{W^2} - \mathbf{I} = 2\varepsilon$ this constitutive law gives

$$\boldsymbol{\Pi} = \boldsymbol{\sigma} = 2\,(\mathrm{tr}\varepsilon)\,\mathbf{I} + 4\varepsilon,$$

which is the classical elastic small perturbation constitutive law, linear function of matrices $(\mathrm{tr}\varepsilon)\,\mathbf{I}$ and ε [5].

4.1 Function $\hat{\Psi}(\mathbf{B})$ Approximation of the Indicator Function of $\mathring{C}_\alpha$

Quantity $\hat{\Psi}(\mathbf{B})$ in the free energy accounts for the resistance of the material to flattening or to crushing. It makes impossible all the principal stretches of matrix $\mathbf{W}$ to be small at the same time, i.e., all the principal stretches cannot be lower than $\alpha > 0$. Parameter α quantifies this resistance to flattening. Function $\hat{\Psi}(\mathbf{B})$ is a smooth approximation from the interior of the indicator function of the set $\mathring{C}_\alpha$ in $\mathscr{M}$. Let $I^{\mathrm{det}}(x)$ be a decreasing non negative smooth approximation of the indicator function of $[\alpha^3, \infty)$ from the interior, i.e., such that $I^{\mathrm{det}}(x) = \infty$ if $x \leq \alpha^3$ (for

instance, $1/(x-\alpha^3)$ for $x > \alpha^3$). Let $I^{\rm cof}(x)$ be a decreasing non negative smooth approximation of the indicator function of $\left[3\alpha^2, \infty\right)$ from the interior, i.e., such that $I^{\rm cof}(x) = \infty$ if $x \leq 3\alpha^2$. Let $I^{tr}(x)$ be a decreasing non negative smooth approximation of the indicator function of $[3\alpha, \infty)$ from the interior, i.e., such that such $I^{tr}(x) = \infty$ if $x \leq 3\alpha$. Then function $\hat{\Psi}$ may be defined by

$$\mathbf{B} \to \hat{\Psi}(\mathbf{B}) = \begin{cases} I^{\rm det}(\det \mathbf{B}) + I^{\rm cof}(\mathrm{tr}(\mathrm{cof}(\mathbf{B}))) + I^{tr}(\mathrm{tr}\mathbf{B}), & \text{if } \mathbf{B} \in \mathring{C}_\alpha, \\ \infty, & \text{if } \mathbf{B} \notin \mathring{C}_\alpha. \end{cases}$$

Note that matrix $\mathbf{W}$ commutes with matrix $\left(d\hat{\Psi}/d\mathbf{B}\right)(\mathbf{W})$ and function $\hat{\Psi}$ satisfies $\hat{\Psi}(\mathbf{I}) < \infty$, and

$$\hat{\Psi}(\mathbf{W}) < \infty \quad \Leftrightarrow \quad \mathbf{W} \in \mathring{C}_\alpha.$$

5 The Constitutive Laws

It is classical to get the constitutive laws with the derivatives of free energy (3) and the derivative of the pseudo-potential of dissipation $D(\dot{\mathbf{B}}, \mathrm{grad}\widehat{\boldsymbol{\Omega}})$, (4), gives the constitutive laws

$$\mathbf{Z} = \mathrm{grad}\Delta\Phi, \tag{5}$$
$$\boldsymbol{\Pi} = \mathbf{R}(\mathbf{S}+\mathbf{A}),\ \mathbf{S} \in \mathscr{S},\ \mathbf{A} \in \mathscr{A},$$
$$\mathbf{S} = (\mathbf{W}-\mathbf{I}) + \frac{d\hat{\Psi}}{d\mathbf{B}}(\mathbf{W}) + \dot{\mathbf{W}},\ \mathbf{A} \in \partial I_{\mathscr{S}}(\mathbf{W}), \tag{6}$$
$$\Lambda = B + \mathrm{grad}\boldsymbol{\Omega} = (\mathrm{grad}\mathbf{R})\mathbf{R}^T + \mathrm{grad}\boldsymbol{\Omega},$$
$$\mathbf{M} = \boldsymbol{\Pi}\mathbf{F}^T - \mathbf{F}\boldsymbol{\Pi}^T.$$

Remark 4 Stress $d\hat{\Psi}/d\mathbf{B}$ is the impenetrability reaction which intervenes to avoid flattening of the material. The constitutive law (6) implies that $\mathbf{W} \in \mathring{C}_\alpha$ because function $\hat{\Psi}(\mathbf{B})$ is differentiable for $\mathbf{B} = \mathbf{W}$. Antisymmetric reaction stress $\mathbf{A}$ insures the stretch matrix $\mathbf{W}$ is symmetric. This reaction matrix is an important quantity of the theory. Position Φ and reaction matrix $\mathbf{A}$ are the main unknowns of the problem. We have

$$\mathbf{A} : \dot{\mathbf{W}} = 0,$$

because $\dot{\mathbf{W}}$ is symmetric and $\mathbf{A}$ is antisymmetric. As expected, reaction $\mathbf{A}$ is a workless reaction, and as usual, the indetermination on workless reaction $\mathbf{A}$ is solved by the related equation of motion.

6 Initial and Boundary Conditions

The solid we consider is at rest at initial time. Let Γ_0, Γ_1 be a partition of $\partial\mathscr{D}_a$. The solid is clamped on part Γ_0 to the immobile obstacle and on part Γ_1 no surface force is applied.

The initial velocity is null

$$\Phi(a,0) = a, \quad \overrightarrow{U}(a,0) = \frac{d\Phi}{dt}(a,0) = 0. \tag{7}$$

On Γ_0, we have

$$\dot{\Phi} = 0, \quad \mathrm{grad}\dot{\Phi} = 0, \quad \frac{\partial}{\partial N}\left(\mathrm{grad}\dot{\Phi}\right) = 0, \quad \boldsymbol{\Omega} = 0.$$

On Γ_1, no load is applied.

Remark 5 Note that condition $\boldsymbol{\Omega} = 0$ on Γ_0 results from condition $\mathrm{grad}\dot{\Phi} = 0$.

7 The Equations

They are the kinematic relationships, the equations of motion and the constitutive laws plus the boundary and initial conditions.

The equations for Φ and $\mathbf{R}$, $\mathbf{W}$ and $\mathbf{A}$ are

$$\mathbf{F} = \mathrm{grad}\Phi, \ \mathbf{W} = \sqrt{\mathbf{F}^T\mathbf{F}}, \quad \mathbf{R} = \mathbf{F}\mathbf{W}^{-1},$$
$$\frac{d\overrightarrow{U}}{dt} = \mathrm{div}\boldsymbol{\Pi} + \mathrm{div}(\Delta\mathbf{Z}) + \overrightarrow{f}, \quad \text{in } \mathscr{D}_a,$$
$$\dot{\Phi} = 0, \quad \mathrm{grad}\dot{\Phi} = 0, \quad \frac{\partial}{\partial N}\left(\mathrm{grad}\dot{\Phi}\right) = 0, \quad \text{on } \Gamma_0,$$
$$\text{no load is applied on } \Gamma_1,$$
$$\boldsymbol{\Pi} = \mathbf{R}(\mathbf{S} + \mathbf{A}),$$
$$\mathbf{S} = (\mathbf{W} - \mathbf{I}) + \dot{\mathbf{W}} + \frac{\partial\hat{\Psi}}{\partial\mathbf{B}}(\mathbf{W}), \quad \mathbf{A} \in \partial I_{\mathscr{S}}(\mathbf{W}),$$
$$\mathbf{Z} = \mathrm{grad}\Delta\Phi,$$
$$\boldsymbol{\Omega} = \dot{\mathbf{R}}\mathbf{R}^T,$$
$$\mathrm{div}((\mathrm{grad}\mathbf{R})\mathbf{R}^T) + \Delta\boldsymbol{\Omega} + \mathbf{R}\left\{\mathbf{A}\mathbf{W} + \mathbf{W}\mathbf{A} + \dot{\mathbf{W}}\mathbf{W} - \mathbf{W}\dot{\mathbf{W}})\right\}\mathbf{R}^T = 0,$$
$$((\mathrm{grad}\mathbf{R})\mathbf{R}^T) + \mathrm{grad}\boldsymbol{\Omega})\overrightarrow{N} = 0, \quad \text{on } \Gamma_1,$$
$$\Phi(a,0) = a, \ \frac{d\Phi}{dt}(a,0) = \overrightarrow{U}(a,0) = 0.$$

Note that the initial and boundary conditions for Φ give the initial condition for $\mathbf{R}$: $\mathbf{R}(a,0) = \mathbf{I}$ and a Dirichlet boundary condition $\mathbf{R} = \mathbf{I}$ on Γ_0.

7.1 Variational Formulation of the Momentum Equations

Let us define the space of the virtual velocities

$$\mathscr{V}(t) = \left\{ \overrightarrow{\varphi}(a,\tau),\ \ 0 \le \tau \le t,\ \ \overrightarrow{\varphi} = 0,\ \text{grad}\overrightarrow{\varphi} = 0,\ \ \frac{\partial}{\partial N}\left(\text{grad}\overrightarrow{\varphi}\right) = 0,\ \text{ on } \Gamma_0 \right\},$$

and the space of the virtual angular velocities

$$\mathscr{V}_{rv}(t) = \left\{ \hat{\boldsymbol{\Omega}}(a,\tau),\ 0 \le \tau \le t, \quad \hat{\boldsymbol{\Omega}} \in \mathscr{A}, \quad \hat{\boldsymbol{\Omega}} = 0, \quad \text{on } \Gamma_0 \right\}.$$

The variational formulations are

$$\begin{aligned}
&(\Phi - a) \in \mathscr{V}(T), \quad \forall \overrightarrow{\varphi} \in \mathscr{V}(T), \\
&\int_0^T \int_{\mathscr{D}_a} \left\{ \frac{d^2\Phi}{dt^2} \cdot \overrightarrow{\varphi} + \mathbf{R}\left[(\mathbf{W} - \mathbf{I}) + \dot{\mathbf{W}} + \frac{\partial \hat{\Psi}}{\partial \mathbf{W}}(\mathbf{W}) + \mathbf{A} \right] : \text{grad}\overrightarrow{\varphi} \right. \\
&\qquad \left. + \ \text{grad}\Delta\Phi : \text{grad}\Delta\overrightarrow{\varphi} \right\} da\, d\tau = \int_0^T \int_{\mathscr{D}_a} \overrightarrow{f} \cdot \overrightarrow{\varphi}\, da\, d\tau,
\end{aligned} \tag{8}$$

and

$$\begin{aligned}
&\boldsymbol{\Omega} = \dot{\mathbf{R}}\mathbf{R}^T \in \mathscr{V}_{rv}(T), \quad \forall \hat{\boldsymbol{\Omega}} \in \mathscr{V}_{rv}(T), \quad \mathbf{R}(a,0) = \mathbf{I}, \\
&\int_0^T \int_{\mathscr{D}_a} (\text{grad}\mathbf{R})\,\mathbf{R}^{\mathbf{T}} : \text{grad}\hat{\boldsymbol{\Omega}} + \text{grad}\boldsymbol{\Omega} : \text{grad}\hat{\boldsymbol{\Omega}}\, da\, d\tau \\
&\qquad = \int_0^T \int_{\mathscr{D}_a} \mathbf{R}\left\{ (\mathbf{A} + \mathbf{S})\mathbf{W} - \mathbf{W}(\mathbf{A}^T + \mathbf{S}^T) \right\} \mathbf{R}^{\mathbf{T}} : \hat{\boldsymbol{\Omega}}\, da\, d\tau.
\end{aligned} \tag{9}$$

The variational formulations are completed with the kinematic relationship

$$\text{grad}\Phi = \mathbf{RW}, \tag{10}$$

and the initial conditions

$$\Phi(a,0) = a, \quad \frac{d\Phi}{dt}(a,0) = 0.$$

8 Properties of the Equations

The coupled system of Eqs. (8) and (9) with kinematic relationship (10) gives the two unknowns: position Φ and reaction $\mathbf{A}$ depending on external force $\overrightarrow{f}$ and on initial conditions (7).

8.1 Property of the Angular Momentum Equation

Let us investigate the angular momentum equation of motion and prove that it gives reaction $\mathbf{A}$ depending on position function Φ and velocity $\dot{\Phi}$.

The angular momentum equation of motion (9) is equivalent to

$$\operatorname{div}\left((\operatorname{grad}\mathbf{R})\mathbf{R}^{\mathbf{T}}\right) + \Delta\boldsymbol{\Omega} + \mathbf{R}\left\{\mathbf{AW} + \mathbf{WA} + \dot{\mathbf{W}}\mathbf{W} - \mathbf{W}\dot{\mathbf{W}}\right\}\mathbf{R}^{\mathbf{T}} = \mathbf{0}, \tag{11}$$

with initial condition $\mathbf{R} = \mathbf{I}$ and the boundary conditions on Γ_0 and Γ_1, gives reaction stress $\mathbf{A} \in \mathscr{A}$ depending on $\operatorname{grad}\Phi$, $\boldsymbol{\Omega}$ and $\dot{\mathbf{W}}$. Reaction stress $\mathbf{A}$ is solution of

$$\mathbf{AW} + \mathbf{WA} = \mathbf{Y},$$

with

$$\mathbf{Y} \in \mathscr{A}, \quad \mathbf{Y} = -\mathbf{R}^{T}\left\{\operatorname{div}\left((\operatorname{grad}\mathbf{R})\,\mathbf{R}^{T}\right) + \Delta\boldsymbol{\Omega}\right\}\mathbf{R} - \left\{\dot{\mathbf{W}}\mathbf{W} - \mathbf{W}\dot{\mathbf{W}}\right\}.$$

For the solution of this equation, the reader may refer to [3], and it is

$$\mathbf{A} = \frac{1}{D}\left\{\left(i_1^2 - i_2\right)\mathbf{Y} - \left(\mathbf{W}^2\mathbf{Y} + \mathbf{Y}\mathbf{W}^2\right\}, \right. \tag{12}$$

where the i_i are the invariants of matrix $\mathbf{W}$ and $D = i_1 i_2 - i_3$

$$i_1 = \operatorname{tr}\mathbf{W}, \quad i_2 = \operatorname{tr}(\operatorname{cof}\mathbf{W}), \quad i_3 = \det\mathbf{W}.$$

Proposition 1 *If $\mathbf{W} \in C_\alpha$, then Eq. (11) gives a unique $\mathbf{A}$ depending on $\mathbf{R}$, $\boldsymbol{\Omega}$, $\mathbf{W}$ and $\dot{\mathbf{W}}$.*

Let us note that within this point of view, angular momentum equations does not give rotation matrix $\mathbf{R}$ depending on $\mathbf{A}(\Phi)$, $\mathbf{W}(\Phi)$ and $\dot{\mathbf{W}}(\Phi, \dot{\Phi})$. as it is usual for such a parabolic equation with respect to $\mathbf{R}$. But on the contrary, the equation gives quantity $\mathbf{A}$ which intervenes in the right hand side of the parabolic equation

$$\operatorname{div}\left((\operatorname{grad}\mathbf{R})\mathbf{R}^{\mathbf{T}}\right) + \Delta\boldsymbol{\Omega} = -\mathbf{R}\left\{\mathbf{AW} + \mathbf{WA} + \dot{\mathbf{W}}\mathbf{W} - \mathbf{W}\dot{\mathbf{W}}\right\}\mathbf{R}^{\mathbf{T}}.$$

9 Solutions

In a convenient mathematical framework, it is possible to prove that variational equations (8), (9) with kinematic relationship (10) and initial conditions (7) have solutions Φ and $\mathbf{A}$ which are local in time: there is a solution up to some time $\hat{T} > 0$ with $\hat{T} \leq T$ [2–4]. Why is it impossible to have a global in time solution? It is a problem of mechanics: modelling is not complete because it does not take into account collisions, i.e., discontinuities of the velocity with respect to time. Even if we have eliminated the possibility of the interruption of the smooth motion resulting from collision with an obstacle or from self-collision, we cannot eliminate internal collisions, i.e., discontinuities of velocity due to flattening or crushing inside the solid (think of pasta being crushed between two fingers). Thus it is possible the motion, the smooth motion, is interrupted at time $\hat{T}$ with $\hat{T} > 0$. To continue the description of the motion, collision theory [7] has to be applied.

10 The Usual Incompressibility Condition

An incompressible material is such that density $\rho_x(\overrightarrow{x}, t)$ is constant with value $\rho_x(\overrightarrow{x}, t) = \rho_a(\overrightarrow{a})$, with $\overrightarrow{x} = \Phi(\overrightarrow{a}, t)$. Due to the mass balance, this constraint is equivalent to

$$\det \mathbf{F} = \det \mathbf{W} = 1. \tag{13}$$

It is taken into account by having the function

$$I_0(\det \mathbf{W} - 1),$$

in the free energy Ψ, where I_0 is the indicator function of the origin of $\mathbb{R}$. This indicator function adds the incompressibility reaction stress

$$\boldsymbol{\Pi}_{reac} = \mathbf{R}\mathbf{S}_{reac},$$

with

$$\mathbf{S}_{reac} \in \frac{d \det \mathbf{W}}{d\mathbf{W}} \partial I_0(\det \mathbf{W} - 1) = -p \operatorname{cof}\mathbf{W}, \ -p \in \partial I_0(\det \mathbf{W} - 1) = \mathbb{R}.$$

Let us note that p is the usual pressure in the Cauchy reaction stress σ_{reac} given by

$$\begin{aligned} \sigma_{reac} &= \frac{1}{\det \mathbf{F}} \boldsymbol{\Pi}_{reac} \mathbf{F}^T = -p \frac{1}{\det \mathbf{W}} \mathbf{R}(\operatorname{cof}\mathbf{W}) \mathbf{W} \mathbf{R}^T \\ &= -p \frac{1}{\det \mathbf{W}} \mathbf{R}((\det \mathbf{W}) \mathbf{W}^{-1}) \mathbf{W} \mathbf{R}^T = -p\mathbf{I}. \end{aligned}$$

Remark 6 Function

$$\mathbf{W} \quad \rightarrow \quad I_0(\det \mathbf{W} - 1),$$

is not convex. But

$$\mathbf{S}_{reac} : \dot{\mathbf{W}} = -p \, \mathrm{cof}\mathbf{W} : \dot{\mathbf{W}} = -p \frac{d \det \mathbf{W}}{dt} = 0.$$

The incompressibility reaction is non dissipative and does not intervene in the Clausius Duhem inequality.

It is also possible to take into account incompressibility with a dissipative function

$$I_0(\det \dot{\mathbf{W}}),$$

The reaction stress is

$$\mathbf{S}^d_{reac} \in \partial I_0(\det \dot{\mathbf{W}}) \frac{d \det \dot{\mathbf{W}}}{d\dot{\mathbf{W}}},$$

giving

$$\mathbf{S}^d_{reac} = -p \, \mathrm{cof}\dot{\mathbf{W}}, \quad -p \in \mathbb{R} = \partial I_0(\det \dot{\mathbf{W}}).$$

Because we have

$$\mathrm{cof}\dot{\mathbf{W}} : \dot{\mathbf{W}} = 3 \det \dot{\mathbf{W}} = 0,$$

the reaction stress does not work: it is non dissipative as expected. It results also that the Clausius Duhem inequality

$$\mathbf{S}^d_{reac} : \dot{\mathbf{W}} = -p \, \mathrm{cof}\dot{\mathbf{W}} : \dot{W} \geq 0,$$

is satisfied.

Remark 7 Dissipative function $I_0(\det(\dot{\mathbf{W}}))$ is not a pseudo-potential because it is not a convex function of $\dot{\mathbf{W}}$ but as already remarked the Clausius Duhem inequality is satisfied. Note also that there is no dual function for the dissipative function.

11 A Physical Incompressibility Condition

The non convexity of functions

$$\mathbf{W} \rightarrow I_0(\det \mathbf{W} - 1), \quad \dot{\mathbf{W}} \rightarrow I_0(\det \dot{\mathbf{W}}),$$

may be a hint that the classical incompressibility condition is perhaps misleading or has some mechanical weakness.

Let us go back to experiments and remark that when tension is applied to a sample, some voids may appear during the evolution mainly at the microscopic level with a volume increase at the macroscopic level. Moreover a phase change may occur, the solid becomes liquid or even vapor and eventually making possible an increase of volume [10]. This behaviour has been described a long time ago by Jean Jacques Moreau to investigate cavitation in fluid mechanics [12, 14]. The water is incompressible but bubbles may appear inside water at the microscopic level when the pressure is null: this is the cavitation phenomenon responsible of water hammers. At the macroscopic level, when the pressure is null, liquid vapour phase change may also occur [10]. It results unilateral condition

$$\det \mathbf{W} - 1 \geq 0. \tag{14}$$

On the contrary, for an incompressible material it is impossible to have interpenetration at the microscopic level. It results

$$\det \mathbf{W} - 1 \leq 0,$$

is impossible. Note that the word incompressible refers to the impossibility to modify the volume by compression. We are motivated to think that condition (14) is perhaps better than condition (13) to account for the actual mechanical behaviour. The set

$$D_1^{\det} = \{\mathbf{B} \in \mathscr{M};\ \det \mathbf{B} - 1 \geq 0\},$$

is such that

$$D_1^{\det} \cap \mathscr{S},$$

is a convex set [11].

The incompressibility constitutive law is assuming smooth evolution

$$\mathbf{S}_{reac} + \mathbf{A}_{reac} \in \partial I_{D_1^{\det} \cap \mathscr{S}}(\mathbf{W}),$$

with symmetric and antisymmetric parts given by

$$\mathbf{S}_{reac} \in \frac{d \det \mathbf{W}}{d\mathbf{W}} \partial I_+(\det \mathbf{W} - 1) = -p \operatorname{cof} \mathbf{W},\ -p \in \partial I_+(\det \mathbf{W} - 1),$$
$$\mathbf{A}_{reac} \in \partial I_{\mathscr{S}}(\mathbf{W}),$$

with

$$\partial I_+(\det \mathbf{W} - 1) = \begin{cases} \mathbb{R}^-, & \text{if } \det \mathbf{W} - 1 = 0, \\ \{0\}, & \text{if } \det \mathbf{W} - 1 > 0. \end{cases}$$

introducing non negative pressure p. If the symmetry of stretch matrix $\mathbf{W}$ is accounted for elsewhere, we may delete reaction $\mathbf{A}_{reac}$ which is already present.

We may also have an incompressibility constitutive law with

$$\dot{\mathbf{W}} \in D_1(\mathbf{W}),$$

where convex cone $D_1(\mathbf{W})$ defined by

$$D_1(\mathbf{W}) = \{\mathbf{B} \in \mathscr{M};\ \mathbf{N}_1(\mathbf{W}) : \mathbf{B} \leq 0\},$$

where

$$\mathbf{N}_1(\mathbf{W}) = \begin{cases} -\text{cof}\mathbf{W}, & \text{if } \det \mathbf{W} - 1 = 0, \\ \mathbf{0}, & \text{if } \det \mathbf{W} - 1 > 0, \end{cases}$$

because

$$\frac{d \det \mathbf{W}}{d\mathbf{W}} = \text{cof}\mathbf{W}.$$

Set $D_1(\mathbf{W})$ contains velocities $\dot{\mathbf{W}}$ such that $\det \mathbf{W} - 1$ remains non negative. Thus by having

$$I_{D_1(\mathbf{W})}(\dot{\mathbf{W}}) + I_{\mathscr{S}}(\dot{\mathbf{W}}),$$

in the pseudo-potential of dissipation. Incompressibility reaction $\mathbf{S}^d_{reac}$ is given by

$$\mathbf{S}^d_{reac} = \begin{cases} -p\,\text{cof}\mathbf{W},\ -p \in \mathbb{R}^-, & \text{if } \det \mathbf{W} - 1 = 0, \\ \mathbf{0}, & \text{if } \det \mathbf{W} - 1 > 0. \end{cases}$$

It is a non negative pressure in case $\det \mathbf{W} - 1 = 0$. We have

$$\mathbf{S}^d_{reac} : \dot{\mathbf{W}} = -p\,\text{cof}\mathbf{W} : \dot{\mathbf{W}} = 0$$

when $\det \mathbf{W} - 1 = 0$ because the evolution is smooth.

Remark 8 Note that if $\det \mathbf{W} - 1 = 0$ the motion being a smooth motion, it is impossible to have either $\text{cof}\mathbf{W} : \dot{\mathbf{W}} < 0$ or $\text{cof}\mathbf{W} : \dot{\mathbf{W}} > 0$. In case we have $\text{cof}\mathbf{W} : \dot{\mathbf{W}} \neq 0$, $\dot{\mathbf{W}}$ is discontinuous with respect to time: there is a collision and collision theory [7] has to be applied.

12 Solution

For the sake of simplicity, we assume the solid interacts with an obstacle by springs applying actions proportional to the gap $(\Phi - a)$ and to its gradient. It results the surface free energy

$$\frac{1}{2}\int_{\Gamma_0^a}(\Phi - a)^2 d\Gamma + \frac{1}{2}\int_{\Gamma_0^a}(\mathrm{grad}\Phi - \mathbf{I})^2 d\Gamma,$$

Besides the body force $\overrightarrow{f}$, no other external action is applied. In particular, neither volume nor surface moments are applied.

12.1 The Mathematical Existence Theorem

The spaces of the virtual linear and angular velocities are (here H^n denotes the usual Hilbert space $W^{n,2}$)

$$\hat{\mathcal{V}} = H^3(\mathcal{D}_a),\ \hat{\mathcal{V}}_{rv} = H^1(\mathcal{D}_a).$$

Assuming external force is smooth, $\overrightarrow{f} \in L^\infty(0, T; L^2(\mathcal{D}_a))$, we prove that there are solutions to the variational equations (16) and (17) given below, up to time $\hat{T} > 0$, such that $\hat{T} \leq T$. If $\hat{T} < T$, there is a collision due to flattening at time T.

The pressure p is a measure $p \in M(Q)$ where $Q = \mathcal{D}_a \times \left]0, \hat{T}\right[$. Then we have in the variational formulation the term

$$< p\,(\det \mathbf{W})\,\mathbf{R}\mathbf{W}^{-1} : \mathrm{grad} V > = < p\mathbf{I} : (\det \mathbf{W})\,(\mathrm{grad} V)\mathbf{W}^{-1}\mathbf{R}^T >,$$

where $p\,(\det \mathbf{W})\,\mathbf{R}\mathbf{W}^{-1}$ is the product of measure p with continuous function $(\det \mathbf{W})\,\mathbf{R}\mathbf{W}^{-1}$. Pressure p may be interpreted

$$-p \in \partial I_+(\det \mathbf{W} - 1), \tag{15}$$

in a suitable weak sense.

The acceleration $d^2\Phi/dt^2$ belongs to the dual space of

$$\left\{\widehat{V} \in L^2(0, \hat{T}; \hat{\mathcal{V}});\quad \mathrm{grad}\widehat{V} \in C(0, \hat{T}; H^2(\mathcal{D}_a))\right\}.$$

Velocity $\dot{\Phi}$ is not continuous with respect to the time because collisions may occur when incompressibility constraint $\det \mathbf{W} - 1 = 0$, becomes active (for instance when a compression is applied to a solid which satisfies $\det \mathbf{W} - 1 > 0$ at the initial time). Concomitantly, the pressure is a measure allowing reaction percussion when the incompressibility constraint becomes active.

For the initial condition, we study the evolution before time $t = 0$ with all the external actions null and solution $\Phi = a$ when $t < 0$ and all the solution are in $L^2(d, \hat{T})$, the beginning of the evolution being at time $d < 0$. One may also remark that the velocity $\dot{\Phi}^- = \lim_{t\to 0,\ t<0} \dot{\Phi}(t)$, the velocity before a possible collision at initial time $t = 0$, is given.

The linear momentum variation variational formulation is

$$
\begin{aligned}
&\Phi \in \left\{ \widehat{V} \in L^2(0,\hat{T};\hat{\mathscr{V}}); \operatorname{grad}\widehat{V} \in C(0,\hat{T};H^2(\mathscr{D}_a)) \right\},\\
&\dot{\Phi} \in L^2(0,\hat{T};H^1(\mathscr{D}_a)) \cap L^\infty(0,\hat{T};L^2(\mathscr{D}_a));\\
&\Phi(a,0) = a, \quad \dot{\Phi}^-(a,0) = 0,\\
&\forall\ \widehat{V} \in \left\{ \widehat{V} \in L^2(0,\hat{T};\hat{\mathscr{V}}); \operatorname{grad}\widehat{V} \in C(0,\hat{T};H^2(\mathscr{D}_a)) \right\},\\
&<<\frac{d^2\Phi}{dt^2}\cdot\widehat{V}>> - < p\,(\det\mathbf{W})\,\mathbf{R}\mathbf{W}^{-1} : \operatorname{grad}\widehat{V} >\\
&\quad + \int_0^t \int_{\mathscr{D}_a} \mathbf{R}\left[(\mathbf{W}-\mathbf{I}) + \dot{\mathbf{W}} + \frac{\partial\hat{\Psi}}{\partial\mathbf{W}}(\mathbf{W}) + \mathbf{A} \right] : \operatorname{grad}\widehat{V}\\
&\qquad + \operatorname{grad}\Delta\Phi : \operatorname{grad}\Delta\widehat{V}\, da\, d\tau\\
&\quad + \int_{\Gamma_0^a} (\Phi - a)\cdot\widehat{V} + (\operatorname{grad}\Phi - \mathbf{I}) : \operatorname{grad}\widehat{V}\, d\Gamma\, d\tau\\
&\quad = \int_0^t \int_{\mathscr{D}_a} \vec{f}\cdot\widehat{V}\, da\, d\tau. \qquad (16)
\end{aligned}
$$

The angular momentum variational formulation is

$$
\begin{aligned}
&\boldsymbol{\Omega} = \dot{\mathbf{R}}\mathbf{R}^T \in\in L^2(0,\hat{T};\hat{\mathscr{V}}_{rv}), \quad \forall\ \widehat{\boldsymbol{\Omega}} \in L^2(0,\hat{T};\hat{\mathscr{V}}_{rv}), \quad \mathbf{R}(\vec{a},0) = \mathbf{I},\\
&\int_0^t \int_{\mathscr{D}_a} (\operatorname{grad}\mathbf{R})\,\mathbf{R}^T : \operatorname{grad}\widehat{\boldsymbol{\Omega}} + \operatorname{grad}\boldsymbol{\Omega} : \operatorname{grad}\widehat{\boldsymbol{\Omega}}\, da\, d\tau\\
&\quad = \int_0^t \int_{\mathscr{D}_a} \mathbf{R}\left\{ (\mathbf{A}+\dot{\mathbf{W}})\mathbf{W} + \mathbf{W}(\mathbf{A}-\dot{\mathbf{W}}) \right\}\mathbf{R}^T : \widehat{\boldsymbol{\Omega}}\, da\, d\tau. \qquad (17)
\end{aligned}
$$

The variational formulations are completed with the kinematic relationship

$$\operatorname{grad}\Phi = \mathbf{R}\mathbf{W},$$

and the initial conditions

$$\Phi(\vec{a},0) = a, \qquad \dot{\Phi}^-(\vec{a},0) = 0.$$

Then the existence theorem is

Theorem 1 *If $\vec{f} \in L^\infty(0,T;L^2(\mathscr{D}_a))$, there exists a time $\hat{T}$, $0 < \hat{T} \le T$, such that there exists position function Φ, reaction matrix $\mathbf{A}$ and pressure p satisfying (16) and (17) with $d^2\Phi/dt^2$, in the dual space of*

$$\left\{\widehat{V} \in L^2(0,\hat{T};\hat{\mathscr{V}}); \quad \operatorname{grad}\widehat{V} \in C(0,\hat{T};H^2(\mathscr{D}_a))\right\},$$
$$\mathbf{A} \in L^2(0,\hat{t};\hat{\mathscr{V}}^*_{rv}),$$

where $\hat{\mathscr{V}}^*_{rv}$ *is the dual space of* $\hat{\mathscr{V}}_{rv}$*, pressure* p *is a positive measure on* $Q = \mathscr{D}_a \times \left]0,\hat{T}\right[$*, satisfying (15).*

References

1. Antman SS (2005) Nonlinear problems of elasticity, 2nd edn. Springer, New York. Appl Math Sci 107
2. Bonetti E, Colli P, Frémond M (2013) The motion of a solid with large deformations. Comptes Rendus de l'Académie des Sciences, Series I 351:579–583
3. Bonetti E, Colli P, Frémond M (2014) 2D motion with large deformations. Bollettino dell'Unione Matematica Italiana 7:19–44
4. Bonetti E, Colli P, Frémond M (2014) The 3D motion of a solid with large deformations. Comptes Rendus Mathematique 352(3):183–187
5. Ciarlet PG (1988) Mathematical elasticity, volume I: three-dimensional elasticity. North-Holland, Amsterdam
6. Ciarlet PG, Gratie L, Iosifescu O, Mardare C, Vallée C (2007) Another approach to the fundamental theorem of Riemannian geometry in $\mathbb{R}^3$, by way of rotation fields. Journal de Mathématiques Pures et Appliquées 87:237–252
7. Frémond M (2007) Collisions. Ed. Dip. Ing. Civ., Università di Roma Tor Vergata, Rome. ISBN 9 788862 960007
8. Frémond M (2009) Grandes déformations et comportements extrêmes. Comptes Rendus Mécanique 337(1):24–29
9. Frémond M (2009) Équilibre d'un solide élastique en grandes déformations. Comptes Rendus Mathematique 347(7):457–462
10. Frémond M (2012) Phase change in mechanics. UMI-Springer lecture notes series, 13. Springer Science & Business Media
11. Frémond M (2016) Virtual work and phase change. Springer series in solid and structural mechanics, 7. doi:10.1007/978-3-319-40682-4
12. Moreau JJ (1965) Sur la naissance de la cavitation dans une conduite. Comptes Rendus Hebdomadaires des Seances de l'Academie des Sciences 259(22):3948–3950
13. Moreau JJ (1966) Séminaire sur les équations aux dérivées partielles. Collège de France, Paris
14. Moreau JJ (1966) Principes extrêmaux pour le problème de la naissance de la cavitation. Journal de Mécanique 5:439–470
15. Moreau JJ (2003) Fonctionnelles convexes. Ed. Dip. Ing. Civ., Università di Roma Tor Vergata, Rome
16. Salençon J (1988) Mécanique des milieux continus. Ellipses, Paris
17. Vallée C (1992) Compatibility equations for large deformations. Int J Eng Sci 30(12):1753–1757
18. Vallée C, Lerintiu C, Chaoufi J, Fortuné D, Ban M, Atchonouglo K (2013) A class of non-associated materials: n-monotone materials. Hooke's law of elasticity revisited. J Elast 112(2):111–138

Crowd-Structure Interaction in Laterally Vibrating Footbridges: Comparison of Two Fully Coupled Approaches

Bachar Kabalan, Pierre Argoul and Silvano Erlicher

Abstract Two models that deal with the crowd-structure interaction have been developed. The first is a 1D continuous model and the other is a 2D discrete one. In this paper, a summary of the formulation of these two models is presented. Both approaches used to represent the pedestrian-structure coupling phenomenon are detailed and compared. We start by introducing the partial and ordinary differential equations that govern the dynamics of both the continuous and the discrete models. First, the equation of dynamics of the footbridge for the case of lateral vibrations is recalled. Then, the Kuramoto phase equation is implemented for describing the coupling between the pedestrians and the laterally moving deck of a footbridge. Results obtained from numerical simulations are presented and compared with available experimental data.

1 Introduction

The vibrations caused by pedestrians walking on footbridges are generally not harmful to the structure, yet they can create for the user a feeling of discomfort and even panic. It is possible among military parades that the rhythmic march of soldiers can set off vibrations at the natural resonance frequency of a bridge. In the history of bridges, the most spectacular disasters under the effect of pedestrians have mainly concerned steel cable suspension bridges. Two notorious examples are the collapses

B. Kabalan (✉)
École des Ponts ParisTech, Université Paris Est, Laboratoire Ville Mobilité Transport,
6 et 8 av. Blaise Pascal, 77455 Marne-la-Vallée, France
e-mail: bachar.kabalan@enpc.fr

P. Argoul
Université Paris Est, IFSTTAR, MAST, SDOA, 14-20 bd. Newton,
77455 Marne-la-Vallée, France
e-mail: pierre.argoul@ifsttar.fr

S. Erlicher
EGIS Industries, 4 rue Dolores Ibarruri, 93188 Montreuil, France
e-mail: silvano.erlicher@egis.fr

M. Frémond et al. (eds.), *Models, Simulation, and Experimental Issues in Structural Mechanics*, Springer Series in Solid and Structural Mechanics 8,
DOI 10.1007/978-3-319-48884-4_11

of the Basse-Chaîne Bridge in Angers France in 1850 and of the Egyptian Bridge in St. Petersburg Russia in 1905 [2]. More recently, several footbridges, built in accordance with the architectural criteria of lightness and elegance, such as the Millennium Footbridge in London [9] and the Léopold-Sédar-Senghor footbridge in Paris [10] have proven to be sensitive to excitations induced by the crossing pedestrians. Thus, crowd-induced vibration of footbridges in the lateral direction has become a topic of heightened interest after the closure of both the previously mentioned footbridges from excessive oscillations [9, 10]. Early investigation on this phenomenon [14] indicated that synchronization between pedestrians and structure (lock-in effect) was the main cause of such large lateral oscillations.

The crowd walking on a bridge imposes a lateral excitation on the structure which has a frequency of about 1 Hz. When a lateral mode of vibration of the footbridge, often the first, has a frequency close to this value, a resonance phenomenon is activated. It follows that the amplitude of oscillations of the bridge increases. If the number of pedestrians is weak, the amplitude of oscillations stays small and pedestrians continue to walk as they would on a rigid floor. If instead the number is high enough (beyond a certain critical number), the oscillations' amplitude becomes larger, enough so that pedestrians are encouraged to change their way of walking, in particular their frequency of walking, until there is a phase synchronization between pedestrians and structure. The behavior of a pedestrian is also influenced by the crowd around him: if the density of the crowd is very low, the walking is "free", i.e. each individual walks as if there was nobody close to him. Conversely, if the crowd is dense, the pedestrian is forced to walk "at the same speed" as the others. On the congested footbridge presented in [14], processing of video images indicated around 20 % of pedestrians as being synchronized.

Several design models have been proposed to tackle this problem. These models have been developed to represent the human induced load e.g. [9, 12, 13, 16, 21, 22, 26, 27], crowd-structure synchronization [7, 20, 30], and the resulting bridge vibrations in the vertical and horizontal directions [15, 31]. In some of these articles [21, 22, 26, 27], the pedestrian is modelled as a single degree of freedom oscillator with different definitions of the restoring force. Following the same approach in [12], the pedestrian has been modelled as a self-sustained oscillator based on a modified hybrid Van der Pol/Rayleigh model. This model has been studied for the walking of the pedestrian on a rigid floor [12] and in the moving floor case [13, 29]. More recently, with reference to the non-autonomous (moving floor) case, Kumar et al. [17] are interested in the analysis of the phase difference between the oscillator entrained response and the external excitation. By these authors' opinion, the study of phase difference during synchronization between pedestrian and the floor is useful to better understand the whole synchronization phenomenon as well as the crowd-structure interaction. So far, two models have been developed during the past decade by Argoul and his collaborators, that deal with this phenomenon for lateral vibrations: (1) the 1D continuous model of Bodgi [3–5], and (2) the 2D discrete model of Pécol [23, 24]. In [3–5], the authors consider the crowd to behave as a compressible fluid

and deal explicitly with the crowd-structure interaction phenomenon. In the other model [23, 24], each pedestrian is represented individually and both the issues of evacuation and crowd-structure interaction are addressed. In this paper, we show how the different aspects of synchronization between a crowd induced force and an oscillating footbridge were treated in each model. More precisely, we give the procedure and the different equations used in each model to calculate the following parameters: (1) the critical number, (2) the synchronization frequency and (3) the displacement amplitude at the steady-state. In what follows, Bodgi's model will be referred to as M1 and Pecol's model as M2.

2 The Motion Equation of the Footbridge Dynamics. The Case of Lateral Vibrations

In M1, where a macroscopic representation is adopted for the crowd, an Euler-Bernoulli beam is used to represent the lateral oscillations of the footbridge. In M2, using a microscopic representation for the crowd, the footbridge's oscillations are governed through a finite element model. In both approaches, the movement equation of the footbridge dynamics is projected on the first lateral mode of the footbridge, having the nearest frequency to the pedestrian's transverse excitation one.

2.1 The 1D Continuous Model (M1)

The movement equation of the footbridge dynamics projected on its first lateral mode used by in M1 reads:

$$\big(M + M_p(t)\big)\ddot{U}_y(t) + C\dot{U}_y(t) + KU_y(t) = F^y(t) \tag{1}$$

where:

- $\psi_1(x)$ is the first lateral modal shape of the footbridge normed such as: $\|\psi_1\|_\infty = 1$ where $\|\cdot\|_\infty$ is the infinity norm defined for a function ϕ in $\mathbb{L}_\infty[0, L]$, by: $\|\phi\|_\infty = \max_{x\in[0,L]}(|\phi(x)|)$, L being the length of the footbridge span,
- $U_y(t)$ is the lateral displacement of the footbridge at the abscissa $\bar{x}$ where $|\psi_1(x)|$ is maximum : $U_y(t) = U_y(\bar{x}, t) = U_y(t) \cdot \psi_1(\bar{x})$,
- M, C, and K are the modal generalized mass, damping and stiffness of the first lateral mode of the footbridge, respectively, i.e. $M = \int_0^L \lambda(x)\psi_1^2(x)dx$, $C = 2\xi_1\omega_1 M$ and $K = \omega_1^2 M$ where $\omega_1 = 2\pi f_1$ and $\lambda(x)$ [kg/m] is the mass per unit length of the footbridge,

- $M_p(t) = \int_0^L m_p(x,t)\psi_1^2(x)dx$ is the modal mass of the crowd,
- $m_p(x,t) = m_{1,p}\eta(x,t)\ell(x)$ is the local mass of the crowd per unit length of the footbridge, m_{1p} being the average mass of a pedestrian,
- $F^y(t) = \int_0^L G\sin\left(\phi^{acc}(x,t)\right)\eta(x,t)\ell(x)\psi_1(x)dx$ is the lateral modal force generated by the pedestrians,
- G is the mean amplitude of the lateral force induced by a pedestrian,
- $\phi^{acc}(x,t)$ is the total phase of the lateral force induced by the pedestrians at position x and time t when they are sensitive to the bridge's acceleration (see Sect. 3.1 below),
- $\eta(x,t)$ is the pedestrians' surface density at position x and time t (ped/m^2),
- $\ell(x)$ is the footbridge's width at position x.

2.2 The 2D Discrete Model (M2)

As for the discrete model M2, some assumptions are first made [23]: the main longitudinal axis of the footbridge is straight and its deck is flat. The footbridge floor displacement doesn't depend on the vertical component, its oscillations are only considered in the horizontal plane and its longitudinal oscillations are considered to be negligible. Finally the non zero component of the footbridge displacement is the lateral one noted U_y and is assumed to be only dependent on the longitudinal component: $U_y\,(q^x,t)$.

The footbridge's lateral mode with a natural frequency closest to that of walking is usually assumed to be sufficient to properly represent the dynamics of the footbridge: $U_y\,(q^x,t) \simeq \psi_1(q^x)\,U_y(t)$. The equation of dynamics is then projected as previously on the first mode of lateral vibrations:

$$\begin{aligned} &M\ddot{U}_y(t) + C\dot{U}_y(t) + KU_y(t) = \sum_{i=1}^{N}\psi_1(q^x_{OC_i}(t))F_i^y(t) \\ &\text{with}\quad F_i^y(t) = -m_i\ddot{u}_i^{abs,y} = -m\left(\ddot{u}_i^{ent,y}(t) + \ddot{u}_i^{rel,y}(t) + \ddot{u}_i^{cor,y}(t)\right) \end{aligned} \tag{2}$$

where:

- m_i is the mass of the ith pedestrian,
- $q^x_{OC_i}(t)$ is the position of the ith pedestrian on the footbridge and θ_i is the angle between $\left(O, \underline{e}_x, \underline{e}_y\right)$ and $\left(C_i, \underline{e}^T_{C_i}(t), \underline{e}^N_{C_i}(t)\right)$ (see Fig. 1),
- C_i is the projection of the pedestrian's center of gravity on the horizontal plane and $\underline{e}^T_{C_i}(t)$ the unit vector tangent to the pedestrian's trajectory,
- N is the total number of pedestrians,
- $\ddot{u}_i^{abs}$ is the absolute acceleration of pedestrian i,

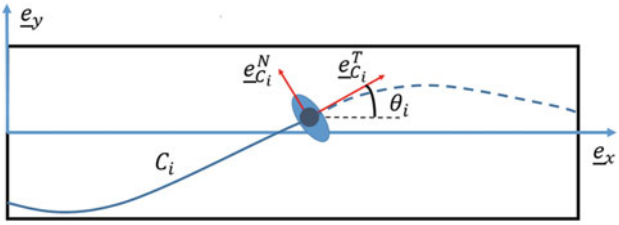

Fig. 1 The position and the trajectory of the ith pedestrian on the footbridge

- $\ddot{u}_i^{ent,y}(t)$ is the acceleration of the non-inertial frame of reference $\left(C_i, \underline{e}_{C_i}^T(t), \underline{e}_{C_i}^N(t)\right)$ with respect to $\left(O, \underline{e}_x, \underline{e}_y\right)$ (see Fig. 1), equal to

$$\begin{aligned}\ddot{u}_i^{ent,y}(t) &= \frac{d}{dt}\left(\psi_1(q_{OC_i}^x(t))\dot{U}_y(t)\right) + \ddot{u}_i^{tr,y}(t) \\ &= \psi_1(q_{OC_i}^x(t))\ddot{U}_y(t) + \frac{\partial\psi_1(q_{OC_i}^x(t))}{\partial q_{OC_i}^x(t)}\dot{u}_i^{tr,x}\dot{U}_y(t) + \ddot{u}_i^{tr,y}(t)\end{aligned} \tag{3}$$

  generating a fictitious force called the d'Alembert force (Lanczos [18]),
- $\ddot{u}_i^{tr,y}(t)$ is the part of $\ddot{u}_i^{ent,y}(t)$ independent from the bridge motion, equal to

$$\ddot{u}_i^{tr,y}(t) = \frac{d^2 q_{OC_i}^x(t)}{dt^2}, \tag{4}$$

- $\ddot{u}_i^{rel,y}(t) = u_i^{osc,y}(t)$ is the acceleration with respect to $\left(C_i, \underline{e}_{C_i}^T(t), \underline{e}_{C_i}^N(t)\right)$ due to the pedestrian's oscillations about his trajectory, equal to

$$\ddot{u}_i^{rel,y}(t) = -\frac{1}{m_i}\left[F_i^{osc,T}\sin\left(2\phi_i^{dis}\right)\sin\left(\theta_i\right) + F_i^{osc,N}\sin\left(\phi_i^{dis}\right)\cos\left(\theta_i\right)\right] \tag{5}$$

  and resulting from the natural way of walking projected on the y-axis (see Fig. 1),
- $F_i^{osc,T}$ and $F_i^{osc,N}$ are the tangential and normal component of the maximum amplitude of the force generated by the ith pedestrian on a rigid floor, respectively,
- θ_i is the angle between the direction of the trajectory and the longitudinal axis of the footbridge,
- $\phi_i^{dis}(t)$ is the phase of the lateral force induced by the ith pedestrian at time t when pedestrians are considered to be sensitive to the bridge's displacement (see Sect. 3.1 below).

The Coriolis acceleration $\ddot{u}_i^{cor,y}(t)$ is considered to be negligible (see Appendix). By rearranging terms into Eq. (2), we obtain:

$$\left[M+\sum_{i=1}^{N} m_i \psi_1^2\left(q_{OC_i}^x\right)\right]\ddot{U}_y+\left[C+\sum_{i=1}^{N} m_i \psi_1\left(q_{OC_i}^x\right)\frac{\partial \psi_1\left(q_{OC_i}^x\right)}{\partial q_{OC_i}^x}\dot{u}_i^{tr,x}(t)\right]\dot{U}_y + K U_y = -\sum_{i=1}^{N} m_i \psi_1\left(q_{OC_i}^x\right)\left(\ddot{u}_i^{tr,y}(t)+\ddot{u}_i^{osc,y}\right) \tag{6}$$

The main differences between Eqs. (1) and (6) stem from the consideration of the d'Alembert force and the pedestrian trajectory. In M2, the acceleration of the non-inertial frame (the footbridge) is considered. This acceleration generates a d'Alembert force that once inserted in Eq. (6) not only adds terms to the footbridge's mass, but also to its damping. This force was not considered in M1. As for the pedestrian trajectory, in [3] it is straight and thus only the normal component of the oscillatory force is considered (which becomes coincident with the y-component). In [23], both terms of the oscillatory force are considered since the pedestrian trajectory is two-dimensional.

3 Synchronization: Modelling the Phase Angle with the Kuramoto Equation

In both models M1 and M2, the phase difference between the structure and pedestrians is introduced as a variable governing the effect of the bridge movement on the pedestrian's gait (synchronization) and its evolution is modeled by the so-called Kuramoto differential equation [25]. Two cases are studied according to the dependence of the synchronization to the bridge acceleration or to its displacement. Yet the pedestrians in each case are sensitive to a different parameter called the synchronization parameter.

3.1 Sensitivity to the Bridge's Acceleration

In M1, it was considered that pedestrians are influenced by the footbridge acceleration. This led to the following form of the Kuramoto equation:

$$\frac{\partial \phi^{acc}}{\partial t}(x,t)=\omega(x)+\frac{\varepsilon}{2}A(t)\left|\psi_1(x)\right|\left(\dot{\Psi}_s(t)\right)^2 \sin\left(\Psi_s(t)-\phi^{acc}(x,t)+\alpha_{M1}\right) \tag{7}$$

where $\omega(x)$ is the lateral angular frequency for free walking; ε quantifies a pedestrian's sensitivity to the bridge's acceleration; $A(t)$ is the amplitude of the displacement of the footbridge i.e. $U_y(t)=A(t)\sin\left(\Psi_s(t)\right)$; $\Psi_s(t)$ is the instantaneous phase

of the lateral modal displacement of the footbridge; the expression $A(t)\psi(x)\left(\dot{\Psi}_s(t)\right)^2$ represents the bridge's acceleration : this means, according to [3–5], that the model postulates that pedestrians are sensitive to this quantity. It was chosen in M1 that $\alpha_{M1} = \pi/2$ indicating that when synchronization occurs, the pedestrian force is in phase with the velocity of the bridge. This choice of α_{M1} agrees with the results obtained from the experiments conducted on the Millennium Bridge [9].

As for M2 [23, 24], the authors used the same model used by [28]. Yet, we should note that the effects of the mode shape and of the crowd mass are considered in this paper. So in this model, the influence of the bridge's displacement on the ith pedestrian is quantified by $\bar{\varepsilon}_i$. The equation used in M2 to govern the synchronization phenomenon is given by:

$$\frac{d\phi_i^{dis}}{dt}(t) = \omega_i + \bar{\varepsilon}_i\, A(t)\psi_1\left(q^x_{OC_i}\right) \sin\left(\Psi_s(t) - \phi_i^{dis}(t) + \alpha_{M2}\right) \tag{8}$$

where ω_i is the natural frequency of the ith pedestrian. It is usually assumed that all pedestrians have the same value of $\bar{\varepsilon}_i = \bar{\varepsilon}$. We still choose $\alpha_{M2} = \pi/2$, to have the lateral force exerted by the ith pedestrian on the footbridge be in phase with latter's velocity when synchronization occurs.

4 Analytical Study

In this study, the analytical expressions for the following parameters are calculated for a particular case ($\mu_\omega = \omega_T$) and the general one ($\mu_\omega \neq \omega_T$): (1) The critical number N_c, greater than which phase synchronization between the structure and the pedestrians could take place, (2) the frequency of synchronization $\omega_s ync$ and (3) the footbridge displacement amplitude at the synchronized steady-state A. We should note that A is found analytically for a particular case and numerically for the general one. For both models M1 and M2, the same mathematical procedure is used to calculate these three parameters. The free walk frequency of pedestrians is assumed to follow a normal distribution with mean μ_ω and standard deviation σ_ω [19]. Two cases are considered: a particular one where μ_ω is equal to the modal frequency of the system crowd-structure $\mu_\omega = \omega_T$ and the general one where $\mu_\omega \neq \omega_T$. In M1 and M2, the modal frequency of the system crowd-structure is given by $\omega_T = \sqrt{K/\left(M + nm_{1p}N_c\right)}$ where $n = (1/N)\int_0^L \eta(x)\ell(x)\left(\psi_1(x)\right)^2 dx$ for M1 model in [3] and $n = (1/N)\int_0^1 \psi_1^2(z)h(z)dz$ for M2 model [24] and $h(z)$ is the probability density function representing the spatial distribution of the pedestrians over the bridge's length ($z_i = q^x_{OC_i}/L$). In what follows, we show the different expressions found for each of the three parameters mentioned at the beginning of this paragraph and for the considered cases.

Table 1 The expression of each parameter found by each model

	M1
N_c	$a_3\Gamma^3 + a_2\Gamma^2 + a_1\Gamma + a_0 = 0$
ω_{sync}	$\frac{8\pi K\sigma_\omega^2 + n\mu_\omega\omega_T^2 N_c G\varepsilon}{n\omega_T^3 N_c G\varepsilon + 8\pi K\sigma_\omega^2}\omega_T$
A	Numerically calculated
	M2
N_c	$\gamma_6 c_1 N_c^3 + \gamma_5 N_c^3 + \gamma_4 c_1 N_c^2 + \gamma_3 N_c^2 + \gamma_2 c_1 N_c + \gamma_1 N_c + \gamma_0 = 0$
ω_{sync}	$\frac{4K\sigma_\omega^2 + nN\bar{F}^{osc,N}\bar{\varepsilon}\bar{\omega}}{4K\sigma_\omega^2 + nN\bar{F}^{osc,N}\bar{\varepsilon}\omega_T}\omega_T$
A	Numerically calculated

4.1 Normal Distribution: $\mu_\omega \neq \omega_T$

In this part, we give in Table 1 the different expressions for N_c, A, and ω_{sync} associated with each model. For more information about the mathematical derivation, we refer the reader to [3–5, 23, 24]. In Table 1, $\bar{F}^{osc,N}$ is the mean of the maximum amplitudes of the normal component of the oscillatory forces generated by the pedestrians.

4.2 Normal Distribution: $\mu_\omega = \omega_T$

Similarly to the previous part, the different expressions for N_c, A, and ω_{sync} associated with each model are given in Table 2. For this particular case, where the mean of the free walk frequencies of the pedestrians is equal to the modal frequency of the system crowd-structure (the most critical case [32]), the analytical expression of the displacement amplitude during the steady-state can be explicitly calculated, where

$$c_0 = \frac{16C^2\sigma_\omega^2}{\varepsilon^2 n^2\pi^2 G^2 K} \quad \text{and} \quad \gamma = \frac{2\sqrt{2\pi}C\sigma_\omega}{n\pi\bar{F}^{osc,N}\bar{\varepsilon}}. \tag{9}$$

Table 2 The different expressions of each parameter found by each of the two models. See Appendix for more details

	M1	M2
N_c	$\frac{1}{2}\left(m_{1p}c_0\sqrt{m_p^2c_0^2 + 8Mc_0}\right)$	$N_c^3 + \frac{M}{nm_{1p}}N_c^2 - \frac{K}{nm_{1p}}\gamma^2 = 0$
ω_{sync}	ω_T	ω_T
A	Analytically calculated	Analytically calculated

5 Testing the Models

Several experiments have been performed on existing footbridges [6, 8]. In their work, the authors of M1 and M2 used some of the results obtained by these experiments in order to estimate the value of ε in the continuous model and $\bar{\varepsilon}$ in the discrete model. Then, they deduced the other parameters (N_c, A, and A) for several footbridges and compared them with the experimental ones and with those obtained from other authors. Bodgi [3] and Pecol [23] considered the following footbridges were considered: Millennium, Léopold Sédar Senghor, Pedro e Ines and Simone de Beauvoir bridges. The results obtained are very close to each other, on one hand, and to the experimental results on the other. In what follows, we will exhibit some of the obtained results.

5.1 Estimating ε and $\bar{\varepsilon}$

The value of ε or $\bar{\varepsilon}$ depends on the oscillation type of the footbridge. The values of the aforementioned parameters were calculated only for the cases of lateral and torsional movements. By using the value of N_c found experimentally for footbridges exhibiting these types of oscillations, it was found that $\varepsilon_{tor} \approx 1.95\,\mathrm{s\,m^{-1}}$ and $\varepsilon_{lat} \approx 4.1\,\mathrm{s\,m^{-1}}$ and $\bar{\varepsilon}_{tor} \approx 42\,\mathrm{m^{-1}\,s^{-1}}$ and $\bar{\varepsilon}_{lat} \approx 30.3\,\mathrm{m^{-1}\,s^{-1}}$ for the torsional and lateral oscillations respectively.

5.2 Calculating N_c

By solving the equations listed in Tables 1 and 2 the value of the critical number N_c is found. The chosen equation depends on the walking frequency of pedestrians. The different walking frequencies used in experiments on the Millennium, Pedro e Ines and the Léopold Senghor bridges are found in Table 3. The values of N_c that were found experimentally and by several authors are given in Table 4. The values of N_c obtained by model M1 are in very good agreement with the experimental ones and are very close to the values obtained by model M2.

5.3 The Displacement Amplitude

The authors of M1 and M2 calculated the analytical expression of the displacement amplitude at the steady state for the case where μ_ω is equal to the modal frequency of the system crowd-structure. They calculated this amplitude numerically and

Table 3 Characteristics of the walking pattern for Millennium/Pedros e Ines and Léopold Sédar Sengho

Footbridge (rad s^{-1})	Millennium/Pedro e Ines	Léopold Sédar Senghor		
Test	Free walk	T1	T2	T3
$\bar{\omega}$	$2\pi(0.93)$	$2\pi(0.7)$	$2\pi(0.75)$	$2\pi(0.75)$
σ_ω	$2\pi(0.093)$	$2\pi(0.093)$	$2\pi(0.093)$	$2\pi(0.0775)$

(T1) very slow free walk; (T2) slow free walk; (T3) slow rhythmic walk [24]

Table 4 The values of the critical number found experimentally and numerically [24]

Footbridge	Millennium	Pedro e Ines	Léopold Sédar Senghor		
Test	Free walk		T1	T2	T3
Experimentally [6, 8]	166	70	138–207	160–184	114–160
[3]	133	70	168	184	155
[24]	166	70	170	184	159
[8, 9]	73	73	91	91	91
[26, 27]	144	120	97	97	97
[21, 22]	181	205	325	325	325
[1]	149	131	128	128	128
[11]	70	79	125	125	125

analytically for several values of the number of pedestrians N crossing the north span of the Millennium Bridge. In M1, the N pedestrians are considered to be uniformly distributed on the footbridge. The density of the pedestrians is constant with respect to time. The obtained results are illustrated in Fig. 2.

In M2, the displacement amplitude was calculated for two types of crowds: (1) walking in-place. These pedestrians simulate walking without changing their position. Their number N is constant; (2) Moving pedestrians. Since N must always be constant, as one of the pedestrian reaches the end of the footbridge, another appears at the beginning. The obtained results are illustrated in Fig. 3.

The values of the amplitude of oscillations at the stationary state obtained analytically and numerically by M1 and M2 are very close. The only case where the error between the two values is relatively high is when the number of pedestrians is equal to 175 for the M1 model and when N is close to N_c for the M2 model. This can be justified by the fact that synchronization occurred only once out of 5 trials (for both cases) which is not enough to obtain valid estimations of the amplitude.

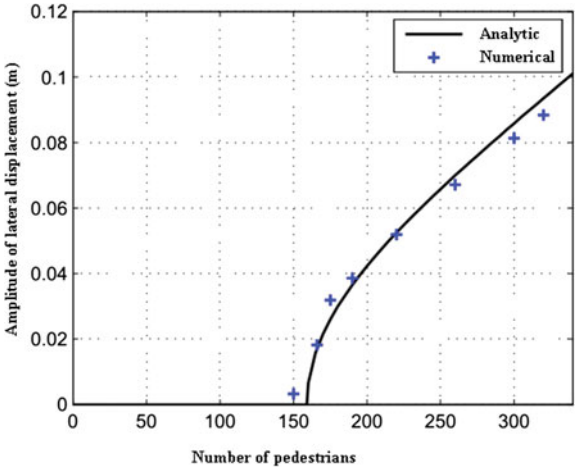

Fig. 2 North span of the Millennium Bridge: Comparison between the analytical and numerical values of the lateral displacement amplitude. μ_ω is equal to the modal frequency of the system crowd-structure [3]

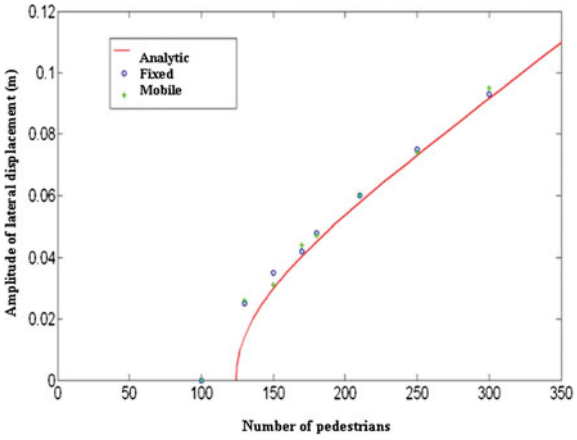

Fig. 3 North span of the Millennium Bridge: Comparison between the analytical and numerical values of the lateral displacement amplitude. μ_ω is equal to the modal frequency of the system crowd-structure [23]

6 Conclusions and Perspective

This paper presents and compares two crowd models developed by P. Argoul and his collaborators since 2005 that study the movement of pedestrians and their interaction with vibrating structures. These models differ in several aspects. First of all, the 1D continuous model (M1) [3–5] is a macroscopic one focusing only on crowd-structure interaction while the 2D discrete model (M2) [23, 24] uses a microscopic representation of the crowd studying evacuation and crowd-structure interaction. Secondly, in M2, a different equation of dynamics than the one in M1 is obtained as a result of considering the d'Alembert force and a 2D pedestrian trajectory. Finally, while both models use an equation of type Kuramoto to represent the synchronization of the induced pedestrian force with the bridge's movement, each one adopts a different sensitivity parameter. In M1, it is assumed that pedestrians are sensitive to the acceleration of the bridge while in M2, Strogatz's approach is preferred where pedestrians are sensitive to the displacement amplitude of the bridge. In future work, the microscopic model M2 will be further developed. First, the case $\alpha_{M2} \neq \pi/2$ will be analyzed. Then an analytical expression for the displacement amplitude for a general case will be searched for. Since numerical simulations were done only for the case of lateral vibrations, it is interesting to run simulations considering vertical vibrations. An advanced step is to study the case where two modes of the bridge affect the crowd's movement.

Acknowledgements The authors would like to thank Joanna Bodgi, Stefano Dal Pont and Philippe Pécol for their significant contribution in the development of the crowd-structure models during her(his) period of work in this research.

Appendix

Coriolis Acceleration Norm in the 2D Discrete Model

We are interested here in the comparison between the amplitude of the Coriolis acceleration norm: $\ddot{\underline{u}}^{cor}(t) = 2\dot{\theta}\underline{e}_z \wedge \dot{\underline{u}}^{rel}(t)$ and the amplitude of the relative acceleration one: $\ddot{u}^{rel}(t)$, in the 2D discrete model. For this purpose, let us consider a pedestrian of mass m walking with a constant tangential velocity v_t on a circular trajectory of radius r. The pedestrian's walking frequency is assumed to be constant: $\dot{\phi}^{dist}(t) = \omega$ and its value is chosen to be: $\omega = 2\pi f = 2\pi\, rd/s$. $\dot{\theta} = \frac{v_t}{r}$ represents the rotational velocity. The pedestrian applies a sinusoidal lateral force on the footbridge given by (see Fig. 1):

$$\underline{F}^{osc}(t) = F^{osc,T} \sin\left(2\phi^{dis}(t)\right)\underline{e}_C^T(t) + F^{osc,N} \sin\left(\phi^{dis}(t)\right)\underline{e}_C^N(t), \qquad (10)$$

and the relative acceleration $\ddot{\underline{u}}^{rel}(t) = -\underline{F}^{osc}(t)/m$ can be easily deduced:

$$\ddot{\underline{u}}^{rel}(t) = -\frac{1}{m}\left[\left(F^{osc,T}\sin\left(2\phi^{dis}(t)\right)\right)\underline{e}_C^T(t) + F^{osc,N}\left(\sin\left(\phi^{dis}(t)\right)\right)\underline{e}_C^N(t)\right] \quad (11)$$

The analytical expression of the velocity is deduced by time-integration of Eq. (11):

$$\dot{\underline{u}}^{rel}(t) = \frac{F^{osc,T}}{2m\omega}\left[\cos\left(2\phi^{dis}(t)\right) - 1\right]\underline{e}_C^T(t) + \frac{F^{osc,N}}{m\omega}\left[\cos\left(\phi^{dis}(t)\right) - 1\right]\underline{e}_C^N(t) \quad (12)$$

The Coriolis acceleration $\ddot{\bar{u}}^{cor}(t) = 2\dot{\theta}\underline{e}_z \wedge \dot{\underline{u}}^{osc}(t)$ is then calculated:

$$\ddot{\underline{u}}^{cor}(t) = \frac{2\dot{\theta}}{m\omega}\left[-F^{osc,N}\left(\cos\phi^{dis} - 1\right)\underline{e}_C^T + \frac{F^{osc,T}}{2}\left(\cos(2\phi^{dis}) - 1\right)\underline{e}_C^N\right] \quad (13)$$

The norm of $\ddot{\underline{u}}^{rel}(t)$ and of $\ddot{\underline{u}}^{cor(t)}$ can be easily deduced:

$$||\ddot{\underline{u}}^{rel}(t)|| = \sqrt{\left[F^{osc,N}\sin\left(\phi^{dis}(t)\right)\right]^2 + \left[F^{osc,T}\sin\left(2\phi^{dis}(t)\right)\right]^2} \quad (14)$$

$$||\ddot{\underline{u}}^{cor}(t)|| = \frac{2v_t}{mr\omega}\sqrt{\left[F^{osc,N}\cos\left(\phi^{dis} - 1\right)\right]^2 + \left[\frac{F^{osc,T}}{2}\cos\left(2\phi^{dis} - 1\right)\right]^2} \quad (15)$$

Upper bounds independent of t can be easily found for each previous norm:

$$\begin{aligned} ||\ddot{\underline{u}}^{cor}|| &\leq B_1 = \frac{2v_t}{mr\omega}\sqrt{\left(F^{osc,N}\right)^2 + \left(\frac{F^{osc,T}}{2}\right)^2} \\ ||\ddot{\underline{u}}^{rel}|| &\leq B_2 = \frac{1}{m}\sqrt{\left(F^{osc,N}\right)^2 + \left(F^{osc,T}\right)^2} \end{aligned} \quad (16)$$

In the numerical application, $m_i = 75\,\text{kg}$, $v_t = 1.34\,\text{m/s}$, $\omega = 2\pi\,\text{rd/s}$, $F^{osc,T} = 120\,\text{N}$ and $F^{osc,N} = 35\,\text{N}$. We study the case when $B_1 \geq B_2$, corresponding to the maximum of $||\ddot{\underline{u}}^{cor}||$ greater than 10 % of the maximum of $||\ddot{\underline{u}}^{rel}||$. This leads to: $r < (22 \cdot v_t)/\omega$ and finally $r < 4.8\,\text{m}$. The horizontal alignment of a footbridge is generally close to that of a straight line. The trajectory of a pedestrian shall admit a generally high radius of curvature and thus the Coriolis acceleration is assumed to be negligible.

Calculating N_c

The 1D Continuous Model (M1)
In the general case, where μ_ω is different from the modal frequency of the system crowd-structure, it has been found in [3] that resolving a third order polynomial gives the value of N_c. By denoting $\Gamma = (N_c G \omega_0 \varepsilon)/(2K)$, this polynomial is:

$$a_3\Gamma^3 + a_2\Gamma^2 + a_1\Gamma + a_0 = 0 \tag{17}$$

where:

$$\begin{aligned} a_0 &= 16\pi^2 C\sigma_\omega^4 \\ a_1 &= 8\pi C\sigma_\omega^2 n\omega_0^2 - \frac{8\pi^3\sigma_\omega^3 nK}{\sqrt{2\pi}} + \frac{4\pi^3 nK}{\sqrt{2\pi}}(\mu_\omega - \omega_0)^2 \\ a_2 &= n^2\omega_0^4 C - \frac{4\pi^2\sigma_\omega n^2\omega_0^2 K}{\sqrt{2\pi}}, \quad a_3 = -\frac{n^3\pi K\omega_0^4}{2\sigma_\omega\sqrt{2\pi}} \end{aligned} \tag{18}$$

The 2D Continuous Model (M2)
Similarly to the continuous model, for the general case ($\mu_\omega \neq \omega_T$), N_c is the solution of the following polynomial [24]:

$$\gamma_6 c_1 N_c^3 + \gamma_5 N_c^3 + \gamma_4 c_1 N_c^2 + \gamma_3 N_c^2 + \gamma_2 c_1 N_c + \gamma_1 N_c + \gamma_0 = 0 \tag{19}$$

where

$$\begin{aligned} \gamma_0 &= -16\sigma_\omega^4 n\bar{m}, \quad \gamma_1 = \frac{8\pi n\sigma_\omega \bar{N}\bar{\omega}\bar{\varepsilon}M}{\sqrt{2\pi}C} - 16\sigma_\omega^4 n\bar{m} \\ \gamma_3 &= -\frac{4n^2\pi\sigma_\omega\bar{N}^2\bar{\varepsilon}^2 M}{\sqrt{2\pi}CK} - \frac{n^2\bar{N}^2\bar{\varepsilon}^2}{K} + \frac{8n^2\pi\sigma_\omega\bar{N}\bar{\omega}\bar{\varepsilon}\bar{m}}{\sqrt{2\pi}C} \\ \gamma_4 &= \frac{4n^2\pi\bar{m}\sigma_\omega\bar{N}\bar{\varepsilon}(2\sigma_\omega^2 - \bar{\omega}^2)}{\sqrt{2\pi K}C}, \quad \gamma_5 = \frac{4n^3\pi\bar{m}\sigma_\omega\bar{N}^2\bar{\varepsilon}^2}{\sqrt{2\pi}CK} \\ \gamma_6 &= \frac{n^3\pi\bar{N}^3\bar{\varepsilon}^3\sqrt{K}}{2\sqrt{2\pi}C\sigma_\omega K^2}, \quad c_1 = \sqrt{M + n\bar{m}N_c} \end{aligned}$$

Notation

A = the displacement amplitude of the footbridge at the steady-state;
$A(t)$ = the amplitude of the displacement of the footbridge;
C = damping of the first lateral mode of the footbridge;
$\bar{F}^{osc,N}$ = the mean of the maximum amplitudes of the normal component of the oscillatory forces generated by the pedestrians;
$F^{y}(t)$ = the lateral modal force generated by the pedestrians;
G = the mean amplitude of the lateral force induced by a pedestrian;
K = stiffness of the first lateral mode of the footbridge;
M = modal generalized mass of the first lateral mode of the footbridge;
$M_p(t)$ = the modal mass of the pedestrians;
N = the total number of pedestrians on the footbridge;
N_c = the critical number;
$U_y(t)$ = lateral modal displacement of the footbridge;
$\ell(x)$ = the footbridge's width at position;
$m_p(t,x)$ = the local mass of pedestrians;
m_{1p} = the average mass of a pedestrian;
$q^{x}_{OC_i}(t)$ = the position of pedestrian i on the footbridge and θ_i is the angle between $(O, \underline{e}_x, \underline{e}_y)$ and $(C_i, \underline{e}^{T}_{C_i}(t), \underline{e}^{N}_{C_i}(t))$;
$\ddot{u}^{cor,y}(t)$ = the Coriolis acceleration;
$\ddot{u}^{ent,y}(t)$ = the acceleration of the non-inertial frame of reference $(C_i, \underline{e}^{T}_{C_i}(t), \underline{e}^{N}_{C_i}(t))$ with respect to $(O, \underline{e}_x, \underline{e}_y)$ that generates a d'Alembert force [18];
$\ddot{u}^{rel,y}_i(t) = \ddot{u}^{osc,y}_i(t) =$ the acceleration with respect to $(C_i, \underline{e}^{T}_{C_i}(t), \underline{e}^{N}_{C_i}(t))$ due to the pedestrian's oscillations about his trajectory resulting from the natural way of walking projected on the y-axis;
$\ddot{u}^{tr,y}_i(t)$ = the part of $\ddot{u}^{ent,y}(t)$ independent from the bridge motion;
$\Psi_s(t)$ = the instantaneous phase of the lateral modal displacement of the footbridge;
ε = quantifies a pedestrian's sensitivity to the bridge's acceleration;
$\bar{\varepsilon}_i$ = quantifies the influence of the bridge's displacement on each pedestrian;
$\eta(x,t)$ = the pedestrians' density at position x and time t;
$\phi^{acc}(x,t)$ = the total phase of the lateral force induced by the pedestrians at position x and time t when they are sensitive to the bridge's acceleration;
$\phi^{dis}_i(t)$ = the phase of the lateral force induced by the ith pedestrian at time t when pedestrians are considered to be sensitive to the bridge's displacement;
ψ_1 = the first lateral modal shape of the footbridge;
$\omega(x)$ = the lateral angular frequency for free walking;
ω_i = the natural frequency of the pedestrian;
ω_{sync} = the frequency of synchronization;
ω_T = the modal frequency of the system crowd-structure

References

1. Abrams DM (2006) Two coupled oscillator models: the Millennium bridge and the Chimera State. PhD thesis, Cornell University
2. Argoul P (2013) Les passerelles. Prise en considération des vibrations sous l'action des piétons. Archéothéma AT26 Les Ponts en France 26:38–43
3. Bodgi J (2008) Synchronisation piétons-structure: applications aux vibrations des passerelles souples. PhD thesis. Ecole Nationale des Ponts et Chaussées
4. Bodgi J (2009) Synchronisation piétons-passerelle: modèle macroscopique et étude analytique. Les 27èmes rencontres de l'AUGC, Saint Malo, France
5. Bodgi J, Erlicher S, Argoul P (2007) Lateral vibration of footbridges under crowd-loading: continuous crowd modeling approach. Key Eng Mater 347:685–690
6. Caetano E, Cunha A, Magalhaes F, Moutinho C (2010) Studies for controlling human-induced vibration of the Pedro E Ines footbridge, Portugal. Part 1: assessment of dynamic behaviour. Eng Struct 32(4):1069–1081
7. Carroll SP, Owen JS, Hussein MFM (2012) Modelling crowdbridge dynamic interaction with a discretely defined crowd. J Sound Vib 331(11):2685–2709
8. Dallard P, Fitzpatrick AJ, Flint A (2001) The Millennium bridge London—problems and solutions. Struct Eng 79(8):15–17
9. Dallard P, Fitzpatrick AJ, Flint A, Le Bourva S, Low A, Ridsdill Smith RM, Willford M (2001) The London Millennium footbridge. Struct Eng 79(22):17–21
10. Dziuba P, Grillaud G, Flamand O, Sanquier S, Tetard Y (2001) La passerelle Solferino: comportement dynamique (Solferino bridge: dynamic behaviour). Bulletin Ouvrages Met 1:34–57
11. Eckhardt B, Ott E, Strogatz SH, Abrams DM, McRobie A (2007) Modeling walker synchronization on the Millennium bridge. Phys Rev E 75(2):021110
12. Erlicher S, Trovato A, Argoul P (2010) Modeling the lateral pedestrian force on a rigid floor by a self-sustained oscillator. Mech Syst Sig Process 24(5):1579–1604
13. Erlicher S, Trovato A, Argoul P (2013) A modified hybrid Van der Pol/Rayleigh model for the lateral pedestrian force on a periodically moving floor. Mech Syst Sig Process 41(1–2):485–501
14. Fujino Y, Pacheco BM, Nakamura S, Warnitchai P (1993) Synchronization of human walking observed during lateral vibration of a congested pedestrian bridge. Earthq Eng Struct Dyn 22(9):741–758
15. Ingolfsson ET (2011) Pedestrian—induced lateral vibrations of footbridges. PhD thesis. Technical University of Denmark
16. Ingolfsson ET, Georgakis CT (2011) A stochastic load model for pedestrian-induced lateral forces on footbridges. Eng Struct 33(12):3454–3470
17. Kumar A, Erlicher S, Argoul P (2015) Phase difference in lateral synchronization of Pedestrian floors using a modified hybrid Van der pol/Rayleigh oscillator. Int J Struct Stab Dyn. doi:10.1142/S021945541550042X
18. Lanczos C (1970) The variational principles of mechanics, 4th edn. University of Toronto Press, Canada
19. Matsumoto Y, Sato S, Nishioka T, Shiojiri H (1972) A study on design of pedestrian overbridges. Trans Jpn Soc Civil Eng 4:50–51
20. Nakamura S, Kawasaki T (2009) A method for predicting the lateral girder response of footbridges induced by pedestrians. J Construct Steel Res 65(8–9):1705–1711
21. Newland DE (2003) Pedestrian excitation of bridges—recent results. In: 10th international congress on sound and vibration
22. Newland DE (2003) Vibration of the London Millennium footbridge: cause and cure. Int J Acoust Vibr 8(1):9–14
23. Pecol P (2011) Modélisation 2D discrète du movement des piétons-Application l'évacuation des structures du génie civil et à l'interaction foule-passerelle. PhD thesis. Université Paris-Est
24. Pecol P, Dal Pont S, Erlicher S, Bodgi J, Argoul P (2011) A 2D discrete model for crowd—structure interaction. In: 4th international conference, footbridge, Wroclaw, Poland

25. Pikowski A, Rosenblum M, Kurths J (2001) Synchronization a universal concept in nonlinear sciences. Cambridge University Press, United Kingdom
26. Roberts TM (2003) Synchronized pedestrian excitation of footbridges. Proc ICE Bridge Eng 156(4):155–160
27. Roberts TM (2005) Lateral pedestrian excitation of footbridges. J Bridge Eng 10(1):107–112
28. Strogatz SH, Abrams DM, McRobie A, Eckhardt B, Ott E (2005) Theoretical mechanics : crowd synchrony on the Millennium bridge. Nature 438(7064):43–44
29. Trovato A, Kumar A, Erlicher S (2014) Stability analysis of entrained solutions of the non-autonomous Modified Hybrid Van der Pol/Rayleigh oscillator: theory and application to pedestrian modeling. Ann Solid Struct Mech 6(1):1–16
30. Venuti F, Bruno L, Bellomo N (2007) Crowd dynamics on a moving platform: mathematical modeling and application to lively footbridges. Math Comput Model 45(3–4):252–269
31. Zivanovic S, Pavic A, Reynolds P (2007) Human-structure dynamic interaction in footbridges. Proc ICE Bridge Eng 158(4):165–177
32. Zivanovic S, Racic V, El-Bahnasy I, Pavic A (2007) Statistical characterization of parameters defining human walking as observed on an indoor passerelle. In: International conference on experimental vibration analysis for civil engineering structures (EVACES)

Computational Modeling of Backward Erosion Piping

Andrea Francesco Rotunno, Carlo Callari and Francesco Froiio

Abstract This work presents a short account of some recent advances in the numerical simulation of backward erosion piping, accomplished in the framework of a collaborative research between Italian and French research groups. After a brief review of the state of the art in engineering practice and research, we outline the key points of a novel approach and show some of the results obtained in an extensive validation work.

1 Introduction

Internal erosion of embankment dams and levees refers to a large class of subtle and harmful hydro-erosion processes amongst the most dreaded for their consequences in terms of damage and failure of hydraulic works [4, 11]. A possible classification of these processes refers to four distinct mechanisms: concentrated leak erosion occurs at the walls of a crack or a pipe within the embankment or its foundation, as a form of tangential erosion due to the inner flow; contact erosion develops at the interface between a coarser and a finer soil, as particles of the latter migrates into the former due to seepage flow parallel to the interface; suffusion is the process of selective erosion of fine particles by the seepage flow through the coarse fraction of a graded soil [10]; backward erosion consists in the detachment of soil particles at an unfiltered exit of the seepage flow, due to drag forces normal to the exit surface.

A.F. Rotunno (✉)
Dipartimento di Ingegneria Civile e Ingegneria Informatica (DICII),
Università degli Studi di Roma "Tor Vergata", via del Politecnico 1,
00133 Roma, Italy
e-mail: a.rotunno@ing.uniroma2.it; andrea-francesco.rotunno@doctorant.ec-lyon.fr

A.F. Rotunno · F. Froiio
École Centrale de Lyon, LTDS, Université de Lyon, 36 av. Guy de Collongue, Lyon, France
e-mail: francesco.froiio@ec-lyon.fr

C. Callari
Università del Molise, via de Sanctis, Campobasso, Italy
e-mail: carlo.callari@unimol.it

M. Frémond et al. (eds.), *Models, Simulation, and Experimental Issues in Structural Mechanics*, Springer Series in Solid and Structural Mechanics 8,
DOI 10.1007/978-3-319-48884-4_12

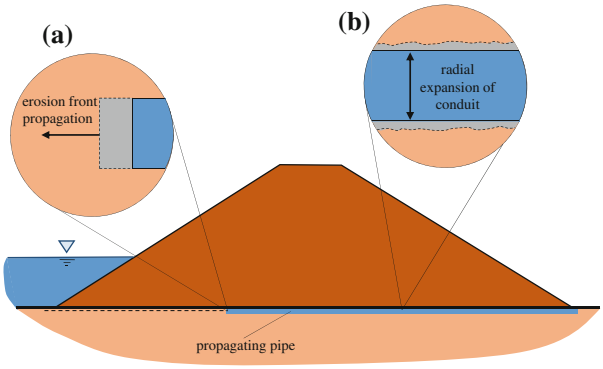

Fig. 1 Schematic representation of backward erosion piping below an embankment foundation

As a complex form of internal erosion involving several of the aforementioned mechanism, backward erosion piping was reported as being responsible for about half of the embankment dam failures accounted for in statistics on large dams [13, 14]. A typical scenario is that of a pipe initiated by backward erosion at the downstream toe of the embankment in the form of a sand boil, though the other erosion mechanisms may contribute or lead the initiation stage. If no adequate filter is present, the initial mechanisms develop into a pipe which evolves, in the progression stage, by the two main and simultaneous processes illustrated schematically in Fig. 1:

(a) *Upstream-oriented propagation of the erosion front*. The pipe works upstream by backward erosion at the inlet section (the erosion front) and propagates through the foundation, the embankment, or both.
(b) *Expansion of the cross-section*. The pipe grows in diameter as its walls are progressively eroded by the inner, turbulent flow. Once a direct hydraulic connection between the pipe and the reservoir is established, the sudden increase of the flow rate accelerates the tangential erosion at the walls, causing uncontrolled enlargement of the conduit.

The failure of the dam, or the levee, may then occur in the form of uncontrolled loss of storage or of a breach due to the collapse of the pipe roof, or even through other mechanisms activated by the piping process (overtopping, slide, etc.).

Internal erosion can be seen as an ageing process and the associated risk is difficult to assess for embankment dams and levees that do not satisfy modern design and construction criteria (e.g., when filters are absent or inadequate). The development ad-hoc modeling tools comes therefore as a priority, on a par with the improvement of monitoring practices, to grant for adequate security standards and enable effective maintenance of hydraulic works at sustainable costs. As to backward erosion piping, the currently-in-use models for engineering practice are still based on empirical or semi-empirical relations, though analytical and numerical models are being proposed (see Sect. 2). Compared to other recent research works focussed on the modeling of either the upstream propagation or (most often) the radial expansion of the pipe, the

original formulation presented herein aims at a unified numerical modeling of both processes. The presentation includes a few, key elements of the numerical model and an example validation on real scale experiments (Sects. 3 and 4, resp.).

2 Backward Erosion Piping

2.1 Engineering Practice

European standards for civil engineering works [6] include general design specifications to prevent the onset of the piping process by means of filters or by structural measures to decrease the hydraulic gradient at candidate onset points (e.g., by increasing the seepage path by means of berms on the downstream side of the embankment, or by impervious screens below its base). Verification against heave is also required, as the latter phenomenon is often found in connection with backward erosion piping.

However, most of existing dams and levees were built at a time when design specifications did not include effective measures against the onset of piping, due to lesser knowledge and feedback on internal erosion phenomena. Hence, the assessment of the safety or of the long-term serviceability of these water retaining structures is based on a judgement on the sensitivity to the hydro-erosion processes likely to initiate piping [12]. Furthermore, especially when there is evidence or suspicion that an erosion pipe is already developing, a model is required, able to assess the likelihood of pipe propagation, considering the hydraulic loading conditions and the characteristics of the embankment-foundation system.

When scaled down to a suitable format for engineering practice, those models are usually reduced to the statement of a critical value of water head expressed as

$$H_{\mathrm{cr}} = \alpha\, L \tag{1}$$

where the non-dimensional coefficient α depends on several factors, including soil properties (granulometry, shear strength, etc.), and L is a representative length of the flow path through the embankment-foundation system. As reported by Terzaghi et al. [28], early empirical rules fitting this format were developed by Bligh [3] and Lane [16] in the first half of last century, based on the so-called "line-of-creep approach", which in turn employs statistical compilations of records of piping failures. More recently, besides the fully empirical approach by Schmertmann [20], Sellmeijer et al. [15, 21, 23] proposed an analytical model focused on the condition of continuing piping erosion, based on almost heuristic assumptions and on a simplified geometry. The model provided an expression for the water head required to sustain the pipe propagation, as a function of the pipe length. Most importantly, a safety criterion in the form (1) was proposed accordingly, as a loss-of-control condition. The original form of Sellmeijer's criterion has been refined based on reduced and full scale tests (see [39] and a more recent attempt in [22]) and is mentioned amongst the reference

methods for the assessment of safety of dams and levees against piping erosion [12, 13].

2.2 Current Research on Piping

In recent years, impulse to the research on backward erosion piping has been given by Dutch experimental programs that have investigated the kinetics of the piping process and the concept of critical head. Among these works there are studies with focus on the impact of the granulometry and relative density of the eroded soil [22, 32, 33], on the role of soil heterogeneity [30, 34], and on the 3D character of the piping process [34, 35]. Of particular importance are those tests performed on full-scale levee models at the IJkdijk facility [22, 31, 32], more than two decades after a previous experimental program at the Deltagoot facility [18]. The goal of this recent set of real-scale experiments was to study the whole process of backward erosion piping in the sandy foundation of a clay levee, from the onset of erosion to the failure of the embankment, and to test some candidate monitoring techniques. Besides research programs in the Netherlands, further experiments on pipe propagation have been carried out on reduced-scale models of different types of water retaining structures [2, 24, 26].

Research with specific focus on the hydro-erosion mechanisms responsible for the upstream-oriented propagation and cross-section expansion of the pipe is also being carried out. More efforts have been put forth, hitherto, on the latter mechanism. In particular, specific experimental protocols have been elaborated by Wan and Fell [36, 37], who developed the so-called hole erosion- and slot erosion tests. Both test procedures enabled the assessment of the approximated linear relation

$$\dot{m}_e = C_e \langle \tau - \tau_c \rangle \tag{2}$$

between the rate of the eroded mass m_e at the wall of the pipe and the "excess" hydraulic shear stress, i.e., the portion of shear stress τ locally exceeding the threshold value τ_c for the onset of tangential erosion (with this excess shear stress expressed by means of the positive-part operator "$\langle \cdot \rangle$" in Eq. 2).

This law for erosion kinetics is also employed in the analytical model developed by Bonelli and Brivois [5], which resulted in a "scaling law" for the time evolution of the cross-section of a cylindrical conduit driving a turbulent flow through a rigid, non-porous, erodible soil. On the same ground, a finite element model for the pipe enlargement mechanism has also been proposed, based on a level-set approach [9]. Further investigations concern the micromechanics of tangential erosion in the hole erosion test and rely on discrete numerical schemes employed for the description of both the solid and fluid phases at the grain scale [17, 25].

In contrast with the number of available studies on the radial expansion problem, only isolated contributions can be acknowledged as regards the front mechanism. A first micromechanical investigation of the front problem has been recently pro-

posed, by discrete numerical modeling with hydro-mechanical coupling. In this study, the arching induced by drag forces and the damage were inferred as the relevant resistance and degradation mechanisms regulating backward erosion at the front [29]. At the macro-scale, a numerical model for the two-dimensional propagation of a pipe with constant cross-section has recently been proposed by Wang et al. [38]. A finite-element formulation able to describe both the 3D propagation and the transverse enlargement of the pipe is proposed in [19]. This method, validated by means of several comparison with available full-scale tests is briefly described in the following section.

3 Main Features of the Proposed Approach

We have recently developed the innovative modeling of both processes characterizing backward erosion piping, namely the upstream-oriented propagation and the expansion of erosion conduits in the embankment-foundation system (see Sect. 1 and Fig. 1). In contrast with [38], our approach is based on a novel 3-D formulation of the equations which govern the localization of erosion in porous media. As schematically illustrated in Fig. 2, we consider the problem of a three-phase porous medium (consisting of water, fluidized solid and solid phases) subjected to erosion localized along a propagating line Γ. We assume that this line coincide with an erosion-induced one-dimensional pipe, where the flow of the mixture of water and fluidized solid concentrates. As a consequence, the mass balance equations for the porous medium and for the pipe read, respectively:

$$\dot{M}_{\mathrm{w}} + \dot{M}_{\mathrm{s}} = -\mathrm{div}\,\mathbf{q}_{\mathrm{w}} - \left(m_{\mathrm{w}}^{\mathrm{fl}} + \sum_{\alpha=\mathrm{w,\,s}} m_{\alpha}^{\mathrm{er}} \right) \delta_{\Gamma} - \sum_{\alpha=\mathrm{w,\,s}} m_{\alpha}^{\mathrm{pr}}\, \delta_{E} \quad \text{in } \Omega \setminus \Gamma \tag{3}$$

$$\frac{\partial Q_{\mathrm{w}}}{\partial s} = m_{\mathrm{w}}^{\mathrm{fl}} + \sum_{\beta=\mathrm{w,\,fs}} m_{\beta}^{\mathrm{pr}}\, \frac{\rho_{\mathrm{w}}}{\rho_{\beta}}\, \delta_{E} \quad \text{in } \Gamma \tag{4}$$

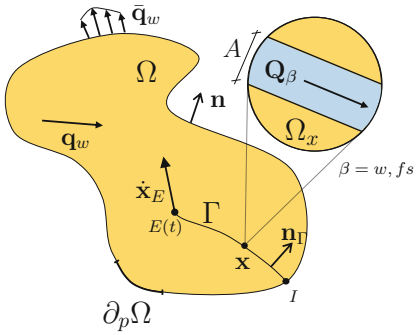

Fig. 2 Schematic representation of a porous solid Ω subjected to localized erosion along a propagating line Γ. A flow conduit of variable area A is located along this line

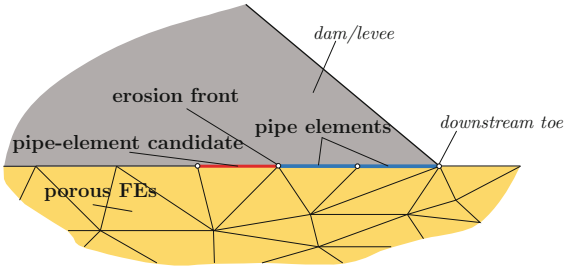

Fig. 3 Example of finite elements arrangement with a-priori known direction of pipe propagation

were M_w and M_s are the fluid and solid mass contents, and $\mathbf{q}_w$ and Q_w are the flows in the porous medium and in the pipe, respectively. The exchange terms m_w^{er}, m_s^{er} are due to the erosion process localized along the erosion line Γ, which leads to pipe enlargement, while m_w^{pr}, m_{fs}^{pr}, m_s^{pr} are a consequence of the propagation of the pipe tip $E(t) \in \Gamma$ (localization along Γ and at E are expressed by the Dirac functions δ_Γ and δ_E, resp.). Furthermore, the exchange term m_w^{fl} is a consequence of the water exchange through the pipe walls, which leads to a discontinuity of Darcy flow in the porous medium, across the erosion line. In the pipe, a turbulent flow is modeled by means of a commonly adopted simplified approach.

The propagation and the enlargement of the pipe are governed by kinetic laws of the kind (2), which model the two erosion processes induced by the Darcy flow normal to the pipe front [40] and by the turbulent flow tangential to the conduit walls [5], respectively. In particular, we assume the propagation as driven by the attainment of a critical porosity at the erosion front $E(t)$. Such critical value characterizes the localized fluidization of the porous medium.

The finite element methods presented in [1, 7] have been extended by integration of the equations governing the problem illustrated above. So far we have considered the very frequent cases in which the most likely orientation of the pipe is known a priori (Fig. 3). As a consequence, the balance equations (3) and (4) are separately integrated on multidimensional and one-dimensional elements, respectively. Furthermore, the aforementioned erosion front propagation is numerically evaluated in a "pipe-candidate" element, which is located upstream of the pipe tip $E(t)$.

We refer to [19] for further details on the governing equations and the proposed computational method.

4 Numerical Example

The computational approach summarized above has been implemented in the general purpose finite element code FEAP [27]. Linear shape functions for pore pressures have been used for both of the elements employed to model the pipe and the porous medium, respectively.

Fig. 4 Levee construction in the IJkdijk large-scale test #2 [32]

As an application example we present the simulation of the IJkdijk full-scale test #2 [22, 31, 32]. Main goal of this test was the experimental investigation of the pipe initiation at the downstream levee toe and of its propagation below the levee foundation up to the embankment failure. To this purpose, as shown in Fig. 4, a test basin was excavated and lined with an impervious facing. The basin was filled with a 3 m thick layer of saturated and compacted sand which served as foundation for the clay levee, whose height and base length were 3.5 and 15 m, respectively. Several pore-pressure gauges were placed at the embankment-foundation interface. The reservoir was gradually filled and the levee collapsed after 143 h.

To simulate this test, we consider the geometry and the boundary conditions on pore pressures and fluid flow illustrated in Fig. 5. In view of the large permeability difference with respect to the sand layer, the clay embankment is treated as impervious. Plane flow conditions are assumed herein. A full, 3-D simulation of this test is presented in [19].

In Fig. 6, our numerical results are presented in terms of pipe front propagation. It can be observed an increasing propagation speed, consistent with an indirect evaluation of the position of the front performed in [22] on the basis of pore pressure measurements.

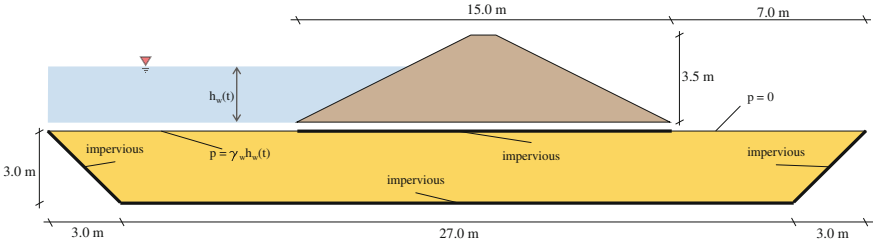

Fig. 5 Simulation domain and boundary conditions for the IJkdijk large-scale test #2

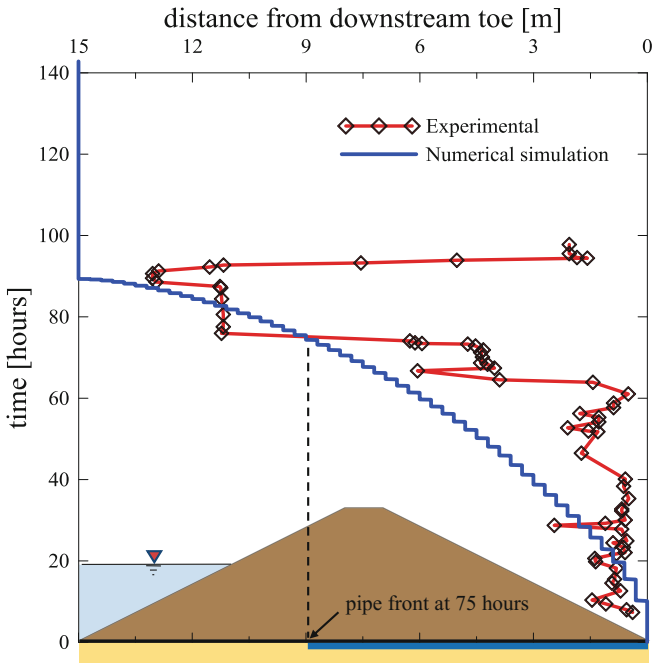

Fig. 6 Calculated propagation of erosion front and indirect evaluation of the front position on the basis of pore pressure measurements [22]

We refer to [19] for several other numerical simulations of available real-scale tests, employed to validate the proposed computational method. Such validation is performed not only in terms of comparisons with the visual detection of the pipe front propagation but also with measurements of the downstream outflows.

5 Concluding Remarks

We have presented the main features of a novel computational method for the simulation of backward erosion piping [19]. In order to position our approach, the state of the art in engineering practice and the recent research in the field has been briefly reviewed. We have outlined the main equations governing the problem at hand, and the simulation of a known real scale test has been presented to illustrate the capability of the proposed method to simulate the piping process.

Acknowledgements The research was financially supported by GIS VOR 2012, LTDS 2012 and PRIN 2010–2011 projects as well as by two PhD and a VINCI mobility fellowships. The research has benefited from several invitations of C. Callari at ECL.

References

1. Abati A, Callari C (2014) Finite element formulation of unilateral boundary conditions for unsaturated flow in porous continua. Water Res Res 50(6):5114–5130
2. Achmus M, Mansour B (2006) Considerations and model tests on the design of river barrages with respect to piping. In: Proceedings of the third international conference on scour and erosion. Amsterdam, The Netherlands
3. Bligh W (1910) Dams, barrages and weirs on porous foundations. Eng News 64(26):708–710
4. Bonelli S (ed) (2012) Erosion of geomaterials. Wiley-ISTE, London, Hoboken
5. Bonelli S, Brivois O (2008) The scaling law in the hole erosion test with a constant pressure drop. Int J Numer Anal Methods Geomech 32(13):1573–1595
6. British Standards Institution (2004) Eurocode 7: geotechnical design—part 1: general rules (BS EN 1997–1:2004). British standards, BSI
7. Callari C, Abati A (2009) Finite element methods for unsaturated porous solids and their application to dam engineering problems. Comput Struct 87:485–501
8. Cheng L, Draper S, An H (eds) (2014) Scour and erosion: proceedings of the 7th international conference on scour and erosion. Perth, Australia
9. Cottereau R, Díez P, Huerta A (2010) Modeling, with a unified level-set representation, of the expansion of a hollow in the ground under different physical phenomena. Comput Mech 46(2):315–327
10. Federico F, Montanaro A (2012) Granulometric stability of moraine embankment dam materials. Int Water Power Dam Construct 64(2):32–36
11. Fell R, Fry J-J (eds) (2007) Internal erosion of dams and their foundations. EDF, IREX, Taylor and Francis/Balkema, Leiden, The Netherlands
12. Fell R, Wan CF, Foster MA (2007) Assessment of the likelihood of initiation of erosion in embankment dams. In: Internal erosion of dams and their foundations, pp 71–102
13. Fell R, MacGregor P, Stapledon D, Bell G, Foster M (2014) Geotech engineering of dams. CRC Press/Balkema, Leiden
14. Foster M, Fell R, Spannagle M (2000) The statistics of embankment dam failures and accidents. Can Geotech J 37(5):1000–1024
15. Koenders MA, Sellmeijer JB (1992) Mathematical model for piping. J Geotech Eng 118(6):943–946
16. Lane E (1935) Security from under-seepage-masonry dams on earth foundations. Trans Am Soc Civil Eng 100(1):1235–1272
17. Lominé F, Scholtès L, Sibille L, Poullain P (2013) Modeling of fluid-solid interaction in granular media with coupled lattice Boltzmann/discrete element methods: application to piping erosion. Int J Numeric Anal Methods Geomech 37(6):577–596
18. de Rijke W (1991) Verificatie piping model: proven in de deltagoot. Technical Report H1202, Deltares (WL), Delft, The Netherlands
19. Rotunno AF, Callari C, Froiio F (2017) A finite element method for localized erosion in porous media with applications to backward piping in levees. In preparation
20. Schmertmann JH (2000) The no-filter factor of safety against piping through sands. The heritage and future of the geotechnical engineering profession, ASCE, judgment and innovation
21. Sellmeijer JB, Koenders MA (1991) A mathematical model for piping. Appl Math Model 15(11):646–651
22. Sellmeijer H, De la Cruz JL, van Beek VM, Knoeff H (2011) Fine-tuning of the backward erosion piping model through small-scale, medium-scale and IJ experiments. Eur J Environ Civil Eng 15(82):1139–1154
23. Sellmeyer JB (1988) On the mechanism of piping under impervious structures. Technische Universiteit, Delft
24. Sharif Y, Elkholy M, Hanif Chaudhry M, Imran J (2015) Experimental study on the piping erosion process in earthen embankments. J Hydraul Eng 141(7):04015012
25. Sibille L, Lominé F, Poullain P, Sail Y, Marot D (2015) Internal erosion in granular media: direct numerical simulations and energy interpretation. Hydrol Proces 29(9):2149–2163

26. Tanaka T, Nagai S, Doi H, Hirose T (2014) Experimental findings regarding piping failure of embankments. In: Scour and erosion: proceedings of the 7th international conference on scour and erosion, pp 87–93
27. Taylor R (2008) FEAP—a finite element analysis program: version 8.2
28. Terzaghi K, Peck R, Mesri G (1996) Soil mechanics in engineering practice. Wiley, New York
29. Tran DK, Prime N, Froiio F, Callari C, Vincens E (2016) Numerical modeling of backward front propagation in piping erosion by DEM-LBM coupling. Eur J Environ Civil Eng, http://dx.doi.org/10.1080/19648189.2016.1248794
30. van Beek VM, Koelewijn AR, Kruse GAM, Sellmeijer JB, Barends FBJ (2008) Piping phenomena in heterogeneous sands: experiment and simulations. In: Proceedings of the 4th international conference on scour and erosion. Tokyo, Japan
31. van Beek VM, De Bruijn H, Knoeff J, Bezuijen A, Forster U (2011a) Levee failure due to piping: a full-scale experiment. In: Burns SE, Bhatia SK, Avila CM, Hunt BE (eds) Scour and erosion: proceedings of the fifth international conference on scour and erosion. San Francisco, California, USA
32. van Beek VM, Knoeff H, Sellmeijer H (2011b) Observations on the process of backward erosion piping in small-, medium- and full-scale experiments. Eur J Environ Civil Eng 15(8):1115–1137
33. van Beek VM, Yao Q, Van M, Barends F (2012) Validation of sellmeijer model for backward piping under dikes on multiple sand layers. In: Proceedings of the 6th international conference on scour and erosion. Paris, France
34. van Beek VM, van Essen HM, Vandenboer K, Bezuijen A (2015) Developments in modelling of backward erosion piping. Géotechnique 65(9):740–754
35. Vandenboer K, Bezuijen A, van Beek VM (2014) 3d character of backward erosion piping: small-scale experiments. In: Scour and erosion: proceedings of the 7th international conference on scour and erosion, pp 81–86
36. Wan C, Fell R (2004a) Investigation of rate of erosion of soils in embankment dams. J Geotech Geoenviron Eng 130(4):373–380
37. Wan C, Fell R (2004b) Laboratory tests on the rate of piping erosion of soils in embankment dams. Geotech Testing J 27(3):295–303
38. Wang D, Fu X, Jie Y, Dong W, Hu D (2014) Simulation of pipe progression in a levee foundation with coupled seepage and pipe flow domains. Soils Found 54(5):974–984
39. Weijers JBA, Sellmeijer JB (1993) A new model to deal with the piping mechanism. In: Brauns J, Herbaum M, Schuler U (eds) Filters in geotechnical and hydraulic engineering. Balkema, Rotterdam, pp 1–23
40. Zhang X, Wong H, Leo C, Bui T (2013) A thermodynamics-based model on the internal erosion of earth structures. Geotech Geol Eng 31(2):479–492

Experimental Analysis of a Tuned Mass Damper with Eddy Currents Damping Effect

Stefania Lo Feudo, Anissa Allani, Gwendal Cumunel, Pierre Argoul, Franco Maceri and Domenico Bruno

Abstract A Tuned Mass Damper (TMD) is a structural passive control device fixed on a structure and composed of a linear oscillator which natural frequency is tuned to that of the structure, or to the dominant resonance frequency. In this paper, an experimental TMD with adjustable stiffness and eddy current damping is proposed. The first step is to check if the dynamical properties of the proposed TMD are constant during the dynamic test and for different values of stiffness and damping. Therefore, the instantaneous modal parameters are evaluated by applying the continuous wavelet transform on the experimental data. Then, the TMD is set with optimal parameters and used to control vibrations of a frame scale model. The structure response with and without the TMD is evaluated from the experimental measurements in case of a shock applied to the top floor.

S. Lo Feudo (✉)
Université Paris-Saclay, ENSTA ParisTech, IMSIA, CNRS, EDF, CEA,
828 bd. de Maréchaux, 91120 Palaiseau, France
e-mail: stefania.lofeudo@unical.it

A. Allani · G. Cumunel
Université Paris-Est, Laboratoire Navier (UMR 8205), CNRS, ENPC, IFSTTAR,
6-8 Avenue Blaise Pascal, 77455 Champs-sur-Marne, France
e-mail: anissa.allani@enpc.fr

G. Cumunel
e-mail: gwendal.cumunel@enpc.fr

P. Argoul
Université Paris Est, IFSTTAR, MAST, SDOA, 14-20 bd. Newton,
77455 Marne-la-Vallée, France
e-mail: pierre.argoul@ifsttar.fr

F. Maceri
Dipartimento di Ingegneria Civile e Ingegneria Informatica (DICII), Università degli Studi di Roma "Tor Vergata", via del Politecnico 1, 00133 Roma, Italy
e-mail: franco.maceri@uniroma2.it

D. Bruno
Dipartimento di Ingegneria Civile, Università della Calabria, Via P. Bucci,
87036 Rende (CS), Italy
e-mail: d.bruno@unical.it

M. Frémond et al. (eds.), *Models, Simulation, and Experimental Issues in Structural Mechanics*, Springer Series in Solid and Structural Mechanics 8,
DOI 10.1007/978-3-319-48884-4_13

1 Introduction

Civil engineering structures can often be subjected to vibrations due to harmonic loads, wind, and ground motions, which may affect the structural comfort and safety. Therefore, in order to reduce vibrations, several control devices were studied and designed in last decades, including Tuned Mass Dampers (TMD). In particular, the TMD, which is constituted in its simplest form by a mass-spring-dashpot system, belongs to the class of passive control devices. Indeed, the TMD may be tuned to a specific mode shape of the main structure, so that in case of vibration an energy transfer activates and a dissipation mechanism appears. First studies were conducted in [6, 8] and some TMD applications in tall buildings or bridges are depicted in [15, 25].

In order to improve the TMD performance, several parameters optimization criteria have been proposed in the literature, mostly dealing with the minimization of the transfer function maximum or energy, and with the pole locations. An optimization criteria class deals with the minimization of the amplitude of the maximum peak of the frequency response, which is commonly called H_∞-norm optimization (for analytic and numerical studies see for instance [6, 21]), whereas another class concerns the reduction of the vibration energy of the system and is referred to as H_2-norm optimization (related studies are [3, 13, 27]). On the other hand, a different procedure based on the position of the system poles was proposed by [9]. The criterion roughly consists in maximizing the modal damping ratio by matching the pairs of the conjugate poles, as done in [16, 23].

However, the performance of the TMD largely depends on the frequency content of the external excitation. Indeed, by looking at the Frequency Response Function (FRF), when a Single Degree-of-Freedom (SDoF) system has to be controlled, it is possible to evidence a bandwidth representing the operating range of the TMD, where the device has positive effects on the structural performance in terms of dynamic amplification. Beyond this range, the TMD may be even harmful for the structure. Therefore, in the past decades, several studies were conducted on TMD applied on structures subjected to harmonic and random excitation, [3], and seismic loading, which efficiency is source of debate [5, 14, 18, 22, 23].

In this study, an innovative experimental TMD, proposed by authors in [19], is further analyzed in order to control vibration of a frame scale model. The TMD, located at the top floor of the structure, has adjustable stiffness and damping, in order to easily obtain the parameters resulting from a numerical optimization.

Eddy currents effect is used to obtain the TMD damping. Indeed, the TMD mass is made of a conductive material, and a permanent magnet is placed above at a certain distance which can be settled. When the TMD oscillates, the mass is subjected to a time-varying magnetic field [12] and eddy currents appear into the conductor generating another magnetic field. A Lorentz force arises but, owing to the conductor resistance, energy is dissipated into heat and vibrations are reduced. The eddy currents damping effect is already adopted in several engineering and mechanical fields,

such as in braking systems, vibration insulation in levitation systems, and structural vibration cancellation [4, 7, 24, 26].

This paper is organized as follows. In the first section, the governing equations in case of a TMD located on a Multiple Degree-of-Freedom (MDoF) structure are presented. The optimization criterion used to determine the parameters of the TMD is introduced in the following section. Then, the eddy currents are briefly introduced and the proposed experimental setup is described. Finally, the efficiency of the TMD for structural vibration passive control of a frame scale model, in the case of its after shock responses is presented, and some concluding remarks are given.

2 TMD Governing Equation

The equations of motion for the N-DoF primary structure, which floors are infinitely stiffs and their masses are concentrated, and for the TMD are given, respectively, by

$$\begin{cases} M_p\ddot{x}_p(t) + C_p\dot{x}_p(t) + K_p x_p(t) = f(t) + f_{TMD}(t) \\ \ddot{x}_d(t) + 2\xi_d\omega_d(\dot{x}_d - \dot{x}_N) + \omega_d^2(x_d - x_N) = 0 \end{cases} \tag{1}$$

where

$$M_p = \begin{bmatrix} M_1 & 0 & \cdots & 0 \\ 0 & M_2 & \cdots & 0 \\ \vdots & \vdots & \ddots & \vdots \\ 0 & 0 & \cdots & M_N \end{bmatrix},$$

$$C_p = \begin{bmatrix} C_1 + C_2 & -C_2 & \cdots & 0 \\ -C_2 & C_2 + C_3 & \ddots & 0 \\ \vdots & \ddots & \ddots & -C_N \\ 0 & 0 & -C_N & C_N \end{bmatrix} \quad K_p = \begin{bmatrix} K_1 + K_2 & -K_2 & \cdots & 0 \\ -K_2 & K_2 + K_3 & \ddots & 0 \\ \vdots & \ddots & \ddots & -K_N \\ 0 & 0 & -K_N & K_N \end{bmatrix}$$

and $x_p = [x_1, x_2, \ldots, x_N]$, ω_d and ξ_d being the angular eigenfrequency and the modal damping ratio of the TMD, respectively, that is $\omega_d = \sqrt{k_d/m_d}$ and $\xi_d = c_d/(2m_d\omega_d)$ where m_d, c_d, and k_d are the TMD's mass, damping and stiffness, respectively. The vector $f_{TMD} = [0, \ldots, 0, c_d(\dot{x}_d - \dot{x}_N) + k_d(x_d - x_N)]^T$ is the force exerted on the primary structure by the TMD. x_N denotes the displacement of the Nth floor primary structure.

Thus, the matrix form of the equations of motion for the global system (N-storey primary structure plus TMD) can be written as

$$\tilde{M}\ddot{\tilde{x}}(t) + \tilde{C}\dot{\tilde{x}}(t) + \tilde{K}\tilde{x}(t) = \tilde{f}(t) \tag{2}$$

where $\tilde{M}, \tilde{C}$, and $\tilde{K}$ are respectively $(N+1) \times (N+1)$ mass, damping, and stiffness matrices of the combined system. $\tilde{x}(t) = \left[x_p \ , \ x_d\right]$ is the displacement vector. x_p and x_d denote the displacements of the primary structure and the TMD. $\tilde{f}(t) = [f(t)\ 0]^T$ is the vector of external forces with $f(t)$ the external excitation applied on the primary structure (vector of dimension $1 \times$ N).

3 Parameters Optimization

The TMD's performance and robustness depend highly on its dynamic properties. Therefore, to properly estimate the value of TMD parameters, several optimization criteria were proposed in the literature [3, 6, 9, 16, 21, 23]. The criterion to adopt is one of the most important design decisions, which can depend on several factors, as the nature of the external excitation, the type of the structure, the technical and economic feasibility, etc. In particular, the optimization criterion chosen in this study belongs to the class of the L_2-norm optimization criteria, which aims to reduce the vibrational energy of the system due to an external excitation. Such a criterion was proved to be quite efficient and robust [1], and in general leads to lower damping ratio values, that is preferable from a practical point of view. The L_2-norm optimization criterion consists in minimizing a cost function which depends on the Frequency Response Function (FRF), i.e. the transfer function for a N-DoF system. In this study, the L_2-norm, defined in Eq. (3) is evaluated within an angular frequency range of interest, $[\omega_{ini}, \omega_{end}]$, according to [1]:

$$C_2(k_d, c_d) = \frac{\left\| \frac{\hat{x}_N}{\hat{f}} \right\|_2}{\left\| \frac{\hat{x}_{0N}}{\hat{f}} \right\|_2} = \frac{\sqrt{\int_{\omega_{ini}}^{\omega_{end}} \left| \frac{\hat{x}_N}{\hat{f}}(\omega) \right|^2 \mathrm{d}\omega}}{\sqrt{\int_{\omega_{ini}}^{\omega_{end}} \left| \frac{\hat{x}_{0N}}{\hat{f}}(\omega) \right|^2 \mathrm{d}\omega}} \tag{3}$$

where $\hat{x}(\omega) = \int_{-\infty}^{+\infty} x(t) \exp(-i\omega t) \mathrm{d}t$ is the Fourier transform for a time signal $x(t)$, $\left| \frac{\hat{x}_N}{\hat{f}}(\omega) \right|$, $\left| \frac{\hat{x}_{0N}}{\hat{f}}(\omega) \right|$ are the moduli of the transfer functions, respectively, and are referred to a force acting on the top floor. In particular, the expressions with the subscript 0 are evaluated without the TMD on the structure. Therefore, for a non-controlled structure, the criterion is equal to one. Hence, by considering a constant mass m_d for the TMD for practical issues, the design parameters to choose are the TMD stiffness and damping coefficient, respectively k_d and c_d, which minimize the cost function C_2.

4 Eddy Currents Damping

Eddy currents are induced in non-magnetic conductive materials when subjected to time varying magnetic fields. In this study, a permanent magnet is considered and a conductive mass oscillates through the magnetic field.

According to [4], by neglecting the surface charge of the conductor, eddy currents density may be expressed as:

$$\vec{J} = \sigma(\vec{v} \times \vec{B}), \tag{4}$$

where σ is the electrical conductivity of the material, $\vec{v}$ is the relative velocity between the magnet and the conductor, and $\vec{B}$ is the magnetic flux density. The cross product $\vec{v} \times \vec{B}$ is the eddy currents electromotive force, which opposes the rate of change with respect to time of the magnetic flux. By virtue of the Lorentz's Law, if the velocity vector has non-zero component in the x-direction (vector $\vec{i}$), the electromotive force is given by:

$$\vec{F} = \int_V (\vec{J} \times \vec{B}) dV = \sigma v_x \int_V [(-B_y^2 - B_z^2)\vec{i} + B_x B_y \vec{j} + B_x B_z \vec{k}] dV, \tag{5}$$

where V is the volume of the conductor.

Therefore, as stated also by [26], the B_x component of the magnetic field has no influence on the electromagnetic force evaluated in the x-direction. Consequently, the damping force in the x-direction is proportional to the velocity vector with opposite direction and the following quantity may be seen as the linear viscous damping coefficient of the TMD:

$$c_d = \sigma \int_V (B_y^2 + B_z^2) dV. \tag{6}$$

5 Experimental Setup

In this section, the experimental setup, consisting of a TMD with adjustable properties (stiffness and damping) located at the top floor of a three stories frame scale model, is described (see Fig. 1). First, after-shock vibrations of the TMD, by fixing the principal structure and so preventing its oscillations, are examined in order to evaluate the properties of the TMD, itself. Then, the principal structure is presented and the value of its modal parameters is estimated for the three first modes.

After shock vibrations are measured by accelerometers located on the TMD and on each structure's floor. In particular, data acquisition is obtained with LabVIEW, whereas signal processing and further calculations are carried out with MATLAB.

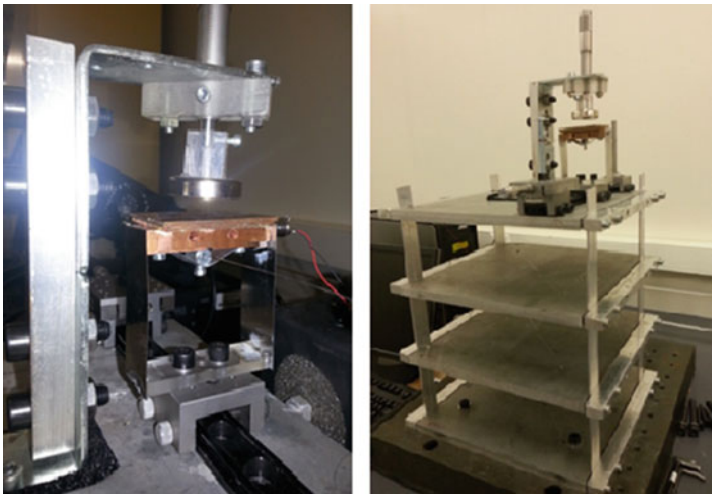

Fig. 1 Experimental Tuned Mass Damper and frame scale model

In particular, mode shapes, modal pseudo frequencies and modal damping ratio are evaluated by means of Continuous Wavelet Transform (CWT), for further details on the modal extraction method please see [17].

5.1 Tuned Mass Damper

The current experimental TMD (see Fig. 1) is made up of a copper mass, weighing 0.15 kg, two thin sheets of spring steel acting as TMD spring, and a slender steel cable. The cable passes through an hollow cylinder fixed on the bottom of the mass so that the more the cable is tensioned, the more the TMD stiffness is high. Indeed, the TMD oscillates transversely with respect to the cable axis, which behaves as two springs connected to the mass. In addition, a permanent magnet is located up to the conductive mass. In this way, eddy currents are induced in the mass owing to the TMD oscillations through the magnetic field, and a damping effect is obtained as described in Sect. 4.

An important feature of the proposed TMD is the ability to easily settle its natural frequency and damping by modifying its configuration. The slender cable is fixed at its extremities and one of the supports can be shifted. The stretching level of the cable can be adjusted and thus the TMD frequency. The moving support can go over a range of 0.4 mm, which will be hereafter denoted as D_1, with a step size of 0.04 mm. The distance between the permanent magnet and the copper mass can also be adjusted, so that the TMD damping can be increased by reducing the vertical gap. In the experiments, the gap is from 3.35 to 5.35 mm, which will be denoted as D_2,

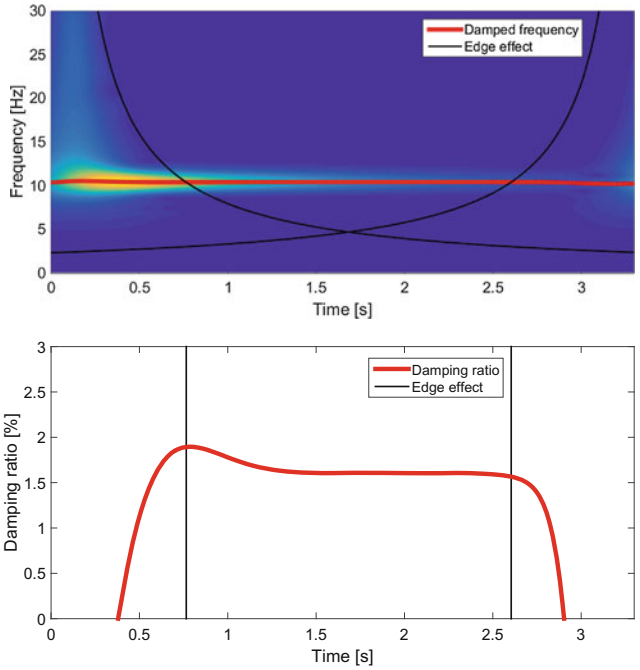

Fig. 2 TMD instantaneous values of pseudo frequency f_d and damping ratio ξ_d for $D_1 = 0.24$ mm and $D_2 = 5.15$ mm

with a step size of 0.2 mm. Therefore a set of 121 TMD configurations have been determined corresponding to a set of 11×11 (D_1, D_2) pairs. Moreover in order to evaluate the TMD properties related to each adjustment of D_1 and D_2, three free response tests have been carried out for each TMD configuration.

In Fig. 2, for given D_1 and D_2 values, results obtained by applying the CWT on the free response signals of the accelerometer located on the TMD are depicted. The instantaneous TMD frequency and damping ratio are evaluated within a domain selected in order to neglect edge effects according to [17]. One advantage of this technique is the possibility to check the linearity or not of the TMD's behavior during the test. As a result, the instantaneous TMD frequency appears to be constant during the dynamic test, whereas the instantaneous damping ratio exhibits a slight non-linearity depending on the intensity of the applied shock as shown in Fig. 2.

Then, the pseudo-frequency $f_d = \omega_d/(2\pi)\sqrt{1-\xi_d^2}$ and damping ratio ξ_d obtained for all TMD configurations in the $(D_1\ ,\ D_2)$ plane are illustrated in Fig. 3. In particular, the values are obtained by averaging the properties over the time and over the three tests carried out for each configuration. Results show that the TMD stiffness depends linearly with the tensile stress of the cable, whereas it is unaffected by the permanent magnet position. On the other hand, the damping ratio increases when the distance between the magnet and the copper mass is reduced (further results may

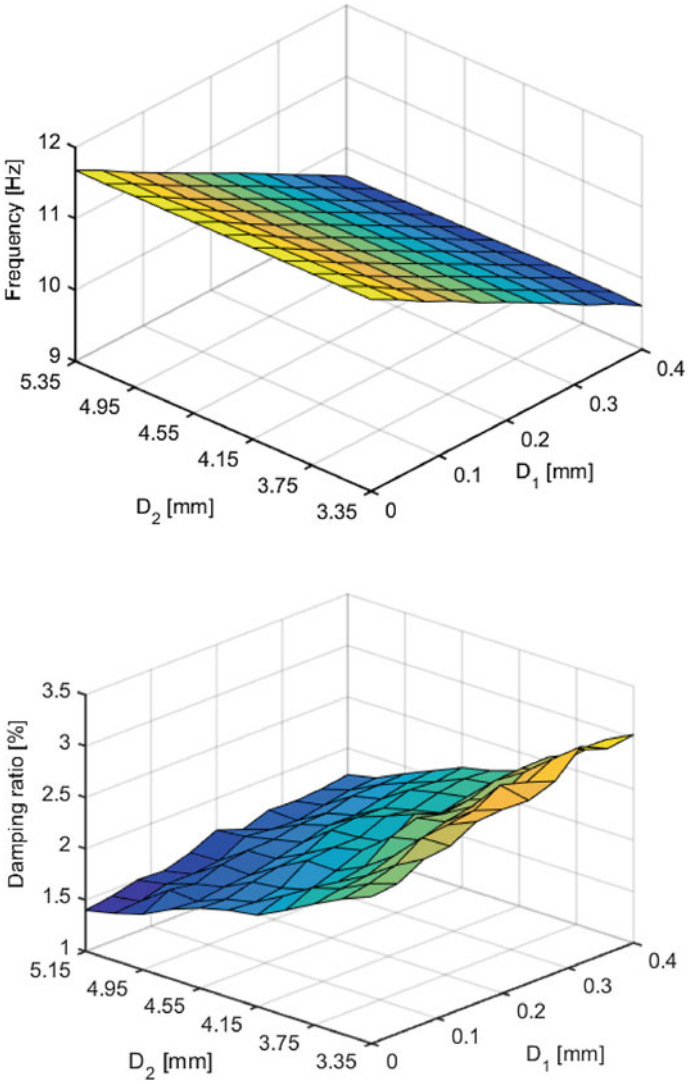

Fig. 3 Evolution of the TMD parameters by moving the cable support (D_1) and the permanent magnet (D_2) position

be found in [19]). However, due to the more important dispersion in obtaining the damping ratio value, the dependency type of this factor regarding the parameters D_1 and D_2 is difficult to determine.

Table 1 Modal frequencies of the frame scale model

Mode	f_{exp} (Hz)	f_{num} (Hz)	MAC (%)	NMD
1	10.77	10.77	99.98	0.0152
2	31.72	31.84	99.93	0.0273
3	48.39	48.04	98.83	0.1087

5.2 *Frame Scale Model*

The frame scale model is composed of four aluminum plates, one fixed to the base and the others supported by four thin aluminum beams placed on two opposite sides of the plates. The weight of the plates is 3.76, 2.43 and 2.43 kg from the top to the bottom. It can be noted that the top floor hosts the permanent magnet and the cable supports, which are included in the mass of the main structure.

The free responses of the three stories have been measured by accelerometers after applying a shock at the top floor without the TMD on the structure. The modal extraction method using CWT has been adopted to evaluate instantaneous values of frequencies and mode shapes. Then, in order to implement a numerical model useful to carry out the TMD optimization procedure, the Modal Assurance Criterion (MAC) was adopted [2, 10]. Indeed, MAC allows computation of numerical stiffness and damping coefficients by minimizing an objective function, J_{obj}, which is defined according to [11] as follows:

$$J_{obj} = \frac{1}{n}\sum_{i=1}^{n}\left[\left|\frac{f_{exp,i} - f_{num,i}}{f_{exp,i}}\right| + NMD_i\right] \tag{7}$$

where

$$MAC_i = \frac{(\phi_{num,i}^T \phi_{exp,i})^2}{(\phi_{num,i}^T \phi_{num,i})(\phi_{exp,i}^T \phi_{exp,i})}, \quad NMD_i = \sqrt{\frac{1 - MAC_i}{MAC_i}} \tag{8}$$

wherein NMD denotes the Normalized Modal Difference [20] and the modal frequencies and mode shapes are denoted as $(f_{exp,i},\ \phi_{exp,i})$ and $(f_{num,i},\ \phi_{num,i})$ in the experimental and in the numerical case, respectively, for the i-th mode. Results are presented in Table 1.

6 Vibration Control

The TMD is placed on the top of the three stories frame structure, and the free vibrations of the frame scale model are recorded and analyzed when an impact force is applied on the top floor of the structure. In particular, the structural response is compared without TMD and when the TMD is on the structure with optimal parameters.

The "experimental" criterion is based on the L_2-norm and on Eq. (3), with $N = 3$. The optimization criterion is evaluated within three frequency intervals around the pseudo angular frequencies of the main structure ($\omega_1, \omega_2, \omega_3$), in order to eliminate the disturbance of spurious peaks due to the table and the magnet support, and it is given by:

$$\tilde{C}_2(D_1, D_2) = \frac{\sqrt{\int_{\omega_1-\Delta\omega_1}^{\omega_1+\Delta\omega_1} \left|\frac{\hat{x}_3}{\hat{f}}(\omega)\right|^2 \mathrm{d}\omega}}{\sqrt{\int_{\omega_1-\Delta\omega_1}^{\omega_1+\Delta\omega_1} \left|\frac{\hat{x}_{03}}{\hat{f}}(\omega)\right|^2 \mathrm{d}\omega}} + \frac{\sqrt{\int_{\omega_2-\Delta\omega_2}^{\omega_2+\Delta\omega_2} \left|\frac{\hat{x}_3}{\hat{f}}(\omega)\right|^2 \mathrm{d}\omega}}{\sqrt{\int_{\omega_2-\Delta\omega_2}^{\omega_2+\Delta\omega_2} \left|\frac{\hat{x}_{03}}{\hat{f}}(\omega)\right|^2 \mathrm{d}\omega}} + \frac{\sqrt{\int_{\omega_3-\Delta\omega_3}^{\omega_3+\Delta\omega_3} \left|\frac{\hat{x}_3}{\hat{f}}(\omega)\right|^2 \mathrm{d}\omega}}{\sqrt{\int_{\omega_3-\Delta\omega_3}^{\omega_3+\Delta\omega_3} \left|\frac{\hat{x}_{03}}{\hat{f}}(\omega)\right|^2 \mathrm{d}\omega}} \tag{9}$$

where $\Delta\omega_1$, $\Delta\omega_2$, and $\Delta\omega_3$ are positive frequency deviations centered around each resonance angular frequency, ω_1, ω_2, and ω_3, respectively. The FRF curves for the third floor (with and without TMD) allow us to calculate the values of the criterion $\tilde{C}_2$ depending on the stretching of the cable (D_1) and the magnet position (D_2). The experimental results obtained for the criterion are plotted on Fig. 4. Figures 5 and 6 depict time signals and FRF of the third floor obtained without TMD and with TMD for $\tilde{C}_2$ maximum and minimum values, respectively. In order to compare them, the time signals obtained with and without TMD are normalized by the maximum value of the associated force signals.

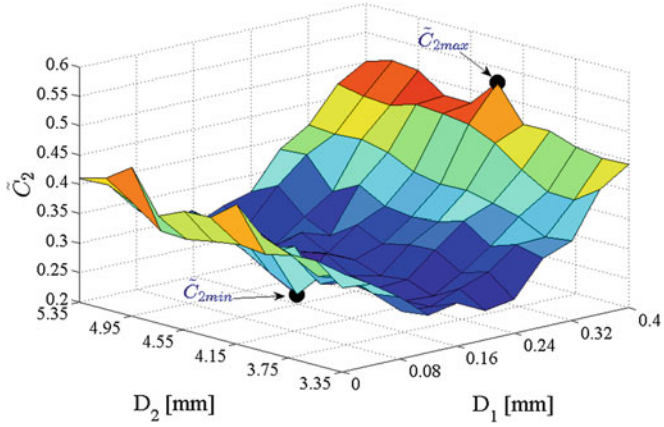

Fig. 4 Optimization criterion values obtained with the experimental TMD for different values of D_1 and D_2, corresponding to stiffness and damping variations, respectively

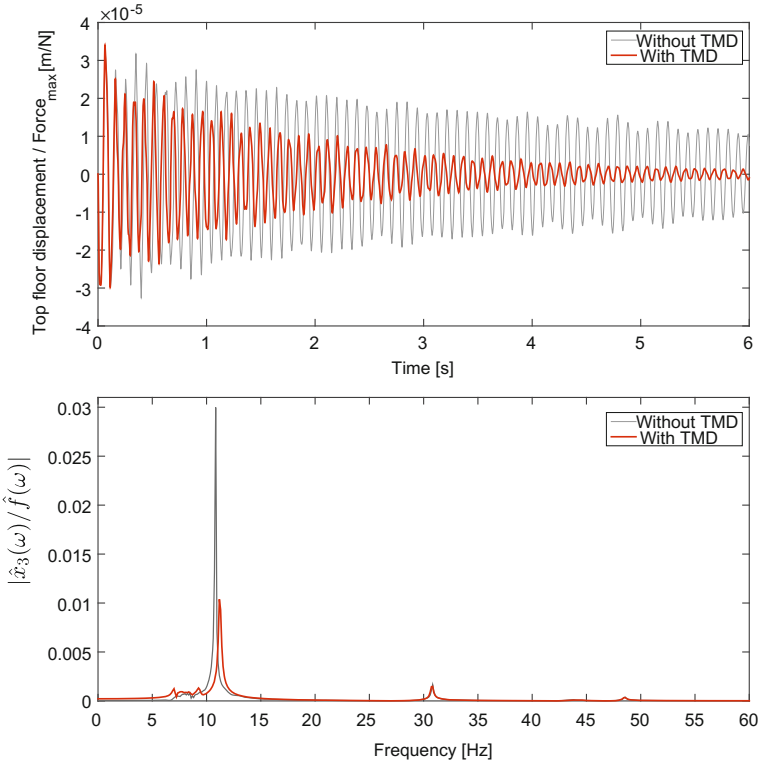

Fig. 5 Experimental time signals and FRF for TMD sets with the $\tilde{C}_2$ maximum values ($D_1 =$ 0.4 mm and $D_2 = 4.35$ mm, corresponding to $f_d = 9.62$ Hz and $\xi_d = 2.23\,\%$)

The combination of damped frequency and damping ratio (f_d,ξ_d) corresponding to the minimum of $\tilde{C}_2$ criterion (f_d=11.04 Hz, ξ_d=2.04 %) is selected as the optimum configuration. However, it should be noted that this is an experimental optimization conducted among a limited range of dynamical properties, namely f_d=9.6–11.7 Hz and ξ_d=1.4–3.1 %. The Fig. 6 shows that the TMD greatly reduces the first peak of the FRF, which is also split into two smaller peaks as expected, and attenuates the amplitude of the displacement time signal.

Finally, a comparison of the experimental results with a numerical model, updated with the experimental properties of the frame scale model (Sect. 5.2) and of the TMD (Sect. 5.1), is conducted and depicted in Fig. 7. The correlation is very satisfying, the difference between experimental and numerical results is only due to the slight shift in the second and third frequencies obtained with the updated method (see Table 1).

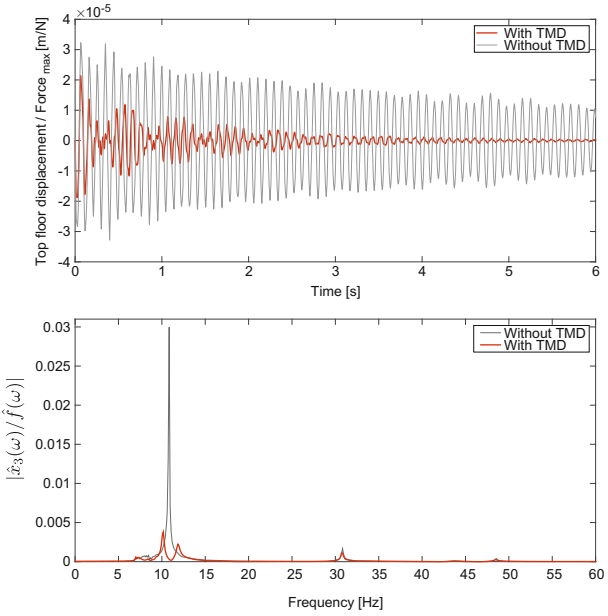

Fig. 6 Experimental time signals and FRF for TMD sets with the $\tilde{C}_2$ minimum values ($D_1 = 0.12$ mm and $D_2 = 4.35$ mm, corresponding to $f_d = 11.04$ Hz and $\xi_d = 2.04\,\%$)

Fig. 7 Comparison between experimental and numerical results for $f_d = 11.04$ Hz and $\xi_d = 2.04\,\%$: displacement time signals and FRF

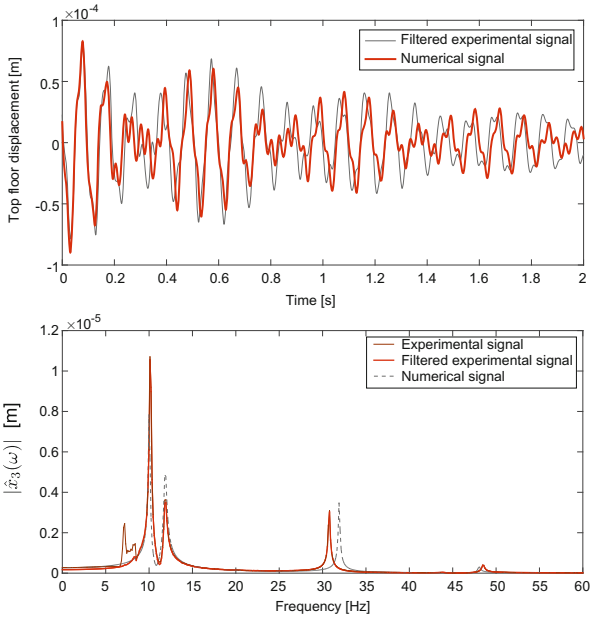

7 Conclusions

In this study, an experimental TMD endowed with adjustable stiffness and eddy current damping is studied. Several vibration tests were performed and the TMDs parameter estimation (damping ratio and frequency) was carried out using a modal identification method based on continuous wavelet transform. The objective was to evaluate the influence of the cable level stress and of the distance between the magnet and the conductive mass, making up the TMD, on the modal parameters of the latter. The eddy currents were shown to be effective to furnish the damping to the TMD device and the damping achieved is of viscous type. In particular, the damping ratio obtained depends on the distance of the circular magnet to the mass of the damper and decreases non-linearly with the considered gap. Conversely, the TMDs stiffness given by the slender cable connected to the mass increases linearly when the tensile stress in the cable is increased.

The TMD is then fixed on the top floor of a three stories frame scale model, and its optimal parameters are experimentally determined in order to control the first mode of the structure submitted to impulsive shocks. The TMD was found to be very effective, with an amplitude reduction of the first resonance of more than eighty percents. Finally, a very good correspondence between numerical and experimental results is shown.

References

1. Allani A (2015) Conception et optimisation d'amortisseurs à masse accordée pour les structures du génie civil. PhD Thesis, Università di Roma Tor Vergata & Université Paris Est
2. Allemang RJ (2003) The modal assurance criterion—twenty years of use and abuse. Sound Vib 14–20
3. Asami T, Nishihara O, Baz AM (2001) Closed-form exact solution to H_2 optimization of dynamic vibration absorber attached to damper linear systems. Trans Jpn Soc Mech Eng 67(655):597–603
4. Bae JS, Hwang JH, Roh JH, Kim JH, Yi MS, Lim JH (2012) Vibration suppression of a cantilever beam using magnetically tuned-mass-damper. J Sound Vib 331(26):5669–5684
5. Bekdaç G, Nigdeli SM (2011) Estimating optimum parameters of tuned mass dampers using harmony search. J Sound Vib 33:2716–2723
6. Den Hartog JP (1956) Mechanical vibrations. McGraw-Hill, New York
7. Ebrahimi B, Khamesee MB, Golnaraghi F (2008) Design and modeling of a magnetic shock absorber based on eddy current damping effect. J Sound Vib 315:875–889
8. Frham H (1909) Device for damped vibrations of bodies. U.S. Patent No. 989958, Oct. 30
9. Fujino Y, Abe M (1993) Design formulas for tuned mass dampers based on a perturbation technique. Earthquake Eng Struct Dyn 22(10):833–854
10. Gambarelli P, Vincenzi L (2015) A surrogate-assisted evolutionary algorithm for dynamic structural identification. CRC Press, Engineering Optimization IV
11. Gentile C (2007) Operational modal analysis of curved cable-stayed bridges, 2nd Int. Operational modal analysis conf, Copenaghen, Denmark
12. Graves KE, Toncich D, Iovenitti PG (2000) Theoretical comparison of motional and transformer EMF device damping efficiency. J Sound Vib 233(3):441–453

13. Greco R, Marano GC (2013) Optimum design of Tuned Mass Dampers by displacement and energy perspectives. Soil Dyn Earthq Eng 49:243–253
14. Hadi MN, Arfiadi Y (1998) Optimum design of absorber for MDOF structures. J Struct Eng 124(11):1272–1280
15. Kwok KCS, Samali B (1995) Performance of tuned mass dampers under wind loads. Eng Struct 17(9):655–667
16. Krenk S (2005) Frequency analysis of the tuned mass damper. J Appl Mech 72:936–942
17. Le TP, Argoul P (2004) Continuous wavelet transform for modal identification using free decay response. J Sound Vib 277(3):73–100
18. Lee C, Chen Y (2006) Optimal design theories and applications of tuned mass dampers. Eng Struct 28:43–53
19. Lo Feudo S, Allani A et al (2015) Experimental tuned mass damper based on eddy currents damping effect and adjustable stiffness. $12^{ème}$ Colloque National en Calcul des structures
20. Mordini A, Savov K (2007) The finite element model updating: a powerful tool for structural health monitoring. Struct Eng Int 17(4):352–358
21. Nishihara O, Asami T (2002) Closed-form solutions to the exact optimizations of dynamic vibration absorbers (minimizations of the maximum amplitude magnification factors). J Vib Acoust 124(4):576–582
22. Rana R, Soong TT (1998) Parametric study and simplified design of tuned mass dampers. Eng Struct 20(3):193–204
23. Sadek F, Mohraz B, Taylor AW, Chung RM (1997) A method of estimating the parameters of tuned mass dampers for seismic applications. Earthq Eng Struct Dyn 26(6):617–636
24. Sodano HA, Bae J (2004) Eddy current damping in structures. Vib Shock Handb 36:469–478
25. Soong TT, Dargush GF (1997) Passive energy dissipation systems in structural engineering. Wiley, New York
26. Wang Z, Chen Z, Wang J (2012) Feasibility study of a large-scale tuned mass damper with eddy current damping mechanism. Earthq Eng Eng Vib 11(3):391–401
27. Zilletti M, Elliott SJ, Rustighi E (2012) Optimisation of dynamic vibration absorbers to minimise kinetic energy and maximise internal power dissipation. J Sound Vib 331:4093–4100

Experimental Study on a Scaled Model of Offshore Wind Turbine on Monopile Foundation

Laura Kerner, Jean-Claude Dupla, Gwendal Cumunel, Pierre Argoul, Jean Canou and Jean-Michel Pereira

Abstract Offshore wind turbines are slender structures with sensitive dynamics, strongly influenced by soil-structure interaction. The structure is subjected to cyclic and dynamic loads with frequencies close to the first natural frequency of the offshore wind turbine. To avoid resonance phenomenon due to external excitations, it is essential to precisely evaluate the initial first natural frequency of the wind turbine and its long term evolution. The present work deals with the design and analysis of a scaled model of an offshore wind turbine with monopile foundation. This study is aimed at experimental evaluation of the initial first natural frequency of this scaled model, followed by the comparison of experimental results with those obtained from the existing analytical models.

L. Kerner (✉) · J.-C. Dupla · G. Cumunel · J. Canou · J.-M. Pereira
UMR 8205 CNRS-ENPC-IFSTTAR, École des Ponts ParisTech,
Laboratoire Navier Université Paris-Est, 6-8 Avenue Blaise Pascal,
77455 Marne-la-vallée, France
e-mail: laura.kerner@enpc.fr

J.-C. Dupla
e-mail: dupla@cermes.enpc.fr

G. Cumunel
e-mail: gwendal.cumunel@enpc.fr

J. Canou
e-mail: canou@cermes.enpc.fr

J.-M. Pereira
e-mail: pereira@cermes.enpc.fr

P. Argoul
IFSTTAR, MAST, SDOA, 14-20 Boulevard Newton, 77455 Marne-la-vallée, France
e-mail: pierre.argoul@ifsttar.fr

M. Frémond et al. (eds.), *Models, Simulation, and Experimental Issues in Structural Mechanics*, Springer Series in Solid and Structural Mechanics 8,
DOI 10.1007/978-3-319-48884-4_14

1 Introduction

Offshore wind turbines are one of the main elements contributing to the international energy transition. Their development rate is exponential in Europe. This phenomenon is illustrated in France with the Grenelle laws, aimed at the installation of wind farms on the north-west coast of France by 2020. These systems will have a total generation capacity of 6 GW.

Offshore wind turbines are submitted to various dynamic loads caused by the environment:

- Wind load: mast and blades are subjected to the wind load with natural frequencies below 0.1 Hz. The part of the mast not obstructed by the blades is only submitted to this load while the other part is also submitted to the blade passing frequency. This frequency (3P) corresponds to three times the frequency of the rotor (1P).
- Wave and currents load: the support structure is submitted to this load with natural frequencies below 0.12 Hz.

These loads and corresponding frequencies are summarised in Fig. 1. To avoid any resonance phenomenon, standard offshore wind turbines are designed as "Soft-Stiff" structures with their first natural frequency lying in the interval between the rotor frequency and the blade passing frequency.

The first natural frequency of the structure is, thus, an essential factor in the design of the offshore wind turbine and needs to be evaluated precisely. In this way, the aim of this work is the evaluation of the initial first natural frequency of an offshore wind turbine. A physical modelling was a relevant option to complete this work.

The first part of this chapter deals with the design of a scaled model of an offshore wind turbine with monopile foundation. As 75% of the actual offshore wind turbine are monopile-supported structures, this typical kind of foundation has been examined. A non-dimensional analysis has been conducted so as to define the relevant scaling factors that will allow us to reliably transcribe the main physical mecha-

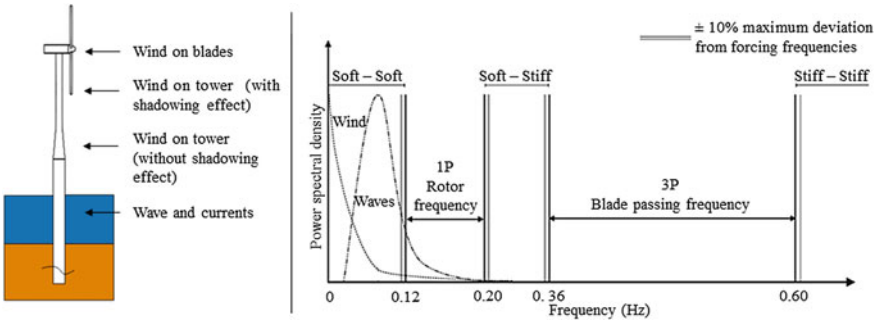

Fig. 1 Forcing frequencies plotted against the power spectral densities for the NREL 5 MW wind turbine [5, 9]

nisms influencing the dynamic response in the scaled model. A 1/100 brass scale model was built.

Experiments were carried out on the scaled model founded in a sandy soil submitted to various vertical stresses. The first natural frequency of the structure and its evolution according to the imposed vertical stress were measured with accelerometer mounted on the structure during free vibration tests.

Finally, an analytical study for the evaluation of the initial first natural frequency of the structure is presented. Different analytical methods have been considered: the standard methods based on Winkler springs and simplified methods based on an Euler-Bernoulli beam with elastic end support. The experimental and analytical results were compared and allowed us to determine the reliability of these methods.

2 Design of an Offshore Wind Turbine's Scaled Model

It is essential to carefully design the scaled model so that its behaviour can be interpreted on a full-scale wind turbine. Based on a full-scale model called prototype, the design of the model will take into account the wind turbine's structure, its dynamics and the relevant physical mechanisms which influence the turbine and the surrounding soil.

In this section, a non dimensional analysis has been conducted on the prototype of an offshore wind turbine and its surrounding soil. This analysis allows us to define the pertinent non-dimensional parameters. The characteristics of the model are then obtained with the prototype characteristics and the non-dimensional parameters.

2.1 Non Dimensional Analysis

The non-dimensional parameters were defined based on the Vaschy-Buckingham theorem or π-theorem. This analysis is divided in two parts: firstly the fluid flows around the structure created by wind, waves and currents and secondly the behaviour of the monopile and its surrounding soil.

2.1.1 Fluid Flows Around the Structure

The offshore wind turbine is submitted to two kinds of fluid flow:

- The wind flow on the mast and the blades
- The waves and currents on the support structure.

Relevant non Dimensional Numbers for Fluid Flow

The Reynolds R_e, Mach M_a, Froude F_r and Weber W_e numbers give informations about the considered fluid flows. These numbers are defined as summarized in Table 1, where the following notation has been adopted:

- ρ: Oncoming flow density (kg/m^3);

Table 1 Relevant non dimensional numbers

Reynolds	Mach	Froude	Weber
$R_e = \frac{\rho V L}{\mu}$	$M_a = \frac{V}{a}$	$F_r = \frac{V}{\sqrt{gL}}$	$W_e = \frac{\rho V^2 L}{\sigma_s}$

- V: Oncoming flow relative speed (m/s);
- L: Structure's dimension, typically the blades' size or the mast's diameter (m);
- a: Speed of sound in the considered environment (m/s);
- g: Gravitational acceleration (m/s^2);
- σ_s: Surface tension of the fluid (N/m).

Wind's speed on the structure doesn't exceed 70 m/s even for extreme wind with 50 years return. For a wind speed V = 70 m/s with a = 340 m/s, the Mach number is around 0.21. Thus, the Mach number will always be below 0.3 for both, the prototype and the scaled model. The Mach number has insignificant influence in this case, hence it has been neglected. Besides, the value $M_a = 0.21$ shows that the considered flow is incompressible. We have obtained similar results for the waves on the offshore wind turbine. Thus, in this case, the wind flow, the waves and the flow of currents can be considered as one incompressible flow. In order to model the structure, the incompressible flow will be considered in the non dimensional analysis.

Incompressible Free Surface Flow

According to Langhaar [14], the non dimensional drag load on the structure can be expressed as follows:

$$F_{drag} = \rho V^2 L^2 f(R_e, F_r, W_e) \tag{1}$$

The drag load depends on the Reynolds, Froude and Weber numbers. The Weber number is usually used for study of droplets and capillarity and can be disregarded in this case. In order to correctly model the flows around the structure, only the Reynolds and Froude numbers must be kept. These non dimensional parameters lead to the model laws summarized in Table 2, where the following scaling parameters have been adopted:

- Length scale: $\Delta = \dfrac{L_{model}}{L_{prototype}}$;
- Density scale: $K_\rho = \dfrac{\rho_{model}}{\rho_{prototype}}$.

If the Reynolds and the Froude numbers are both retained, only a full scale model can be considered. Hence, it is not possible to keep these two non dimensional parameters simultaneously. The exposure to waves and currents holds special importance in case of offshore wind turbines. These interactions are specifically defined by the Froude number. Thus, only the Froude number and its scaling factors were considered in order to design the model.

2.1.2 Monopile Foundation and Surrounding Soil

Just as wind and wave flows on the structure, the soil-structure interaction is one of the main criteria that has to be taken into account to design the model. In this section, a non dimensional analysis, focused on the monopile and its surrounding soil, allows us to define the relevant non dimensional groups.

Monopile Foundation: Stress and Strain

In this case, we have considered a monopile foundation submitted to a point load which is equivalent to the wind and waves resultant load on the structure. The relevant parameters to define the non dimensional stress and strain on the monopile are introduced in Table 3.

Using the π-theorem, the non-dimensional stress and strain on the monopile can be expressed as follows:

$$\sigma_p = \frac{F_g}{D_p^2} f\left(\frac{F_g}{E_p D_p^2}, \frac{y}{D_p}, \nu_p\right) \tag{2}$$

$$\varepsilon_p = \frac{F_g}{E_p D_p} f\left(\frac{F_g}{E_p D_p^2}, \frac{y}{D_p}, \nu_p\right) \tag{3}$$

Table 2 Reynolds and Froude model laws

Physical parameters	Unit	Reynolds scaling factors	Froude scaling factors
Length	m	Δ	Δ
Time	s	Δ^2	$\sqrt{\Delta}$
Frequency	Hz	Δ^{-2}	$\frac{1}{\sqrt{\Delta}}$
Speed	m/s	Δ^{-1}	$\sqrt{\Delta}$
Acceleration	m/s^2	Δ^{-3}	1
Weight	kg	$K_\rho \Delta^3$	$K_\rho \Delta^3$
Load	N	K_ρ	$K_\rho \Delta^3$

Table 3 Relevant parameters to define the non dimensional stress and strain on the monopile

Dimension	D_p	Monopile's diameter
Loads	F_g	Global point load on the wind turbine
	y	Lever arm's of the point load, moment on foundation being $M = F_g y$
Other parameters	E_p	Monopile's Young modulus
	ν_p	Monopile's Poisson ratio

Table 4 Relevant parameters to define the non dimensional stress in the soil around the pile

Dimension	D_p	Monopile's diameter
Loads	F_g	Global point load on the wind turbine
	y	Lever arm's of the point load, moment on foundation being $M = F_g y$
Other parameters	G	Soil's shear modulus

In this case, stress and strain in the foundation depend on the same non dimensional parameters. To preserve the behaviour of the foundation, these 3 non-dimensional groups must be kept constant between the prototype and the model: $F_g/(E_p D_p^2)$, y/D_p and ν_p.

Soil around the Monopile Foundation

The rotation of rotor and the loads due to wind and waves on the structure, create vibrations in the mast and the monopile. Hence, lateral motion of the pile causes a deformation field in the soil around the foundation. This deformation influences the soil stiffness. Thus, this phenomenon has an important impact on behaviour of the structure and needs to be taken into account for the scaled model. The relevant parameters to define the non dimensional stress in the soil around the pile are introduced in Table 4.

Using the π-theorem, the non-dimensional stress σ_{soil} in the soil around the foundation can be expressed as follows:

$$\sigma_{soil} = \frac{F_g}{D_p^2} f\left(\frac{F_g}{G D_p^2}, \frac{y}{D_p}\right) \tag{4}$$

Two non-dimensional groups allow us to preserve the behaviour of the soil. The first group $\frac{F_g}{G D_p^2}$ corresponds to the soil's strain as shown in [5]. The second group y/D_p is the same as the one found previously to express the strain and stress in the monopile.

Fontainebleau sand (NE34) was used in the experiments. It is essential to evaluate the impact of the grain size ratio between the model and the prototype. For a hollow pile in sand, the friction between soil and pile needs to be taken into account. According to Sedran et al. [16], it is possible to use the same sand for the prototype and the model if loads are below the ultimate tensile strength or if the ratio between the pile diameter and the grain size is: $D_p/D_{sand} \geq 30$. In addition to the non dimensional groups described above, this inequality needs to be checked.

Summary of the non Dimensional Groups

In conclusion, to design the scaled model and environmental loads, the Froude number and resulting scaling factors in Table 5 have to be kept constant. To model accurately the physical mechanisms in the foundation and its surrounding soil, the following non-dimensional groups given in Table 6 have to be considered.

Table 5 Froude model laws

Physical parameters	Unit	Froude scaling factors
Length	m	Δ
Time	s	$\sqrt{\Delta}$
Frequency	Hz	$\frac{1}{\sqrt{\Delta}}$
Speed	m/s	$\sqrt{\Delta}$
Acceleration	m/s^2	1
Weight	kg	$K_\rho \Delta^3$
Load	N	$K_\rho \Delta^3$

Table 6 Non-dimensional groups

	Physical mechanisms	Non-dimensional groups
Soil	Stress/strain	$\frac{F_g}{G D_p^2}$
	Grain size	$\frac{D_p}{D_{sand}} \geq 30$
Soil/monopile	Stress/strain	$\frac{y}{D_p}$
Monopile	Stress/strain	$\frac{F_g}{E_p D_p^2}$
	Poisson's ratio	ν_p

2.2 *From the Prototype to the Scaled Model*

In the previous section, scaling factors and non-dimensional groups have been defined so as to design the scaled model. However, these factors need to be implemented to a full-scale model to obtain the final dimensions of the scaled model as described in Fig. 2. Based on a reference offshore wind turbine, a 1/100 scale model was defined in this section.

2.2.1 5 MW Reference Offshore Wind Turbine

The NREL 5-MW offshore wind turbine was considered here as a prototype to design the scaled model as it is difficult to find the exact dimensions of a full scale offshore wind turbine. The National Renewable Energy Laboratory (NREL) defined a standardized offshore wind turbine based on prototype wind turbines as Multibrid M5000 and REpower 5M and on the conceptual models used in the WindPACT, RECOFF and DOWEC projects [12]. The characteristics of the wind turbine on monopile foundation used in this section are available in [6, 12] and showed on Fig. 2.

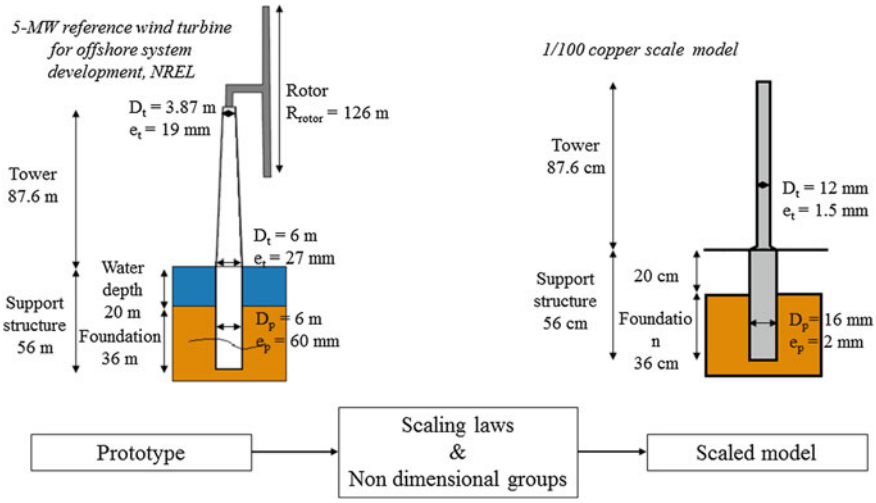

Fig. 2 Design steps: from the 5 MW reference offshore wind turbine prototype to the 1/100 brass scale mode

Table 7 Brass model characteristics

Physical quantities	Units	Values	
		Mast	Support structure
Mass	g	388	441
Length	mm	876	560
Diameter	mm	12	16
Thickness	mm	1.5	2
Natural frequency	Hz	56	120

2.2.2 1/100 Brass Scale Model

The model was obtained from 5 MW reference offshore wind turbine using the Froude model laws. It was decided to design a 1/100 scale model, the length scaling factor was necessarily equal to: $\Delta = L_{model}/L_{prototype} = 100$.

A dense and flexible metal was required to design the scaled model. Thus, lead, zinc, brass and copper were considered. The chosen material for the model is brass with a density $\rho = 8800\,\text{kg/m}^3$ and a Young modulus $E = 100\,\text{MPa}$ as a lead pile would be too fragile and brass piles are easily commercially available in comparison to zinc piles. The characteristics for the scaled model were obtained as reported in Table 7.

With these characteristics, the Froude model laws were considered in the scaled model. In this way, the model will recreate accurately the behaviour of an offshore wind turbine submitted to wave and current flows.

Table 8 Non-dimensional groups

	Physical mechanisms	Non-dimensional groups	Prototype	Model
Soil	Stress/strain	$\frac{F_g}{G D_p^2}$	$5.2 \cdot 10^{-4}$	$1.3 \cdot 10^{-4}$
	Grain size	$\frac{D_p}{D_{sand}} \geq 30$	$1.7 \cdot 10^3$	80
Soil/monopile	Stress/strain	$\frac{y}{D_p}$	9.2	34.4
Monopile	Stress/strain	$\frac{F_g}{E_p D_p^2}$	$3.7 \cdot 10^{-7}$	$1.1 \cdot 10^{-7}$
	Poisson's ratio	ν_p	0.30	0.37

2.2.3 Non-dimensional Groups

To complete the design of the model, the non dimensional groups were considered so as to model properly the foundation and its surrounding soil. The results in Table 8 were obtained for the prototype and the model.

The non dimensional groups of the prototype and the model are in the same order of magnitude. Also, the grain size ratio is higher than 30 in both cases. Thus, we can assume that the brass scaled model will accurately recreate the relevant physical mechanisms linked to soil-structure interaction.

Based on the design of the model, an experimental 1/100 scale model was set up. It was made up of an assembly of a 876 mm mast and a 560 mm support structure. The technical specifications (length, diameter, thickness, frequency) can be referred from Table 7. The only small change was the density of the material which was considered to be 8800 kg/m^3 in the design. The density of material (brass) used was slightly below the design consideration and was equal to 8500 kg/m^3.

3 Experimental Study, 1/100 Brass Scale Model

As the first natural frequency of an offshore wind turbine is a major criteria in the design of the structure, its accurate evaluation is essential. Thus, the soil-structure interaction, which strongly influences the structure's response, needs to be taken into account. The brass model will allow us to study its first natural frequency and its evolution according to the soil vertical confinement stress σ'_V from 0 to 200 kPa. These values correspond to the effective vertical stress of soil from the ground surface (0 kPa) to the bottom of the real monopile (200 kPa).

Table 9 Fontainebleau sand properties [11]

D_{50} (mm)	C_u	e_{min}	e_{max}	ρ_s (g/cm^3)	Angularity	Colour
0.21	1.5	0.56	0.88	2.65	Sub-rounded	Light beige

3.1 Set-Up and Experimental Procedure

In this section, the different steps of the experimental set-up are presented, followed by the typical test results obtained.

Soil sample: Fontainebleau Sand
The material used for the soil sample is the Fontainebleau sand NE34. It is one of the reference sand in France for research studies. The main properties of the sand are summed up in Table 9.

General Description
The sand sample was installed in a cylindrical tank with a 55 cm diameter and 45 cm depth. The sand was placed by layer: 9 layers of 5 cm each. The chosen relative density was $I_D = 0.7$. The brass model was then installed in the sand with a mallet. 36 cm of the support structure was driven in the soil in accordance with the NREL offshore wind turbine with a 36 m monopile foundation. To simplify the scaled model, we decided to model only the mast and the support structure. The rotor/nacelle assembly could be modelled by a point mass fixed on top of the mast. Finally, an accelerometer was attached with a strong glue on top of the model.

A vibration exciter was used to impose a brief impact on top of the model in order to measure the first natural frequency of the structure. The accelerometer registers the response of the structure.

To control the vertical confinement stress σ'_V of the soil, a rubber membrane filled with water and a metallic cover were introduced on top of the tank. This membrane allowed us to apply vertical stress by means of water pressure controlled by a servo-valve and measured with a pressure transducer. For the description of the set up refer to Fig. 3.

The first natural frequency of the structure was measured for the following soil vertical confinement stress $\sigma'_V = 0$, 10, 50, 100, 150 and 200 kPa. Five measures were done for each case.

Typical Results
The acceleration of the structure was registered after a brief impact. The graph in Fig. 4 shows the typical result obtained. The Fast Fourier Transform of the data allowed us to get the natural frequencies of the model. To get precise results, the data were actually analysed with wavelet transform [7] to obtain the natural frequencies.

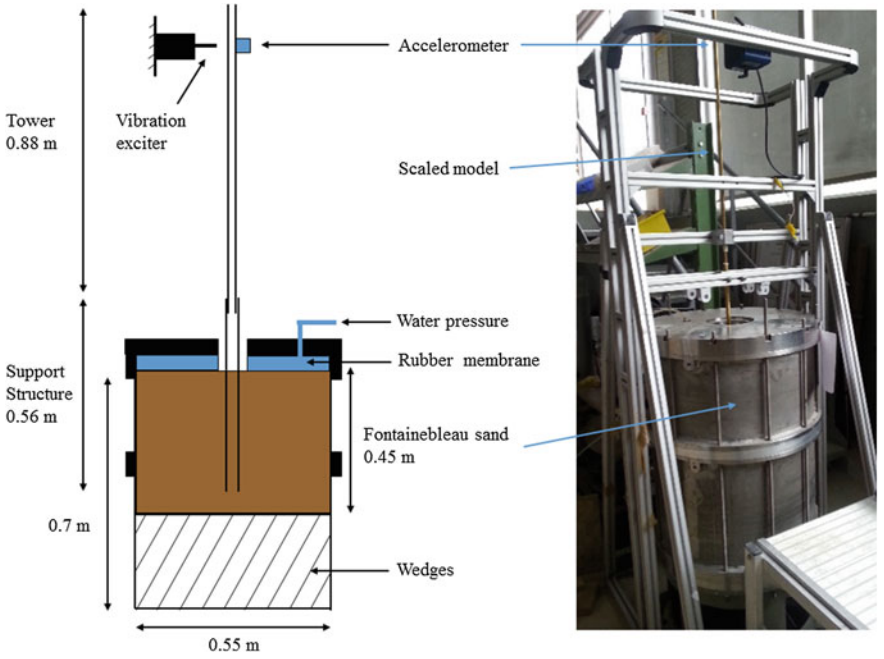

Fig. 3 Setting up diagram and picture of the experiment

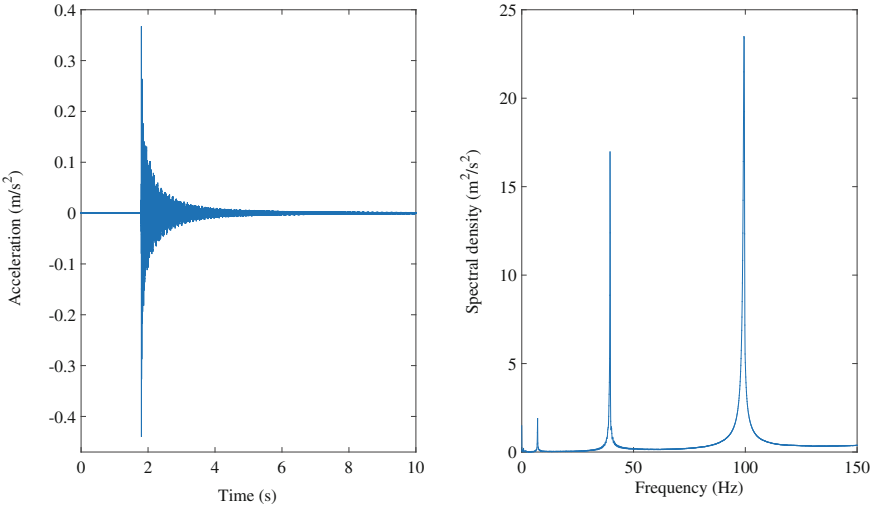

Fig. 4 Free response of the accelerometer after a brief impact and its Fast Fourier Transform

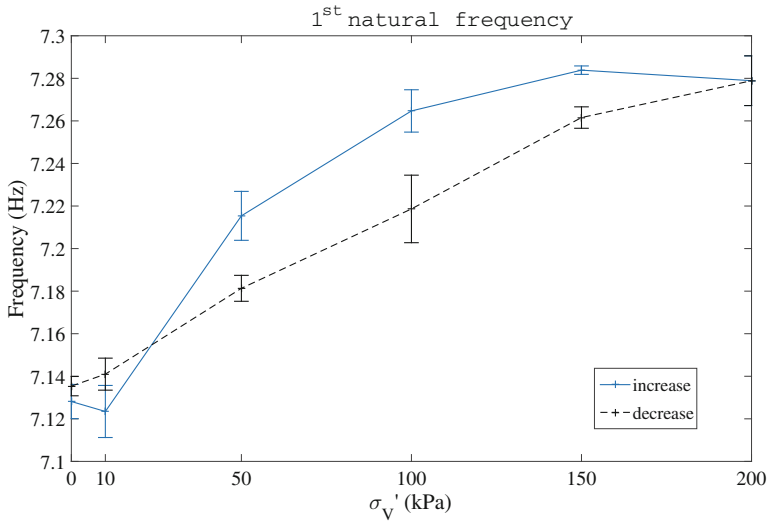

Fig. 5 Distribution of the first natural frequency of the structure with soil confinement stress

3.2 Results and Discussion

All the results have been gathered on the graph in Fig. 5. Five measures of the natural frequencies of the structure had been taken for a given confinement stress. These measures allowed us to check the uncertainty: less than 0.4% of the measured natural frequency.

The measures were done while increasing the stress (see the blue curve in Fig. 5) and decreasing the stress (the black curve). The general trend is the growth of the natural frequency of the model with the growth of the confinement stress in the soil. This result confirms that the stiffness of the soil has an important influence on the response of the structure. In fact, a 2.2% increase in the frequency was observed as the pressure increased from 0 to 200 kPa. Moreover, the natural frequency of the system was in general, higher during the increase of the confinement stress than during its decrease.

In the following section, the experimental results are compared to the results from the existing analytical methods for offshore wind turbines.

4 Analytical Study

To estimate the first natural frequency of an offshore wind turbine by considering its soil-structure interaction, three different methods can be considered:

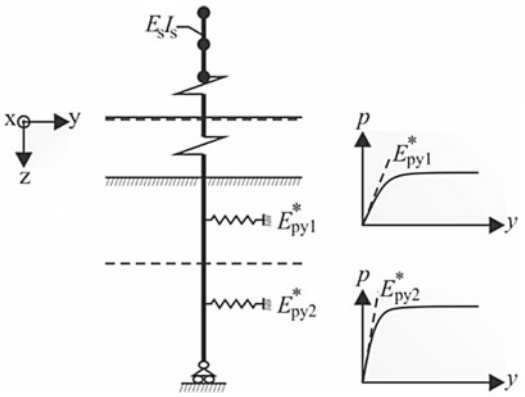

Fig. 6 API model: beam on the non-linear Winkler foundation (see [8])

- Standard method based on an Euler-Bernoulli beam on nonlinear Winkler foundation
- Simplified method based on an Euler-Bernoulli beam with elastic end support;
- FEM method.

This study is focused on the first two methods and the comparison with experimental work.

4.1 State-of-the-art, Analytical Models for Monopile Foundation

Monopiles for offshore wind turbines are usually designed using the official standards: the API [3] or the DNV standard [9]. In these guides, design of the foundation is based on the Winkler method. The wind turbine is modelled as a Euler-Bernoulli beam on nonlinear horizontal springs along the foundation. The behaviour of the springs is evaluated using p–y curves defined for sand in the standard and shown in Fig. 6. The initial stiffness E_{py} of each spring is given by the slope of the tangent to the p–y curve passing through the origin:

$$E_{py} = \left(\frac{dp}{dy}\right)_{y=0} = k\,z \tag{5}$$

The stiffness E_{py} depends on the initial modulus of subgrade reaction k (in Pa/m) and the considered depth z. k is a function of friction angle Φ and the relative density of the sand I_D.

This model is calibrated against the response of small diameter piles with a length to diameter ratio between 30 and 50 (for an offshore wind turbine this ratio is ranging between 4 and 8) according to [15]. Also, the p–y curves were calibrated considering piles with a flexible behaviour instead of the rigid behaviour of offshore wind turbine

monopiles. Finally, the soil-structure interaction in this method depends only on the characteristics of the soil, the structure is not taken into account.

The standard API method is then not well suited for offshore wind turbines. Indeed, the in-situ measurements from Walney offshore wind farm showed that there was an underestimation of the first natural frequency of the structure with an error between 5 and 7% [13]. Under small loads, the stiffness of the soil is underestimated. To overcome this issue, Kallehave [13] developed a modified API method which takes into account the diameter of the structure and thus increases the initial stiffness of springs E_{py}:

$$E_{py} = k \cdot z_{ref} \left(\frac{z}{z_{ref}}\right)^b \left(\frac{D}{D_{ref}}\right)^c \qquad Kallehave\ [13] \tag{6}$$

with

k	Initial modulus of subgrade reaction (Pa/m);
$z_{ref} = 2.5$ m	Reference depth;
$D_{ref} = 0.61$ m	Reference diameter;
$b = 0.6$	Dimensionless parameter governing the course of the initial stiffness with the depth;
$c = 0.5$	Dimensionless parameter.

However, the stiffness of the soil is overestimated by the API method under extreme loads [18] and a new method has been proposed by Sorensen [17] to reduce the initial stiffness of the soil. Therefore, E_{py} is defined as follows:

$$E_{py} = a \left(\frac{z}{z_{ref}}\right)^b \left(\frac{D}{D_{ref}}\right)^c \phi^d \qquad Sorensen\ [17] \tag{7}$$

with

$a = 50$ MPa	Reference value;
$z_{ref} = 1$ m	Reference depth;
$D_{ref} = 1$ m	Reference diameter;
ϕ	Internal friction angle;
$b = 0.6, c = 0.5, d = 3.6$	Dimensionless parameters.

An analytical model for offshore wind turbines supported on flexible foundation was proposed by [2, 4]. This method can make a quick estimation of the natural frequency of the system. In these models the offshore wind turbine is modelled by an Euler-Bernoulli beam founded on two springs (lateral and rotational springs) [2] or three springs (lateral, rotational and cross-coupling stiffness) [4], respectively. The springs are named as follow (see also in Fig. 7):

- K_L: lateral spring;
- K_R: rotational spring;
- K_{LR}: cross spring.

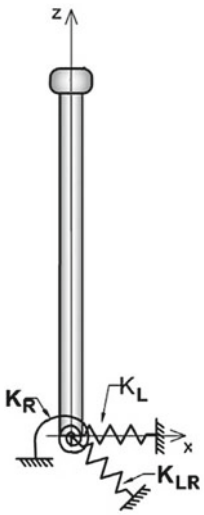

Fig. 7 Simplified model with elastic end support [4]

For estimation of the stiffness of springs, different methods are available:

- The Eurocode 8 part 5 [10] provides their values in Annex C "Pile-head static stiffness" considering pile's diameter, depth and three soil models;
- Experimental measurements defined in [2].

The authors presented two resolutions: an analytical and an approximate solutions. Both these methods are taken into account for the scaled model presented here.

More complex analytical and FEM models have also been defined to evaluate the influence of soil structure interaction for an offshore wind turbine [1, 8, 19]. We focused on the two methods described before as they provide a quick estimation of natural frequencies of the offshore wind turbine considering soil-structure interaction.

4.2 Standard API Model and Modified Standard Models

In this section, the first natural frequency of the scaled model was calculated considering 3 different methods:

- The standard API method;
- Sorensen method [17]: modified API method;
- Kallehave method [13]: modified API method.

The scaling factors defined in Table 5 were used to evaluate the initial stiffness of the soil. E_{py} expressed in Pascal, was then multiplied by the scaling factor $K_\rho \Delta$. For the modified API methods, the reference diameter was multiplied by the length

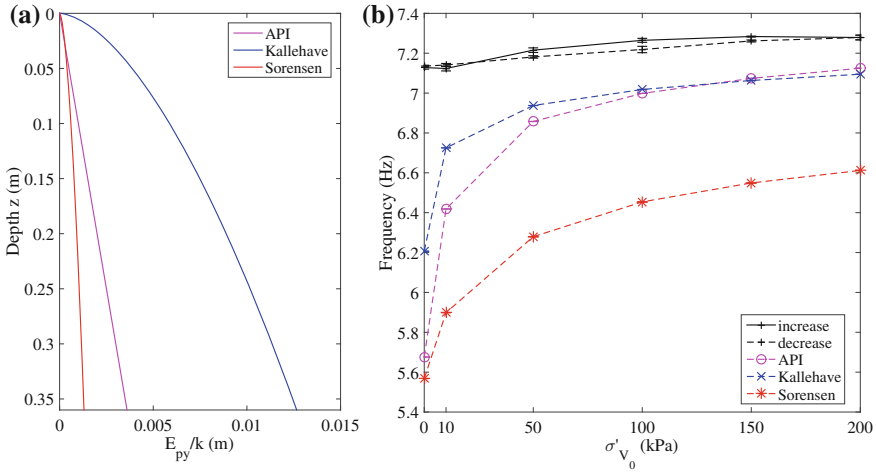

Fig. 8 (**a**) Evolution of E_{py} with depth for API and modified API methods. (**b**) First natural frequency of the structure according to the soil confinement stress for API. Comparisons with Sorensen and Kallehave models

scaling factor Δ. The scaled initial stiffness of the soil for API and modified API methods is shown in Fig. 8a. The first natural frequency were then calculated with the considered API and modified API methods. Figure 8b shows the obtained results which consists of distributions of the first natural frequency with the confinement stresses ranging from 0 to 200 kPa.

The analytical methods always underestimated the measured frequencies and these average errors are found:

- API method 7%;
- Kallehave method 5%;
- Sorensen method 13%;

The following inequality is then obtained for the measured and the calculated frequencies: $f_{Sorensen} \leq f_{API} \leq f_{Kallehave} \leq f_{scaledmodel}$. This trend is similar to the in-situ measurements and the calculated frequency presented by [13]. It can be concluded that the behavior of the scaled model represents correctly the behavior of a real offshore wind turbine.

4.3 Adhikari and Arany Models

In this section, the first natural frequency was calculated with the simplified methods proposed by Adhikari [2] and Arany [4]. The graphs in Fig. 9 show the results obtained for the following methods:

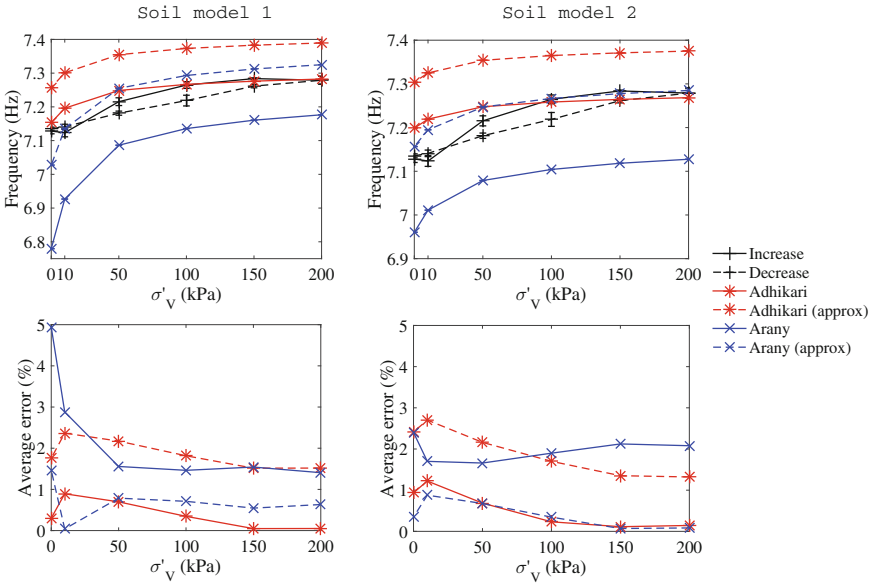

Fig. 9 First natural frequency of the structure according to the soil confinement stress for Adhikari and Arany models and the corresponding average errors

- Adhikari method: analytical and approximate results;
- Arany method: analytical and approximate results.

The first natural frequency and the average errors in the experimental results were calculated for each confinement stress. Two soil models were considered as defined in the Eurocode 8 [10]:

- Soil model 1: $E = E_s\, z/d$;
- Soil model 2: $E = E_s\, \sqrt{z/d}$;

with E is the Young's modulus of the soil model, E_S Young's modulus of the soil at the depth of the pile diameter, z the pile depth and d the pile diameter.

For both methods, the obtained results closely matched the experimental measurements with an average error below 5%. It was observed that for different soil models, trend of the obtained curves was similar. Moreover, the analytical Adhikari method and the approximate Arany method give the best results with an average error between 0.1 and 1.2%.

In our case, there is no necessity of including a cross spring in the model to obtain accurate results. In fact, the Adhikari method is well adapted to our experimental results. The chosen soil model impacts the calculated first natural frequency as it influences the value of the spring stiffness: K_L and K_R. Thus, a more precise experimental evaluation of these coefficients is needed.

5 Conclusions

In this study a 1/100 brass scale model was designed with the help of Froude model laws and non-dimensional groups linked to the monopile and its surrounding soil. This model recreated the behaviour of a full-scale offshore wind turbine and was found to be a relevant tool for the study of the initial first initial frequency of the structure.

The experimental measurements on the 1/100 scale model show the evolution of this natural frequency with the vertical confinement stress of the soil. The frequency increases with the confinement stress σ'_V. This result confirms the importance of precise evaluation of the soil parameters and their influence on the response of the structure.

These results were then compared to the standard API method, two modified API method as well as Adhikari and Arany methods. The standard method always underestimated the natural frequencies. It underlines that this method is not well adapted to offshore wind turbine and needs to take a more precise account of the monopile and the soil parameters. In fact, the modified API method defined by Kallehave showed results in better agreement with the experimental measurements as they consider the pile diameter for the calculations. Moreover, this comparison allowed to validate the scaled model which represents well the behavior of a real offshore wind turbine. The best results were obtained with Adhikari model with an average error below 1.2%. Even if this method is less complex, it is better suited for the modelling of the monopile and soil.

Experimental evaluation for the spring stiffness would allow us to improve the evaluation of the first natural frequency of the structure and is the aim of our future work. Moreover, the scaled model has been designed considering its dynamic behaviour. Thus, an analytical and experimental study of the response of the structure to the dynamic loads will also be carried out in the future.

References

1. Achmus M, Abdel-Rahman K (2012) Design of piles for offshore wind energy foundations with respect to horizontal loading. In: Proceedings of the twenty-second international offshore and polar engineering conference, vol 4, pp 143–150
2. Adhikari S, Bhattacharya S (2012) Dynamic analysis of wind turbine towers on flexible foundations. Shock Vibr 19:37–56
3. American Petroleum Institute (2000) API RP 2A-WSD. Recommended practice for planning, designing and constructing fixed offshore platforms working stress design
4. Arany L, Bhattacharya S, Hogan SJ, Macdonald J (2014) Dynamic soil-structure interaction issues of offshore wind turbines. In: Proceedings of the 9th international conference on structural dynamics, EURODYN, pp 3611–3618
5. Bhattacharya S, Lombardi D, Wood DM (2011) Similitude relationships for physical modelling of monopile-supported offshore wind turbines. Int J Phys Model Geotech 11:58–68
6. Bir G, Jonkman J (2008) Modal dynamics of large wind turbines with different support structures. Int Conf Offshore Mech Arctic Eng 6:669–679

7. Cumunel G (2008) Long-gage fiber optic extensometers for dynamic structural monitoring. PhD thesis, ENPC
8. Damgaard M, Zania V, Andersen LV, Ibsen LB (2014) Effects of soil-structure interaction on real time dynamic response of offshore wind turbines on monopiles. Eng Struct 75:388–401
9. Det Norske Veritas (2010) Offshore Standard DNV-OS-J101, design of offshore wind turbine structures
10. Eurocode 8 (2004) Eurocode 8: design of structures for earthquake resistance—Part 5: foundations, retaining structures and geotechnical aspects
11. Feia S, Sulem J, Canou J, Ghabezloo S, Clain X (2014) Changes in permeability of sand during triaxial loading: effect of fine particles production. Acta Geotech
12. Jonkman JM, Butterfield S, Musial W, Scott G (2009) Definition of a 5-MW reference wind turbine for offshore system development. Technical Report NREL/TP-500-38060
13. Kallehave D, LeBlanc Thilsted C, Liingaard MA (2012) Modification of the API p–y formulation of initial stiffness of sand. In: Offshore site investigation and geotechnics: integrated technologies—present and future, London, UK
14. Langhaar HL, Charcosset C, Sdille M (1956) Analyse dimensionnnelle et thorie des maquettes
15. Lombardi D, Bhattacharya S, Wood DM (2013) Dynamic soil-structure interaction of monopile supported wind turbines in cohesive soil. Soil Dyn Earthq Eng 49:165–180
16. Sedran G, Stolle DFE, Horvath RG (2001) An investigation of scaling and dimensional analysis of axially loaded piles. Can Geotech J 38:530–541
17. Sorensen SPH, Ibsen LB, Augustesen AH (2010) Effects of diameter on initial stiffness of p–y curves for large-diameter piles in sand. Num Methods Geotechn Eng 907–912
18. Thieken K, Achmus M, Lemke K (2015) A new static p–y approach for piles with arbirary dimensions in sand. Geotechnik 38:267–288
19. Zania V (2014) Natural vibration frequency and damping of slender structures founded on monopiles. Soil Dyn Earthq Eng 59:8–20